Loughborough University

Pilkington Library

Author/Filing Title ......DANSON, N......

....

Accession/Copy No.

Vol. No. .... | Class Mark ....

2 6 JUN 1998 | LOAN COPY

040147092X

BADMINTON PRESS
18 THE HALFCROFT
SYSTON
LEICESTER LE7 1LD
ENGLAND
TEL 0116 260 2917
FAX 0116 269 6639

NOVEL TECHNIQUES FOR THE CONTROL OF THE PROPERTIES OF REACTIVELY SPUTTERED THIN FILMS

by

Nigel Danson

A Doctoral Thesis submitted in partial fulfilment of the requirements for the award of

Doctor of Philosophy of Loughborough University

August 1996

© by Nigel Danson 1996

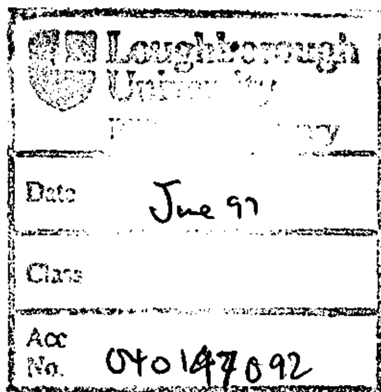
9910191X

ABSTRACT

Precise control techniques are of fundamental importance in the accurate deposition of optical, mechanical, electrical and magnetic thin films. The objective of this work was two fold: to devise and evaluate novel control systems for reactive sputtering primarily oxide films, and investigate the effects of these processes on resultant film properties.

Throughout the work the industrial scalability of the results was constantly borne in mind, since laboratory scale advancements may not naturally extend to large scale processes. The deposition process involved supply of reactive species, and energy to the substrate where desired compounds were formed. However, inherent in the reactive sputtering process are the dual problems of uncontrolled cathode arcing and of a partial pressure hysteresis instability caused by reactions also occurring at the target. Furthermore, properties such as stress are affected by the ion bombardment produced whilst magnetron sputtering. Before any consistent repeatable film results could be obtained these problems had to be specifically addressed and novel techniques devised in order to overcome them.

The well established technique of Plasma Emission Monitoring (PEM) was investigated, and further simplified by monitoring the potential appearing on the magnetron cathode, a measure of cathode status. Using this as an input to an active feedback loop enabled accurate control of reactive gas admission. An alternative to this, termed Sequential Pulsed Plasma Anodisation (SPPA), was developed from first principles, increasing process tolerance and overcoming problems which still remained. This consisted of pulsing the reactive gas flow, first to deposit a layer of metal and then to anodise that layer to obtain the desired film stoichiometry.

Although power supplies were tested that had extrinsic means of arc suppression, eliminating the cause of the arcs was found to be more effective. A medium frequency (AC) rectified power supply was developed for this purpose and aided the tight control

necessary in an iterative deposition system. However, it is of little use obtaining precise stoichiometry if associated film properties such as intrinsic or thermal stress, density, resistivity, or optical properties are found deleterious to the performance of the coating. To understand fully the effects of ion bombardment on these properties control of the ion flux was obtained by an electron-collecting-anode placed directly in front of the magnetron.

Compound coatings reactively sputtered during this work have been the optical films of SiO_2, TiO_2 and Indium tin oxide and ZnO:Al for applications requiring transparent conducting media.

Striving to optimise coatings for the environments for which they were designed demanded the development of a rapid interferometric stress analysis instrument. Further techniques of measuring film properties included; resistivity, spectrophotometry, ellipsometry, and Auger analysis.

ACKNOWLEDGEMENTS

Described in this thesis is work that could not have possibly been undertaken without the kind help, support and guidance of my supervisor, Professor R.P. Howson. I have learnt many things from his approach to the subject and I offer my sincere thanks.

I am also very grateful to Professor K. R. A. Ziebeck for allowing me to study in the Department of Physics and providing me with departmental sponsorship.

Special gratitude is also expressed to Raj & Ramesh in the electronics workshop and all the members of the departmental workshop. Their help and technical guidance was invaluable throughout this work.

Thanks also go to all the members of the Physics Department for their advice and friendship. Thanks to all the ladies in the general office for their light-hearted chats, without which, my time in the department would not have been the same. Special thanks go to past and present members of the Thin Films Group; Rick, Gareth and Martin. All of whom offered support and advice when things seemed to be going nowhere. Special thanks also go to my parents who have supported me throughout the last three years both financially and personally. Without their help I would have never been able to pursue a higher degree.

To Ann for her support and belief

THANKS

TABLE OF CONTENTS

CHAPTER 1 : INTRODUCTION

CHAPTER 2 : THE GLOW DISCHARGE AND SPUTTERING PROCESS

2.1 DISCHARGE THEORY AND PLASMA CHARACTERISATION **5**
2.1.1 The plasma 5
2.1.2 Electron and ion temperatures 5
2.1.3 Isolated probe in a glow discharge 6
2.1.4 Probe measurements in a plasma, the Langmuir probe. 8
2.2 DC GLOW DISCHARGE **10**
2.2.1 Fundamental regions of the discharge 10
2.2.2 Sustenance of the discharge 12
2.2.2.1 Secondary electron emission 13
2.3 THE PHYSICAL SPUTTERING PROCESS **13**
2.3.1 Ion impact processes 14
2.3.2 Sputter yield, threshold and efficiency 15
2.3.3 Preferential Sputtering 17

CHAPTER 3 : MAGNETRON THEORY AND DESIGN

3.1 COMPETING DEPOSITION TECHNOLOGIES **20**
3.1.1 Evaporation 20
3.1.2 Sputtering without a magnetic confinement field 21
3.1.2.1 Ion beam sputtering 21
3.1.2.2 DC Diode Sputtering 21
3.1.2.3 DC Triode Sputtering 24
3.1.2.4 Radio Frequency (RF) Sputtering 25
3.1.3 Advantages of Magnetron Sputtering 26
3.2 MAGNETRON FUNDAMENTALS **27**
3.2.1 Electron confinement 30
3.2.1.1 In a magnetic field 30
3.2.1.2 In an electric field 32
3.2.1.3 In a combined field 32
3.2.2 Voltage, Current and Pressure Relationships 36
3.3 VARIOUS PLANAR MAGNETRON CONFIGURATIONS **38**
3.3.1 Balanced 39
3.3.2 Unbalanced 40
3.3.3 Magnetron advancements 41
3.4 TARGET UTILISATION AND COATING UNIFORMITY **42**

CHAPTER 4 : REACTIVE MAGNETRON SPUTTERING

4.1 INSTABILITIES IN REACTIVE SPUTTERING **45**
4.1.1 Differential target poisoning 45
4.1.1.1 The elemental mode 45
4.1.1.2 The poisoned mode 45
4.1.2 The hysteresis effect and solutions 46
4.1.3 Differential cathode poisoning 51
4.2 EXISTING TECHNIQUES FOR GAS CONTROL **53**
4.2.1 Partial pressure control 53
4.2.2 Light emission from a plasma 53
4.2.3 Cathode potential 56
4.2.4 Feedback control 57
4.3 TARGET ARCING AND SOLUTIONS **59**
4.3.1 Arc mechanisms 59
4.3.2 Arc suppression 65
4.3.3 AC sputtering and the TwinMAG™ 66
4.4 COMPETING TECHNIQUES **69**
4.4.1 RF sputtering of insulating cathodes 69
4.4.2 Compound targets 69
4.4.3 Successive Plasma Anodisation (SPA) 70

CHAPTER 5 : THIN FILM FORMATION AND STRUCTURE

5.1 FACTORS INFLUENCING THIN FILM GROWTH **74**
5.1.1 Particles arriving at the substrate 76
5.1.2 Substrate self-bias 78
5.1.3 Ion bombardment at the substrate 78
5.1.3.1 The ion/atom ratio 80
5.2 THIN FILM NUCLEATION THEORY **82**
5.2.1 Stages prior to continuous film formation 82
5.2.2 Interface formation 85
5.3 MORPHOLOGY AND STRUCTURE ZONE MODELS **86**
5.3.1 Microstructure 86
5.3.2 Densification 89
5.3.3 Crystal structure and grain size 91
5.3.4 Film topology 93
5.4 COMPOUND FORMATION **94**
5.4.1 Refractive index 95
5.5 STRESSES IN THIN FILMS **98**
5.5.1 Stress models 100
5.5.1.1 Tensile stress models 101
5.5.1.2 Compressive stress models 102
5.5.1.3 Impurity model 102
5.5.1.4 Forward sputtering or atomic peening model 103
5.5.2 Dependence on deposition parameters 104

Chapter 6 : Experimental Apparatus and Procedure

6.1 Vacuum system configuration **110**
6.1.1 Construction 110
6.1.2 Operating methodology 112
6.1.3 The pumping system 113
6.1.4 Gas admission and flow measurements 113
6.1.4.1 Noble gas specifics 114
6.1.4.2 Reactive gas specifics 114
6.2 Magnetron design and performance **114**
6.2.1 Construction and mounting 115
6.2.2 Target utilisation 118
6.3 The electron-collecting-anode **119**
6.4 Magnetron power deliverance **120**
6.4.1 The MDX Magnetron driver 121
6.4.1.1 AC Driver with and without output rectification. 121
6.5 Process control techniques **124**
6.5.1 Measure of target status 125
6.5.1.1 Voltage used as an indication of target status, ϕ_v 125
6.5.1.2 Plasma emission used as an indication of target status, ϕ_e 125
6.5.2 The feedback control unit 128
6.5.2.1 Continuous feedback control (CFC) 129
6.5.2.2 Successive pulsed plasma anodisation (SPPA) 130
6.5.3 The compacted oxide targets 132
6.6 Target specifications **133**
6.7 Deposition procedure **134**
6.8 *In situ* measurements **135**
6.8.1 Substrate temperature 135
6.8.2 Ion bombardment 136

Chapter 7 : Film Evaluation and Analysis

7.1 Optical constant assessment **139**
7.1.1 Ellipsometry 139
7.1.2 Transmittance and reflectance 140
7.2 Mechanical properties : Intrinsic stress **142**
7.2.1 The Stoney Formulation 142
7.2.2 Interferometric analysis 146
7.2.2.1 Curvature determination and measurement 147
7.2.2.2 Thermal compensation stage construction 151
7.3 Thickness determination **153**
7.3.1 Tolansky technique - Fizeau fringes 154
7.4 Electrical characteristics **155**
7.4.1 Sheet Resistance 156
7.5 Auger electron spectroscopy (AES) analysis **158**

Chapter 8 : Results I : Preliminary Work

8.1 Chromium (Cr) **160**

8.2 TITANIUM (TI) 161
8.2.1 Langmuir probe measurements 161
8.2.1.1 Argon partial pressure, Ar_{pp} 162
8.2.1.2 Anode 163
8.2.2 Stress 164
8.2.2.1 Argon partial pressure 164
8.2.2.2 Anode 165
8.3 CHAPTER SUMMARY 166

CHAPTER 9 : RESULTS II : FEEDBACK CONTROL - A NEW APPROACH

9.1 THE CONTROL SIGNAL : VOLTAGE OR LIGHT EMISSION 168
9.2 THE CONTROL METHOD : CONTINUOUS OR PULSED. 169
9.2.1 Continuous feedback control (CFC) 169
9.2.1.1 Process instability to arcs 171
9.2.2 Successive Pulsed Plasma Anodisation (SPPA) 172
9.2.2.1 The pulse waveform 172
9.2.2.2 Factors affecting the SPPA process 173
9.2.2.3 Initialisation routine 176
9.3 CHAPTER SUMMARY 178

CHAPTER 9 : RESULTS III : MATERIALS

10.1 OPTICAL FILMS 180
10.1.1 Titanium dioxide, TiO_2 180
10.1.2 Silicon dioxide, SiO_2 183
10.2 TRANSPARENT CONDUCTING OXIDES (TCO) 190
10.2.1 Indium tin oxide, ITO 190
10.2.1.1 Compacted oxide ITO target 191
10.2.1.2 Indium tin target 198
10.2.1.3 Comparison of the two sputtering techniques 200
10.2.2 Zinc aluminium oxide, ZnO:Al 200
10.2.2.1 ZnO:Al Compacted oxide target 201
10.2.2.2 Zn:Al tiled target 202
10.3 ALUMINIUM OXIDE, AL_2O_3 209
10.4 THE ION/ATOM RATIO 211
10.5 CHAPTER SUMMARY 212

CHAPTER 11 : CONCLUSIONS AND FUTURE WORK

CHAPTER 1

INTRODUCTION

In recent years there has been an increase in the number of applications of thin films, particularly in the fields of optics and electronics. Currently, the majority of these coatings are deposited using conventional thermal evaporation. This technique suffers from imperfections such as low packing density, low hardness, and poor resistance to environmental factors because of the low thermal energy of the evaporated material.

As the need for more efficient performance and precise, high quality thin films has arisen, together with the advancement of multilayer coatings the development of existing alternative techniques has been sought. One such technique is that of magnetron sputtering, the deposition tool used throughout this work. This technique has the advantage of energetic film activation because of its low pressure operation and *in situ* self-bias, caused by the magnetic field arrangement. Materials can be deposited with high packing density, high deposition rates, and more importantly, at room temperature using this technique.

The majority of the materials required by the thin film industry, however, are not single element coatings but compound films. These can be sputtered by radio frequency power, from compound targets, but this technique suffers from poor deposition rates and expensive peripherals. A more versatile technique, reactive sputtering, is used during this work to sputter the metal constituent in an atmosphere containing the reactive gas, forming the desired compound on the substrate. However, this suffers from major control problems caused by a partial pressure hysteresis instability owing to the reaction process also occurring at the target.

Ideally, in high rate reactive sputtering, the reaction would occur only at the substrate and away from the cathode. Obviously, this is not totally possible, and thus, the need for control of the reactive gas flow arises. A process has previously been described to control continuously the flow of reactive gas by monitoring the radiation stimulated in the discharge. This technique is known as plasma emission monitoring (PEM).

However, during this continuous control process, the target is still slightly poisoned by the reactive gas and, owing to local erosion at the cathode surface, the target poisoning is differential. When sputtering materials such as Al_2O_3 and SiO_2, a highly insulating film is formed on these distinct regions of the cathode. These films create another problem inherent in reactive sputtering when using DC power application. That problem is uncontrolled cathode arcing and is caused by the build-up of charge on the part of the cathode surface that is covered by the insulating compound.

The objective of this thesis was two-fold. Firstly, to devise and evaluate novel techniques for the control of the reactive sputtering process and secondly, to analyse the effect these techniques had on resultant film properties.

A novel process is described that consisted of sputtering a layer of target material and then anodising the layer with a self-biased oxygen plasma. The technique, termed successive pulsed plasma anodisation (SPPA), involved pulsing the reactive gas into the system in response to parameters indicative of the poisoned state of the target. Both the plasma emission and the cathode voltage were investigated as measures of the target poisoning. The process proved to be successful for the deposition of optical, electrical and mechanical films, offering greater versatility, increased process tolerance and more precise control over film stoichiometry than other control techniques such as continuous feedback control. In particular, the pulsed gas process solved the very difficult problem of reactively sputtering from a target composed of two different materials. The results obtained for the deposition of zinc aluminium from such a composite target, showed that the technique of pulsing the reactive gas enabled films of low resistivity to be produced.

The thesis is arranged in eleven distinct chapters. Chapters 2-5 contain the background necessary for a full understanding of magnetron sputtering and the processes developed. Chapter 2 introduces and characterises the glow discharge and then goes on to relate this to a simple DC sputtering system. A description of the sputtering system relevant to this work, magnetron sputtering, is given in detail in chapter 3, along with a review of other deposition tools used in the coating industry. Control of the reactive sputtering process was the main objective throughout the work described in this thesis. Therefore, chapter 4 details extensively the problems associated with introducing a reactive component to the deposition environment. Chapter 5 characterises the formation of a thin film onto a

substrate with particular emphasis on the parameters associated with an unbalanced magnetron. The chapter details the effects controlled ion bombardment, created by the unbalanced magnetron, has on the growing film. It goes on to discuss the effects of the film structure on intrinsic stress, a parameter characterised for all the materials deposited during the research period.

Chapter 6 describes the experimental apparatus used during the work, and details the general experimental procedure followed. A significant part of this chapter concentrates on the technical details of the control systems developed for reactive sputtering. This chapter also describes the operation of the medium frequency rectified power supply developed during this work for cathode arc elimination. Films were analysed for electrical, optical and mechanical behaviour and a description of the characterisation techniques used is given in chapter 7. Stress was analysed throughout the work and a detailed description of its measurement, using a purposely devised interferometric technique, is also given in this chapter.

Chapters 8, 9 and 10 present the results obtained together with appropriate discussion. The preliminary results, for non-reactive deposition of metals, are given in chapter 8 along with a description of the ion bombardment control techniques used. Chapter 9 characterises the behaviour of the SPPA process in terms of the general deposition of a compound. The main body of results for all the materials deposited, using the various reactive sputtering techniques developed, is presented in chapter 10. This chapter is set out into classes of materials beginning with the optical coatings, TiO_2 and SiO_2, then transparent conducting oxides of ITO and ZnO:Al, going on to mention briefly Al_2O_3. Following the results and their discussion, each chapter concludes with a concise collection of the findings, in the chapter summary.

Chapter 11 offers concluding remarks and suggestions for further research on the basis of the results presented throughout the work.

CHAPTER 2

THE GLOW DISCHARGE AND SPUTTERING PROCESS

To understand fully the concepts of a glow discharge, a thorough knowledge of an idealised homogeneous plasma is needed. Based on this well-defined model, the physics of a more general discharge, a glow discharge, can be derived. The following chapter introduces and characterises a plasma and relates this to the glow discharge. Referring to this glow discharge, the fundamental phenomena relevant to the sputtering process, the deposition technique used throughout this work, can be understood.

2.1 DISCHARGE THEORY AND PLASMA CHARACTERISATION 5
2.1.1 The plasma *5*
2.1.2 Electron and ion temperatures *5*
2.1.3 Isolated probe in a glow discharge *6*
2.1.4 Probe measurements in a plasma, the Langmuir probe. *8*
2.2 DC GLOW DISCHARGE 10
2.2.1 Fundamental regions of the discharge *10*
2.2.2 Sustenance of the discharge *12*
2.2.2.1 Secondary electron emission 13
2.3 THE PHYSICAL SPUTTERING PROCESS 13
2.3.1 Ion impact processes *14*
2.3.2 Sputter yield, threshold and efficiency *15*
2.3.3 Preferential Sputtering *17*

2.1 Discharge theory and plasma characterisation

2.1.1 The plasma

A plasma can be defined as a partially ionised (an ionised fraction of 1×10^{-4} in sputtering plasmas) gas consisting of equal numbers of positive and negative charges and a different number of un-ionised neutral molecules. Furthermore, for a collection of charged particles to be considered a plasma, the characteristic diameter of the plasma, d_p, must be much greater than the Debye length, λ_D. The Debye length is defined as the minimum distance over which charged particles with different signs can maintain electrical neutrality [1] and will be defined quantitatively in section 2.1.3. Owing to the fact that charged particles can move freely in a plasma they are not defined in terms of size or number as are many other phenomena, but in terms of density.

2.1.2 Electron and ion temperatures

The plasma of a glow discharge is continually in equilibrium, maintaining a steady state of electron and ion densities. Thus, recombination of the various species must be balanced by ionisation of neutral atoms and molecules. It can be shown that, for electrons within a plasma gas, their average energy is characterised by kT_e

$$\frac{1}{2} m_e \bar{v}_e^2 = \frac{3}{2} k T_e \qquad [2.1]$$

where $\bar{v}_e$ is the mean electron speed and T_e is the electron temperature in the plasma which follows a Maxwell-Boltzmann distribution. The average electron temperature within a glow discharge is ~2 eV. However, there are often two populations of electrons with different T_e.

2.1.3 Isolated probe in a glow discharge

If an isolated probe is placed into the plasma then it will be bombarded by electrons and ions with current densities of

$$j_e = \frac{en_e\overline{v}_e}{4} \qquad [2.2]$$

$$j_i = \frac{en_i\overline{v}_i}{4}. \qquad [2.3]$$

However, the mean speed of ions is much smaller than that of electrons, $\overline{v}_i << \overline{v}_e$, and the probe immediately starts to build up a negative charge. This charge attracts ions and repels electrons and their quasi-random motion in the region of the probe is disturbed. Eventually, an equilibrium condition is reached, such that the ion flux is balanced by the electron flux. This mechanism is referred to as ambipolar diffusion. Moreover, an electric field is created in this region, the plasma, at the plasma potential, V_p, and the probe at a floating potential, V_f. Figure 2.1 shows the potential gradient associated with this phenomena. Only electrons with enough kinetic energy to overcome this potential barrier reach the probe whereas ions are accelerated towards the probe.

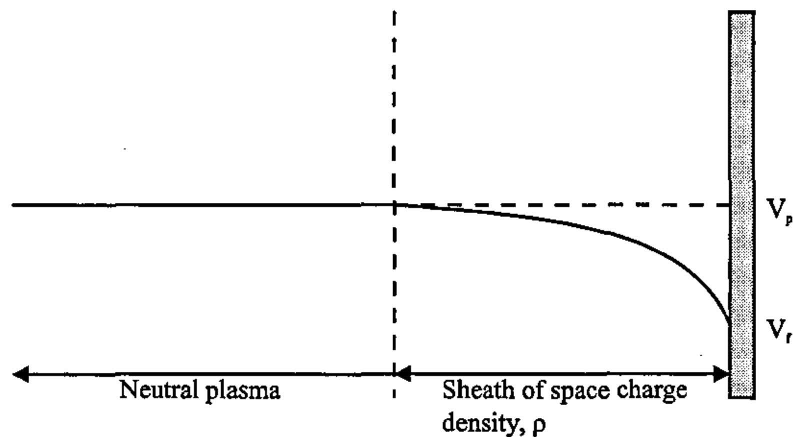

Figure 2.1 : The potential gradient associated with a sheath

It can be shown that under ideal conditions the plasma potential is given by

$$V_p = kT_i \ln\left(\frac{2}{q_i}\right) \tag{2.4}$$

where T_i and q_i are the temperature and charge of the ions involved. The total current from a probe of area A_p is

$$I = -eA_p\left(\frac{1}{4}n_i\overline{v}_i - \frac{1}{4}n_e\overline{v}_e\right) \approx \frac{1}{4}eA_p n_e \overline{v}_e > 0. \tag{2.5}$$

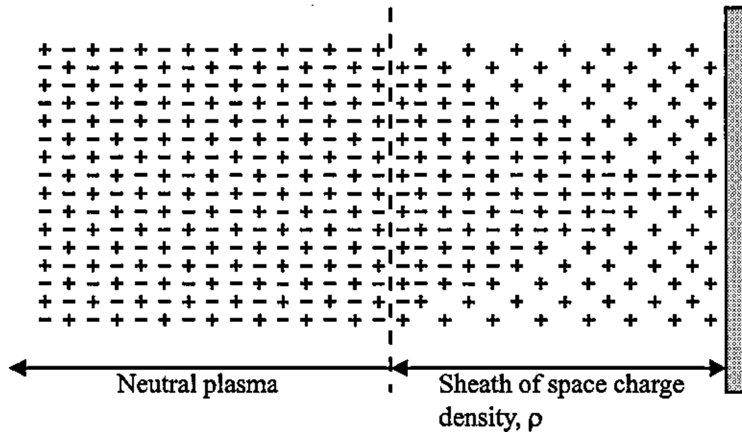

Figure 2.2 : The distribution of charge within a sheath

Figure 2.2 shows the formation of a sheath, a space charge of net positive charge, around the probe. This region is depleted in electrons, and thus, does not glow to the same intensity as the surrounding plasma and is termed the 'dark space'. It is characterised by Poisson's equation and it can be shown [2] that the potential difference, V_p-V_f, is given by

$$V_p - V_f = \frac{kT_e}{2e}\ln\left(\frac{m_i T_e}{m_e T_i}\right). \tag{2.6}$$

It should be noted that ions accelerated by the sheath will strike an electrically isolated substrate with a kinetic energy equivalent to the sheath voltage, typically ~20 V [3]. This has several severe consequences in thin film deposition processes such as sputtering.

One such consequence is that the inter-atomic binding energies of a thin film, which are typically ~ 1-3 eV, may be affected by these energetic ions.

Another important term used in defining the behaviour of a plasma glow discharge is the Debye length, as introduced earlier. It describes the radius of a sphere outside which any interactions causing fluctuations to the plasma potential are attenuated and is quantitatively characterised in equation 2.7.

$$\lambda_D = \left(\frac{kT_e \varepsilon_0}{n_e e^2} \right)^{\frac{1}{2}}. \qquad [2.7]$$

This result describes λ_D as a function of n_e and T_e, and is independent of the plasma gas.

Another factor important in measuring the characteristics of a plasma, and moreover, in determining the ion and electron current at the substrate, is the mean free path, λ_m, given by

$$\lambda_m = \frac{\overline{v}_s}{\nu} \qquad [2.8]$$

where ν is the collision frequency and $\overline{v}_s$ is the root mean square velocity.

2.1.4 Probe measurements in a plasma, the Langmuir probe.

Section 2.1.3 introduced the formation of a sheath around an electrically isolated probe placed in a glow discharge. The following section describes the effects of placing a probe with an associated bias voltage into the discharge. A return current path is created by an electrically conducting wall connected to ground as shown in figure 2.3a. The current/voltage (I/V) characteristics of the single probe are shown in figure 2.3b.

When the probe is biased positive with respect to the local plasma potential, V_p, the flux of all the negative particles to the probe is collected and electron current saturation occurs, I_{se}. At a given potential, the electron and ion current densities are equal, $j_e = j_i$, and the total probe current is zero. As mentioned earlier, the probe potential at this point is the floating potential, V_f. For $V > V_p$ the net current density at the probe, j, is given by equation 2.9.

$$j = \frac{en_i\overline{v}_i}{4}\exp\left(-\frac{e\left(V - V_p\right)}{kT_i}\right) - \frac{en_e\overline{v}_e}{4}. \qquad [2.9]$$

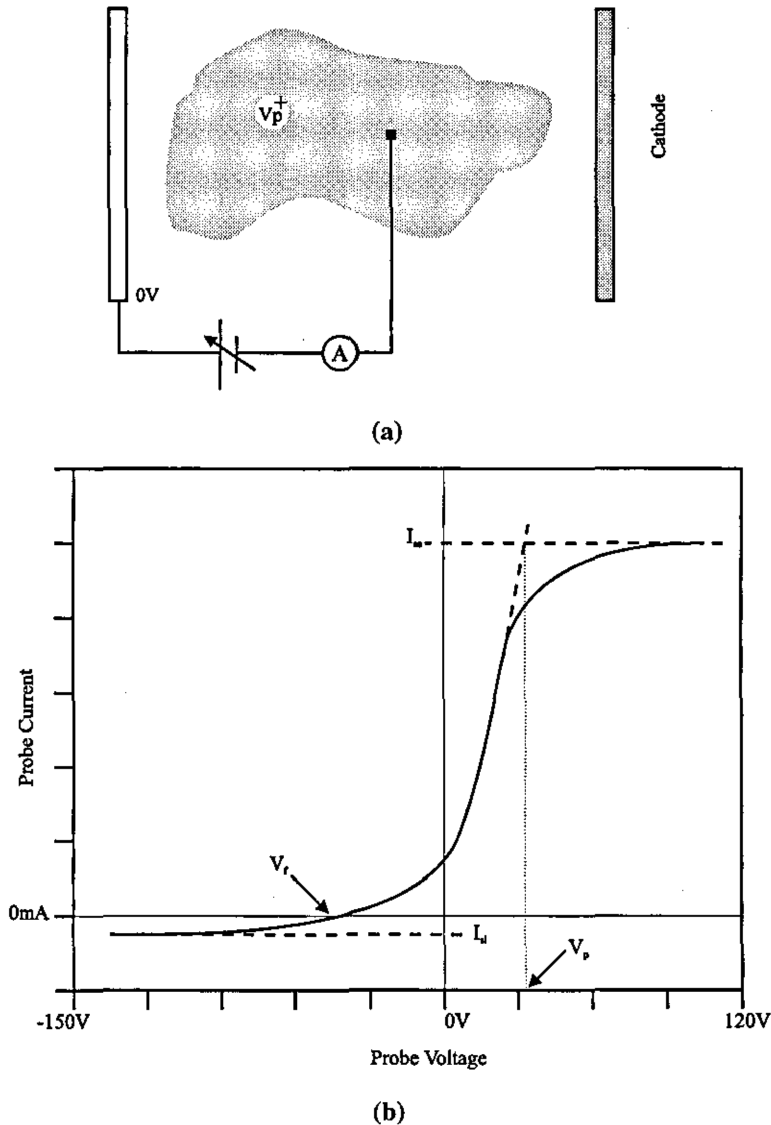

Figure 2.3 : (a) Schematic of probe measurements within a plasma, (b) Typical I/V characteristic of the probe

It can be seen from this equation that V_p is well defined at the knee of the curve in figure 2.3b.

When the probe is biased negatively with respect to the local plasma potential, ions are collected and the ion saturation current, I_{si}, is measured. For $V < V_p$

$$I_{si} = A_p\left[\frac{en_i\bar{v}_i}{4} - \frac{en_e\bar{v}_e}{4}\exp\left(-\frac{e(V_p - V)}{kT_e}\right)\right]. \quad [2.10]$$

2.2 DC Glow discharge

Although throughout this work, magnetron sputtering was the sole deposition technology used, as an introduction to sputtering, simple DC glow discharges are dealt with below without any reference to the effects of magnetic confinement. Chapter 3 introduces magnetron sputtering and relates the fundamental results obtained in the following section to plasma confinement in the vicinity of the cathode.

A DC glow discharge is, in many respects, described by the theory of a homogeneous plasma and the equations derived in section 2.1 can be used in quantifying some regions of the discharge. It should be noted, however, that a glow discharge does not have the well defined potential or equilibrium conditions of a plasma and the following section strives to emphasise the differences between the practicality of obtaining a discharge and the theoretical nature of an idealised plasma.

2.2.1 Fundamental regions of the discharge

Figure 2.4 illustrates the main regions of interest in a glow discharge obtained by applying a large potential (~1000 V) between the two electrodes. Set out below is a brief description of these regions detailing their luminosity, potential, physical nature and electric field characteristics. To try to describe qualitatively the phenomena occurring in a glow discharge, recombination, ionisation and energy loss processes are explained.

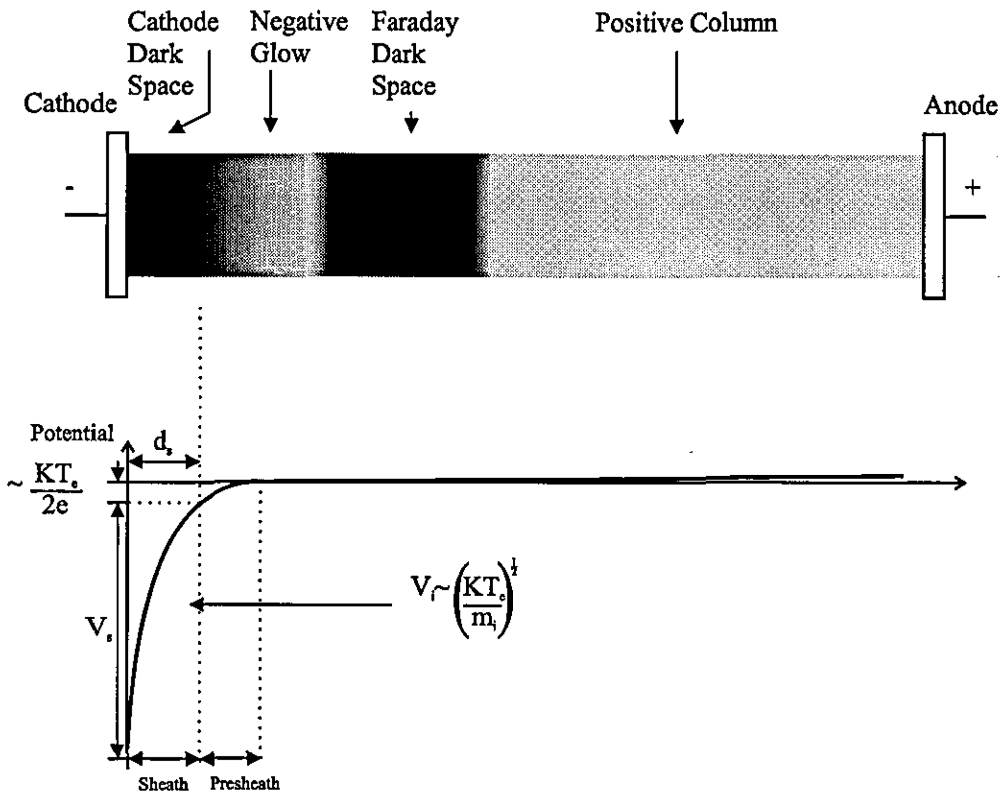

Figure 2.4 : Fundamental regions of a glow discharge

Cathode Dark Space

The cathode dark space is a plasma sheath, as described in section 2.1.3, and is caused by the negative potential at the cathode. This negative voltage with respect to the plasma potential creates a large electric field that accelerates ions and depletes the region of electrons. In this sheath region, very little ionisation occurs, resulting in a dark space of little or no luminosity. There is a similar sheath at the anode, but it is too thin to be observed by the naked eye.

Negative Glow

In both the negative glow region and the positive column region, the glow discharge most closely resembles the physics of a plasma. The negative glow region is characterised by a bright glow which is the result of the excitation and recombination processes of ions and high energy secondary electrons accelerated through the cathode dark region. The

origin of these secondary electrons will be discussed in section 2.2.2.1. Since the electrons screen the ions, the latter are not aware of the existence of the electrodes and they move through the negative glow by diffusion, rather than drifting in the field. However, this is not the case in a magnetron arrangement as will be explained in chapter 3.

Faraday Dark Space

The secondary electrons enter the negative glow with essentially the full cathode potential and, through a series of recombination and excitation collisions, lose their energy to a point where they are no longer able to produce additional ions. At this point electrons accumulate and form another dark region because they have insufficient energy to cause any excitation. This region is called the Faraday Dark Space.

Positive Column

In this region there is a slight electric field and a steady supply of electrons which are accelerated towards the anode.

2.2.2 Sustenance of the discharge

In order to sustain the discharge there must be a numerically equal ion-electron pair generation rate. However, electrons and ions are lost at the anode and cathode. The processes occurring include electron-ion recombination, ion neutralisation by Auger emission at the target, and an equivalent electron loss into the external circuit at the anode.

Simplistically, the self-sustaining feature of the discharge depends only on the emission of sufficient electrons at the cathode by positive ions from the negative glow and subsequent ionisation caused by these electrons.

2.2.2.1 Secondary electron emission

As will be seen in the next section, many processes occur when a particle impinges upon a surface and, depending on the energy of the particle, one of the possible results is that an electron is emitted. For incident ions the number of electrons emitted per ion is called the secondary electron coefficient.

These electrons play an important role in sustaining the glow discharge by ionisation of neutral sputtering gas atoms which in turn bombard the cathode and release more secondary electrons in an avalanche process [4-9]. As will be seen in chapter 3, the secondary electron emission can be confined by a magnetic field.

A secondary electron can be emitted by an electron, an ion, a neutral or photon bombardment.

2.3 The Physical Sputtering Process

When a surface is bombarded by charged species, various phenomena take place, one of which is the ejection of particles of the surface material. Simplistically, these particles are then deposited onto the substrate to form a thin film. This process is known as physical sputtering, and is the basis of the deposition technique used throughout this work.

Physical sputtering, as applied to the deposition of atoms on surfaces, was first used to coat Astronomical mirrors in 1877 [10] and in the following century and a half has been used for many coating purposes. These include mirror coatings, anti-reflection coatings on ophthalmic lenses, electrically conducting transparent screens, security coatings, interference filters, sunglasses and electrochromics.

However, as will be introduced in the following sections, as the kinetic energy of the bombarding species increases, various different phenomena can occur. The following

sections aim to analyse the processes occurring at the cathode and factors affecting the rate of deposition at the substrate in a basic sputtering arrangement.

2.3.1 Ion impact processes

Physical sputtering is governed by the kinetic energies of the bombarding ions. When a noble gas ion is accelerated towards the target, usually the cathode of the sputtering system, by the voltage applied to it, then one of the following five phenomena can occur, as illustrated in figure 2.5.

- At energies less than 5 eV the interaction is essentially confined to the outermost surface of the target material and the noble gas ion will be reflected back, probably being neutralised in the process.

- A secondary electron may be emitted because of electronic transitions in the surface material.

- The ion may become implanted into the target - ion implantation.

- Some structural rearrangement can occur in the target material, from vacancies and interstitials, to larger lattice defects such as changes of stoichiometry, mixing, and lattice destruction.

- A series of collisions (collision cascade) can occur, leading to the ejection of a target atom - **sputtering**. This occurs when the energies of the ions in the plasma are in the correct range for sputter deposition. This range varies but sputtering occurs when the kinetic energies exceed the binding energies of the target atoms by 3H (where H=Heat of sublimation of the target material).

The collision cascade does not always result in the ejection of a sputtered atom but chance plays its part and the collisions can proceed further and further into the target

material, their energy being dissipated as heat in lattice vibrations. Thus, the sputtering process is very inefficient (~1%).

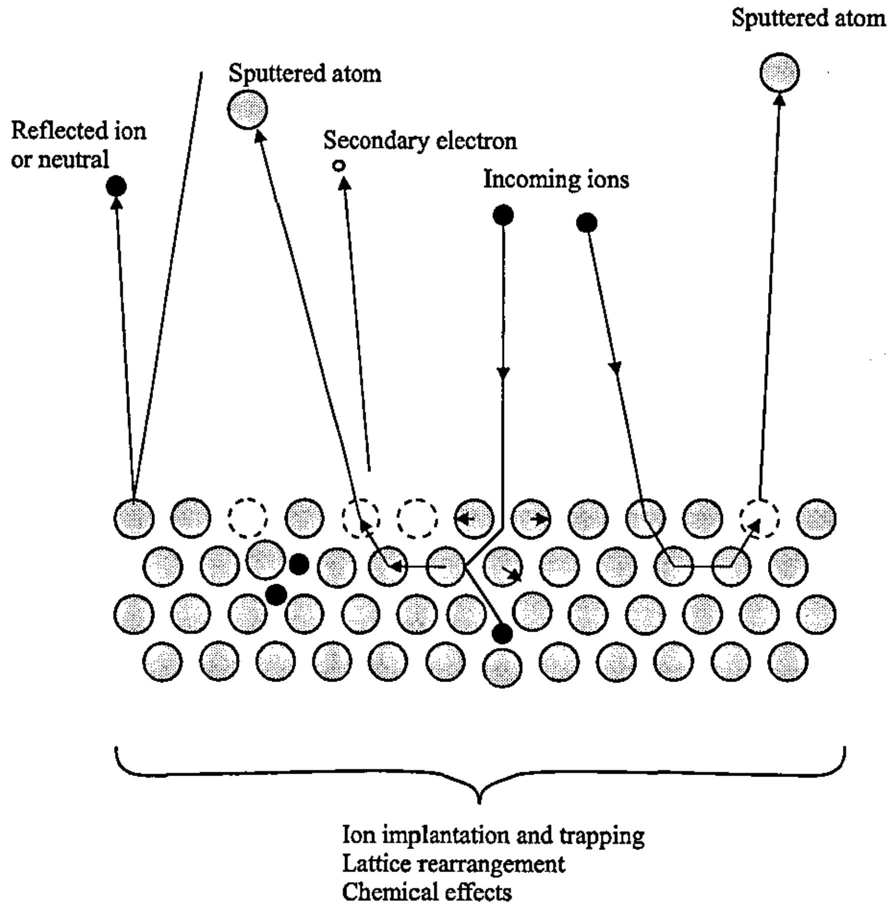

Figure 2.5 : Process following ion impact during sputtering

2.3.2 Sputter yield, threshold and efficiency

The sputter yield [11-13], S, is defined as the number of target atoms ejected per incident atom. Obviously this parameter depends on the masses of both the incident and target atoms and the energy, E, of the incident ions. It is very difficult to understand all of the surface interaction phenomena involved that contribute to the yield at the surface, but as the mass of incident ions is increased, there is a general exponential increase in yield. This increase continues to a plateau at maximum momentum transfer, when $M_i=M_t$, and then decreases [14]. The sputtered atoms are ejected from the target surface with considerable kinetic energy, for example 50-100 times higher than in vacuum

evaporation [15,16]. The yield is also dependent on crystallographic directions, hence, for polycrystalline targets sputtering can lead to an increase in target surface roughness.

The theoretical model developed by Sigmund [17] in 1969 has been highly successful in predicting the value of the sputtering yield for medium to high-energy ions (10-100 keV) incident normally on a target.

Generally, however, in the sputtering process described throughout this work, the ion energies are below 1 keV. Sputter yield data can also be interpreted in terms of Sigmund's analysis which gives the sputtering yield, S, for ion energies, E_i, below 1 keV and larger than the surface binding energy, U_o

$$S = \frac{3\alpha}{4\pi^2} \frac{4m_i m_t}{(m_i + m_t)^2} \frac{E_i}{U_0} \qquad [2.11]$$

where m_i and m_t are the masses of the incident ion and target respectively. Alpha, α, concerns the geometry of the scattering event and is evaluated numerically to vary between 0.15 and 1.5 [17]. Equation 2.11 shows that the yield at low energies is proportional to the bombarding ion energy and inversely proportional to the heat of sublimation. Seah [18] has analysed results from Wehner [19] and Oechsner [20] and produced a set of pure element sputtering yields for 500 eV argon ions, given in table 2.1, for the elements sputtered throughout this work.

Element		Sputter Yield (experimental)
Zinc	Zn	5.07
Indium	In	3.27
Tin	Sn	2.69
Copper	Cu	1.92
Chromium	Cr	1.51
Aluminium	Al	1.38
Oxygen	O	1.33
Titanium	Ti	1.25
Silicon	Si	1.02

Table 2.1 : Pure elemental sputter yields for 500 eV Argon ions [18]

A more complete set of experimental sputtering yields covering ions over the energy range 0.1 to 100 keV has been compiled by Andersen [14]. Above 50 eV, an increase in sputter yield is associated with an increase in ion energy as equation 2.11 predicts, however, a decrease in yield is observed above about 30 keV. This decrease is attributed to the penetration of the ions deep into the lattice where a large proportion of their energy is lost.

Streinbruchel [21], by combining results from various papers, arrived at a formula that was more convenient and satisfied energies above 1 keV

$$S = \frac{5.2}{U_0} \frac{Z_t}{\left(Z_t^{\frac{2}{3}} + Z_i^{\frac{2}{3}}\right)^{\frac{3}{4}}} \left(\frac{Z_i}{Z_t + Z_i}\right)^{0.67} E^{\frac{1}{2}}. \qquad [2.12]$$

Here, the sputter yield is inversely proportional to the target binding energy for bombardment energies in the range 100 eV - 10 keV. Therefore, any stable compound formed, *i.e.* with a negative heat of formation, at the surface of the cathode, will have a larger binding energy than the original element and so have a lower sputter yield. This has immediate consequences for reactive sputtering where compounds of the reactive gas and target element form at the cathode surface as well as at the substrate. It will be shown in the following chapters that this problem requires precise techniques to control the flow of the reactive gas into the chamber and to overcome the sputter rate instability.

2.3.3 Preferential Sputtering

When sputtering from a compound target, such as indium-tin, a change in surface composition is observed. This phenomenon is usually referred to as preferential sputtering and is a consequence of the different sputtering yields of each surface constituent. The general result is that the surface is depleted of the higher sputter yield element until a steady-state value is reached. Lower energies and lower ion masses tend to increase the depletion and if either is varied a new steady-state surface composition is

reached. Preferential sputtering also affects oxide targets, the systems generally becoming depleted of oxygen under ion bombardment [22]. Preferential sputtering has profound implications for alloy target sputtering, including nodule formation, surface transition time delays owing to external parameter changes, and increased arc formation. These phenomena will be highlighted throughout this work.

Chapter 2 References

[1] **Krall, N.A. & Trivelpiece, A.W.**, (1973). *'Principles of Plasma Physics'*, McGraw-Hill, New York.

[2] **Chapman, B.N.**, (1980). *'Glow Discharge Processes'*, Wiley, New York.

[3] **Pulker, H.K., Haag, W., Buhler, M., Moll, E.**, *Proceedings of IPAT 85, Munich (CEP Consultants Ltd.)*, 299.

[4] **Chapman, B.N., Downer, D. & Guimaraes, L.J.M.**, (1974). *J. Appl. Phys.*, 45, 2115.

[5] **Brodie, I., Lamont, L.T. & Myers, D.O.**, (1969). *J. Vac. Sci. Technol.*, 6, 124.

[6] **Shintani, Y., Nakanishi, K., Takawaki, T. & Tada, O.**, (1975). *Jpn. J. Appl. Phys.*, 14, 1875.

[7] **Ball, D.J.**, (1972). *J. Appl. Phys.*, 43, 3047.

[8] **Benninghoven, A.**, (1971). *Surf. Sci.*, 28, 541.

[9] **Benninghoven, A.**, (1973). *Surf. Sci.*, 35, 427.

[10] **Wright, A.W.**, (1877). *Am. J. Sci.*, 13, 49.

[11] **Steinbruchel, Ch.**, (1985). *Appl. Phys.*, A36, 37.

[12] **Steinbruchel, Ch.**, (1985). *J. Vac. Sci. Technol.*, A3, 1913.

[13] **Sigmund, P.**, (1983). *'Sputtering by Ion Bombardment II'*, ed. by Behrish, R., Topics, Appl. Phys., 52.

[14] **Anderson, H.H.**, (1981). *'Topics in Applied Physics'*, ed. by Behrish, R., Springer-Verlag, New York, 47, 145.

[15] **Chopra, K.L.**, (1969). *'Thin Film Phenomena'*, McGraw-Hill, New York.

[16] **Ridge, M.I.**, (1984). Ph.D. Thesis, Loughborough University of Technology, U.K.

[17] **Sigmund, P.**, (1969). *Phys. Rev.*, 184, 383.

[18] **Seah, M.P.**, (1981). *Thin Solid Films*, 81, 279-287.

[19] **Wehner, G.K.**, (1985). *Methods of surface analysis*, p.5.

[20] **Oechsner, H.**, (1975). *Applied Physics*, 8, 185.

[21] **Steinbruchel, Ch.**, *Appl. Phys.*, A36, 37.

[22] **Holm, R., & Storp, S.**, (1977). *Appl. Phys.* 12, 101.

CHAPTER 3

MAGNETRON THEORY AND DESIGN

Throughout this work only one deposition technique was used in order to maintain at least one process parameter. Whilst it is recognised that there are more useful coating techniques from the point of view of pure research and characterisation of deposition parameters, magnetron sputtering was selected for this work always bearing in mind its applicability to industrial scale operation. The following chapter first introduces briefly alternative deposition technologies for thin film deposition so that comparisons can be made between them and magnetron sputtering. Following this, the concept of the magnetron device will be developed prior to description of its use as a reactive processing tool, in chapter 4.

3.1 COMPETING DEPOSITION TECHNOLOGIES 20
3.1.1 Evaporation 20
3.1.2 Sputtering without a magnetic confinement field 21
3.1.2.1 Ion beam sputtering 21
3.1.2.2 DC Diode Sputtering 21
3.1.2.3 DC Triode Sputtering 24
3.1.2.4 Radio Frequency (RF) Sputtering 25
3.1.3 Advantages of Magnetron Sputtering 26
3.2 MAGNETRON FUNDAMENTALS 27
3.2.1 Electron confinement 30
3.2.1.1 In a magnetic field 30
3.2.1.2 In an electric field 32
3.2.1.3 In a combined field 32
3.2.2 Voltage, Current and Pressure Relationships 36
3.3 VARIOUS PLANAR MAGNETRON CONFIGURATIONS 38
3.3.1 Balanced 39
3.3.2 Unbalanced 40
3.3.3 Magnetron advancements 41
3.4 TARGET UTILISATION AND COATING UNIFORMITY 42

3.1 Competing Deposition Technologies

The following section introduces techniques, other than magnetron sputtering, that are commonly used to deposit thin films. Many processes, other than the ones listed below, are also used to deposit thin films; including arc discharges, hydrolysis, molecular-beam epitaxy and chemical vapour deposition.

3.1.1 Evaporation

Vacuum evaporation dates back to 1857 when Faraday [1] exploded metal wires in an inert atmosphere. The possibility of depositing films by evaporation was discovered in 1887 by Nahrwold [2]. During the last 35 years, evaporation has become more widely used within the industrial environment for an increasing number of applications. Examples include anti-reflection coatings, front-surface mirrors, interference coatings, sunglasses, decorative coatings, cathode-ray tubes, and, in the last 10 years, electronic circuits.

Advantages	Disadvantages
One of the most inexpensive deposition techniques available.	Owing to the different melting points of various materials, alloy composites and compounds are very difficult to deposit.
Films of high purity can be deposited from high purity source evaporant. *e.g.* astronomical mirrors.	Porous films are difficult to avoid because of the angle of incidence of the flux of the depositing material.
The monitoring and control of the deposition is simple.	Very few processing variables are available for film property control.
The 'line-of-sight' trajectory allows the use of masks to define complex patterns. *e.g.* for semiconductor processing.	Film thickness uniformity is poor because of 'line-of-sight' trajectory.

Table 3.1 : Advantages and disadvantages of evaporation

Vacuum evaporation is a Physical Vapour Deposition (PVD) process in which material from a thermal vaporisation source reaches the substrate without collision with gas molecules. The process is 'line-of-sight' with typical operating pressures in the range 10^{-5} torr to 10^{-9} torr.

3.1.2 Sputtering without a magnetic confinement field

Although it will be shown in the next section that the use of magnetic confinement in sputtering is the most efficient, controllable and high rate process available, it is useful to review conventional DC and RF sputtering techniques.

3.1.2.1 Ion beam sputtering

Ion beam sputtering involves bombardment of a target material with a high energy ion beam (hundreds to thousands of electron volts). The beam, usually an inert or reactive gas, is directed at the target which is sputtered onto a nearby substrate. Isolation of the substrate from the ion generation process can be obtained by this deposition technique rather than the conventional DC diode sputtering configurations. Greater versatility of the deposition parameters can be obtained and the ion beam current and energy can be independently controlled. This flexibility characterises ion beam deposition as a useful research technique in the study of thin film growth processes [3].

3.1.2.2 DC Diode Sputtering

This is the basic form of sputtering that was introduced throughout chapter 2. Although the technique will produce films of many types, the range of stoichiometries, deposition rate, film structure and density achievable are severely limited by the low ionisation and high pressure operation characteristics of this technique. Its only uses are for films of low quality, such as contact metallisation, and for *in situ* cleaning. However, a great deal

of interest has been shown in the production of four and five-element compound superconducting films [4,5].

Figure 3.2a shows the basic configuration of a DC diode glow discharge sputtering system. Typically, a DC diode argon sputtering plasma will be operated between 10 and 100 mtorr by applying a potential of the order of kilovolts across the electrodes. This will give a current density of between 1 and 10 $mAcm^{-2}$ in the discharge. The sputtering process is as described in chapter 2. Positive ions strike the target, ejecting neutral atoms and electrons, the latter helping to sustain the glow discharge. The high pressure operating regime creates many problems and is the major disadvantage in DC diode sputtering. The ions that impinge on the target surface do not have the full cathode potential, owing to thermalisation and charge exchange collisions between the accelerating ions and the residual gas neutrals. The higher the gas pressure, the lower the mean energy of particles that strike the film surface. However, electrons that are accelerated from the cathode obtain high energies with which they impinge on the substrate surface, giving rise to substrate-film heating.

Advantages	**Disadvantages**
Large areas can be covered with good uniformity.	Low deposition rates.
Plasma fills entire deposition chamber - plasma cleaning possible *in situ.*	Surface heating owing to accelerated secondary electrons.
Target material well utilised.	Target poisoned by reactive contaminants extinguishing plasma.
	Only electrical conductors can be used as sputtering targets.
	Reduced film adhesion because of the low energy with which the neutrals impinge on the substrate.
	Contamination of the film by the inert gas used to support the discharge.

Table 3.2 : Advantages and disadvantages of DC diode sputtering

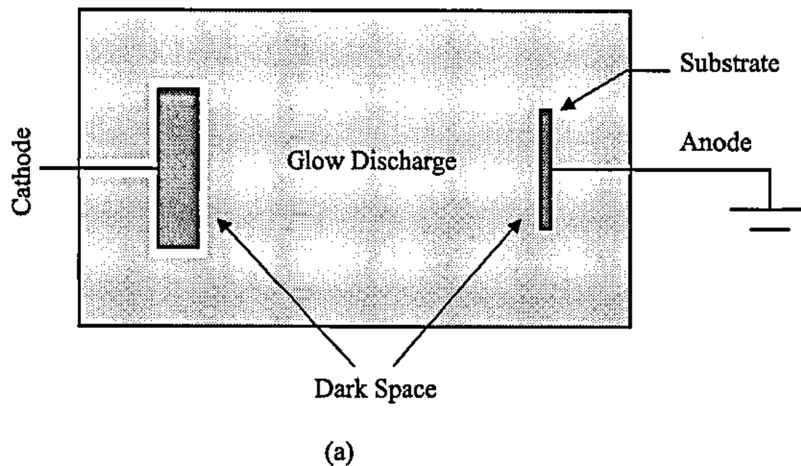

(a)

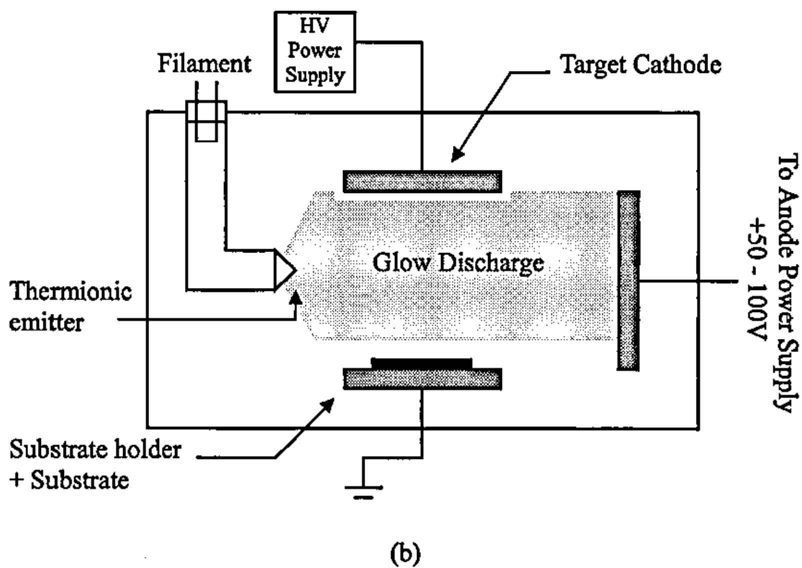

(b)

Figure 3.2 : Configuration of basic DC sputtering systems. (a) DC Diode (b) DC Triode

For the operation of glow discharge systems at less than 20 mTorr there should be an additional source of electron injection, other than the secondary electrons emitted from the cathode. Such a modification was first made by Gawehn [6], who reported the use of a high frequency coil around the chamber to induce plasma formation. An alternative source was implemented by Vratny [7], who superimposed radio frequency power on the DC bias to the cathode. Both these methods reduce the operating pressure, but there are more beneficial deposition techniques that can be used for achieving the same aim.

3.1.2.3 DC Triode Sputtering

In an ideal system, the parameters affecting the discharge are independent of each other and can be varied over a wide range. DC diode sputtering does not allow this because the cathodic current is voltage and pressure dependent. The process is shifted from the normal glow region to the arc region following an increase in cathode voltage and the gas pressure has to be increased. As described in section 3.1.2.2, this increase is detrimental to the deposition process because of the reduction in mean free path. Triode sputtering produces a very high ion density, allows operation at much lower pressures than a two-terminal glow discharge, and allows control of the target current density, independent of target voltage. Electron injection into the discharge is achieved with a hot cathode, emitting electrons thermionically.

Advantages	Disadvantages
High ion density	Difficult to scale up because of problems involved in producing a large, uniform thermionic arc discharge
Allows operation at lower pressures (≤1 mtorr)	Non-uniformity from very large flat targets
	Difficult to control electron injection with sufficient accuracy to maintain repeatable results [8]

Table 3.3 : Advantages and disadvantages of DC triode sputtering

As shown in figure 3.2b the cathode is a heated tungsten filament, able to withstand ion bombardment for long periods. The external coil produces a magnetic field that aids plasma confinement and reduces the operating pressure. The anode is biased positively with respect to the substrate to avoid electron deflection causing inhomogeneities in the plasma density at the target.

The process is initiated by generating a low voltage (~50 V), high current (5-20 A) arc discharge between the thermionic filament and main anode. Ion density in the plasma

can be controlled in triode sputtering by either varying the electron emission current, or the voltage used to accelerate the electrons.

3.1.2.4 Radio Frequency (RF) Sputtering

In conventional DC systems, the target needs to be conducting, otherwise positive charge would quickly accumulate. This leads to an increase in current density and arc formation, extinguishing the glow discharge. Hines *et al* [9] described a technique for eliminating this charge accumulation by bombarding the substrate with both an ion beam and an electron beam. However, a more practical process was introduced by Wehner in 1955 [10] utilising a high-frequency discharge.

Typically, in RF sputtering, a blocking capacitor is connected between the target and RF power supply, while the substrate and chamber walls are connected to ground. When a low frequency alternating current is applied between the electrodes, the system behaves as if there were two cathodes, with dark space being present in front of each. The system behaves as a succession of short lived DC discharges and relies on secondary electrons from the electrodes to maintain the discharges. When this frequency is increased above ~50 kHz the operating pressure of the discharge is reduced. However, the effect levels off above several megahertz and 13.56 MHz is the most widely chosen frequency, as it is permitted by international communication authorities for technical purposes. Electrons in a RF discharge have random motion owing to their extra energy obtained from oscillating within the field and repeated gas collisions. This random component of motion is increased until they have sufficient energy to ionise the gas atoms with which they are colliding. Thus, the high voltage necessary with DC sputtering to maintain the discharge is not needed by the RF glow.

The electrons are able to follow the rapidly changing electric fields in a RF discharge owing to their higher mobilities than ions. Therefore, many more electrons reach the surface of the dielectric target in the positive half-cycle than ions will during the negative half cycle, and both electrodes acquire a constant negative self-bias with respect to the

plasma. This bias repels electrons and creates an ion-rich sheath in front of the target, analogous to Crooke's dark space in DC sputtering.

Probably one of the main disadvantages of RF sputtering is the low deposition rates, even when using magnetic fields to trap the otherwise lost electrons [11,12]. A technique termed AC sputtering, however, will be described in chapter 4, and was used throughout this work. This technique is analogous to RF sputtering, but utilises a lower frequency, in the mid-kHz range, to the same effect, but without the major disadvantages associated with the higher frequencies.

Advantages	Disadvantages
Insulating compounds such as SiO_2 [13] and Al_2O_3[14] may be deposited	Electrons are more easily lost to the glow because RF discharge is confined between two electrodes
	Discharge can occur in unwanted areas and earth plate design is critical
	Accurate tuning of an impedance matching network is required.
	Environmental shielding is required to protect against the interference 13.56 MHz radiation produces.
	Low deposition rates of typically 1 $Ås^{-1}$
	Undesirable induced RF voltages can occur on the substrate surface without adequate grounding

Table 3.4 : Advantages and disadvantages of RF sputtering

3.1.3 Advantages of Magnetron Sputtering

The main advantages that magnetron sputtering has over diode sputtering are increased deposition rate and controllable ion bombardment at the substrate. In a commercial

environment, product output is of uppermost importance and the slow rates associated with the previous techniques means they are becoming industrially redundant. The shortcomings of conventional diode systems can be overcome by using magnetic fields to enhance the discharge, allowing operating pressures to decrease by two orders of magnitude by increasing the electron ionisation of gas atoms.

3.2 Magnetron fundamentals

In the following section, the physics of electron confinement and magnetic field design, which distinguish the magnetron from conventional diode sputtering, will be discussed. It will be shown that the most efficient arrangement is that of the planar magnetron, first described on liquid surfaces in 1959 by Kesaev and Pashkova [15] and on solid planar surfaces in 1974 by Chapin [16]. Furthermore, advances in basic magnetron design, that enable tighter control of the process parameters, will be reviewed both qualitatively and quantitatively.

Permanent magnets are used in magnetron configurations to confine electrons near the cathode surface. The magnets are generally arranged such that they create a field that electrons spiral around and hop through as described in the basic illustration of figure 3.3. The **E^B** force causes the electron to also move normal to the **E^B** plane and, if the magnetic field is arranged appropriately, the electrons will form a circulating current on the surface.

Confining the electrons in this manner reduces the collision and charge exchange collision probabilities in the majority of the gas discharge because of the low pressures now sustainable. Moreover, this reduces the cathode potentials but still allows high-energy, high-current ion flux which gives a high sputtering yield and rate.

Principally, there are two possible geometries as illustrated in figure 3.4, the cylindrical magnetron where the target is formed in the shape of a cylinder, and the planar magnetron.

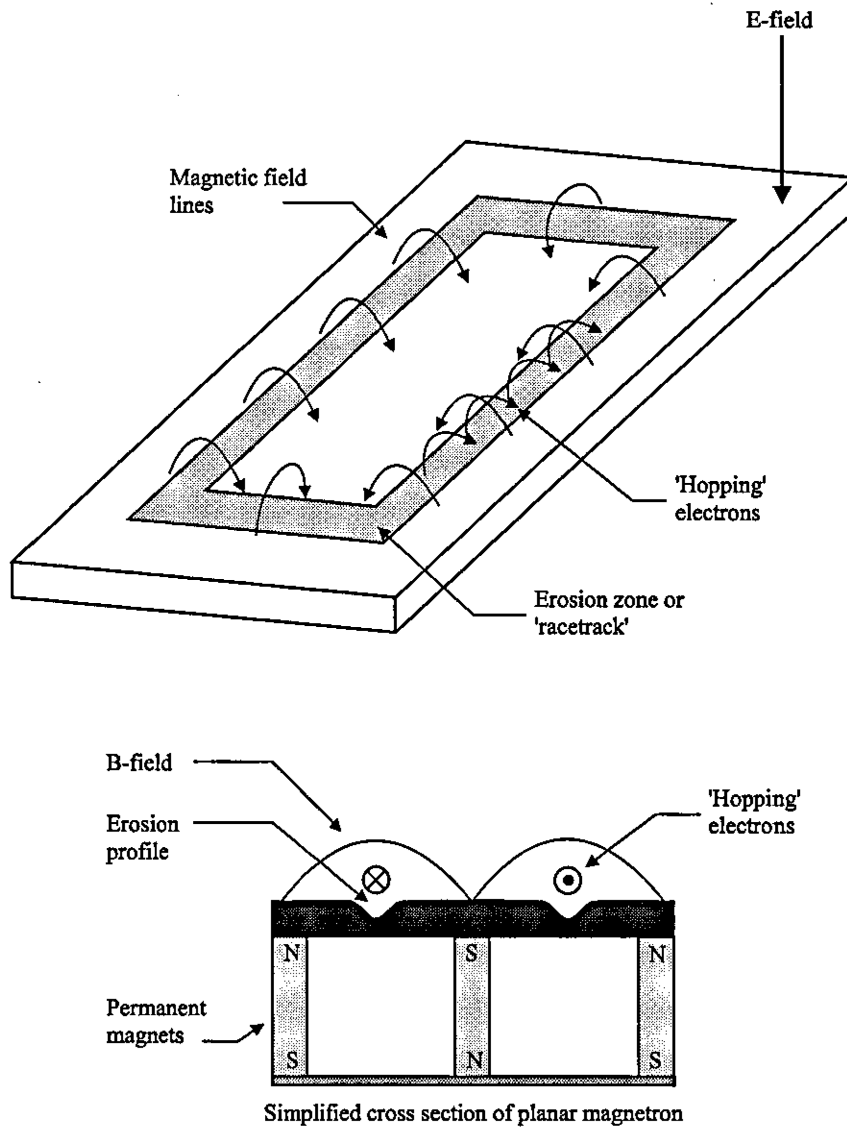

Figure 3.3 : Electron hopping above a planar magnetron

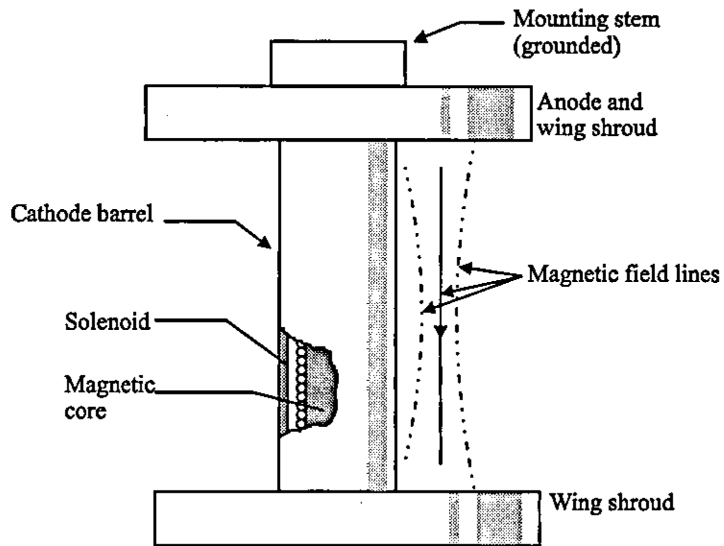

(a)

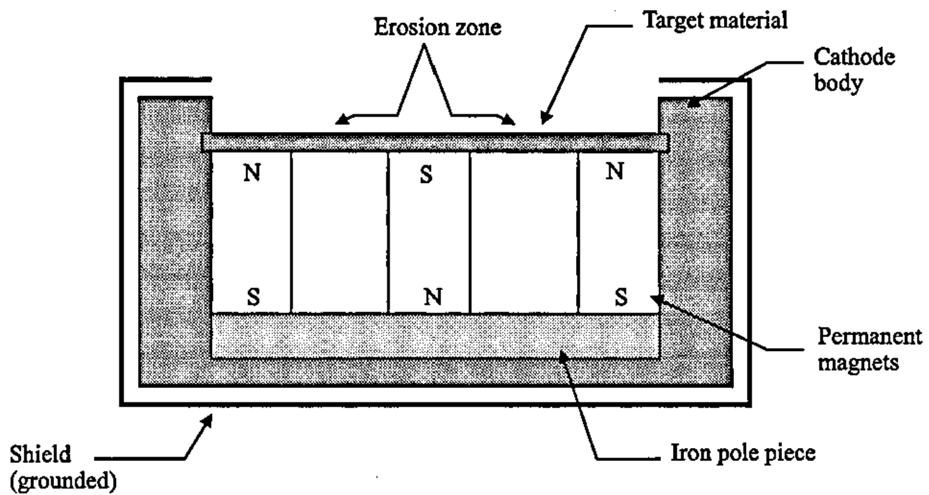

(b)

Figure 3.4 : Sputter source configurations. (a) Cylindrical (b) Planar

3.2.1 Electron confinement

Electrons are the only charged particles within a sputtering system that are significantly affected by magnetic fields, as the ions are too massive.

3.2.1.1 In a magnetic field

It is useful to first characterise the movement of an electron in a magnetic field, before examining the more complex case of a combined electric and magnetic field. When an electron of charge, e, mass, m_e, and velocity, **v**, interacts with a uniform magnetic field, **B**, it experiences a force

$$\mathbf{F_B} = e(\mathbf{v} \wedge \mathbf{B}) \qquad [3.1]$$

as illustrated in figure 3.5. Any electrons travelling parallel to the magnetic field will be unaffected, since their vector product will be zero.

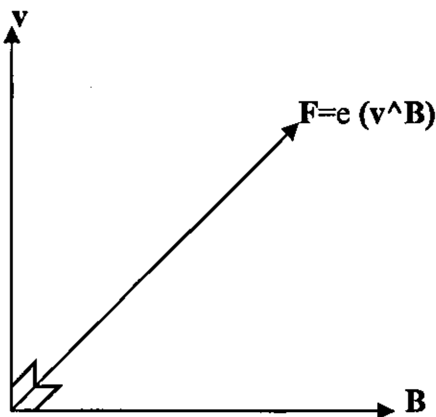

Figure 3.5 : Force on an electron in a uniform magnetic field

Assuming that an electron is moving with its velocity at an angle, α, to the **B** field, then the net force on that electron will be Bevsinα and the electron moves in a circular path depicted in figure 3.6, the radius of which is given by equation 3.2.

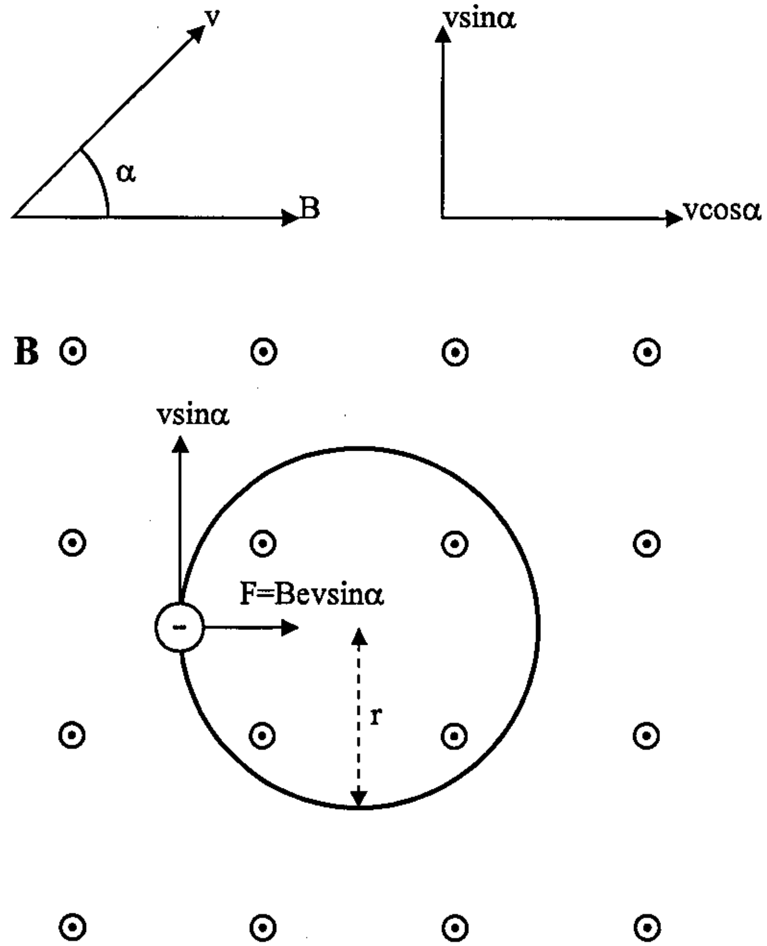

Figure 3.6 : Circular motion of an electron in a magnetic field

$$r = \frac{m_e v \sin\alpha}{Be}. \qquad [3.2]$$

Coupled with the velocity vcosα parallel to B, the general motion will be a helix, figure 3.7.

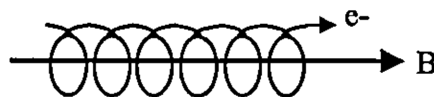

Figure 3.7 : General helix motion of an electron in a magnetic field

3.2.1.2 In an electric field

If an electron of charge, e, is placed at any point in an electric field, **E**, then it experiences a force, $\mathbf{F_E}$, where

$$\mathbf{F_E} = e\mathbf{E}. \qquad [3.3]$$

3.2.1.3 In a combined field

Figure 3.8 illustrates the electric and magnetic fields above a magnetron cathode. Outside the dark space, the electrical field is essentially zero, as explained in section 2.2.1, and the electron is only affected by the magnetic field. The following section explains the behaviour of the electron within the dark space owing to the **E^B** field.

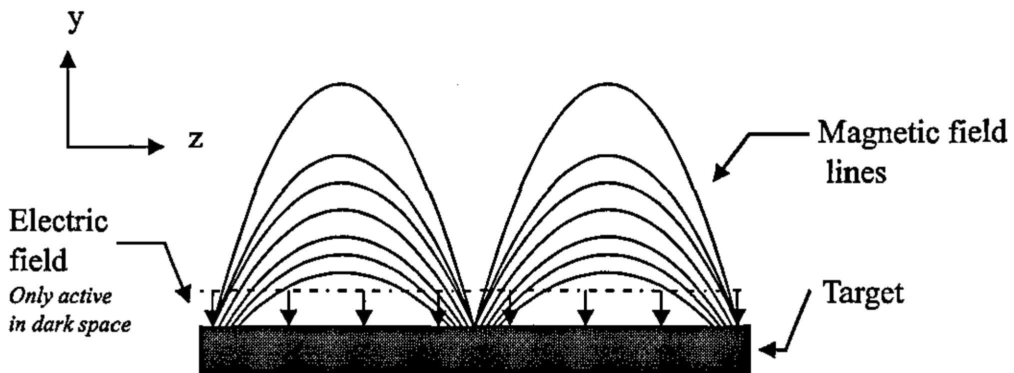

Figure 3.8 : Electric and magnetic fields above the magnetron cathode

The Lorentz force combines the effects of an electric field and magnetic field at a point to give a total force, **F**, on the electron moving with velocity, **v**, and is given by

$$\mathbf{F} = e(\mathbf{E} + \mathbf{v} \wedge \mathbf{B}) \qquad [3.4]$$

allowing the trajectories of electrons free to move under the action of **E** and **B** fields to be calculated.

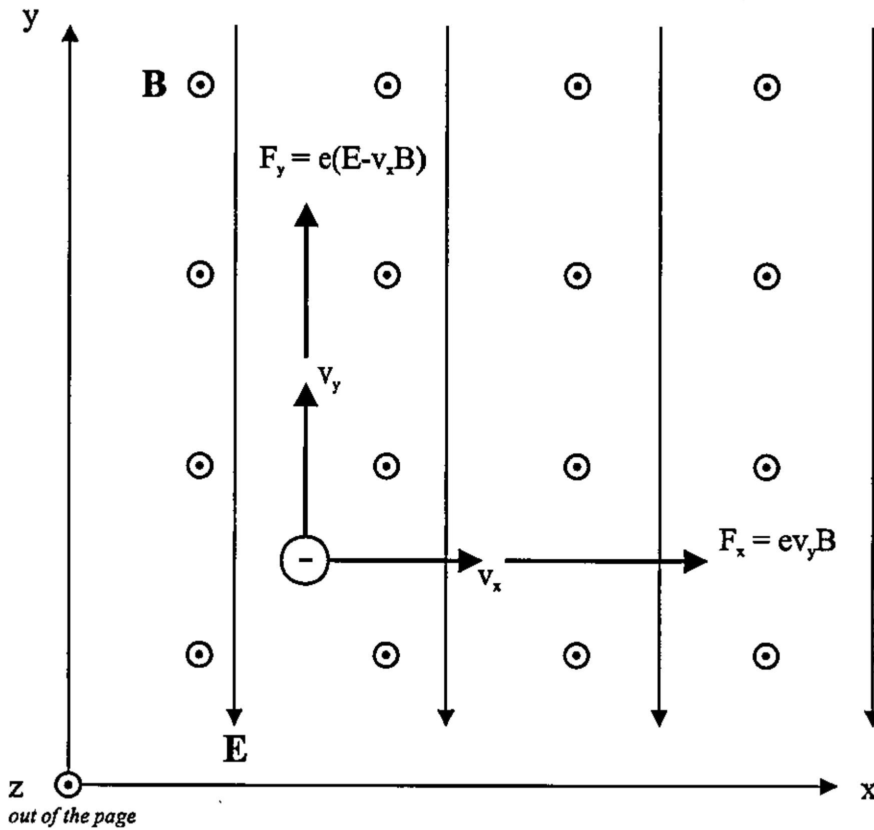

Figure 3.9 : Force on electron arising from combined **EB** field

Referring to figure 3.9, any z-component of velocity will remain unchanged because no force acts along this axis (out of the page). Hence, any motion beginning in the xy-plane will remain there. Given any initial velocity, the general trajectory can be obtained by solving the equations of motion.

$$F_y = m\ddot{y} = e(E - v_x B) \qquad [3.5]$$

$$F_x = m\ddot{x} = ev_y B \qquad [3.6]$$

If, however, the initial velocity, v_y, is zero and $v_x = E/B$, then both F_x and F_y are zero and remain so. Therefore, of all the particles entering the fields with velocity perpendicular to both, only those with v = E/B are undeflected. It is clear that an electron moving with v = E/B experiences no force in the y-direction and is effectively in a zero y-field. A non-zero y-field will only come into effect when v_x differs from E/B.

Hence, let $v_x = u_x + E/B$, where u_x is initial velocity, and the equations of motion become

$$F_y = eu_x B \quad [3.7]$$

$$F_x = ev_y B. \quad [3.8]$$

If the system was viewed from an origin, moving with an x-velocity of E/B, equations 3.7 and 3.8 would represent the equations of motion.

The resultant motion from a fixed origin is, thus, a combination of a uniform linear drift velocity and a uniform circular motion in the same plane, the latter being generated by the influence of B perpendicular to the initial direction of the electron. The angular acceleration is mv^2/r, and is equal to the magnetic force evB, so the radius of the circular velocity can be written as $v = E/B$, in which case

$$r = \frac{Em}{B^2 e}. \quad [3.9]$$

An effect similar to the creation of the dark space seen in diode sputtering, where a space-charge region is formed in front of the cathode, is observed in the magnetron. However, the magnetron 'dark space' is difficult to model, but is assumed to have a thickness of ~0.5 mm and the electric field only acts within this region.

Figure 3.10 shows the net motion of the electron above the cathode. The electron is initially subject to the **E^B** force, but only in the dark space region. This force gives a component of velocity at a small angle to the normal. In reality, the magnitude of the electric field is significantly greater than that of the magnetic field and the ejection direction is essentially normal to the cathode surface, through the dark space. On escaping the dark space, the electron experiences a force solely owing to the magnetic field, **v^B**, as described by equation 3.1. This circular orbit takes the electron back into the dark space with energy equivalent to that with which it left (the electrons have a mean free path of ~1 m). The electron reaches the cathode, is repelled and re-ejected

normally to the cathode surface. This series of ejections and circular orbits continues with the electron travelling around the erosion zone of the cathode, its movement characterised by semicircular 'hoops'. The electrons that follow these paths are termed primary electrons. Electrons are also free to follow the field lines in a cyclic orbit and these are termed ultimate electrons, these electrons are primary electrons that have given up most of their energy.

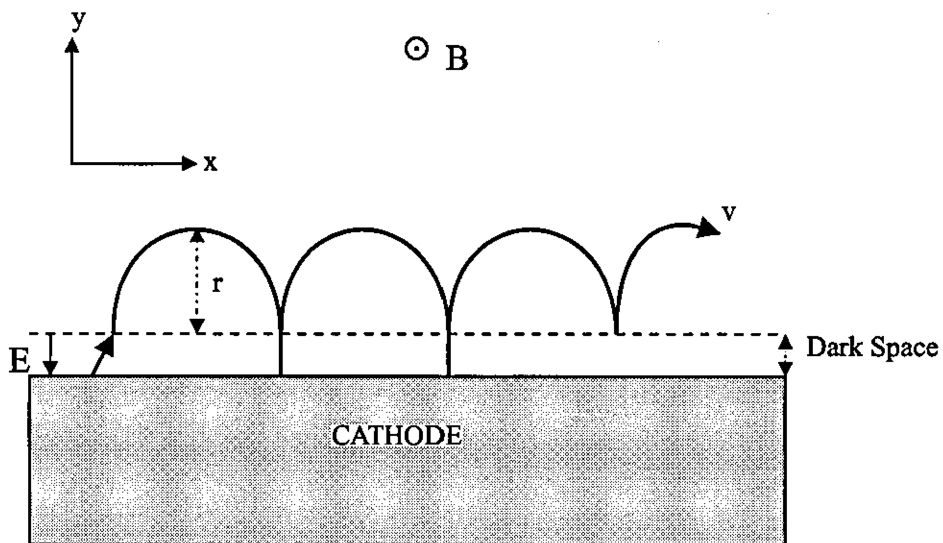

Figure 3.10 : Net motion of electron above the magnetron cathode

In a typical planar magnetron with the following operational characteristics

Magnetic field : **500 Gauss**
Operating potential : **500 V**
Sputtering pressure : **3 mtorr argon**

the dark space will be ~0.5 mm and have an electric field of ~10^6 Vm^{-1}, which results in the radius of the circular component of the electron ~1.5 mm. The electron drift velocity will be approximately 10^7 ms^{-1}. These figures are specifically for primary electrons, electrons that are hopping across the magnetic field lines.

3.2.2 Voltage, Current and Pressure Relationships

The normal operating conditions for a planar magnetron are approximately 2-8 mtorr of Ar at 250-700 V. Under these conditions, current densities vary from 2 to 50 $mAcm^{-2}$. Figure 3.11 shows a typical I/V curve. The functional relationship between operation current, I, and voltage, V, for a planar magnetron is given empirically by

$$I = kV^n \qquad [3.10]$$

where k and n are constants.

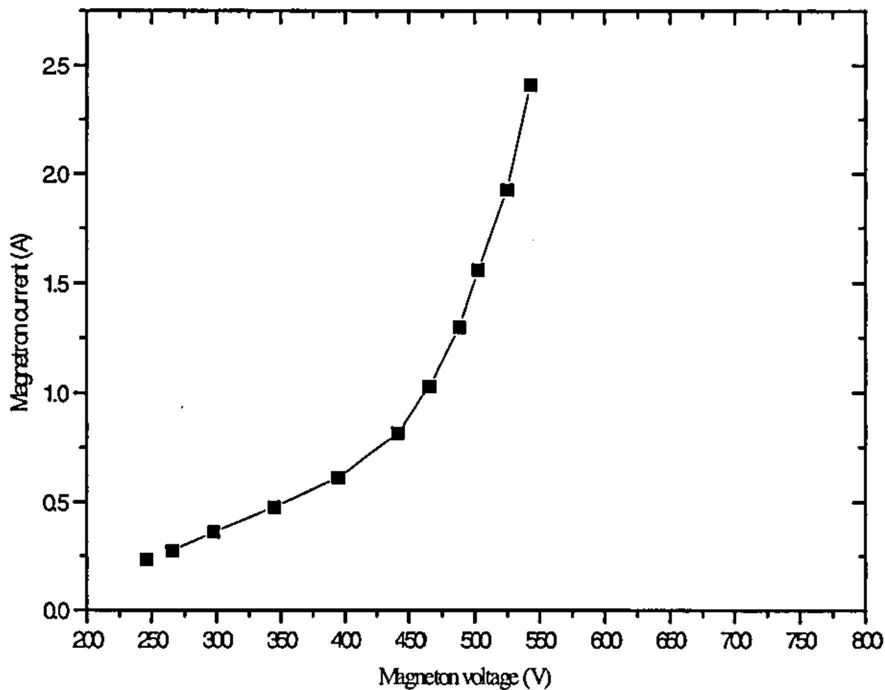

Figure 3.11 : Typical I/V operating characteristics for a DC magnetron

The exponent, n, generally in the range of 5 to 15, represents the effectiveness of the electron trap. When n assumes a high value in the range, the voltage change is slow for large changes in discharge current and can, in most experiments, be ignored. Both n and k depend strongly on magnetron design, gas-target combination, magnetic configuration and other experimental parameters.

It has been shown by Spencer *et al* [18], that the operating potential is also greatly affected by magnetic field strength. They showed that for higher current densities, higher magnetic field strengths are required. Figure 3.12 [17] shows the dependence of magnetron potential on magnetic field strength at the centre of the pole gap for various current densities. It can be seen that there is a critical field strength below which magnetron operation is unstable.

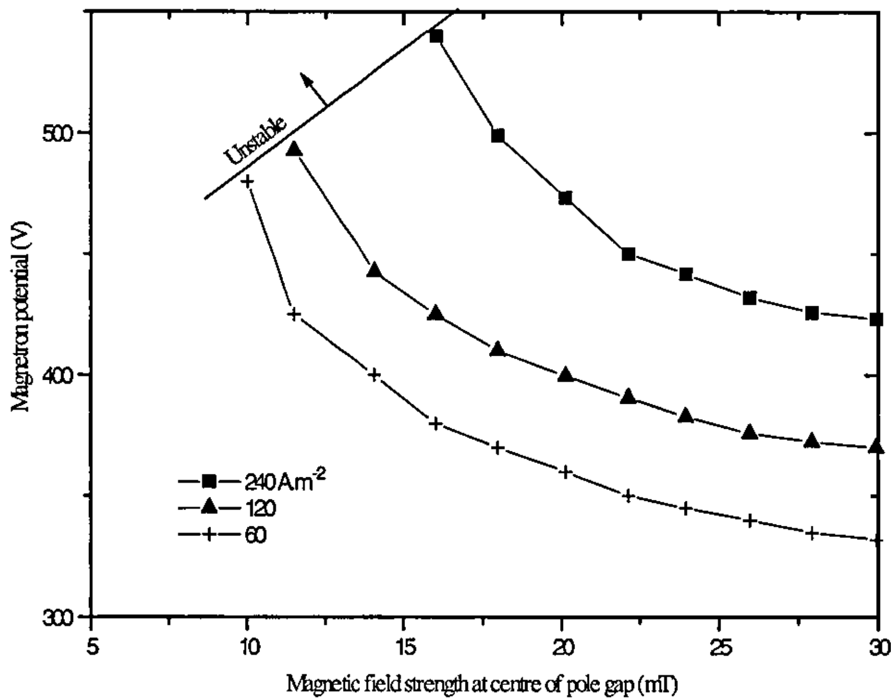

Figure 3.12 : Effect of magnetic field strength on magnetron operating potential [17]

Thornton [19] determined the minimum potential, v_{min}, to sustain a discharge, to be proportional to the reciprocal product of the ion collection efficiency, e_i, and the fraction of the full complement of ions that is made by the average primary electron before it is lost from the system, e_e. These parameters obey the configuration of the magnetic field, and therefore, as the flux linking the magnetron and the substrate increases, these parameters decrease and the minimum potential to sustain the discharge increases.

3.3 Various planar magnetron configurations

Much work has been undertaken to develop the most efficient, controllable and impurity free planar magnetron [20,21] but only during the last ten years has the potential to use magnetron sputtering as a source of beneficial ion bombardment been realised. Pulker in 1988 [22] and many others [23-26] have proved the need for ion bombardment in quality ion plated coatings, whereas temperature sensitive plastic coatings necessitate a large target-substrate separation to ensure that the plasma cloud is confined near the target and does not touch the substrate.

Effects of ion bombardment during sputtering include densification of the film, preferentially orienting the crystallites in the deposit and modifying its microstructure. These effects are usually attributed to resputtering of the condensing species, or to increasing the adatom mobility [27,28]. Published works on the magnetic fluxes reaching the substrate are minimal. Schiller *et al* [29] reported that for most DC magnetrons, the ion fluxes are usually 5-10% of the deposition flux and Fraser & Cook [30] were perhaps the first to recognise the potential of the technique. They discussed the effect of using 'aiding' and 'opposing' magnets behind the substrate to increase ion flux. The pioneering work, however, was undertaken in 1985 by Window and Savvides whose three papers [31-33] investigated ion fluxes by examining three different magnetron configurations. They went on to quantify and characterise magnetrons in two states of magnetic field which they termed 'balanced' and 'unbalanced'. The following section aims to review these configurations and their implications on magnetron sputter deposition.

Figure 3.4b illustrated the main construction features of a planar magnetron. The main cathode body usually consists of a stainless steel casing with a planar front surface to which the target is attached. Permanent magnets are inserted into this body to produce a toroidal magnetic field. When operational in a particular region, the magnetic fields are perpendicular to the electrical field, and this region forms a closed path on the target surface. The centre magnet and outer ring are magnetically shunted at the back side by an iron pole piece. The cathode is surrounded by an aluminium ground shield, the

purpose of which is to restrict ion bombardment and sputtering to the target only. This prevents the sputtering of the target backing plate and mechanical supports that would cause film contamination.

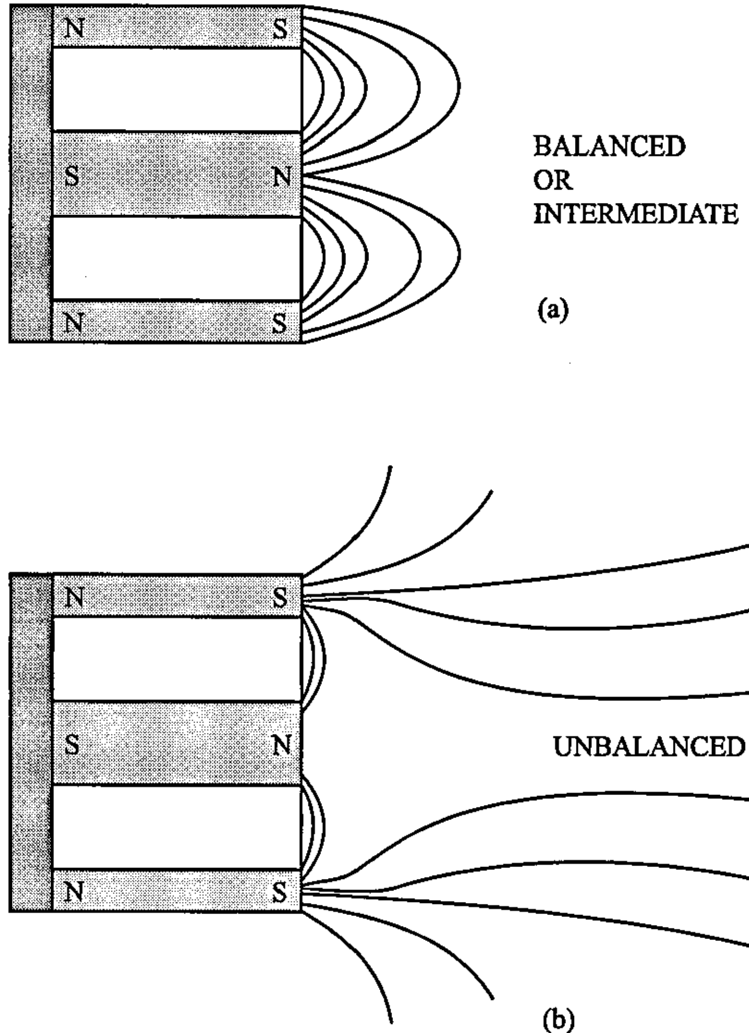

Figure 3.13 : Magnetic configurations of a planar magnetron. (a) Balanced (b) Unbalanced [33]

3.3.1 Balanced

Figure 3.13a shows a planar magnetron in a balanced arrangement. So far in the work presented here, all the magnetrons described have been of the balanced type. In this type, all the field lines pass from the centre to the annular pole, creating close confinement of the electrons within a small volume above the cathode. Very few electrons escape and

bombard the substrate in this configuration, and hence, because of the small Debye length in magnetron plasmas, very little ion bombardment occurs.

3.3.2 Unbalanced

Figure 3.13b illustrates an unbalanced configuration where the majority of the field lines originate from the annulus and are obtained by having an annular magnet much stronger than the cylindrical centre magnet. This design is easily identifiable by observation of the plasma confinement provided by the leaking field lines as illustrated in plate 3.1. Another method of design for an unbalanced magnetron involves only an annular magnet, with the cylindrical central magnet being replaced by an iron core. This is analogous to the unbalanced magnetron used in the work by Window and Savvides but has a more unbalanced nature. Throughout this research, a magnetron of this type was used and is described in more detail in chapter 6.

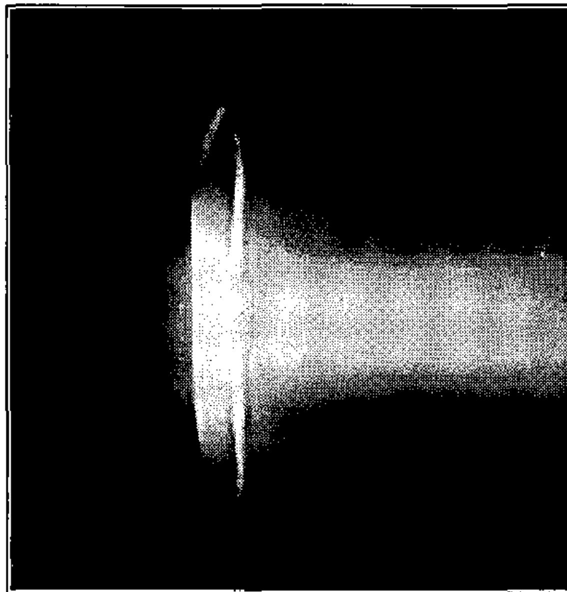

Plate 3.1 : Photograph of plasma showing leaking field lines in unbalanced magentron

The 'plume' of discharge extending towards the substrate is caused by the secondary electrons spiralling around the B-field lines, exciting gas atoms which then produce a photon by electrons decaying from one energy level to another, as will be described in chapter 4. The electrons take ions with them owing to the Debye length being very small

in a magnetron. These ions then strike the substrate and the substrate forms a negative potential as described in section 2.1.3. The potential is termed the self-bias and is the potential that insulated substrates will assume. It is this potential that contributes to the ion bombardment of the growing film and is generally of the order of 30 V [34-36]. Moreover, the self-bias enables ion bombardment on insulating substrates and films, a process not available by externally biasing the substrate.

The unbalanced magnetron provides a comparatively simple, low cost solution for ion-assisted vacuum deposition. It serves the dual purpose of supplying a deposition flux, coincident with a flux of ions and electrons, the magnitude of which can be varied. For insulating substrates, the equalisation of ion and electron currents allows the substrate to develop a self-bias of around -30 V with respect to the plasma, with an incident current density of around 5 $mAcm^{-2}$, dependent on deposited species.

3.3.3 Magnetron advances

One of the primary concerns when designing a magnetron is to obtain the correct type and positioning of the magnetic field. In the past 15 years Howson *et al* [37] have made many advances to the design of the basic planar magnetron to overcome various problems.

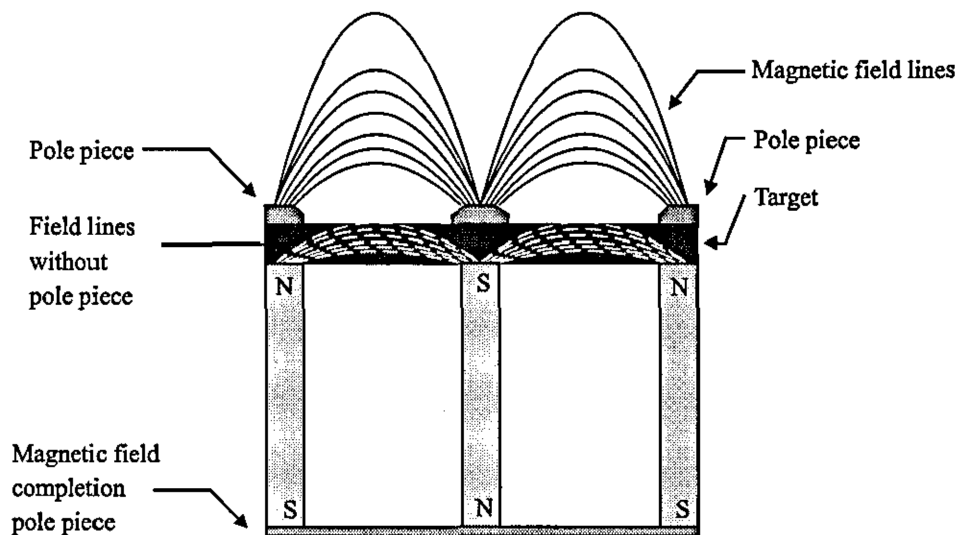

Figure 3.14 : Magnetic field line design, the use of pole pieces

Probably one of the most significant problems is obtaining a magnetic field outside the target. If a sputtering target is attached to the top of a magnetic arrangement, then the magnetic field lines are confined within the target material. This results in a significantly reduced sputtering rate and at worst no electron confinement. Figure 3.14 demonstrates this problem together with a solution. It has been proposed [20] that if the target was fixed by magnetic, and if possible non-conducting, pole pieces, then the magnetic field lines would emerge from the outer pole pieces and re-enter the magnetron at the central piece. This would enable efficient operation of the magnetron and maximise sputtering rates.

3.4 Target utilisation and coating uniformity

Although confinement of the electrons by magnetic fields increases the sputtering rate and decreases the operating pressures of the sputtering process, it does have disadvantages in that there is an associated localised erosion of the target. Furthermore, this erosion is not uniform but has a strong 'V' shape [18]. If electrons emerging from the dark space feel a force owing to a uniform parallel component of magnetic field, then the erosion zone would be uniform. This component is not uniform, however, and the parallel component of the B-field increases as the centre of the erosion zone is reached. This results in a greater density of electrons at this point and more collisions, creating more ions, and thus, preferentially sputtering the cathode surface in this location.

CHAPTER 3 REFERENCES

[1] **Faraday, M.**, (1857). *Phil. Trans.*, 147, 145.

[2] **Nahrwold, R.**, (1887). *Ann. Physik*, 31, 467.

[3] **Colligon, J.S.**, (1995). *J. Vac. Sci. Technol.*, A13(3), 1649-1657.

[4] **Hong, M., Kwo, J., Chen, C.H., Kortan, A.R. & Okada, M.**, (1988). *AIP Conf. Proc.*, (USA), 182, 127.

[5] **Schubert, J., Poppe, U. & Sybertz, W.**, (1989). *Less Common Met.*, 151, 277.

[6] **Gawehn, H.**, (1962). *A. Agnew Phys.*, 14, 458.

[7] **Vratny, F.**, (1967). *J. Electrochem. Soc.*, 114, 505.

[8] **Maniv, S.**, (1983). *Vacuum*, 33, 215.

[9] **Hines, R.L. & Wallor, R.**, (1961). *J. Appl. Phys.*, 32, 202.

[10] **Wehner, G.K.**, (1955). *'Sputtering by ion bombardment'*, in Advances in Electronics and Electron Physics, Vol VIII, ed. Martin, L., Academic Press, New York.

[11] **Lin, I. & Wu, M.S.**, (1992). *Semicond. Sci. Technol.*, 7, 2.

[12] **Saito, Y. & Shiosaki, T.**, (1991). *Jpn. J. Appl. Phys.*, Part 1, 30, 9B.

[13] **Santamaria, J., Sanchez-Quesada, F., Gonzalez-Diaz, G., Iborra, E. & Rodriguez-Vidal, M.**, (1985). *Thin Solid Films*, 125, 299.

[14] **Kumar, C.V.R.V. & Mansing, A.**, (1989). *J. Appl. Phys.*, 65, 1270.

[15] **Kesaev, I.G., & Pashkova, V.V.**, (1959). *Sov. Phys. Tech. Phys.*, 4, 254.

[16] **Chapin, J.S.**, (1974). *The Planar Magnetron Res. Dev.*, 25, 37-40.

[17] **Spencer, A.G.**, (1989). *'High rate reactive magnetron sputtering'*, Ph.D. Thesis, Loughborough University of Technology, U.K..

[18] **Spencer A.G., Bishop C.A., Howson R.P.**, (1987). *Vacuum*, 37, 363-366.

[19] **Thornton, J.A.**, (1978). *J.Vac.Sci.Tech.*, 15, 171.

[20] **Hall, G.W.**, (1993). *'Control of the properties of semiconducting thin films deposited using magnetron sputtering'*, Ph.D. Thesis, Loughborough University of Technology, U.K..

[21] **Ja'fer, H.A.**, (1993). *'Plasma assisted deposition using an unbalanced magnetron'*, Ph.D. Thesis, Loughborough University of Technology, U.K.

[22] **Pulker, H.K.**, (1988). *SPIE*, Vol. 1019, Thin Film Technologies III, 138-147.

[23] **Marinov, M.**, (1977). *Thin Solid Films*, 46, 267.

[24] **Martin, P.J., Macleod, H.A., Netterfield, R.P., Pacey, C.G. & Sainty, W.G.**, (1983). *Applied Optics*, 22(1), 178-184.

[25] **Greene, J.E.**, (1983). *CRC Crit. Rev. Solid State Mater. Sci.*, 11, 47.

[26] **Sproul, W.D.**, (1983). *Thin Solid Films*, 107, 141.

[27] **Thornton, J.A. & Penfold, A.S.**, (1978). in *'Thin film processes'*, ed. by Vossen, J.L. & Kern, W., Academic, New York, 75.

[28] **Movchan, B.A. & Demchishin, A.V.**, (1969). *Phys. Met. Metallogr.* (USSR), 28, 83.

[29] **Schiller, S., Heisig, V. & Goedicke K.**, (1977). *Thin Solid Films*, 40, 327.

[30] **Fraser, D.B. & Cook, H.D.**, (1977). *J. Vac. Sci. Technol.*, 14, 147.

[31] **Window, B. & Savvides, N.**, (1986). *J. Vac. Sci. Technol.*, A4, 196-202.

[32] **Window, B. & Savvides, N.**, (1986). *J. Vac. Sci. Technol.*, A4, 453-456.

[33] **Window, B. & Savvides, N.**, (1986). *J. Vac. Sci. Technol.*, A4, 504-508.

[34] **Rohde, S.L., Petrov, I., Sproul, W.D., Barnett, S.A., Rudnik, P.J. & Graham, M.E.**, (1990). *Proc. 17th Int. Conf. on Metall. Coatings & 8th Int. Conf. on Thin Films*, San Diego, U.S.A..

[35] **Howson, R.P., Ja'fer, H.A. & Spencer A.G.**, (1993). *Vacuum*, 44(3/4), 191-195.

[36] **Oka, K.**, (1988). *'Plasma activated growth of reactively sputtered optical thin films'*, Ph.D. Thesis, Loughborough University of Technology, U.K..

[37] **Thin Films Group**, (1981-1996). Loughborough University of Technology, U.K..

CHAPTER 4

REACTIVE MAGNETRON SPUTTERING

Many industrial applications demand not only well characterised, single element coatings, but also complex compound materials. This requirement imposes additional considerations upon the process designer in that not only does the metal constituent have to be well controlled but also the reactive component. This chapter will develop the concept of sputter deposition of compounds, explaining the fundamental problems with the process, control techniques necessary for accurate stoichiometry prediction and the comparative large scale applicability of these techniques. Furthermore, competing techniques such as sputtering from a compacted oxide target will be discussed. To establish a sound basis for the newly developed techniques arising from this thesis, only existing techniques will be detailed in this chapter.

4.1 INSTABILITIES IN REACTIVE SPUTTERING 45
4.1.1 Differential target poisoning *45*
4.1.1.1 The elemental mode 45
4.1.1.2 The poisoned mode 45
4.1.2 The hysteresis effect and solutions *46*
4.1.3 Differential cathode poisoning *51*
4.2 EXISTING TECHNIQUES FOR GAS CONTROL 53
4.2.1 Partial pressure control *53*
4.2.2 Light emission from a plasma *53*
4.2.3 Cathode potential *56*
4.2.4 Feedback control *57*
4.3 TARGET ARCING AND SOLUTIONS 59
4.3.1 Arc mechanisms *59*
4.3.2 Arc suppression *65*
4.3.3 AC sputtering and the TwinMAG™ *66*
4.4 COMPETING TECHNIQUES 69
4.4.1 RF sputtering of insulating cathodes *69*
4.4.2 Compound targets *69*
4.4.3 Successive Plasma Anodisation (SPA) *70*

4.1 Instabilities in reactive sputtering

To the uninitiated, the solution to the process requirement of compound formation would be to introduce a back-fill reactive gas partial pressure during sputtering of the metal component in order to create the compound at the substrate. Unfortunately, as will be shown throughout this chapter, this is rarely possible because of a variety of inherent features, such as differential target poisoning, reactivity of the cathode material and a pronounced non-linearity between reactive gas partial pressure and flow rate.

4.1.1 Differential target poisoning

When depositing compound coatings reactively from a metallic target, RF, AC, or DC discharges can be applied. The advantages of using a medium or high frequency power supply over a DC supply will be discussed in section 4.3. Depending on the flow rate of reactive gas, two distinct operating regimes can be distinguished [1], the elemental mode and the poisoned mode. The key concept in reactive magnetron sputtering is controlling the state of the target surface.

4.1.1.1 The elemental mode

At low reactive gas flow rates, the target is free of reactive gas species and only pure metal is sputtered. Any reactive gas immediately reacts with the sputtered metal atoms, and hence, a low partial pressure of reactive gas exists owing to this gettering effect. In the elemental mode, the sputtering rate is virtually unchanged from sputtering in pure Argon.

4.1.1.2 The poisoned mode

At higher reactive gas flow rates, the target surface becomes partially or totally coated with reactive gas species, and is characterised by a much reduced deposition rate. The

transition from elemental to poisoned mode is normally abrupt and exhibits a hysteresis behaviour.

4.1.2 The hysteresis effect and solutions

When the poisoned state is reached and the reactive gas flow is reduced to a point lower than that of the initial transition, the target stays poisoned with reactive products until a lower flow is reached. At this lower value, the reaction products on the target surface are sputtered away and the target switches back to an elemental mode.

All process parameters (cathode voltage, rate, total pressure, etc.) show a more or less pronounced hysteresis loop as a function of reactive gas flow, f_r. The classic model of the effects of the states upon the system pressure is shown in figure 4.1. A constant pressure, p_a, is maintained by the flow of non-reactive gas, f_a, into the continually pumped system. The dashed (-..-..) line represents the linear increase in total pressure that would be expected from increasing f_a alone with the discharge off. However, the total pressure does not increase in this way because the gas reacts with the metal. As shown by the solid line, the system pressure, p, remains constant at its initial value, p_a, until a flow rate, f_{r1}, when it rises to a new value, p_1. If no sputtering took place, the value of p at this total flow rate would be p_0 so that $\Delta p = p_0 - p_1$ is the reduction in system pressure owing to the reactive sputtering. Once the equilibrium value of p has been established, changes in f_r cause p to change linearly, the value of Δp between the system pressure, with and without reactive sputtering, being constant at each value of f_r. If f_r is reduced to f_{r2}, Δp increases and the system pressure decreases from p_2 to the initial value p_a. Generally, the transition between the two target modes occurs abruptly at f_{r2} and f_{r1}, and as a result depends on the direction of the transition.

Sproul [2] describes the hysteresis effect more quantitatively, and his explanatory hysteresis loops for both pressure and deposition rate versus flow of TiN_x are reproduced in figures 4.2a and 4.2b. There is no initial change in nitrogen partial pressure, N_{pp}, because all the reactive gas combines with the sputtered metal. When the flow reaches

point B, then N_{pp} suddenly rises because sufficient nitrogen is present to cause a compound to form on the target surface. As a consequence, the titanium sputter rate falls off, and the amount of nitrogen consumed by the process also drops. Hence, there is a large increase in N_{pp}, and further increase in nitrogen flow beyond this point will result in a linear increase in N_{pp} above point C. The N_{pp} does not decrease along the same path if nitrogen flow is now decreased. The N_{pp} stays high until the nitrided target surface is broken through and metal is sputtered once more. At this point, D, the nitrogen consumption increases rapidly, with a corresponding drop in N_{pp} to the original level.

Referring once again to Schiller's model and figure 4.1, the magnitude of the critical reactive gas flow, f_{r2}, is a measure of the basic stability of the system. The higher the value of f_{r2} at which the corresponding stability can be maintained, the greater the degree of reaction between the metal and reactive species. To obtain compound species at the substrate, at the desired degree of reaction, it is necessary to obtain a high degree of stability. Methods of process control within this otherwise unstable system, shown by the hysteresis in figure 4.2 will be described in section 4.2.4.

In 1988, Spencer *et al* [4] developed a conceptual model to quantify the pressure instability causing the hysteresis effects in the parameters previously identified. They did this by isolating the effects of increasing the partial pressure of reactive gas at the target and substrate, then combining the two effects to give the reactive gas consumption model. Figure 4.3 details the origins of the reactive gas consumption from the film. The target surface is continuously poisoned and then sputtered clean. Where the poisoning rate exceeds the cleaning rate, a partially poisoned state exists, and increasing the reactive gas pressure will increase the proportion of the target area that is poisoned. The resulting decrease in metal flux and sputter rate continues until the target is completely poisoned, at which point the metal flux remains essentially constant, figure 4.3a. With low reactive gas pressures, the rate of formation of the compound film at the substrate is limited by the arrival rate of the metal flux and by the utilisation of the reactive gas, and so the metal film is initially formed. As the reactive gas pressure is increased, the deposited film becomes less metallic, eventually saturating in an over-stoichiometric state, figure 4.3b.

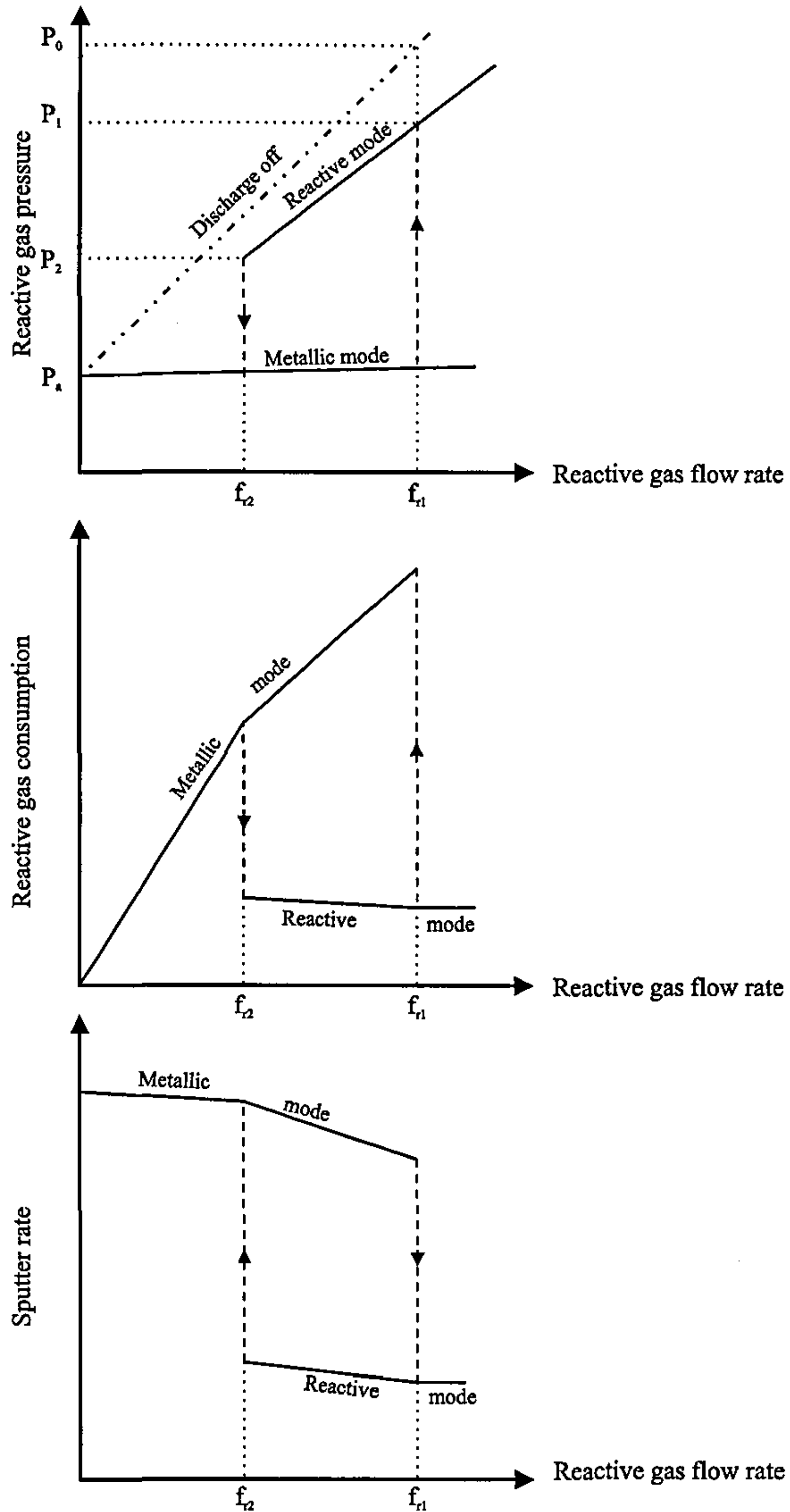

Figure 4.1 : Operating modes for a magnetron discharge [3]

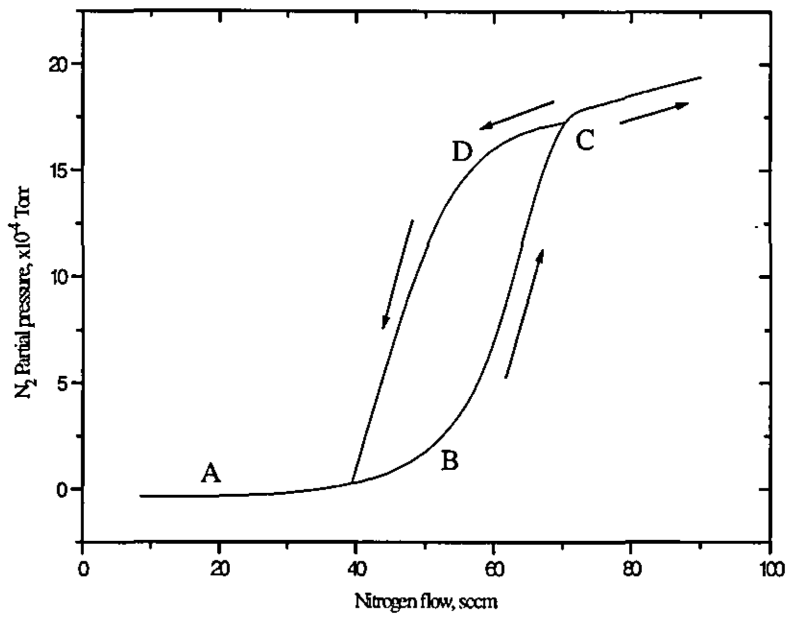

(a)

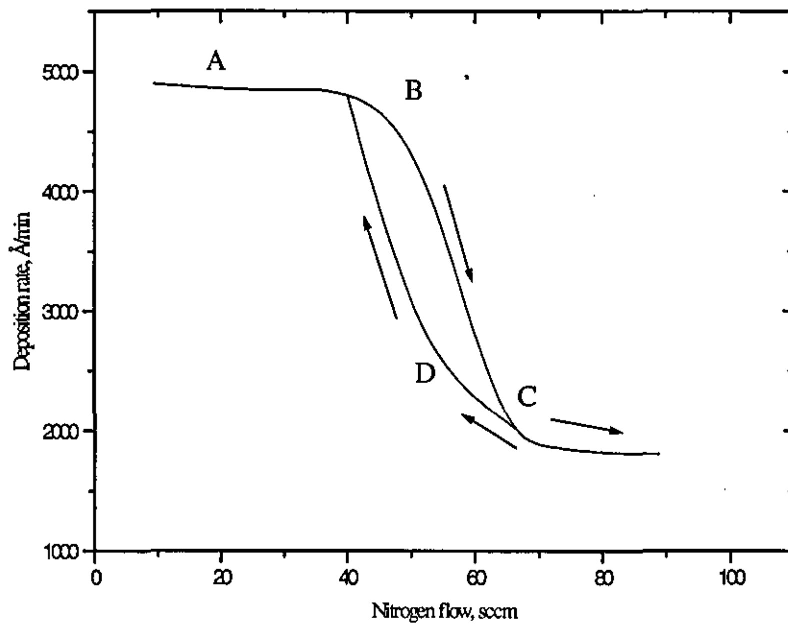

(b)

Figure 4.2 : Nitrogen partial pressure versus nitrogen flow rate for reactive sputtering of TiN_x [2]

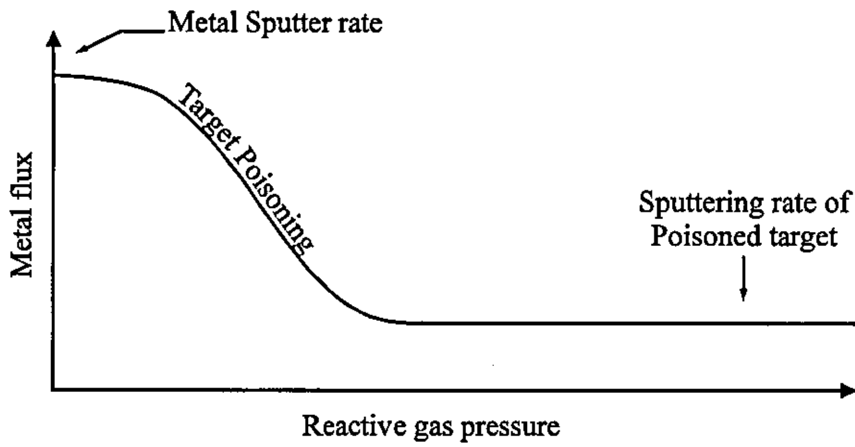

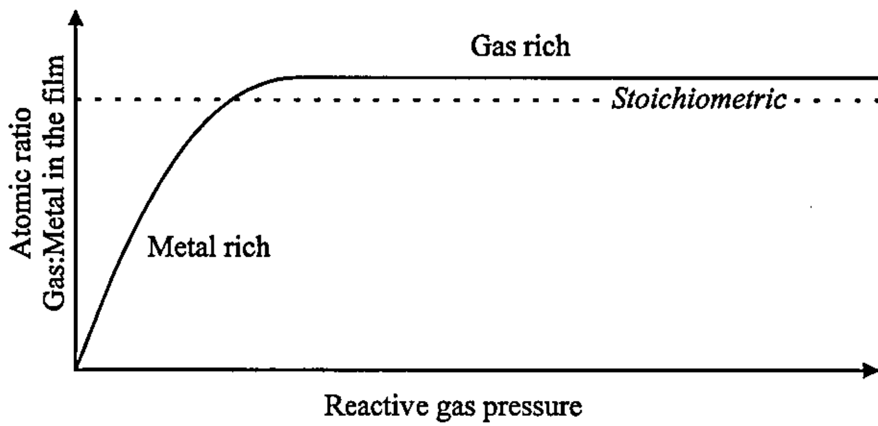

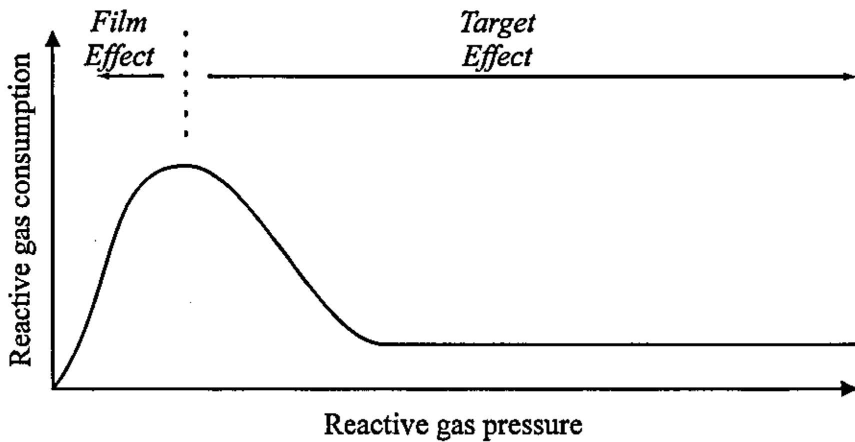

Figure 4.3 : Origins of reactive gas consumption by the film [4]

The processes at the target and substrate combine to give the complete reactive gas consumption curve of figure 4.3c. Spencer [5] confirmed the results of the model with experimental data for the oxygen consumption of titanium. Figure 4.4 shows the unstable region in which the process is uncontrollable using manual pressure control alone.

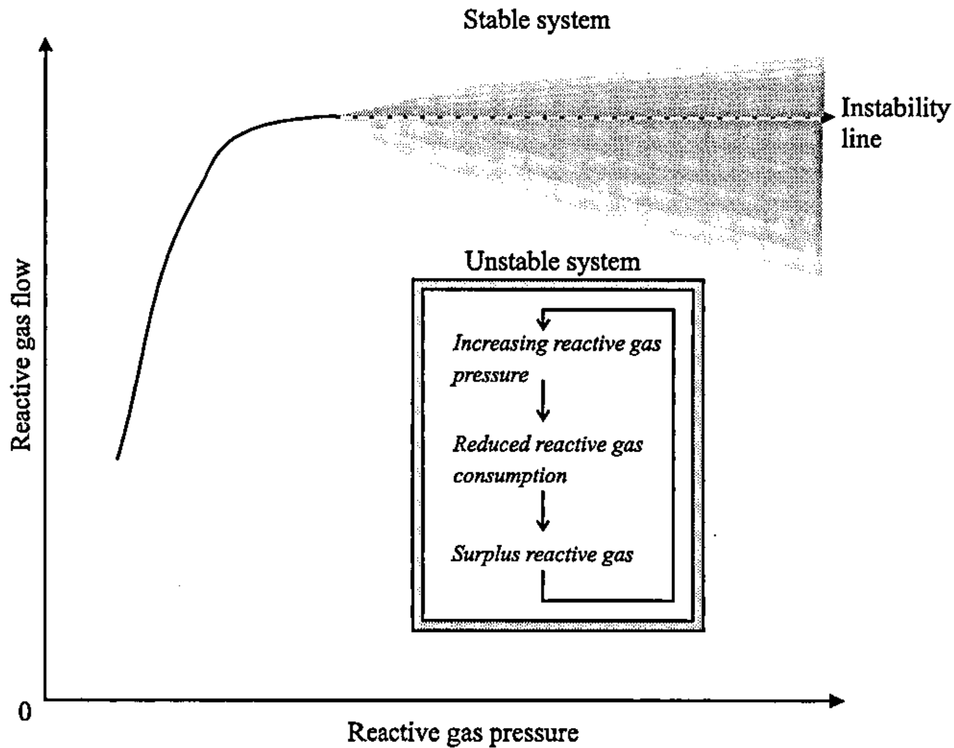

Figure 4.4 : The mechanism that causes the instability in reactive magnetron sputtering

4.1.3 Differential cathode poisoning

It was identified by Schiller *et al* [3] that owing to the inhomogeneous discharge density of magnetrons caused by the erosion zone, the sputter rate and oxidation rate are not constant over the target surface and show a pronounced site dependence. As a result, the degree of oxide coverage, Θ, on the target must also be site dependent. This leads to the possibility of three states existing simultaneously on the target surface; fully poisoned, fully metal, or partially poisoned. Their diagram is reproduced in figure 4.5, and shows the variation in Θ across a target cross-section surface with x being the distance from the centre. A peak is seen in the metal sputtering rate at the centre of the erosion zone, whilst the poisoning rate is fairly uniform. A consequence of this is that the centre of the

erosion zone stays metallic and the periphery becomes poisoned with reaction products. This is a widely recognised feature of reactively sputtered targets, and has been used as a diagnostic aid for determining the plasma discharge characteristics of planar magnetrons [6].

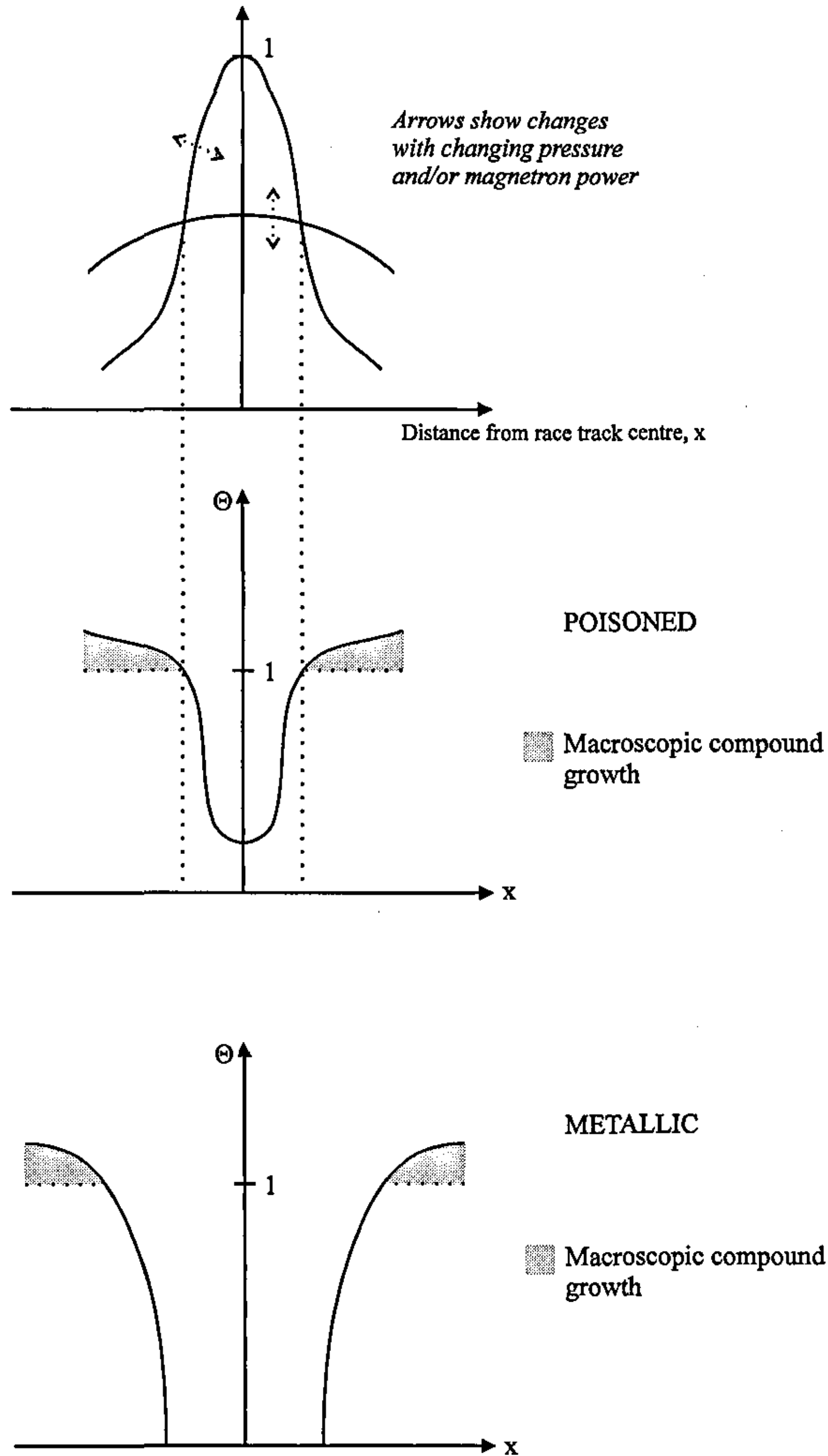

Figure 4.5 : Differential magnetron cathode poisoning [3]

4.2 Existing Techniques for Gas Control

To achieve precise control of the target state, and thus, maximise the deposition rate, whilst keeping tight stoichiometry control, the degree of poisoning at the target needs to be accurately measured. This measurement can be used as a process parameter indicative of target state and as the feedback signal in an automatic control system. Such a system was that alluded to by Schiller in his early paper [1], where the control parameters were spectral emission lines from the plasma. The following section details different ways of measuring the state of the target and plasma and explains how these parameters can be used to control the flow of oxygen within the system. It should also be noted that much research has been carried out on alternative feedback control mechanisms. One of the most successful pieces of work involved controlling the magnetron power at constant reactive gas flow and magnetron current [7].

4.2.1 Partial pressure control

Reactive gas partial pressure is an accurate measure of target status. However, measurement is usually very difficult and suffers from large time delays.

The reactive gas pressure can be measured using a mass spectrometer [8]. This technique of measurement suffers from time delays because of both remote positioning from the reaction zone, and stability and reliability problems caused by filament ageing. Electron impact excitation has been used in a control loop to measure the reactive gas partial pressure [9]. This system is much smaller than a mass spectrometer and does not require separate pumping, thus allowing the gauge to be placed closer to the reaction zone.

4.2.2 Light emission from a plasma

Observations of light emission from discharges, and their use as a diagnostic tool is not new. Von Hippel [10] first observed emission spectra of sputtered atoms in 1926, and

Stuart and Wehner [11] later showed that the emission intensity in the plasma was proportional to the sputter yield of the particular target being used. Sawatzky and Kay [12] showed that the emission intensity from a polycrystalline copper target could be used as an indicator of sputter yield, and Stirling and Westwood [13] have used emission and absorption spectroscopy to study the sputtered species from an aluminium target.

The emission of light in the positive column of a DC plasma results from electron transitions between two energy levels, with the line spectrum being characteristic of their atomic species. Enjouji *et al* [14] assumed excitation to be caused by electron-inelastic neutral atom collisions, so that the excitation and emission process of metal atoms could be expressed as follows

$$M + e \rightarrow M^{*} + e \qquad [4.1]$$

$$M^{*} \rightarrow M + h\nu \qquad [4.2]$$

where M represents the metal atom in the ground state and M* the metal atom in the emitting state.

Assuming excitation by inelastic electron collisions, the emission intensity at a point, x, in the discharge, corresponding to the transition between energy levels, i and j, is given by

$$I(x) = N(x)P_i(x)T_{ij}g(\lambda) \qquad [4.3]$$

where N(x) is the density of sputtered atoms, $P_i(x)$ is the probability of exciting an electron to state I, T_{ij} is the probability that the electron will decay back to state j, and g(λ) is the fraction of emitted photons corresponding to this transition that are collected. Schiller *et al* [15] stated that the intensity of a chosen spectral line at any point in the discharge is proportional to the number of level transitions from j to i per unit time and unit volume,

$$I_{ij} = \frac{n_k^*}{\tau_{ij}} \approx 10^8 . n_k^* s^{-1} \qquad [4.4]$$

where n_k^* is the number of atoms per unit volume having an excitation level, j, and τ_{ij} is the lifetime of the excitation level, usually [16] of the order of 1-10 ns. Greene [17] showed that the total number of excitation collisions per second per atom is given by

$$P_i(x) = \int n_e(x, v_e) \sigma_{exc}(v_e) dv_e \qquad [4.5]$$

$$\therefore P_i(x) = \frac{1}{(2m_e)^{1/2}} \int E_e^{-1/2} \sigma(E_e) n(x, E_e) dE_e \qquad [4.6]$$

where n_e, m_e and E_e are the electron population density, mass and kinetic energy respectively and σ_{exc} is the excitation cross-section.

Enjouji *et al* [14] obtained the following linear relationship between deposition rate, R, emission intensity, I, and target current, J_t,

$$R_d \propto \frac{I}{J_t}. \qquad [4.7]$$

It has been found experimentally [18] that the relationship between the intensity of the tantalum emission line at 481 nm, the discharge current and power is linear when operating in the metal mode, in the pressure range 0.1 to 1 Pa. This linearity is also found in the relationship between discharge intensity and deposition rate. At operating pressures below 0.1 Pa, however, the linearity is only found within a restricted power range. With a discharge power of 3 kW, the intensity increased by a factor of 2.4, when the pressure was increased from 0.1 to 1 Pa. The corresponding increase in deposition rate over the same pressure range was only 1.3.

To summarise, there is a linear correlation between the intensity of light emission from a discharge and the magnetron parameters of current, power and deposition rate. These

relationships, combined with the strong pressure dependence, enable the emission intensity to be used either as a diagnostic tool for determination of target or plasma status, or as a control parameter in reactive sputter deposition.

4.2.3 Cathode potential

The cathode target potential, or target current, can also be used as a measure of target status [19-21]. In much of the work on controlled reactive sputtering, however, reference is made to the cathode potential, but seldom to controlling the process using the potential as a measure of target status.

The voltage shows a similar transition, for the majority of materials, to the partial pressure curve of figure 4.3a. The cathode voltage is usually reduced when the target becomes poisoned because the oxide has a higher secondary electron coefficient than the metal. Thus, the current in the system is increased and the voltage reduced owing to the maintenance of constant power. This is not always the case, however, and some materials (Zr, Ti) show an initial voltage increase, followed by a decrease in cathode voltage, as will be detailed in this work.

Control Signal	Advantages	Disadvantages
Partial pressure	Direct measure of instability.	Very slow (large time constant) arising from remote acquisition.
Plasma emission	Fast feedback (small time constant).	Instrument drift. Production durability.
Cathode potential	Very fast (small time constant). Convenient.	Poor long term drift owing to target erosion. Low sensitivity in certain regions of reactive gas pressure.

Table 4.1 : Advantages and disadvantages of possible control signals used in reactive sputtering

4.2.4 Feedback control

Once a suitable control signal, indicative of the state of the target surface, has been obtained, this signal can be used in a feedback control loop. A typical control loop is that of Plasma Emission Monitoring (PEM), first detailed by Schiller *et al* [15] in 1987, which is arguably the most reliable reactive control instrument in use at present.

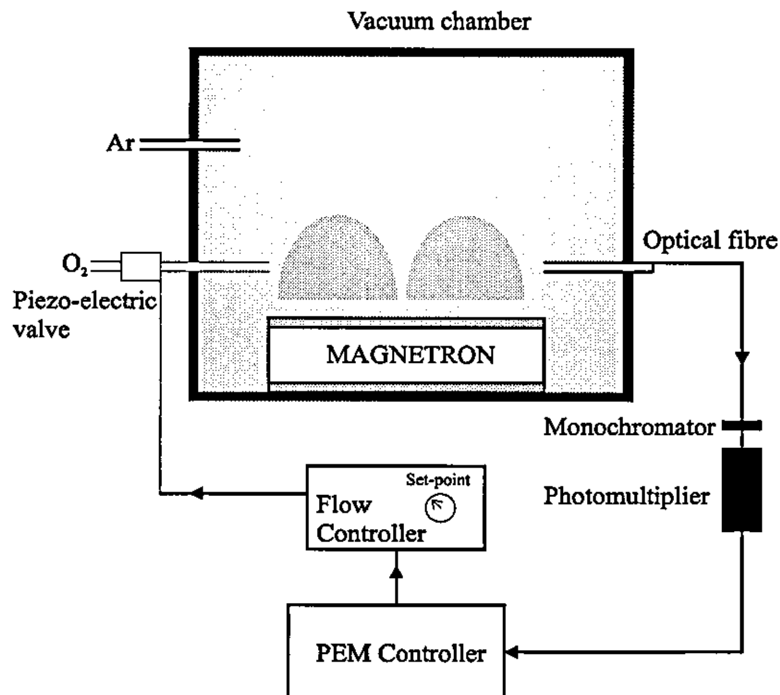

Figure 4.6 : Plasma Emission Monitoring (PEM) control loop

The PEM and other feedback equipment specific to the system used throughout this work will be described in chapter 6, but the general principle, with reference to PEM, is given here.

The usual format of a PEM control loop is illustrated in figure 4.6. The process is initiated when the target is in elemental mode, so that a 100% reference signal can be identified. Another 0% reference signal is also needed when the target is fully poisoned. An optical fibre views the plasma across the target surface diameter in order to maximise the light intensity received by the controller. Care has to be taken to ensure that the end of the fibre bundle does not become coated with sputtered material, which would reduce the magnitude of the transmitted signal. Furthermore, the fibre must 'see' a full cathode

diameter to avoid false indications of target mode, which may occur if the fibre is directed at the periphery, where oxide tends to accumulate. In addition to the emission lines corresponding to the target, there will be emission lines present in the discharge resulting from electron transitions for Ar, the reactive gas, carbon compounds from contamination sources and H_2 and O from water vapour dissociation.

To filter out the background and unwanted line emissions, a monochromator is used to select only the desired line emission of the target or reactive gas. The wavelength of the monochromator is chosen so that the signal it passes is unaffected by nearby argon or unwanted emission lines. From the monochromator, the signal is fed to a photomultiplier and converted into an electrical signal, which then passes to the controller. The controller compares the normalised incoming signal with an operator-selected 'set-point' of emission intensity. Should the set-point be lower than the incoming signal, the controller automatically opens a piezo-electric control valve to admit a flow of reactive gas to the system. The addition of reactive gas causes a change in target mode, so that a smaller area of its surface sputters metal, and the emission signal falls to a new level, indicative of the target state. Automatic adjustment of the valve continues until the magnitudes of the set-point and input signal are equal, at which point the controller holds the process stable. Piezo-electric valves are used because of their quick response, so that, providing the time constant of the control loop is not too long and the gas admission not too remote from the plasma, the system will react to the onset of a poisoned target by reducing reactive gas flow to move the process back towards the knee of the hysteresis loop of figure 4.3a.

McMahon *et al* [22] investigated a way of achieving optimum control of the reactive planar magnetron sputtering process, using the cathode voltage. They used a constant gas flow into the system and controlled the voltage to a pre-set value by varying the target current. This enabled them to keep the target surface from poisoning and allowed accurate stoichiometric control of the deposited film. This technique of maintaining a constant reactive gas flow has been widely used [7,23,24]. It will be shown in this work, however, that control of the reactive gas flow using voltage as a measure of target status is possible and can be used for many materials.

4.3 Target Arcing and Solutions

One of the main problems encountered when sputtering a metal in a reactive environment is target arcing. Inevitably, reactive gas reaches the target surface whilst sputtering. As mentioned earlier, in section 4.1.3, there is a non-uniform plasma density in front of the magnetron and differential poisoning occurs at the target surface, the reaction products forming an insulating layer outside of the erosion groove, figure 4.7. The frequency of these arcs increases with the insulating properties of the compounds being deposited. Hence, arcs cause major problems when depositing SiO_2 and Al_2O_3, such as a decrease in the stability of the reactive gas control process and the emission of target particulates. The following section details various mechanisms through which these arcs form and existing techniques for their suppression.

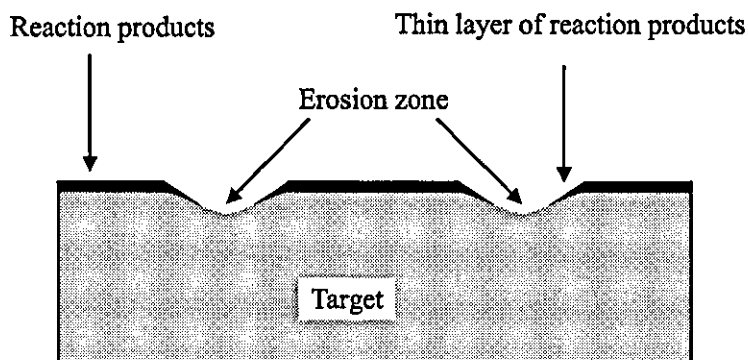

Figure 4.7 : Differential poisoning of the cathode surface

4.3.1 Arc mechanisms

Figure 4.8 [25] represents an enlarged schematic of the target surface and plasma. Positive ions are accelerated out of the plasma towards the target by a negative cathode voltage, U_c. In the race-track these ions cause the ejection of target material and are neutralised from the capture of electrons supplied by the power source. On the left side of the illustration, an oxide layer is formed outside the race-track where the sputtering rate is very low. In this region no electrons are available to compensate the positive charge of arriving ions, therefore, the surface steadily charges up, eventually reaching the plasma potential. Before this occurs, however, voltage breakdown of the oxide layer is much more likely.

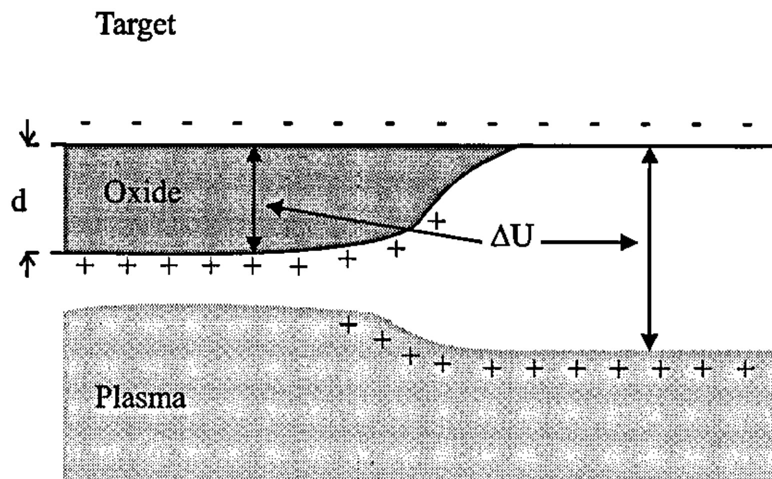

Figure 4.8 : Voltage drop between the plasma and partial oxide layer formed on the target [25]

Szczyrbowski *et al* [26] proposed a model to calculate the electric field build up in an insulating layer formed on the target.

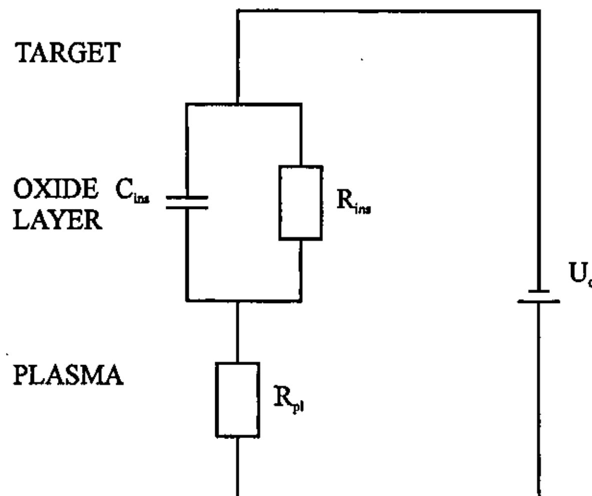

Figure 4.9 : Equivalent electrical circuit of target - insulating layer - plasma system [26]

The system as shown in figure 4.8 can be represented as an equivalent electrical circuit, figure 4.9. The insulating layer behaves like a capacitor and a resistor connected in parallel. R_{ins} and C_{ins} represent the resistance and capacitance of the insulating layer, where C_{ins} depends mainly on the film thickness. R_{pl} represents the plasma impedance in the region of the target covered by the insulator. In the following analysis it is assumed

that the surface current of the film is negligible compared to the current across the insulating layer, and that the plasma potential is zero.

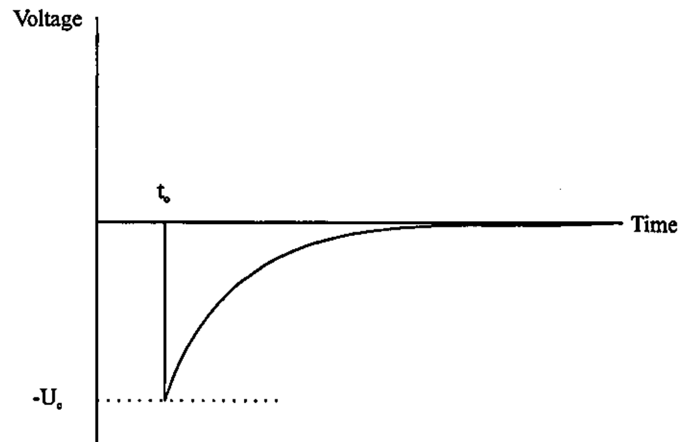

Figure 4.10 : Time dependence of the surface potential created on the insulating layer [26]

Initially, at t_0 (shown in figure 4.10), the insulating layer will start to charge positively. The potential of the film surface exposed to the plasma rises towards zero as plotted, the maximum potential being reached when the plasma current towards the layer, j_p, is equal to the current across the layer, j_l. Hence,

$$j_p = j_l \qquad [4.8]$$

where the current density across the layer is given as

$$j_l = \frac{U_c - V}{\delta . d} \qquad [4.9]$$

and U_c is the cathode potential, V is the potential of the dielectric layer surface exposed to the plasma, and d and δ are the thickness and the specific resistivity of the layer, respectively. The ion current density, J_p, is given by the relationship by Child-Langmuir [27] for a space charge limited current as

$$j_p = \frac{4\varepsilon_0}{9}\left[\frac{2e_i}{m_i}\right]^{1/2}\frac{V^{3/2}}{D^2} = AV^{3/2}. \qquad [4.10]$$

In this relationship, ε_0 is the vacuum dielectric constant, e_i and m_i are the ion charge and mass respectively, and D is the thickness of the cathode sheath. Combining and rearranging equations 4.8, 4.9 and 4.10 gives

$$(U_c - V)^2 = (\delta . d . A)^2 V^3 \qquad [4.11]$$

the quantity (U_c-V) representing the potential drop on the considered dielectric layer.

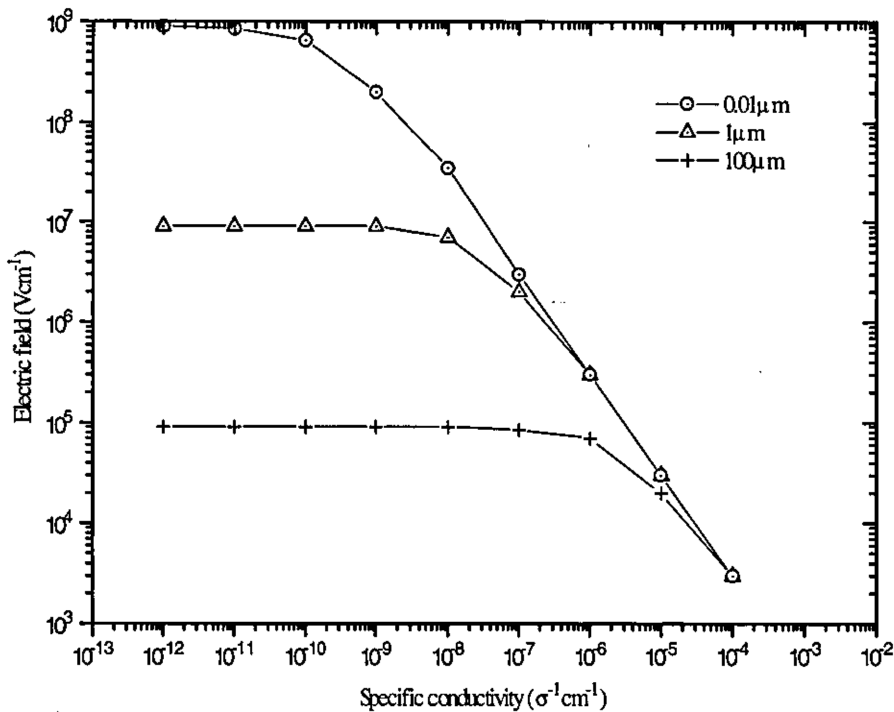

Figure 4.11 : Electrical field versus specific conductivity of the insulating layer formed on the cathode surface

Figure 4.11 [26] is a plot of the electric field versus the specific conductivity in an insulating layer. The individual plots are for films with various thicknesses as shown. The calculations have been performed with the following parameters;

Sputter gas	**Argon**
D (Sheath thickness)	**1 mm**
U_c (Cathode potential)	**700 V**

For most dielectric materials, including SiO_2, the breakdown field, E_{bd}, is in the range of 10^6 Vcm^{-1}. Hence, from comparisons with figure 4.11, it can be seen that the electrical field in an insulating layer with a specific conductivity, $\sigma = 1/\delta$, higher than 10^{-7} $(\Omega cm)^{-1}$, can never surpass the value of its breakdown field, independent of film thickness. This is true, and has been proved experimentally, for SnO_2, ZnO, In_2O_3. It should be pointed out, however, that for the same materials, the process becomes unstable in a gas atmosphere with a surplus of oxygen, because the specific resistivity of the deposited film increases with oxygen partial pressure.

For films with specific conductivities lower than 10^{-7} $(\Omega\ cm)^{-1}$ one always has to deal with layers charged above their electrical breakdown field, since thickness of re-deposited materials on the target surface ranges from zero, close to the erosion zone, to a maximum value away from it. Al_2O_3, SiO_2 and ZrO_2 usually have a specific conductivity lower than 10^{-7} $(\Omega\ cm)^{-1}$. This implies instability in the reactive process which has been confirmed by experiment [26].

The striking of an arc can be described as follows, figure 4.12. The event starts with an electrical breakdown of the thin dielectric layer as described above. This is likely to trigger a micro-arc which in turn can trigger a bipolar arc. It should be noted, however, that the breakdown does not necessarily result in a bipolar arc in each case. In the case of SiO_2 [25], micro-arcs can easily occur at frequencies as high as several kHz. Investigations [28] have shown that it is about one micro-arc out of a thousand that results in a bipolar arc. These arcs produce particulates which contaminate the growing layer on the substrate. In addition, sufficient charge can be injected into the plasma to cause it to collapse into a self-sustaining arc discharge.

Most magnetron targets arc on initial operation, after exposure to air, because of the formation of thermal oxides, even when sputtering in an inert gas. As this oxide is sputtered off (seen as a change in magnetron potential) the arcing frequency decreases.

Arc producing mechanisms, arc lifetimes and arc frequencies are all dependent on the sputtered material. Beisswenger *et al* [25] have, however, examined the behaviour of

different materials and noticed certain trends. They showed that the arcing frequency increases exponentially with time for SiO_2 and SnO_2, figure 4.13. Furthermore, they stated that at arcing frequencies above 200 arcs per hour, coating uniformity is no longer guaranteed owing to the active electrical circuitry cut-offs in the DC power supply.

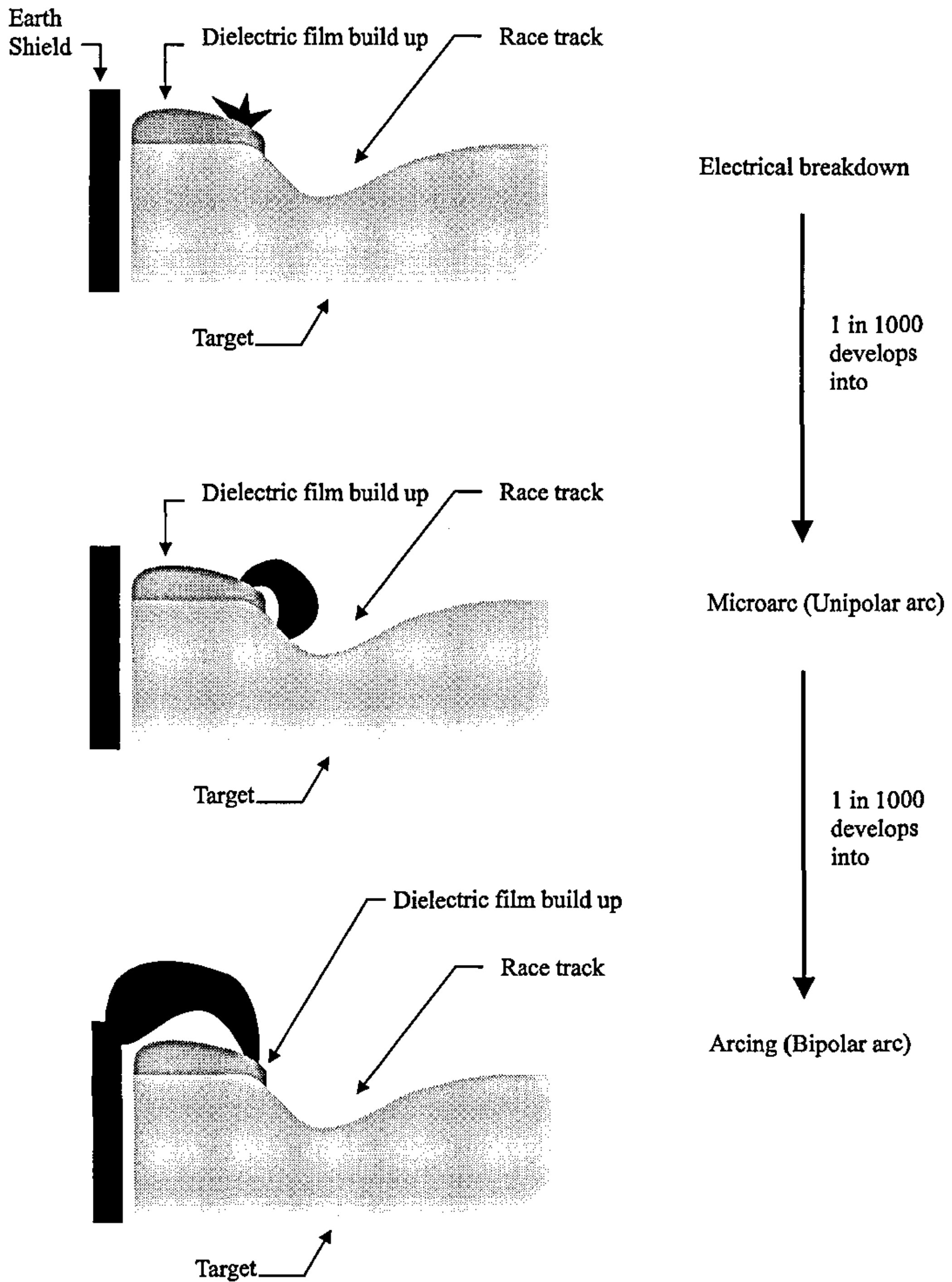

Figure 4.12 : Formation of a bipolar arc

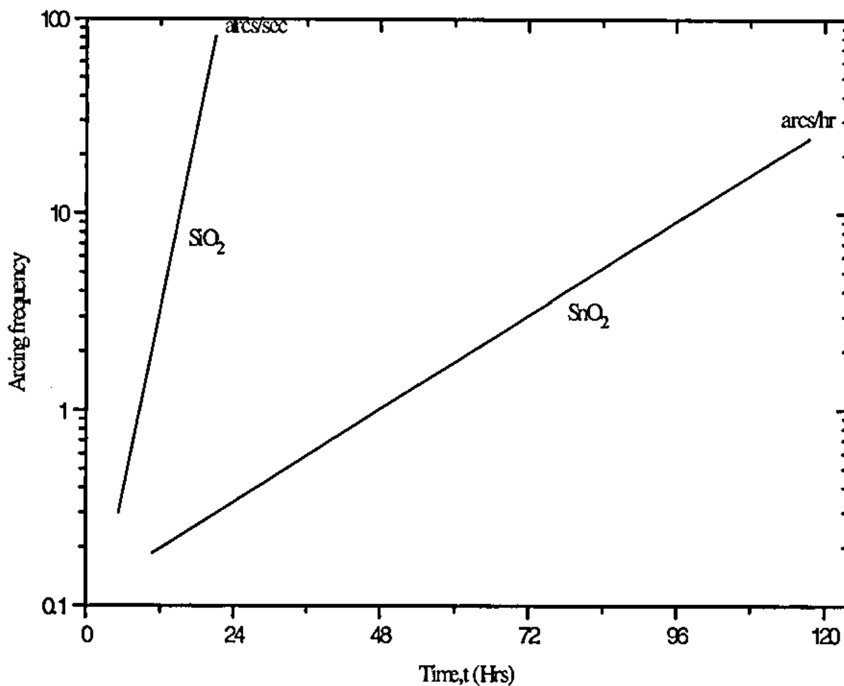

Figure 4.13 : The increase of arcing frequency with time when reactively sputtering SiO_2 and SnO_2 [25]

4.3.2 Arc suppression

This basic understanding of arc formation has led to the development of various techniques for the realisation of arc free, DC reactive magnetron sputter processes. Many extrinsic arc suppression units have been built to detect arcs and extinguish them before they become a serious problem.

Traditional electrical solutions minimise the energy of a single arc by immediately switching off the voltage supply to the target. In a well designed switching power supply, the typical 'down time' between the onset of an arc and the re-establishment of normal operation is 10 ms and a minimum of approximately 1 J will be fed into the arc. Figure 4.14 [29] illustrates a typical arc waveform for a DC supply.

The role of arc suppression units is two-fold. Firstly, to minimise the stored energy in the supply's output. thereby reducing arc energy. Secondly, to detect rapidly the arc and shut off the supply. Their operation principle is based on an electronic switch which

causes a very fast reversal of the cathode voltage polarity, resulting in a complete elimination of charged particles which carry the arc. A typical waveform for the ENI DCG-100 with Arckill™ is shown in figure 4.15. The total 'down time' is now reduced to approximately 50 μs. These units have been successfully used to deposit very reactive materials such as Al_2O_3 at high rates and with good stability [30].

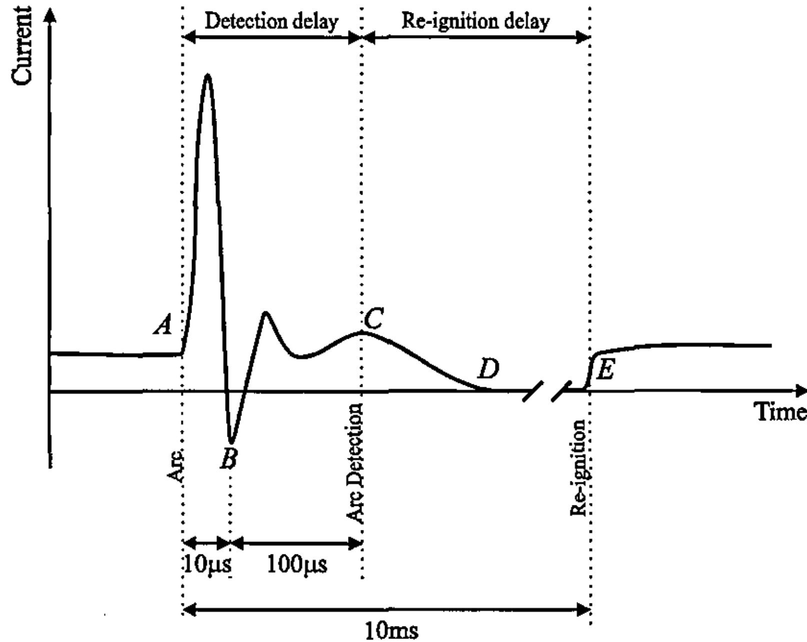

Figure 4.14 : Typical arc waveform for a DC supply [29]

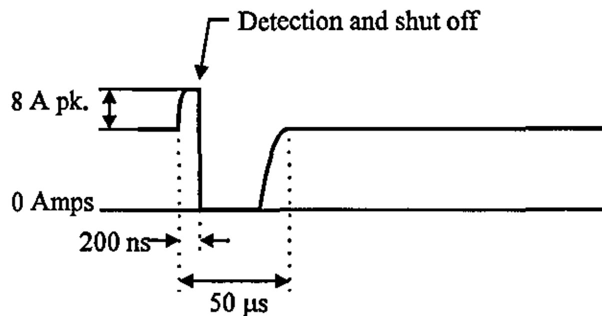

Figure 4.15 : Typical arc waveform for a DC supply with Arckill™ [29]

4.3.3 AC sputtering and the TwinMAG™

Arc suppression units eliminate the arc on detection and can be thought of as extrinsic devices. However, it is possible to achieve intrinsic elimination (suppressing the

formation of an arc) by various techniques, including AC sputtering [25,31] and Pulsed Magnetron Sputter Technology (PMST) [28,32-36]. These systems suppress the charging of an insulating layer on the cathode by using an alternating voltage generator.

If the DC magnetron driver is replaced by a square wave AC generator, a time dependence similar to that in figure 4.10 can be assumed for the negative half cycle. Furthermore, the positive charge accumulated during this cycle is neutralised by the electron bombardment during the next half cycle. The following theory [26] estimates the electrical field in the insulating layer versus the frequency of the applied square wave.

The potential change on the surface exposed to the plasma may be written as

$$\frac{dV}{dt} = -\frac{i}{C_{ins}} \qquad [4.12]$$

where C_{ins} is given by

$$C_{ins} = \frac{\varepsilon_0 \varepsilon_1 S}{d} \qquad [4.13]$$

where S is the surface area and ε_1 is the dielectric constant of the film.

The Child-Langmuir relation, equation 4.10, can be used again for the plasma current. Assuming a square wave generator, the following expression is obtained for the surface potential

$$V = \frac{1}{\left(\frac{1}{\sqrt{U_c}} + \frac{1}{4} B\tau \right)^2} \qquad [4.14]$$

where τ is the wave period and

$$B = \frac{4d}{9\varepsilon_1} \left[\frac{2e_i}{m_i} \right]^{1/2} \frac{1}{D^2}. \qquad [4.15]$$

Hence, the electrical field, E, in the layer is

$$E = E_0 \left[1 - \frac{1}{\left(1 + \frac{1}{4}\sqrt{E_0 d}B\tau\right)^2} \right] \qquad [4.16]$$

where

$$E_0 = \frac{U_c}{d}. \qquad [4.17]$$

Figure 4.16 shows a plot of electric field versus frequency for a square wave generator. The value of the accumulated electrical charge on the insulating layer decreases with increasing frequency as expected. Moreover, at 50 kHz the electrical field in a film of thickness, τ_f = 1 μm, drops by two orders of magnitude. Above this frequency, the sputter rate significantly drops and it is for these reasons that the optimum sputtering frequency is between 40 kHz and 70 kHz.

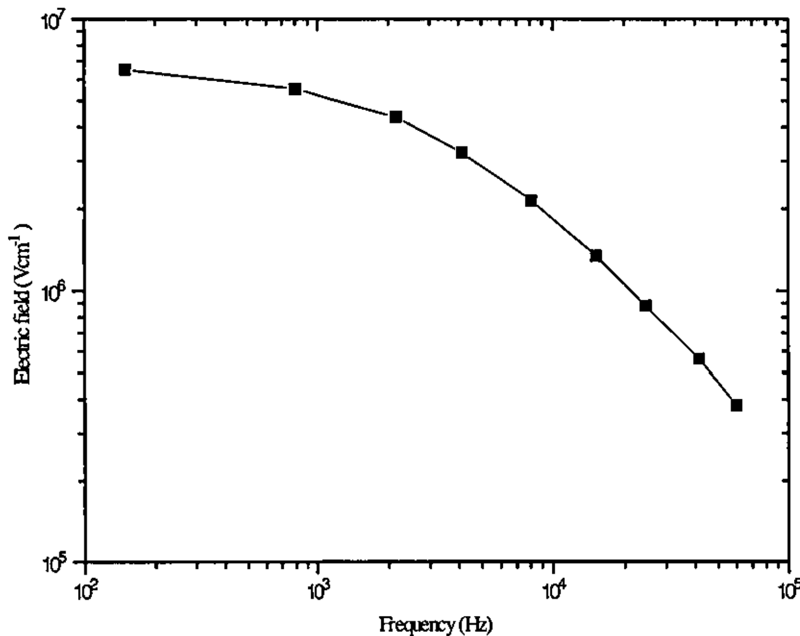

Figure 4.16 : Electric field in an insulating layer formed on the cathode surface versus applied frequency

Many workers have reactively sputtered films using pulsed units attached to their existing DC supplies. These include Al_2O_3, SiO_2, and TiO_x [32]. Furthermore, various techniques now exist to utilise the advantages of medium frequency (MF) sputtering [37]. The problem of this MF technique is that no sputtering takes place during the positive cycle of the pulse. The TwinMAG™ arrangement [38] solves this problem by using two identical magnetrons. The two anti-phase outputs of the AC supply are connected to the magnetrons. At any time, one of the electrodes is negatively biased and acts as a sputtering source, whilst the other acts as an anode dissipating any built up charge [37,39].

4.4 Competing Techniques

Over the last 10 years, reactive sputtering has emerged as the leading technique in the deposition of compound films. It does, however, have limitations and needs expensive control instrumentation and precise initialisation to ensure optimum and repeatable results. Other techniques for depositing oxide, nitride and other compound materials have proved successful for certain applications. Their limitation, however, is usually in the reduced deposition rate achieved, a factor that is of major importance in the majority of industrial applications. The following section details these competing techniques.

4.4.1 RF sputtering of insulating cathodes

Section 3.1.2.4 details the specifications of RF sputtering. These RF powered magnetrons can be operated with dielectric compound targets, but for economic mass production on large scales, their use is prohibited because of low deposition rates, high equipment costs (power supply and matching networks), and scaling problems.

4.4.2 Compound targets

Although only RF supplies can be used to power highly insulating compound targets, there now exists a breed of low conductivity targets. Materials such as ITO and ZnO:Al

can now be sputtered from compacted (sometimes called compounded) oxide targets. These targets are made by compressing powder of the desired composition under high pressure and temperature and can be powered by DC supplies.

The technique of sputtering from a compacted, partially conducting target usually involves the addition of a small amount of oxygen into the sputtering environment. This is because the target is made oxygen deficient to allow for any small changes in sputtering conditions and to compensate for any drift in target stoichiometry owing to preferential sputtering.

It has been shown [40] that the sintering density of compacted targets is a key factor in obtaining the maximum deposition rate. Lewis *et al* [40] showed that increasing the sintering density in a ZnO:Al target from 66% (porous) to 93% (no pores apart from grain boundaries) gives a two-fold increase in deposition rate. This work will show that deposition rates comparable to those obtained by reactive sputtering are now possible using compacted targets.

4.4.3 Successive Plasma Anodisation (SPA)

A control technique has recently been demonstrated [41] which is termed Successive Plasma Anodisation (SPA). This is an alternative to the simultaneous supply of reactants to the growing film, found with both conventional PEM and cathode-voltage control, in which successive layers are formed of monolayer thickness, then plasma anodised. Silicon is deposited onto the substrate in one position, then rotated to another to be anodised by an oxygen plasma. Separating the deposition and reaction stages has been shown to give advantages in reactive sputtering.

This process forms the basis of a precision coating machine for the coating of ophthalmic lenses which is completely stable and can operate with a minimum of control systems [42] and is shown in figure 4.17. It does, however, suffer from limitations introduced by mechanically rotating the substrates, such as a significantly reduced deposition rate. Furthermore, arcing is still a problem owing to reactive gas reaching the deposition stage.

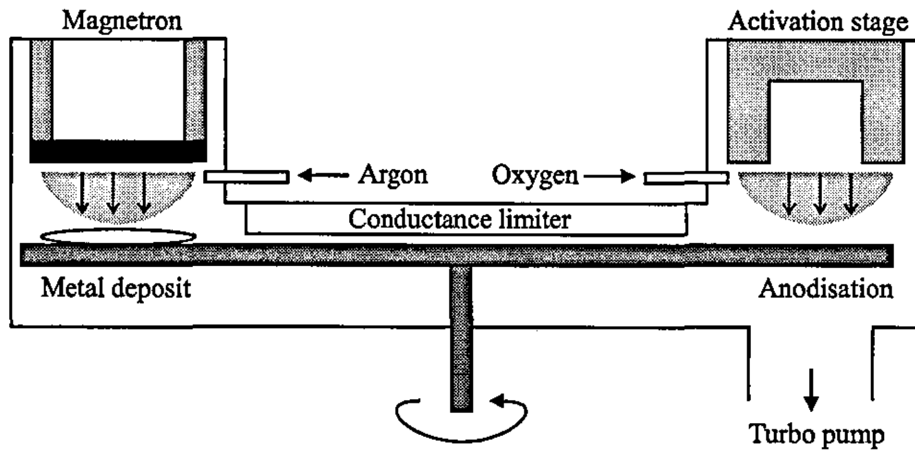

Figure 4.17 : Deposition of compound materials by successive plasma anodisation (SPA)

This investigation considers the use of a SPA process separated in time, without mechanical movement, but pulsing the reactive gas [43,44] in response to a control signal proportional to the degree of target poisoning.

CHAPTER 4 REFERENCES

[1] **Schiller, S., Beister, G. & Sieber, W.**, (1984). *Thin Solid Films*, 111, 259.

[2] **Sproul W.**, U.S. Patent 4428812

[3] **Schiller, S., Heisig, U. & Goedicke, K.**, (1979). *Thin Solid Films*, 64, 455-467.

[4] **Spencer, A.G., Howson, R.P. & Lewin, R.W.**, (1988). *Thin Solid Films*, 158, 141.

[5] **Spencer, A.G.**, (1988). *'High rate reactive magnetron sputtering'*, Ph.D. Thesis, Loughborough University of Technology, U.K.

[6] **Fukami, T. & Shintani, F.**, (1987). *Thin Solid Films*, 151, 373.

[7] **Oyama, T., Ohsaki, H., Ogata, Y., Watanabe, S. & Shimizu, J.**, (1995). *Proc. of the 3rd ISSP*, Tokyo.

[8] **Hmiel, A.F.**, (1985). *J. Vac. Sci. Technol.*, A3(3), 592-595.

[9] **Sproul, W., Rudnik, P. & Gorgol, C.**, (1989). *R. d. D.*, 79-82.

[10] **von Hippel, A.**, (1926). *Ann. Phys.*, (Leipz), 80, 672.

[11] **Stuart R.V. & Wehner G.K.**, (1962). *J. Appl. Phys.*, 33, 2345.

[12] **Sawatzky, E. & Kay, E.**, (1966). *Rev. Sci. Instrum.*, 37, 1324.

[13] **Stirling, A.J. & Westwood, W.D.**, (1970). *J. Appl. Phys.*, 41, 742.

[14] **Enjouji, K., Murata, K. & Nishikawa S.**, (1983). *Thin Solid Films*, 108, 1.

[15] **Schiller, S., Heisig, U., Steinfelder, K., Strumpfel, J., Friedrich, A. & Fricke, R.**, (1987). *Proc. Int. Conf. on Ion Plating & All. Techn.*, Brighton, p.223.

[16] **Herzberg, G.**, (1945). *'Atomic Spectra and Atomic Structure'*, Dover, New York.

[17] **Greene, J.E.**, (1978). *J. Vac. Sci. Technol.*, 15(5), 1718.

[18] **Schiller, S., Heisig, U., Steinfelder, K. & Strumpfel, J.**, (1982). *Thin Solid Films*, 96, 235.

[19] **Schiller, S., Heisig, U., Steinfelder, K. & Strumpfel, J.**, (1979). *Thin Solid Films*, 63, 369.

[20] **Maniv, S., Miner, C. & Westwood, W.D.**, (1981). *J. Vac. Sci. Technol.*, 18, 195-198.

[21] **Ohsaki, H.**, (1995). *Proc. of the 3rd ISSP*, Tokyo.

[22] **McMahon, R., Affinito, J. & Parsons, R.R.**, (1982). *J. Vac. Sci. Technol.*, 20(3), 376-378.

[23] **Affinito, J. & Parsons, R.R.**, (1984). *J. Vac. Sci. Technol.*, A2, 1275-1284.

[24] **Frach, P., Heisig, U., Gottfried, Ch. & Walde, H.**, (1993). *Surface & Coatings Technol.*, 59, 177.

[25] **Beisswenger, S., Faber, R. & Szczyrbowski, J.**, (1995). *Proc. of the 3rd ISSP*, Tokyo, 331-340.

[26] **Szczyrbowski, J. & Braatz, C.**, (1992). *SPIE*, 1727, 122-136.

[27] **Lanmuir, I.**, (1924) *General Electrical Review*, 26, 731.

[28] **Schiller, S., Goedicke, K. & Kirchoff, V.**, (1993). *7th Int. Conf. on Vacuum Web Coating*, Miami, Florida, U.S.A.

[29] **Sellers, J.**, (1993). *ENI Tech Note.*

[30] **Sproul, W.D., Graham, M.E., Wong, M.S., Lopez, S., Li, D. & Scholl R.A.**, (1995). *J. Vac. Sci. Technol.*, A13(3), 1188.

[31] **Beisswenger, S.**, (1991). *Proc. of the 1st ISSP*, Tokyo, 137-147.

[32] **Graham, M.E. & Sproul, W.D.**, (1994). *Soc. of Vac. Coaters, 37th Ann. Tech. Conf. Proc.*, 275.

[33] **Schiller, S., Kirchhoff, V. & Kopte, T.**, (1995). *Proc. of the 3rd ISSP*, Tokyo.

[34] **Pond, B.J., Du, T., Sobczak, J. & Carniglia, C.K.**, (1992). *Proc. of the Optical Soc. of America.*

[35] **Frach, P., Heisig, U., Gottfried, Ch. & Walde, H.**, (1993). *Surface and Coatings Technol.*, 59, 177.

[36] **Schiller, S., Goedicke, K., Reschke, J., Kirchhoff, V., Schneider, S. & Milde, F.**, (1993). *Surface and Coatings Technol.*, 61, 331.

[37] **Scholl, R.A.**, (1995). *Proc. of the 3rd ISSP*, Tokyo, 37-46.

[38] **Beister, G., Beisswenger, S., Brauer, G., Dietrich, E., Kukla, R., Szczyrbowski, J. & Teschner, G.**, (1993). *Glastech. Ber.*, 66, 175-183.

[39] **Brauer, G., Dicken, W., Szczyrbowski, J., Teschner, G. & Zmelty, A.**, (1995). *Proc. of the 3rd ISSP*, Tokyo, 63-70.

[40] **Lewis, B.**, (1996), *SVC Conference proceedings*, Philadelphia.

[41] **Howson, R.P.**, (1994). *Pure & Appl. Chem.*, 66(6), 1311-1318.

[42] **Applied Vision Ltd.**, (1991).Technical literature.

[43] **Toyoda, S., Kiyota, T., Tamagawa, K. & Yamakawa H.**, (1993). *Materials Science and Engineering*, A163, 167.

[44] **Aronson, A.J., Chen, D., and Class, W.H.**, (1980). *Thin Solid Films*, 72, 535-540.

CHAPTER 5

THIN FILM FORMATION AND STRUCTURE

Having now examined the processes occurring in a gas discharge and that of physical sputtering in chapters 3 and 4 the following chapter aims to review the current progress in determining how a sputtered film forms by examining its microstructure, crystal-structure, and stress. The implications of variable ion bombardment at the substrate is considered along with various other factors affecting film growth. This is followed by a more detailed examination of the various structure zones formed in the growth of thin films. Finally, a review of the mechanisms occurring in the formation of stress in thin films is given. Only continuous films prepared at temperatures at which thermally activated annealing processes, such as grain growth, defect annihilation, and mass transport, are absent are described. This represents the conditions under which the films were made throughout this work.

5.1 FACTORS INFLUENCING THIN FILM GROWTH 74
5.1.1 Particles arriving at the substrate *75*
5.1.2 Substrate self-bias *78*
5.1.3 Ion bombardment at the substrate *78*
5.1.3.1 The ion/atom ratio 80
5.2 THIN FILM NUCLEATION THEORY 82
5.2.1 Stages prior to continuous film formation *82*
5.2.2 Interface formation *85*
5.3 MORPHOLOGY AND STRUCTURE ZONE MODELS 86
5.3.1 Microstructure *86*
5.3.2 Densification *89*
5.3.3 Crystal structure and grain size *91*
5.3.4 Film topology *93*
5.4 COMPOUND FORMATION 94
5.4.1 Refractive index *95*
5.5 STRESSES IN THIN FILMS 98
5.5.1 Stress models *100*
5.5.1.1 Tensile stress models 101
5.5.1.2 Compressive stress models 102
5.5.1.3 Impurity model 102
5.5.1.4 Forward sputtering or atomic peening model. 103
5.5.2 Dependence on deposition parameters *104*

One of the main advantages that magnetron sputtering has over other deposition techniques, such as evaporation, is that the average energies of the sputtered atoms are greater. For example, the average energy of evaporated atoms is between 0.1 and 1 eV while the average energy of sputtered atoms is approximately one order of magnitude higher at 1 - 10 eV [1]. Moreover, in unbalanced magnetron sputtering the substrate surface can also receive energy from electrons and associated positive ions, that are subsequently accelerated through the substrate negative self-bias. Added to this, non-thermalised reflected high energy neutrals bombard the substrate surface providing an additional energy source. This increase in bombardment overcomes the problems of poor sample environmental durability associated with the porous microstructure coatings obtained with evaporation by the formation of dense structures that are resistant to the absorption of moisture.

The physical vapour deposition process, sputtering, can be split up into five distinct stages;

- Ejection of target material from the cathode.
- Transport of the vapour through the deposition ambient.
- Condensation of the sputtered atoms (adatoms) onto the substrate with the adoption of energy from the energy impact, the substrate temperature and energy communicated to it by energetic particles.
- Nucleation and interface formation with the substrate material.
- Formation and subsequent growth of a continuous film.

With an additional stage when reactively sputtering;

- The growth and formation of a reactive compound.

5.1 Factors influencing Thin Film Growth

It is first useful to review the processes occurring at the cathode target as described in section 2.4. Figure 5.1 illustrates the particles emerging from the cathode. The

following section examines the major influences sputtering has on the growing film with particular reference to the substrate self-bias and ion bombardment.

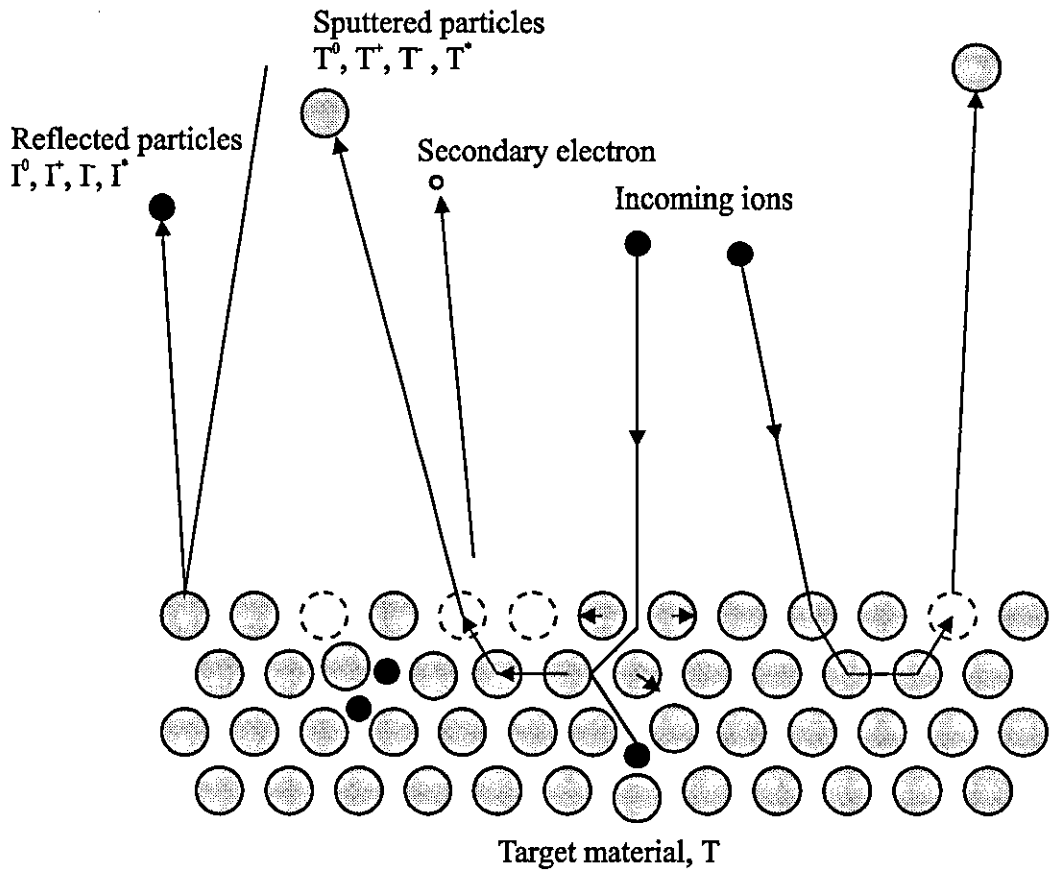

Figure 5.1 : Processes occurring at the cathode target

5.1.1 Particles arriving at the substrate

Andritschky *et al* [2] have performed a quantitative analysis on the particles arriving at the substrate and determined their contribution to substrate heating.

It was shown in chapter 3 that an unbalanced magnetron allows some of the plasma that would be otherwise localised at the target cathode to be directed to, and impinge upon, the growing film surface [3]. The following section outlines the particles associated with this unbalance, and other species that bombard the film whilst growing. Figure 5.2 illustrates the various particles arriving at the substrate.

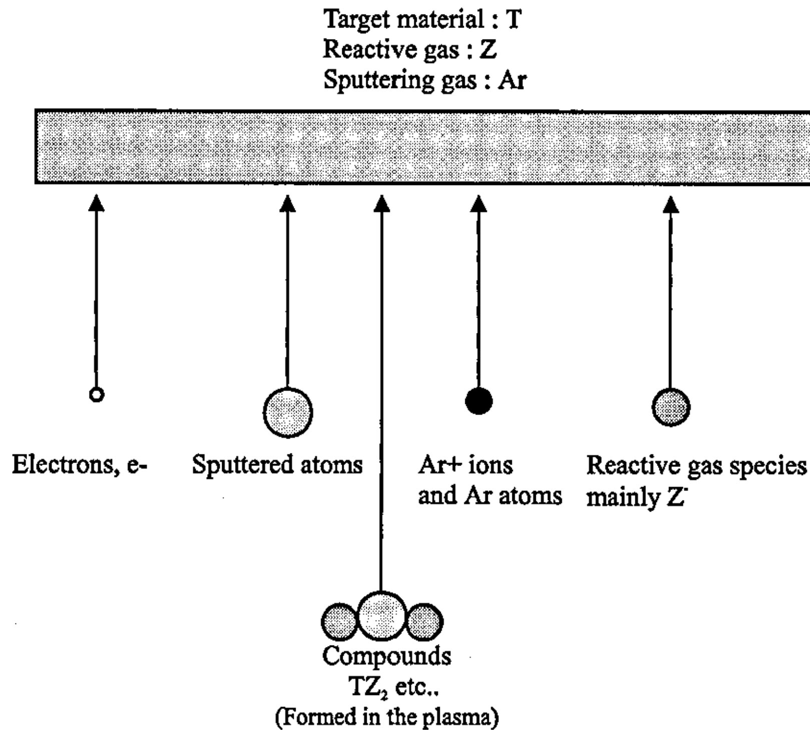

Figure 5.2 : Various species arriving at the substrate

Sputtered atoms

The target material is usually sputtered as neutral because if any positive ions are emitted they cannot escape the negative target field. Furthermore, the small percentage of negative target ions emitted are generally involved in compound formation in reactive sputtering. These ions that are created by sputtering at the target or in the target dark space do, however, have a certain influence on deposition conditions if they arrive at the growing film because they are accelerated with the partial or full cathode potential and have energies in the range 200 to 400 eV.

Electrons

Electrons form a major part of bombardment at the substrate and owing to their high mobility, compared to positive ions, the substrate acquires a negative self-bias as will be explained in more detail in section 5.1.2.

Low energy thermal electrons from the glow discharge, of typical energies in the range 0.2-2 eV, represent some of electrons reaching the film surface. However, only the more energetic of them will be able to surmount the sheath, created by the self-bias, at the substrate.

In addition to the low energy electrons there is bombardment by fast electrons. Electrons are emitted from the target by ion and other impact processes, as explained in section 2.3, and are trapped by the magnetic field. Some of the electrons, however, escape from this region, are entrained by the unbalance field lines, and impinge onto the substrate with an average energy dependent on the effectiveness of the magnetron balance [4,5]. Figure 5.3 shows how an escaping electron can follow the magnetic field lines leaving the target surface.

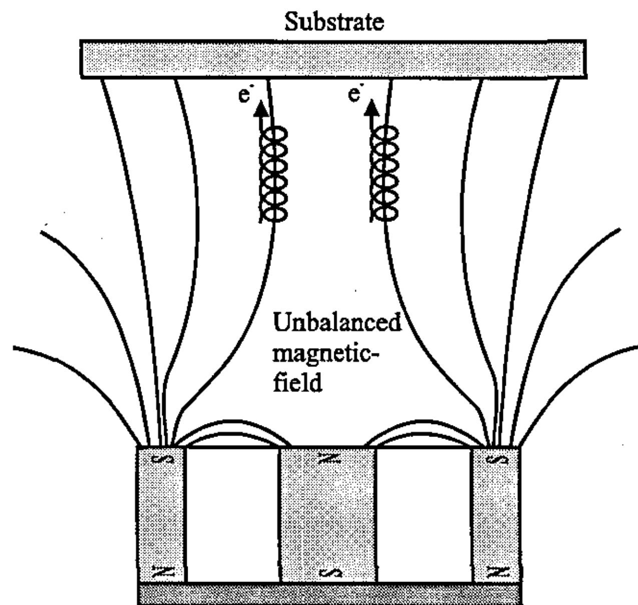

Figure 5.3 : Cross section of magnetron showing escaping path for electrons

Sputtering gas (Argon, Ar)

Argon ions are the most abundant of the various positive ions and are responsible for the majority of ion bombardment at the substrate. These positive ions are accelerated across the substrate dark space and, because of its size, undergo few collisions. It has been

shown that, in addition to the Ar^+ ions, other species bombard the growing film including Ar^{++} and Ar_2^+.

Negative ions

In addition to electrons and the negative ions of the sputtered material, negative ions of any reactive material introduced into the system form part of the ion bombardment at the substrate. As with all negative ions, however, they need sufficient energy to overcome the electric field at the substrate caused by the potential gradient of the dark space.

5.1.2 Substrate self-bias

As mentioned in the latter section and in the basic glow discharge theory, an insulating substrate placed in a plasma acquires a self-bias [6]. This self-bias forms an important role in thin film formation when using an unbalanced magnetron and is usually sufficient to produce adequate ion bombardment. Adding an additional external bias only increases substrate temperature, decreases deposition rate [7], and promotes surface re-sputtering. This self-bias increases in magnitude depending on the severity of the unbalance in the planar magnetron [8].

As shown by Howson *et al* [6] this bias can reach up to -100 V, producing ion current densities of up to 100 mA/cm^2, by using different external magnetic configurations and through the use of electromagnets [9-11].

5.1.3 Ion bombardment at the substrate

It has been well documented that bombardment at the substrate during film growth by atoms, ions and electrons can significantly affect film morphology and properties [12-16]. One of the earliest demonstrations of film modification by ion bombardment was reported by Mattox and Kominiak in 1972, who interrupted the columnar growth in tantalum by biasing the substrate. When used selectively, controlled ion bombardment has been shown to increase the film density and hardness [17-20], enhance optical and

electrical properties [21,22], modify the film's stoichiometry [23-25] and inherent intrinsic stress [26]. Much research has been done in the field of Ion Assisted Deposition (IAD), using many different ion sources, and many good review articles exist [27-29]. The following section aims to highlight some of the more salient points with particular reference to the work undertaken throughout the research period using an unbalanced magnetron as the deposition source.

Control of the flux and energy of the ions arriving at the surface can be achieved by several means. The latter section detailed the existence of a substrate self-bias that accelerates positive ions arriving at the substrate creating a current density of several milliamps per square centimetre. This current is proportional to the substrate potential. Flux and energy control can also be achieved by altering the partial pressure of the sputtering gas. Some scattering of the ions occurs during transit through the ambient inert sputtering gas and variation in partial pressure causes an increase in this scattering leading to attenuation of both the particle flux and energy. This relationship between coating pressure and ion energy has received much attention and has a significant effect on the stresses inherent in the films as is described in this work. Other factors including magnetron power, degree of unbalance have been shown to affect the ion bombardment at the substrate [22].

Figure 5.4 [30] illustrates processes occurring at the substrate at various ion energies. Ion bombardment during initial stages of film growth can affect surface mobility of the adatoms, accelerating nucleation, growth, and coalescence of the nuclei. The main physical processes occurring at the film surface because of ion bombardment are;

- Initial desorption or sputtering of impurities from substrate surface by ion impact.

- Re-sputtering of the coating material after a certain amount of time at higher energies and fluxes resulting in degradation of properties.

- Transfer of momentum from the incident ion to incoming vapour atoms/molecules, thus, increasing their adatom mobility.

- Three dimensional motion of atoms caused by momentum transfer, *i.e.* not only in the plane of the substrates but also downwards toward the substrate surface.

- Mixing at some depth below the surface.

- The generation of defects in the growing film.

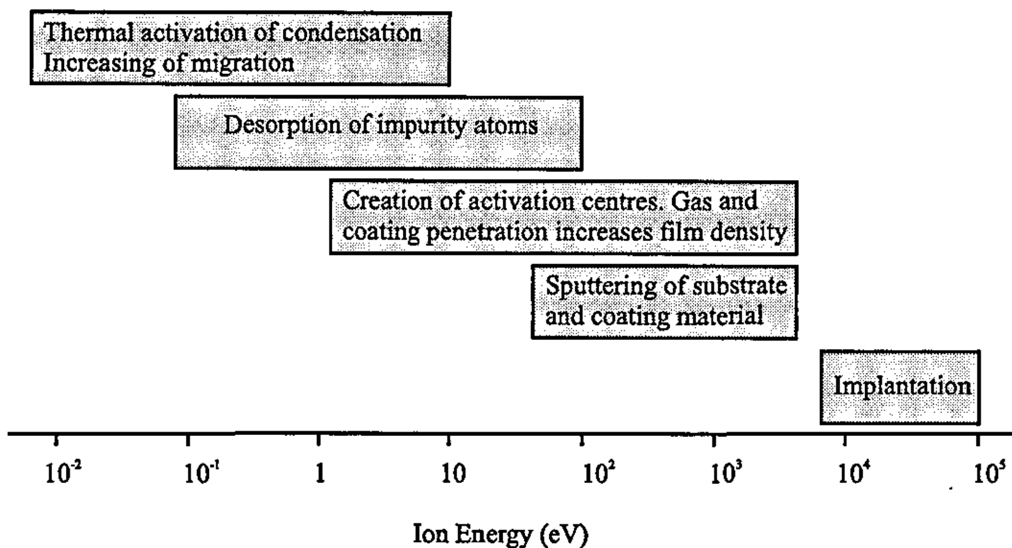

Figure 5.4 : Processes occurring at substrate as a function of the energy of the ions incident upon it [30]

It can be seen that to maximise the effect of ion bombardment energies ranging between 15 eV and 60 eV need to be used.

Throughout the following chapter reference will be made to the effects ion bombardment has on film properties, including surface morphology, film structure, stress, and electrical and optical properties.

5.1.3.1 The ion/atom ratio

It has been determined that ions contribute to the majority of the bombardment at the substrate. It, therefore, seems sensible to relate the flux of these ions to the flux of the

cathode material atoms. This ratio represents a relative ion bombardment rather than absolute bombardment and can be used to compare the effects of increased substrate surface energy per depositing atom. In this work reference will be made to this ratio and the following section details its calculation on a quantitative basis.

The calculations are achieved using the following assumptions;

- The sputter flux is uniform in all directions.
- Fast neutrals are neglected from the calculations involving material and ion transport to the substrate.
- The density of the film is assumed to be equal to that of the bulk material. This approximation is not true for the majority of films but it is usually within 30% of the bulk value.

The ion saturation current at the substrate, I_{si}, is simply divided by the charge carried by a single ion to give the number density of ions per square centimetre per second, n_i

$$n_i = \frac{I_{is}}{e}. \qquad [5.1]$$

The number of atoms present in the film after 1 second, n_a, assuming a substrate area of A_s=1 cm^2 is given by

$$n_a = \frac{R\rho_f}{m_a} \qquad [5.2]$$

where R is the film deposition rate, ρ_f is the film density (bulk density used as film density is unknown), and m_a is the mass of a single deposition atom.

Therefore, the ion to atom ratio is given by equation 5.3.

$$\frac{n_i}{n_a} = \frac{I_{is} m_a}{eR\rho_f}. \qquad [5.3]$$

If an impinging ion has energy, E_i, the energy per depositing atom, E_p can be calculated

$$E_p = E_i \frac{n_i}{n_a}. \qquad [5.4]$$

It has been shown [21] that film properties can be modified by ion bombardment if E_p is equal to, or greater than 1 eV. Thus, changes in the film properties are controlled by the incident ion energy, the substrate ion current density, and the deposition rate [31]. The energy per impinging ion, E_i, can be calculated from the floating potential of the substrate, V_p. If each ion is singly charged and the plasma potential is assumed to be 0 V then eV_p represents the energy of the incident ion.

5.2 Thin film Nucleation theory

Any film grown by physical vapour deposition exhibits different electrical, mechanical, magnetic and optical properties to those of the bulk material. These differences result from the way that the film is formed and can vary vastly from one film to another. Much scanning electron microscope (SEM) work has been done to investigate the formation of a thin film and Poppa *et al* [32] performed some *in situ* measurements of nucleation and film growth with remarkable results. The following section describes the formation of a film in the initial stages of growth, and the factors affecting the various stages of the film formation.

5.2.1 Stages prior to continuous film formation

Figure 5.5 schematically represents the basic formation of a thin film. It is described here in four separate stages.

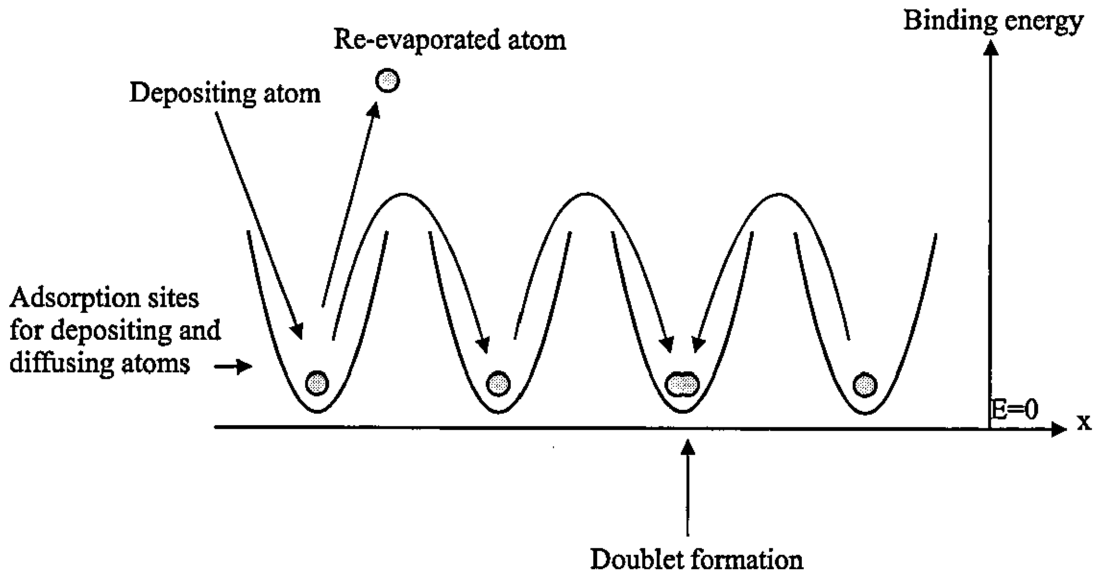

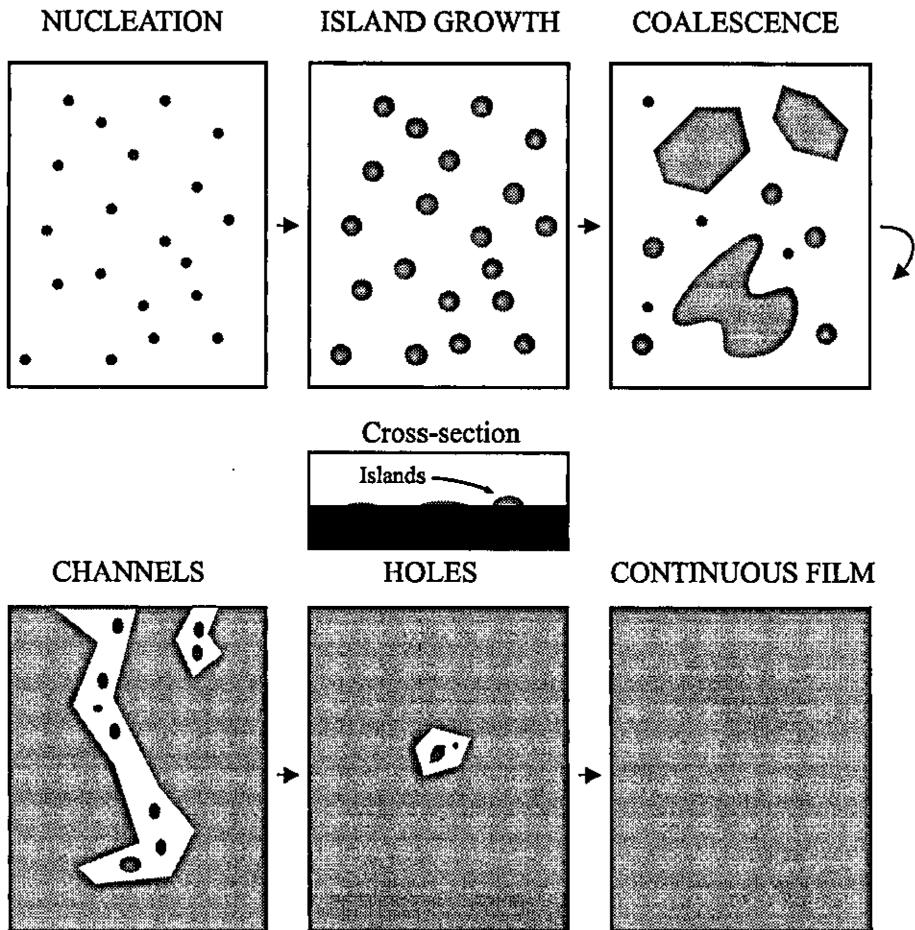

Figure 5.5 : Various stages of initial film growth.

Nucleation

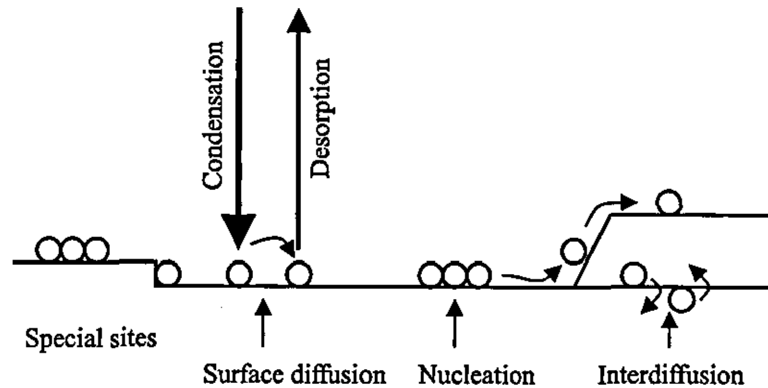

Figure 5.6 : Atomic processes occurring at the surface during growth [26]

One of many phenomena can occur when atoms of the deposition material arrive and condense at the substrate surface, as illustrated in figure 5.6. The most likely, however, is diffusion, where the atom 'hops' from one adsorption site to another. After some time the atom will either re-evaporate or combine with another atom, creating a doublet which is less mobile and, thus, more stable than a single atom. These doublets then form triplets and so on, the whole process being termed nucleation and leading to the formation of quasi-stable islands of 10-100 atoms and having number densities of 10^{10} cm^{-2}. Heterogeneous nucleation is important as the first step in the formation of a thin film.

Island growth

The quasi-stable islands then grow in size rather than in number, eventually growing large enough to touch each other. The growth of the islands is three dimensional as depicted in figure 5.5 (cross-section) but growth parallel to the surface is greater than growth normal to it. This effect being magnified by an increase in energy supply to the surface by a process such as ion bombardment, thus, increasing the surface diffusion. Chopra [33] compared the saturation densities for evaporated and sputtered silver films. Initially the island density ($\sim 10^{11}$ cm^{-2}) was greater for the sputtered films, decreasing in both cases as deposition continued, but dependent on substrate temperature and deposition method.

Eventually, if the impinging atoms are mobile enough, they will find the lowest energy sites consistent with crystal growth. This growth, however, depends also on the substrate, deposition rate and surface energy. During sputtering, the rates are far too high and the atoms rarely find the energetically favourable lattice positions. Furthermore, the low temperatures used with unbalanced sputtering and the high energy ion bombardment are not conducive to crystallite growth.

The coalescence stage

When the islands grow large enough to come into contact then coalescence occurs. The coalescence of two rounded islands, is characterised by a decrease in total projected area of the islands on the substrate and increase in height, as observed by Pashley *et al* [34]. This phenomena has been observed by transmission electron microscopy (TEM), and it appears that the islands often display liquid-like behaviour during coalescence. The behaviour leads to secondary nucleation of the uncovered areas of the substrate.

The continuous film

The coalescence stage continues until the film reaches continuity, this may not occur in some cases until the mean film thickness is several nanometres. However, Chopra [33] found that sputtered films became continuous at a much smaller thickness than evaporated films, and he attributed this to the higher bombardment energy associated with sputtering.

5.2.2 Interface formation

The interfacial regions formed between a substrate and film form an important part of the deposition process. These boundaries dictate such properties as the adhesion of the film to the substrate and electrical contact resistance and can be classified as abrupt, diffusion, compound and 'pseudo-diffusion' [35].

Generally the most desirable situation is to have a high nucleation density, which means having strong chemical interaction between the adatom and the surface (*e.g.* titanium and glass, *c.f.* gold and glass). This in turn means that each deposited atom can form a chemical compound with the surface material and/or they can diffuse into one another. The abrupt interface is not desirable because of the formation of voids, mainly owing to growth vertically, and not parallel to the substrate surface.

5.3 Morphology and Structure Zone Models

The morphology and structure of a coating determines the majority of its electrical, mechanical, optical and topological properties [36]. It is, therefore, of paramount importance to know how to deposit a film with a defined structure. The following section details the growth process once nucleation has taken place developing the existence of several inter-related parameters in the formation of film morphology.

5.3.1 Microstructure

Common microstructure features were first identified by Movchan and Demchishin in 1969 [37] during their work on metal and metal oxide deposits. They proposed a model, figure 5.7 showing how the film structure depends on the ratio between the temperature of the substrate during deposition, T_s and the melting temperature of the material deposited, T_m. This model was termed a 'structure-zone diagram' (SZD) and consisted of three zones, each with its own characteristic microstructure and physical properties. In zone 1, for $T_s/T_m < 0.3$, the film consists of a very open columnar morphology (plate 5.1) of tapered columns that have increasing diameters with increasing temperature, domed structured tops, and are separated by voided boundaries. These columns can extend through the whole film, and work on TiN has shown columnar crystals 1-3 mm in length [38]. The zone above T_1, for which $0.45\text{-}0.5 < T_s/T_m > 0.3$, is characterised by a transition zone where the voids between columns start to fill in and for $T_s/T_m > 0.45\text{-}0.5$ (zone 3) a fully dense film is formed though some columnar structure can still be seen until temperatures near the melting point are reached were the grain growth occurs. The

transition between zones 2 and 3 is gradual, explaining the sloped demarcation of this boundary in the figure.

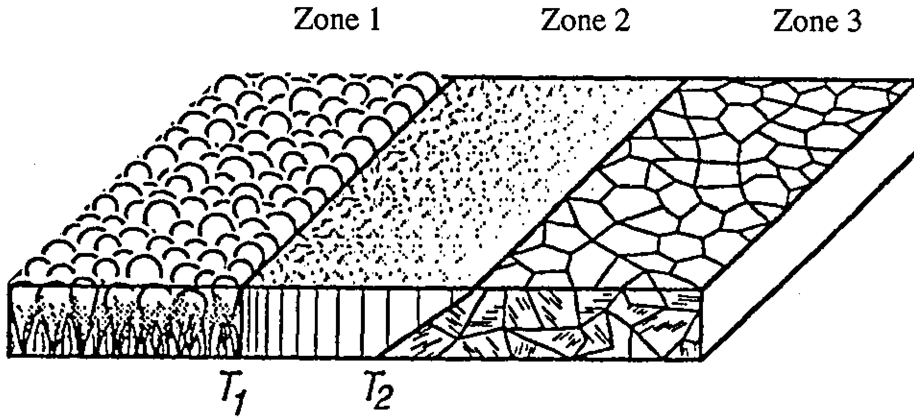

Figure 5.7 : Movchan and Demchishin structure zone diagram [37]

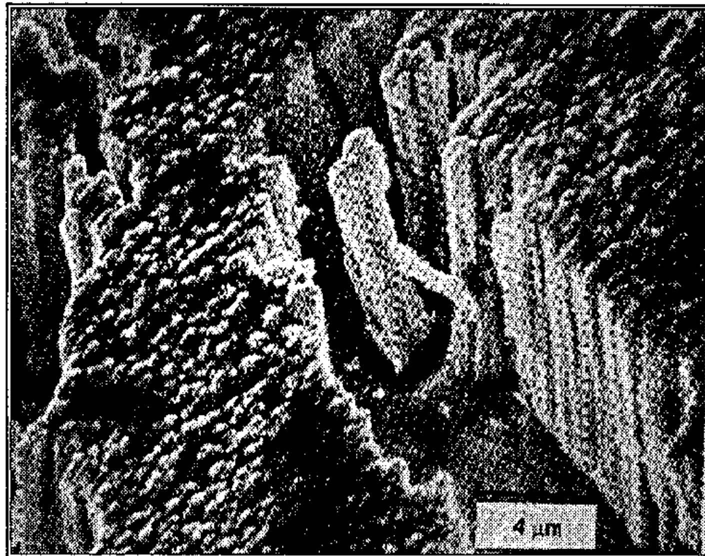

Plate 5.1 : SEM picture showing columnar structure in a thin film

Thornton [39,40] extended this model in 1974 by adding an additional axis to account for the influence of the working gas pressure, figure 5.8. Increasing the partial pressure of the inert gas in the chamber consequently decreases the energy of the particles arriving at the substrate. This is because of an increase in collisions, and hence a reduction in

retained ion energy. This reduction in energy leads to a reduction in adatom mobility and, hence, promotes the growth of a more porous zone 1 type structure.

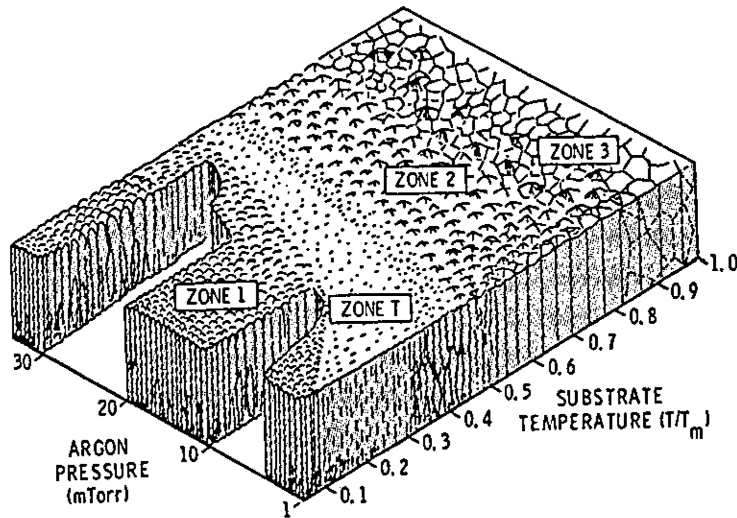

Figure 5.8 : Thornton's structure zone diagram [39]

Furthermore, this growth is compounded by atomic shadowing, figure 5.9, owing to an increase in the oblique component of the angle of incidence of the deposition flux. Thornton also added an additional zone to those proposed by Movchan and Demchisin, which he termed 'zone T'. This zone consists of a 'dense array of poorly defined fibrous grains', and represents the transition between zone 1 and zone 2.

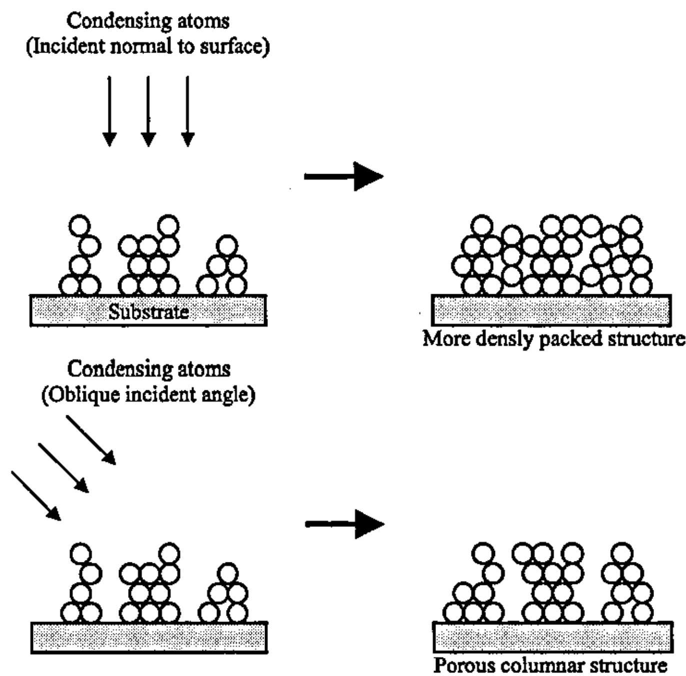

Figure 5.9 : Illustration of atomic shadowing

5.3.2 Densification

One of the first effects of ion bombardment that was noted was the densification of films, and an improvement in their effectiveness as etch barriers when deposited over metallic layers [41]. Since then film densification by the elimination of the columnar microstructures leading to a less porous structure has been shown to produce films less susceptible to environmental change over a period of time. Moreover the structures approach that of the bulk material and compounds have characteristics similar to the bulk values.

The major factors influencing film density (*i.e.* a decrease in porous columnar structure) are adatom mobility, substrate roughness, film contamination, film thickness, and flux impingement direction.

Increased adatom mobility has the greatest influence on the film density and is brought about by increasing the surface energy. The usual method for achieving this is increasing substrate temperature [42] but this leads to problems with temperature sensitive substrates. Therefore, ion assisted deposition methods have to be employed and the following section will concentrate on ion bombardment and its role in film densification.

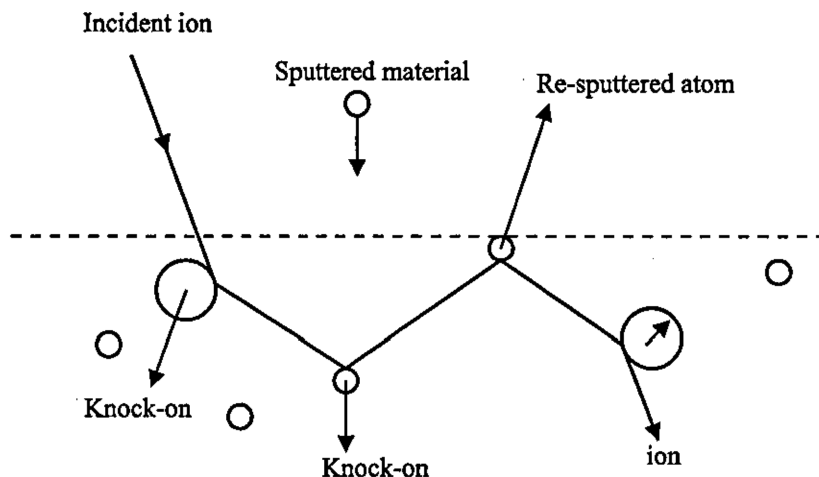

Figure 5.10 : Representation of various processes that occur during ion bombardment [44]

The thermal spike model by Muller [43] was the first to simulate ion assisted densification and assumed it to result from a thermal spike created by an incident ion. It was, however, found that both the lifetime of the spike (10^{-11} s) and its diameter (~100 atoms) was not sufficient to explain the observed behaviour. The model by Muller, however, did prove successful and figure 5.10 [44] shows the fundamental process associated with ion bombardment. Muller explained that the most important processes are the collisional cascade and penetration of ions to a depth of a few interatomic spacings.

Vacancies near the surface which are caused by bombarding ions are partially refilled by the newly arriving vapour atoms and for a sufficiently large ion to atom ratio, n_i/n_a, the latter mechanism will result in downward packing of material. Hence, the films will no longer grow in a porous columnar type 1 structure but instead grow in densely packed structures. Figure 5.11 [45] shows the main microstructure modifications for increasing ion bombardment.

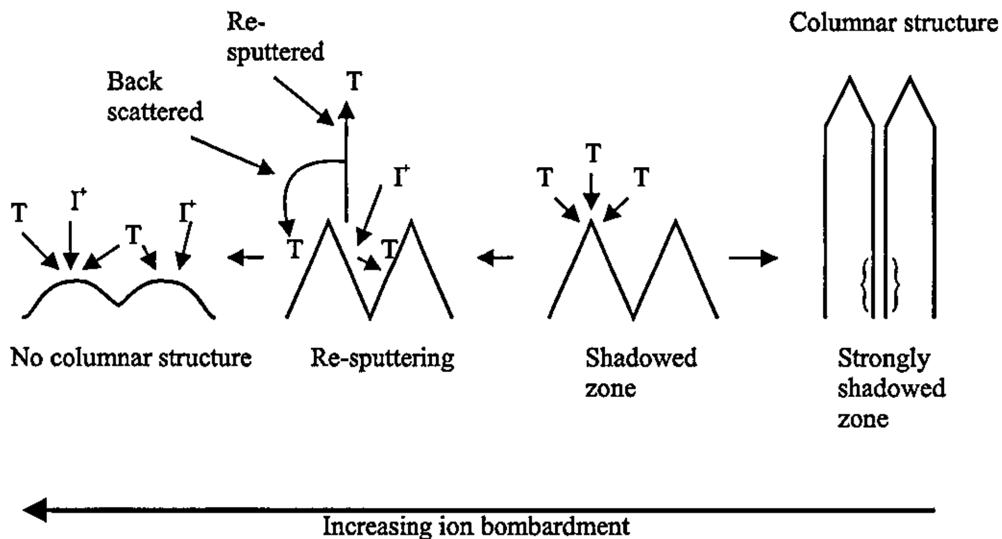

Figure 5.11 : Microstructure modifications obtained by ion bombardment during film growth [45]

The following conclusions relating to structure modification were demonstrated by Muller *et al* [46] using a molecular dynamics approach;

- Atoms overhanging columnar voids (figure 5.12) are removed by ion bombardment causing the voids to remain open until they are filled by depositing atoms.

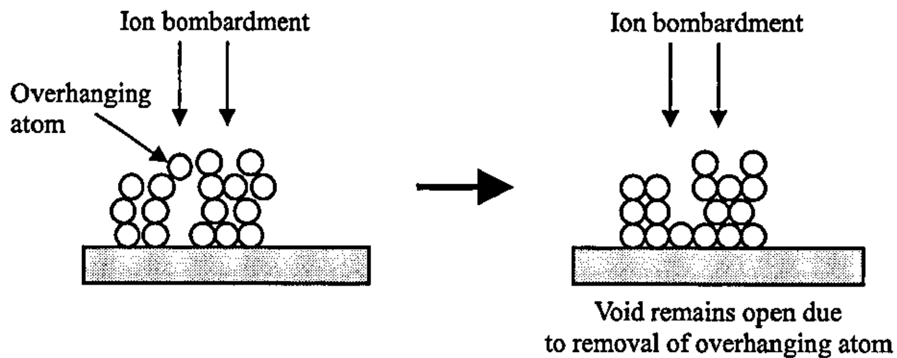

Figure 5.12 : Removal of overhanging atoms by ion bombardment.

- Voids left by any sputtered atoms are refilled.

- Major mechanisms causing improved layer growth are increased surface diffusion, local heating, collapse of voids and recrystallisation.

Associated with the increase in film density is a reduction in deposition rate. However, this reduction in deposition rate is not solely caused by densification but is compounded by resputtering of the growing film and selective removal of impurities such as oxygen atoms [47].

5.3.3 Crystal structure and grain size

When crystalline material is grown during the deposition stage crystal grains are formed, the size of the grains dependent on the adatom mobility. An increase in mobility leads to an increase in grain size. At the interface of these grains, grain boundaries are formed and contribute to the total energy of the film. During recrystallisation, grain boundary migration occurs and contributes to epitaxial growth. Grain boundaries form a important part in the formation of film morphology and contribute to the mechanical, electrical and optical properties of the coatings.

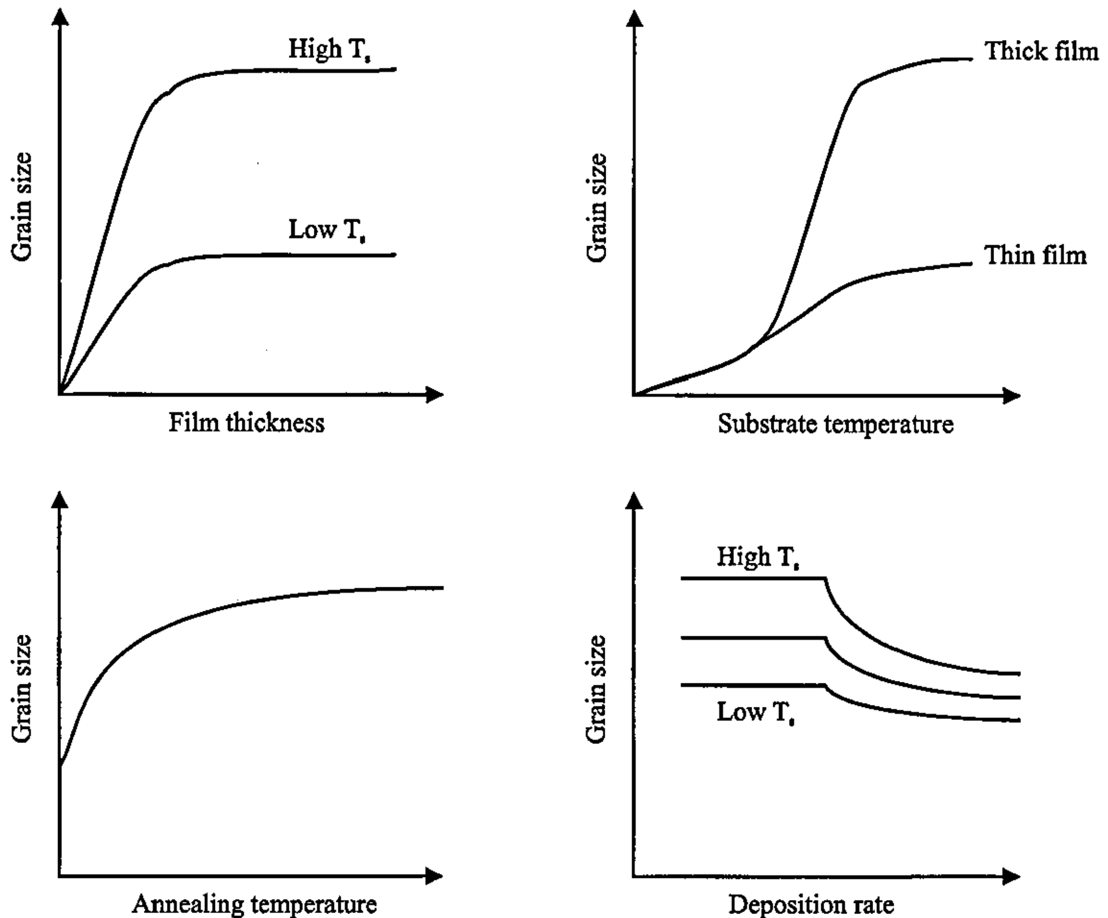

Figure 5.13 : Dependence of grain size on film thickness, substrate temperature, annealing temperature, and deposition rate [48]

Many studies have been performed on the effects of various process parameters on the grain size and figure 5.13 details some of the more prominent results [48]. The common feature in the behaviour illustrated is that the grain size saturates at certain values of the deposition variables. With film thickness as the variable, this must mean that new grains are nucleated on top of the old ones after a certain thickness has been reached. Grain size naturally increases with increasing substrate temperature because of an increases in surface mobility. An effect analogous to increasing the substrate temperature is increasing ion bombardment which has been shown to affect grain size in crystal growth [44,49-51] on heated substrates. However, tantalum pentoxide [44] films grown on unheated substrates were found to be amorphous even with 500 eV of energy through ion bombardment. Increasing the bombardment still further did introduce a crystal structure but none of the films showed any preferred orientation and had to be post-deposition annealed to achieve crystallinity. Al-Robaee *et al* [52,53] have reported that certain films

including zirconia and alumina can form a crystal structure at low temperatures under IAD, however, they do not form some of the crystal phases associated with elevated *in situ* or post-deposition annealing. The dependence of grain size on deposition rate is less obvious but can be explained on the basis that deposition atoms just arriving at the surface, although possessing a larger surface mobility, become buried under subsequent layers at high deposition rates, before much diffusion can take place [53].

Löbl *et al* [54] have shown that substrate temperature and energy of the particles impinging on the substrate are the relevant parameters determining the film structure. They proved it possible to promote the three different crystal phases and control the grain sizes of TiO_2 by varying the process energy.

5.3.4 Film topology

The film surface depends on the surface of the substrate and the microstructure of the film and can vary from a smooth highly reflective surface to a rough milky surface with a matt appearance. As has been shown in the preceding sections there are two physical mechanisms which govern the porosity and, thus, surface roughness of a growing film; surface mobility of the condensing atoms and crystallisation of the film.

When the film microstructure is porous and consists of columnar structures the surface is rough, this condition being characteristic of low surface mobility, *i.e.* $E<E_m$, E_m corresponding to the energy of a fully developed surface mobility. When $E_{cr}>E>E_m$, where E_{cr} is the energy relating to film crystallisation, the deposited film shows a very dense fibrous grained microstructure with a very smooth surface. This transition from a rough to smooth surface has been demonstrated in many experiments [55-58].

When the energy $E>E_{cr}$ then the film crystallises during deposition, a condition difficult to achieve by only *in situ* unbalanced ion bombardment for most materials, and the surface roughness is determined by the size of the crystallised grains [59].

5.4 Compound formation

During reactive deposition the plasma of a non-reactive inert sputtering gas contains species of reactive gas and sputtering of the metal constituent in this atmosphere initiates the growth of compounds on the substrate surface.

Reaction of the depositing species occurs both in the ambient gas and with the co-deposited or absorbed species on the surface. Generally, however, this reaction has a probability of less than unity and may be aided by 'activating' the reactive gaseous species by forming radicals, excited species and ions in the plasma or enhancing the surface energy. These activated species (*e.g.* O, O^* (meta-stable), O^+, O_2^-, O_2^+, O^- and O_3), are more chemically reactive than the non-activated species (*i.e.* O_2) and can release their stored energy on contact with the surface. This activation can, therefore, be achieved by either raising the temperature of the substrate or increasing the energy of the impinging atoms and ions. The latter technique of increasing ion bombardment is preferred because it serves the dual purpose of increasing the reaction probability in the plasma atmosphere and at the substrate without massive increases in substrate temperature. Bombarding the surface with energetic particles, such as accelerated ions (*n.b.* oxygen ions contribute to the ion bombardment during reactive sputtering), also promotes chemical reaction by decomposition of adsorbed species.

Pawlewicz *et al* [60] sputtered reactively from a titanium metal target and investigated the influence of Ar/O_2 ratio in the sputtering gas and the substrate temperature on stoichiometry, grain size and phase composition. In general the rutile content increases with O_2 partial pressure. Figure 5.14 [60] shows the effect of substrate temperature on grain growth indicating that larger grains are associated with higher substrate temperatures. However, as power levels are increased the deposition rate inhibits grain growth as explained qualitatively in section 5.3.3. Moreover, grain growth was found to be inhibited by increased ion bombardment resulting in a predominately glassy structure with grain size less than 10nm.

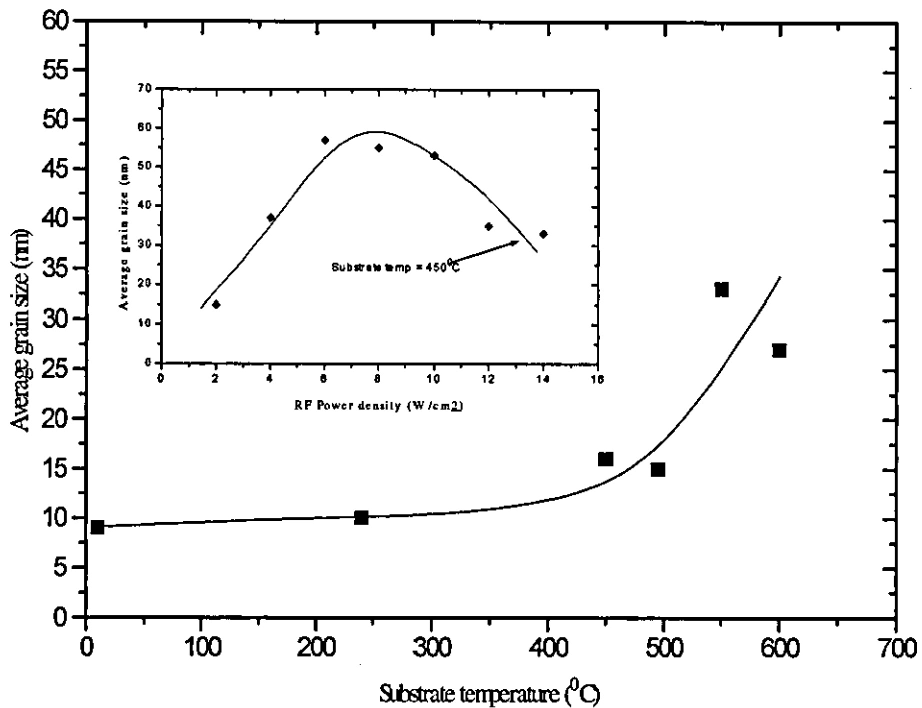

Figure 5.14 : Dependence of grain size on substrate temperature for TiO_2 rutile coatings [60]

5.4.1 Refractive index

Throughout this work the refractive index of the optical coatings deposited was used as a measure of film stoichiometry and is one of the most important properties governing the performance of optical devices. The following section details the effects that film structure has on refractive index and reviews any significant publications.

As discussed, in section 5.3.2, ion bombardment eliminates micro porosity and voids which results in densification of films and, thus, optimum refractive indices approaching bulk values [61] are obtained. For example, ZrO_2 films show an initial increase in refractive index and reach the highest value at a critical ion energy and current density, figure 5.15 [62]. Increasing the energy still further results in index reduction owing to film degradation which can be attributed to preferential re-sputtering and gas incorporation.

Densification of thin films by ion bombardment also assists in reducing the sensitivity of the refractive index to environmental conditions, as often occurs in porous columnar films. Water absorption is associated with voids in the films and the index in these regions alters from 1 to 1.33, significantly affecting the performance of the films, particularly multilayer coatings.

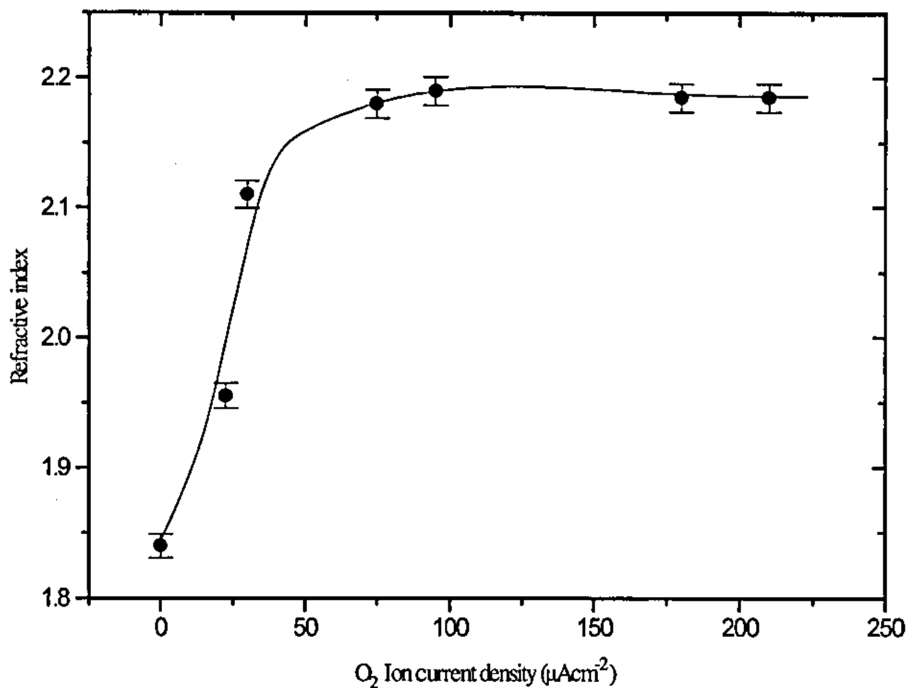

Figure 5.15 : Variation in refractive index of ZrO_2 films as a function of oxygen ion current density [62]

The ability to alter the stoichiometry of a film by controlling the ion bombardment has been used in a wide variety of systems [63-65]. Used in conjunction with oxygen partial pressure control, as described in chapter 4, ion bombardment can alter the structure of the compound film and a range of indices are achievable. Al-Robaee *et al* [53] reported a refractive index transition from 1.65 to 1.74 in aluminium oxide films by varying the energy of the oxygen ion bombardment. The production of films with a variable composition has received much attention recently [66] and represents a way of producing high quality optical filters without internal interfaces, which have historically been the weak points for corrosive environmental applications. In addition, increased computing power has led to design techniques for filters where a range of indices of refraction are

assumed ('rugate filters'), rather than the conventional two index stacks as illustrated in figure 5.16.

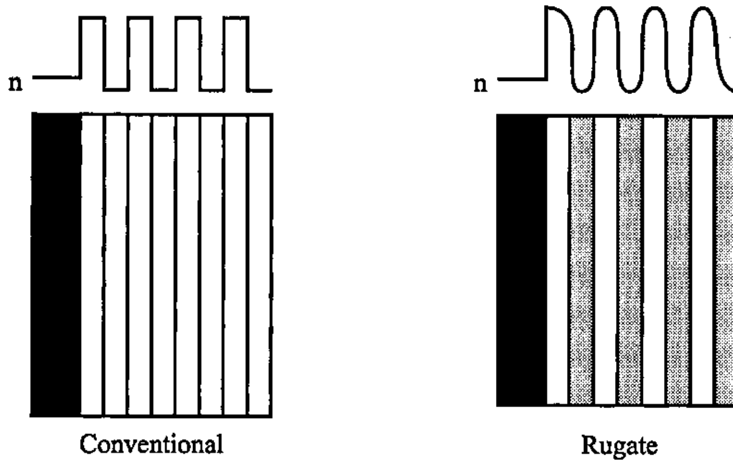

Figure 5.16 : Multilayer stack and rugate filter

Pawlewicz *et al* [60] found that the refractive index of TiO_2 coatings was directly related to their grain size, as shown in figure 5.17. Small grain sizes of less than 10 nm give refractive indices of only 2.05 whereas high indices of up to 2.5 can be achieved at the expense of larger grain size and, hence, increased light scattering of the coatings.

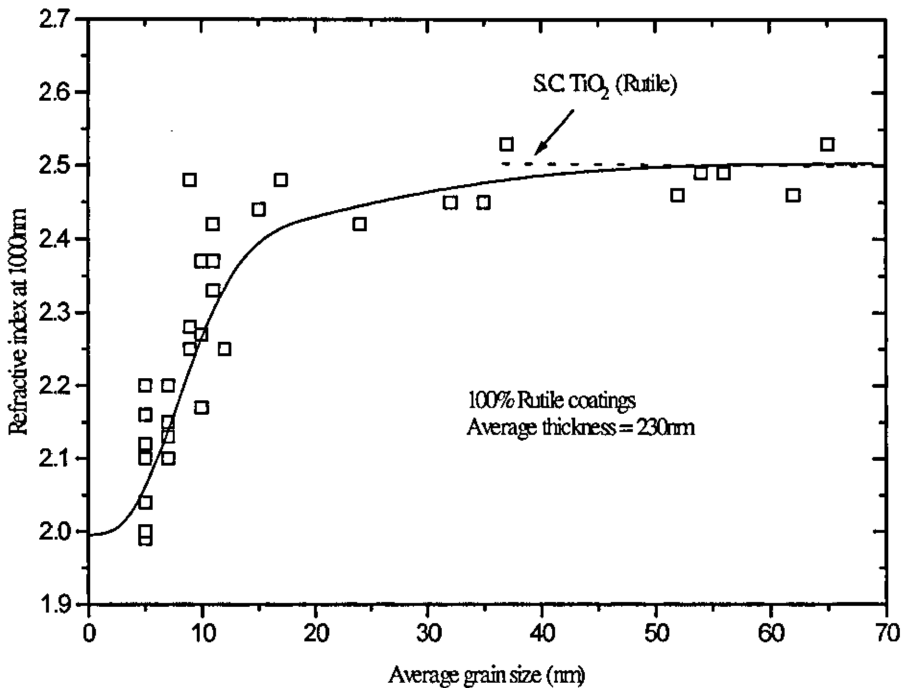

Figure 5.17 : Influence of grain size on the refractive index in TiO_2 coatings [60]

Much work has been undertaken on modelling the refractive index of a thin film on the film's density and associated bulk values. Harris *et al* [67] modified an equation by Bragg and Pippard [68] relating film refractive index, n_f to both the bulk and void refractive indices, n_s, and n_v respectively and the film packing density.

$$n_f^2 = \frac{(1-\rho)n_v^2 + (1+\rho)n_v^2 n_s^2}{(1+\rho)n_v^2 + (1-\rho)n_s^2} \qquad [5.5]$$

where ρ is given by

$$\rho = \frac{\text{Volume of solid part of the film}}{\text{Total volume of the film (columns + voids)}} . \qquad [5.6]$$

This relationship is very effective for obtaining an indication of the densification in films and, under optimised conditions of ion beam parameters, all IAD films have a packing density of one.

5.5 Stresses in thin films

All films of one kind or another, whether deposited by sputtering, evaporation or any PVD technique are found to be in a state of stress. Whilst the stress can be of assistance (*e.g.* in optical multilayers) it is more often detrimental to the film's reliability, quality and performance, and hence, is an increasingly important technological issue. Furthermore, excessive tensile stress can cause substrate cracking, and delamination occurs when compressive stress is greater than film adhesion. On a less catastrophic scale, the stress can affect the optical, electrical and magnetic properties of the film. It is, therefore, of the uppermost importance that the stresses in a coating are both understood and controllable.

It is not always important to minimise the stress within the coating. In some applications, a certain amount of intrinsic stress is of paramount importance. In anti-reflection coatings for ophthalmic purposes, the stress state has to be precisely controlled

to different amounts on the concave and convex surfaces of the lenses. Added to this, work has been published [69] exploiting the applications of high compressive stress. This includes the production of high pressure phases of materials, and preferred orientation in films by compressive stress.

Measurements on the stresses in thin films were first made in the nineteenth century, when Mills [70], in 1877, determined the stress present in films chemically deposited on glass thermometer bulbs. This work was confirmed by Bounty [71] in 1879, and thirty years later the subject was put on a more quantitative basis for electrodeposited films by Stoney [72]. In the past eighty years, since Stoney published his formulation for calculating the stress on a thin glass slide, much research has been undertaken to determine the origin of these stresses.

Hoffman [73] published the first comprehensive review of stress in thin films in 1966, and Campbell [74] extended this review to look at sputtered films, attributing compressive stress to impurities. Arguably, the most important work came from D'Heurle [75] in 1972, as he was the first to study the effects that energetic particles had on the film stress, and he described compressive stress as being caused by lattice distortion produced by backscattered particles incident on the growing film, calling the process 'atomic peening'. This phrase is frequently used in stress literature and appropriately describes the stress generating mechanism.

Many films have been studied since D'Heurle's work, including metallic, insulating and semiconducting materials, to examine the origin of stresses in thin films and the influence of sputtering parameters. Many reviews have been published, of which the most notable are by Windischmann [76] and Doerner and Nix [77]. The two authors most worthy of a mention are Hoffman and Thornton because of their influence in advancing our understanding and knowledge in the mechanisms of stress in thin films. A perspective on their contributions is given by Hoffman [78]. They identified the stress transition from compression to tension for chromium [79] and have published more than thirty papers on stress in the period 1974-1985. This includes work on;

- Identifying the fundamental factors responsible for the stress transition [79-82].

- Confirmation of the Atomic Peening Model (APM).

- Identifying stress dependence on pressure, target/gas mass ratio, cathode shape, substrate orientation, bias and substrate-target distance [79-84].

The following chapter aims to highlight the main areas of achievement in understanding the mechanisms behind stress in thin films, relating the findings to both film structure and performance. Furthermore, a detailed description of the effects various deposition parameters have on the stresses within a coating will be given.

5.5.1 Stress models

During the formation of a sputtered film, it is inevitable that atomic forces are created such that the film is in a state of stress. This total stress can be either tensile or compressive and results from a combination of intrinsic and extrinsic components as depicted by equation 5.7

$$\sigma = \sigma_{intrinsic} + \sigma_{extrinsic}. \qquad [5.7]$$

The extrinsic stress is caused by both external and thermal stresses. The thermal stress in the film is created because of a thermal mismatch between the expansion coefficients of the film and substrate. The intrinsic stress is that owing to the film structure, and thus, is necessarily a process sensitive property, *i.e.* it can be altered by the chamber pressure, base pressure, substrate-target distance, substrate bias, substrate temperature (not to be confused with thermal stress), magnetron power, sputtering gas, ion bombardment current and substrate material.

The following sections aim to review some of the models that have been suggested as the origin of stresses in thin films.

5.5.1.1 Tensile stress models

As seen in the previous sections, thin films deposited by magnetron sputtering exhibit a spectrum of microstructures, depending on the process conditions and throughout this section reference will be made to the zone structure diagram of Thornton. No single model exists for all the tensile stress data. Models applicable to polycrystalline films, where grain boundaries may be the physical basis for the stress, do not apply to amorphous or single crystal films.

When a porous zone 1 structure (with reference to Thornton's model of figure 5.8) is formed, owing to low adatom mobility, interatomic forces act across the micropores created and so such films are usually under tensile stress [79,85] provided that impurity related compressive stresses are absent. Figure 5.18 illustrates this basic mechanism that creates tensile stress within a film.

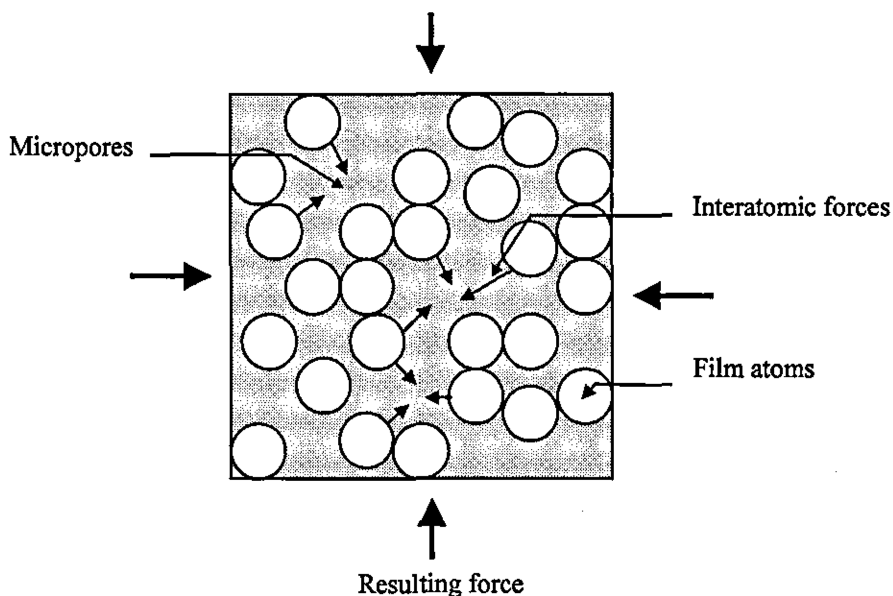

Figure 5.18 : Representation of porosity in thin film leading to tensile stress

A more specific grain boundary relaxation model, proposed by Finegan and Hoffman [86-88], exists for polycrystalline films such as ZrO_2 and TiO_2 and is illustrated schematically in figure 5.19 [89]. As the film growth progresses through morphological stages (nuclei formation, island formation, coalescence and continuous film), interatomic attractive forces acting across the gaps between contiguous grains cause an elastic relaxation of the grain walls.

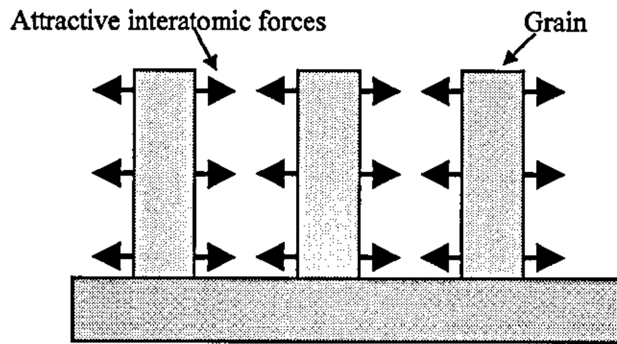

Figure 5.19 : Schematic representation of the grain boundary relaxation model [89]

5.5.1.2 Compressive stress models

There are two models that account for the compressive stress observed whilst sputtering under certain conditions; one owing to impurities in the film and one owing to atomic peening or densification. The latter of these two is the major cause of compressive stress, whilst the former can cause a film, that would otherwise be in tension, to exhibit a compressive nature.

5.5.1.3 Impurity model

Frequently, pure films have tensile stresses that depend on the type of material, the deposition technique and the film thickness. The inclusion of foreign materials in the film can cause not only a reduction in tensile stress but a shift to compressive stresses [90,91]. Gas incorporation into a metal lattice often leads to compressive stresses resulting from a metal lattice expansion.

The degree to which the shift from tensile to compressive stress occurs depends on the melting point of the material (which determines the void fraction), its reactivity, and the chemical nature of the impurities. No quantitative impurity model exists, but a qualitative model by Windischmann [76] states that lattice distortion is produced by;

- Incorporation of atoms of a size different from the host.

- Reaction at grain boundaries (*e.g.*, oxidation or hydrogenation) producing a phase with a different molar volume.

- Grain surface reduction.

Many studies have been made on the effect of oxygen incorporation into a sputtered film. Alexander and Hoffman [92] observed stress levels to depend inversely on the measured oxygen content in Ni films. Abermann *et al* [93-95] showed residual oxygen had the most significant effect on the stress in experiments with Ag, Au, and Cu in O_2, H_2, H_2O, N_2, CO, and CH_4.

Molecular dynamics experiments on the effects of gas impurities and ion bombardment on stresses in sputtered films by Fang *et al* [96] showed that compressive stress is owing to the trapped gas and concurrent ion bombardment during growth.

5.5.1.4 Forward sputtering or atomic peening model.

As mentioned earlier, D'Heurle [75] suggested that the compressive stress observed in sputtered films was caused by energetic particles bombarding the film ('atomic peening'). Peening, by ion bombardment or lower working gas pressure, causes atoms to be incorporated in the growing film with a density higher than would be obtained otherwise, since with sufficient energy, atoms may be forced into spaces too small to accommodate them under thermal equilibrium conditions. The gas atoms can then be packed tightly by the concurrent ion bombardment, resulting in a compressive stress in the film.

In the absence of ion bombardment, it is unlikely that the gas atoms will be trapped in the film tightly. However, both entrapment of the gas impurity and the atomic peening mechanism, which strongly depends on the power input, working pressure, and mass ratio between the adatom and background gas, play important roles in determining the state of the intrinsic stress.

5.5.2 Dependence on deposition parameters

The intrinsic stress in films can be expressed categorically in the following three summarising statements;

- The nature of the stresses in a film are directly linked to the microstructure.

- The microstructure is dependent on the thermal (T/T_m) and kinetic energy (E_{KE}) of the deposition process.

- The kinetic energy is composed of two fundamental entities; particle flux, Φ, and energy, E, which are expressed by their product either as the normalised energy or momentum.

Hence, the degree that Φ and E are altered by the deposition parameters will determine the stress state the film is in and the magnitude of the stress. However, to elucidate the mechanism by which bombardment influences film growth, and hence stress, requires knowledge of the exact particles involved, their flux, Φ, and energy, E. In plasma based processes, however, such as unbalanced magnetron sputtering, this is experimentally difficult and was not performed during this research period. The ion current, I_{si}, at the substrate was measured during this work, however, and the ratio of ions to depositing atoms was also calculated.

Probably one of the most investigated parameters affecting intrinsic stress within a sputtering deposition environment is ambient gas pressure. Table 5.1 summarises some of the studies that have been performed for various materials deposited by DC magnetron sputtering.

The characteristic stress transition curve was obtained during this work for chromium and is given in chapter 8.

Material	Sputtering gas	Reference
Cr	Ar	[79] [81]
Al, V, Zr, Nb, W	Ar	[85]
Ti, Ni, Mo, Ta	Ar	[97]
Cu	Ar	[98]
Mo	Ar	[99]
Si	Ne, Ar, Kr, Xe	[100]
W	Ar	[101]
Mo	Ne, Ar, Kr, Xe	[82]

Table 5.1 : A review of stress studies that have been performed on the magnetron sputtering of various metals

The stress in sputtered films can depend also on the mass of the target, M_t, and the sputtering gas M_i. It has been shown that as the sputtering gas mass, M_i, decreases the stress transition pressure increases [102].

CHAPTER 5 REFERENCES

[1] **Carter, G. & Colligon, J.S.** (1968). 'Ion bombardment of Solids' (Heineman, London).

[2] **Andritschky, M., Guimaraes, F. & Teixeira, V.** (1993).*Vacuum,* 44, 809-813.

[3] **Window, B. & Savvides, N.**, (1986). *J. Vac. Sci. Technol.*, A4, 504-508.

[4] **Window, B. & Harding, G.L.** (1990). *J. Vac. Sci. Technol.,* A8(3), 1277-1282.

[5] **Sproul W.D.** (1991). *Surf. Coat. Technol.*, 49, 284-289.

[6] **Howson, R.P., Jafer, H.A.. & Spencer, A.G.** (1993). *Vacuum,* 44, 191-195.

[7] **Jouan, P.Y. & Lemperiere, G.** (1994).*Thin Solid Films,* 237, 200-207.

[8] **Howson, R.P., Spencer, A.G., Oka, K., Lewin, R.W.** (1989) *J. Vac. Sci. Technol. A*, 7, 1230-1234.

[9] **Howson, R.P., Mustapha, N., Jafer, H.A. & Stenlake, E.M.** (1991). *Proc. 8th Int. Conf. on Ion Plasma Assisted Techniques,* Brussels, CEP Consultants, Edinburgh, 328-333.

[10] **Jafer, H.A., Howson, R.P., Stenlake, E.M. & Spencer, A.G.** (1991). *Proc. 8th Int. Conf. on Ion Plasma Assisted Techniques,* Brussels, CEP Consultants, Edinburgh, 334-339.

[11] **Howson, R.P. & Jafer, H.A.** (1992). *J. Vac. Sci. Technol.,* A10(4), 1784-1790.

[12] **Marinov, M.** (1977). *Thin Solid Films,* 46, 627.

[13] **Rossnagel, S.M. & Cuomo, J.J.** (1988). *Vacuum,* 38, 73-81.

[14] **Rossnagel, S.M. & Cuomo, J.J.** (1989). *Thin Solid Films,* 171, 143-156.

[15] **Kay, E., Parmigiani, F. & Parrish, W.** (1988). *J. Vac. Sci. Technol.,* A6(6), 3074-3081.

[16] **Mattox, D.M.** (1989). *J. Vac. Sci. Technol.,* A7(3), 1105-1114.

[17] **Hultman, L., Munz, W-D., Musil, J., Kadlec, S., Petrov, I. & Greene, J.E.** (1991). *J. Vac. Sci. Technol.,* A9(3), 434-438.

[18] **Savvides, N. & Bell, T.J.** (1992). *J. Appl. Phys.,* 72(7), 2791-2796.

[19] **Richter, F., Kupfer, H., Giegengack, H., Schaaeschmidt, G., Scholze, F., Elstner, F. & Hecht, G.** (1992). *Surf. Coat. Technol.,* 54/55, 338-342.

[20] **Shih, K.K., Smith, D.A. & Crowe, J.R.** (1988). *J. Vac. Sci. Technol.,* A6(3), 1681-1685.

[21] **Rossnagel, S.M. & Cuomo, J.J.** (1988). *Vacuum,* 38, 73-81.

[22] **Spencer, A.G., Oka, K. & Howson, R.P.** (1988). *Vacuum,* 38(8-10), 857-859.

[23] **Petrov, I., Hultman, L., Sundgren, J.E. & Greene, J.E.** (1992). *J. Vac. Sci. Technol.,* A10(2), 265-272.

[24] **Sproul, W.D., Rudnik, P.J. & Graham, M.E.** (1989). *Surf. Coat. Technol.,* 39/40, 355-363.

[25] **Jankowski, A.F. & Schrawyer, L.R.** (1992). *Surf. Coat. Technol.,* 54/55, 349-354.

[26] **Windischmann, H.,** (1992). *Critical Reviews in Solid State and Materials Sciences,* 17(6), 547-596.

[27] **Bovard, B.G.** (1991). *Thin Solid Films,* 206, 224-229.

[28] **Mohan, S. & Krishna, M.G.** (1995). *Vacuum,* 46(7), 645-659.

[29] **Colligon, J.S.** (1995). *J. Vac. Sci. Technol.,* A13(3), 1649-1657.

[30] **Howson, R.P.,** (1994). *Pure and Appli. Chem.,* 66, 1311-1318.

[31] **Musil, J. & Kadlec, S.** (1990). *Vacuum,* 40(5), 435-444.

[32] **Poppa, H., Heinemann, Kl., Elliot, A.G.,** (1971) *J. Vac. Sci. Technol.,* 11, 666.

[33] **Chopra, K.L.** (1966). *J. Appl. Phys.,* 37, 3405.

[34] **Pashley, D.W., Stowell, M.J., Jacobs, M.H. & Law, T.J.,** (1964). *Phil. Mag.,* 10, 127.

[35] **Mattox, D.M.** (1994). *'Educational Guides to Vacuum Deposition Technology',* Soc. of Vacuum Coaters.

[36] **Musil, J., Matous, J., Vlcek, J., Koydl, L. & Muller, K.** (1994). *Czechoslovak Journal of Physics,* 44(6), 565-574.

[37] **Movchan, B.A. & Demchisin, A.V.** (1969). *Phys. Met. Metallogr.,* 28, 83.

[38] **Zhang, S. & Zhu, W.** (1993). *Journal of Materials Processing Technology,* 39, 165-177.

[39] **Thornton, J.A.** (1974). *J. Vac. Sci. Technol.,* 11, 666.

[40] **Thornton, J.A.** (1975). *J. Vac. Sci. Technol.,* 12, 830.

[41] **Mattox, D.M. & Kominiak, G.J.,** (1972) *J. Vac. Sci. Technol.,* 9, 528

[42] **Thornton, J.A.** (1986). *J. Vac. Sci. Technol.,* A4, 3059.

[43] **Muller, K.H.** (1986). *J. Vac. Sci. Technol.,* A4, 184.

[44] **Mohan, S. & Krishna, M.G.** (1995). *Vacuum,* 46(7), 645-659.

[45] **Pulker, H.K.,** (1984). *'Coatings on Glass,* ed. by Pulker, H.K., Elsevier, New York, 252.

[46] **Muller, K.H., Netterfield, R.P. & Martin, P.J.** (1987). *Phys. Rev. B,* 35, 2934.

[47] **Jouan, P.Y. & Lemperiere, G.** (1994). *Thin Solid Films,* 237, 200-207.

[48] **Thun, R.** in G. Haas (ed.), (1964). *'Physics of thin films',* Academic Press Inc., New York, Vol I, p.187.

[49] **Van Vechten, D., Hubler, G.K., Donovan, E.P. & Correll, F.D.** (1990). *J. Vac. Sci. Technol.,* A8, 821.

[50] **Hubler, G.K., Van Vechten, D., Donovan, E.P. & Carosella, C.A.** (1990). *J. Vac. Sci. Technol.,* A8,831.

[51] **McNally, J.J.** (1986). *Ph.D. thesis,* University of New Mexico, Albuquerque, New Mexico, USA.

[52] **Al-Robaee, S., Subbanna, G.N., Narasimha Rao, K. & Mohan, S.** (1994). *Vacuum,* 45, 97.

[53] **Al-Robaee,S., Ghanashyam Krishna, M., Subbanna, G.N., Narasimha Rao, K. & Mohan, S.** (1991). *J. Mater. Research,* 9, 2688.

[54] **Lobl, P., Huppertz, M. & Mergel, D.** (1994). *Thin Solid Films,* 251, 72-79.

[55-58] 3-6 Paper 133

[59] **Musil, J., Matous, J., Vlcek, J., Koydl, L. & Muller, K.** (1994). *Czechoslovak Journal of Physics,* 44(6), 565-574.

[60] **Pawlewicz, W.T., Martin, P.M., Hays, D.D. & Mann, I.B.** (1982). *SPIE,* 325, 105-116.

[61] **Pulker, H.K., Haag, W., Buhler, M. & Moll, E.** (1985). *5th Int. Conf. on Ion & Plasma Assisted Techniques,* 107-114.

[62] **Martin, P.J., Netterfield, R.P. & Sainty, W.G.** (1984). *J. Appl. Phys.,* 55, 235.

[63] **Hwangbo, C.K., Lingg, L.J., Lehan, J.P., Macleod, H.A. & Suits, F.** (1989). *Appl. Opt., 28(14),* 2779-2784.

[64] **Case, F.C.** (1989). *J. Vac. Sci. Technol.,* A7, 1194-1198.

[65] **Netterfield, R.P., Martin, P.J. & McKenzie, D.R.** (1990). *J. of Mater. Sci. Ltrs.,* 9(8), 972-974.

[66] **Bovard, B.G.** (1991). *Thin Solid Films,* 206, 224-229.

[67] **Harris, M., Macleod, H.A., Ogura, S., Pelletier, E. & Vidal, B.** (1979). *Thin Solid Films,* 57, 176.

[68] **Bragg, W. & Pippard, A.B.** (1953). *Acta. Cryst.,* 6, 865.

[69] **McKenzie, D.R.,** (1993). *J. Vac. Sci. Technol.,* B11(5), 1928-1935.

[70] **Mills, E.J.,** (1877). *Proc. Roy. Soc. London,* 26, 504.

[71] **Bouty, M.,** (1879). *Compt. Rend.,* 88, 714.

[72] **Stoney, G.C.,** (1909). *Proc. Roy. Soc. London,* A32, 172.

[73] **Hoffman, R.W.,** (1966). *'Physics of Thin Films, Vol. 3',* ed. by Haas, G. & Thun, R.E., Academic Press, New York, 211.

[74] **Campbell, D.S.,** (1970). *'Handbook of Thin Film Technology',* ed. by Maissel, L.I. & Glang, R., Mc-Graw Hill, New York, 12.

[75] **D'Heurle, F.M. & Harper, J.M.E.,** (1989). *Thin Solid Films,* 171, 81-92.

[76] **Windischmann, H.,** (1992). *Critical Rev. in Solid State and Mat. Sci.,* 17, 547-596.

[77] **Doerner, M.F. & Nix, W.D.**, (1988). *CRC Critical Rev. in Solid State and Mat. Sci.*, 14, 225.

[78] **Hoffman, D.W.**, (1994). *J. Vac. Sci. Technol.*, A12, 953-961.

[79] **Hoffman, D.W. & Thornton, D.W.**, (1977). *Thin Solid Films*, 40, 355-363.

[80] **Thornton, J.A. & Hoffman, D.W.**, (1980). *27th. National Syposium of the American Vacuum Society.*

[81] **Hoffman, D.W. & Thornton, J.A.**, (1982). *J. Vac. Sci. Technol.*, 20(3), 355.

[82] **Hoffman, D.W. & Thornton, J.A.**, (1980). *J. Vac. Sci. Technol.*, 17, 380.

[83] **Hoffman, D.W. & Thornton, J.A.**, (1979). *J. Vac. Sci. Technol.*, 16, 134.

[84] **Hoffman, D.W. & Kukla, C.M.**, (1985). *J. Vac. Sci. Technol.*, A6, 2600.

[85] **Hoffman, D.W. & Thornton, J.A.** (1977). *Thin Solid Films*, 45, 387-396.

[86] **Finegan, J.D. & Hoffman, D.W.** (1959). *J. Appl. Phys.*, 30, 597.

[87] **Hoffman, D.W.** (1976). *'Physics of Non-Metallic Thin Films'*, NATO Advanced Study Institute Series, Vol. B-14, ed. by Dupuy, C.H. & Cachard, A., Plenum, New York, 273.

[88] **Doljack, F.A. & Hoffman, D.W.** (1972). *Thin Solid Films*, 12, 71.

[89] **Thornton, J.A. & Hoffman, D.W.** (1989). *Thin Solid Films*, 171, 5.

[90] **Puchert, M.K., Timbrell, P.Y., Lamb, R.N. & McKenzie, D.R.**, (1994). *J. Vac. Sci. Technol.*, A12, 727-732.

[91] **Priest, J., Caswell, H.L. & Budo, Y.**, (1962). *Vacuum*, 12, 301.

[92] **Alexander, P.M. & Hoffman, R.W.** (1976). *J. Vac. Sci. Technol.*, 13, 96.

[93] **Abermann, R. & Koch, R.** (1979). *Thin Solid Films*, 62, 195.

[94] **Abermann, R. & Koch, R.** (1980). *Thin Solid Films*, 66, 217.

[95] **Koch, R., Leonhard, H. & Abermann, R.** (1982). *Thin Solid Films*, 89, 117.

[96] **Fang, C.C., Jones, F. & Prasad, V.**, (1993). *J. Appl. Phys*, 74(7), 4472-4482.

[97] **Thornton, J.A. & Hoffman, D.W.**, (1977). *J. Vac. Sci. Technol.*, 14, 164.

[98] **Entenberg, A., Lindberg, V., Fletcher, C., Gatesman, A. & Horwath, R.**, (1987). *J. Vac. Sci. Technol.*, A5, 3375.

[99] **Cuthrell, R.E., Mattox, D.M., Peeples, C.R., Dreika, P.L. & Lamppa, K.P.**, (1989). *J. Vac. Sci. Technol.*, 6, 2914.

[100] **Thornton, J.A. & Hoffman, D.W.**, (1981). *J. Vac. Sci. Technol.*, 18, 203.

[101] **Vink, T.J., Walrave, W., Daams, J.L.C., Dirks, A.G., Somers, M.A.J. & Van Den Aker, K.J.A.**, (1993). *J. Appl. Phys*, 74, 988-995.

[102] **Este, G. & Westwood, W.D.** (1987). *J. Vac. Sci. Technol.*, A5, 1892.

CHAPTER 6

EXPERIMENTAL APPARATUS AND PROCEDURE

It is necessary to have a thorough understanding of the experimental apparatus and procedure for the results to be fully appreciated. The following chapter details the specifications of all the apparatus used throughout this work. The technical aspects of the experimental procedure are also given. A significant part of this chapter concentrates on the details of the control techniques developed throughout this work.

6.1 VACUUM SYSTEM CONFIGURATION 110
6.1.1 Construction 110
6.1.2 Operating methodology 112
6.1.3 The pumping system 113
6.1.4 Gas admission and flow measurements 113
6.1.4.1 Noble gas specifics 114
6.1.4.2 Reactive gas specifics 114
6.2 MAGNETRON DESIGN AND PERFORMANCE 114
6.2.1 Construction and mounting 115
6.2.2 Target utilisation 118
6.3 THE ELECTRON-COLLECTING-ANODE 119
6.4 MAGNETRON POWER DELIVERANCE 120
6.4.1 The MDX Magnetron driver 121
6.4.1.1 AC Driver with and without output rectification. 121
6.5 PROCESS CONTROL TECHNIQUES 124
6.5.1 Measuring of target status 124
6.5.1.1 Voltage used as an indication of target status, ϕ_v 125
6.5.1.2 Plasma emission used as an indication of target status, ϕ_e 125
6.5.2 The feedback control unit 127
6.5.2.1 Continuous feedback control (CFC) 128
6.5.2.2 Successive pulsed plasma anodisation (SPPA) 129
6.5.3 The compacted oxide targets 131
6.6 TARGET SPECIFICATIONS 132
6.7 DEPOSITION PROCEDURE 133
6.8 *IN SITU* MEASUREMENTS 134
6.8.1 Substrate temperature 134
6.8.2 Ion bombardment 135

6.1 Vacuum system configuration

6.1.1 Construction

The vacuum system, as illustrated in figure 6.1 and plate 6.1, was designed in-house. The chamber was constructed of 20 mm thick aluminium, comprising no internal or external welds. It maintained a base pressure of 1×10^{-6} torr using only joints made by M8 bolts and epoxy resin. During pumpdown there is a small amount of bowing in each face, but this is considered to assist initial sealing of the hinged chamber door. The deposition source, as detailed in section 6.2, is housed in the centre of the door that forms one end of the system.

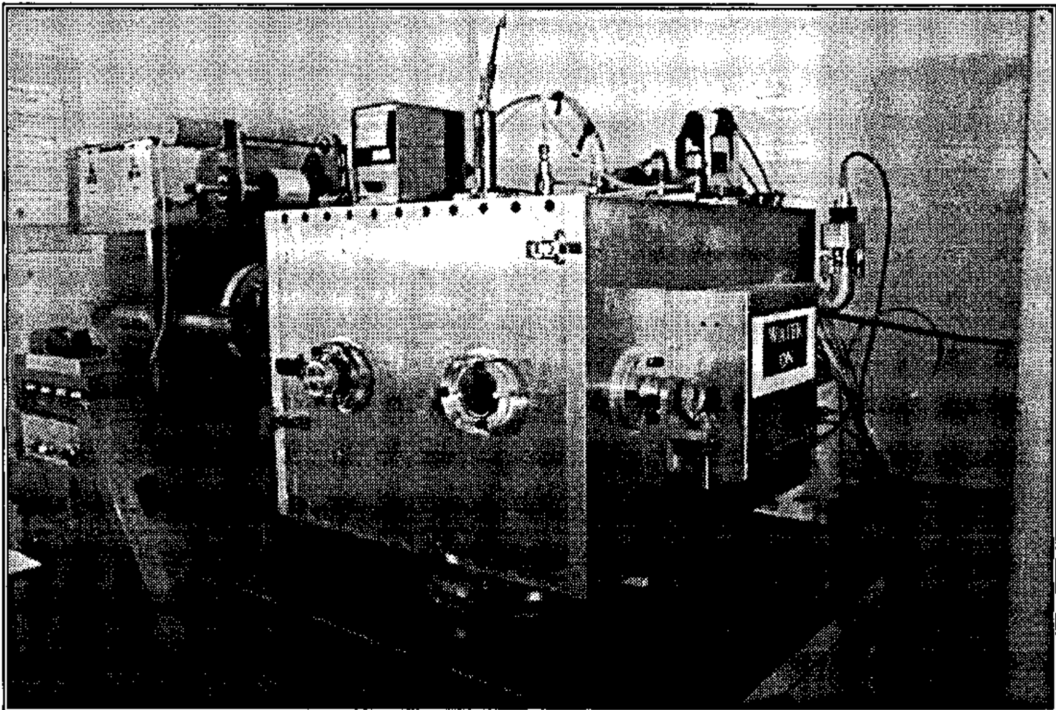

Plate 6.1 : The depostion system - External

There are several feed-throughs of various sizes located around the system. The pumping port, 20 cm in diameter, is located in the chamber base and the associated pumping peripherals will be detailed in section 6.1.3. As will be shown later, sputtering partial pressure affects factors such as sign and magnitude of film stress, film density and film

structure. It is, therefore, of paramount importance to have a reliable, quick response pressure gauge for both base and working pressures. Chamber base pressure and deposition partial pressures were quantified by an Edwards penning gauge model CP25-K and pirani gauge model PRL10 respectively. The former was mounted in the chamber door sufficiently far from the magnetron to avoid interacting magnetic fluxes. In addition, the penning discharge was not operated during reactive processing, to prevent unnecessary contamination of the central electrode of the gauge.

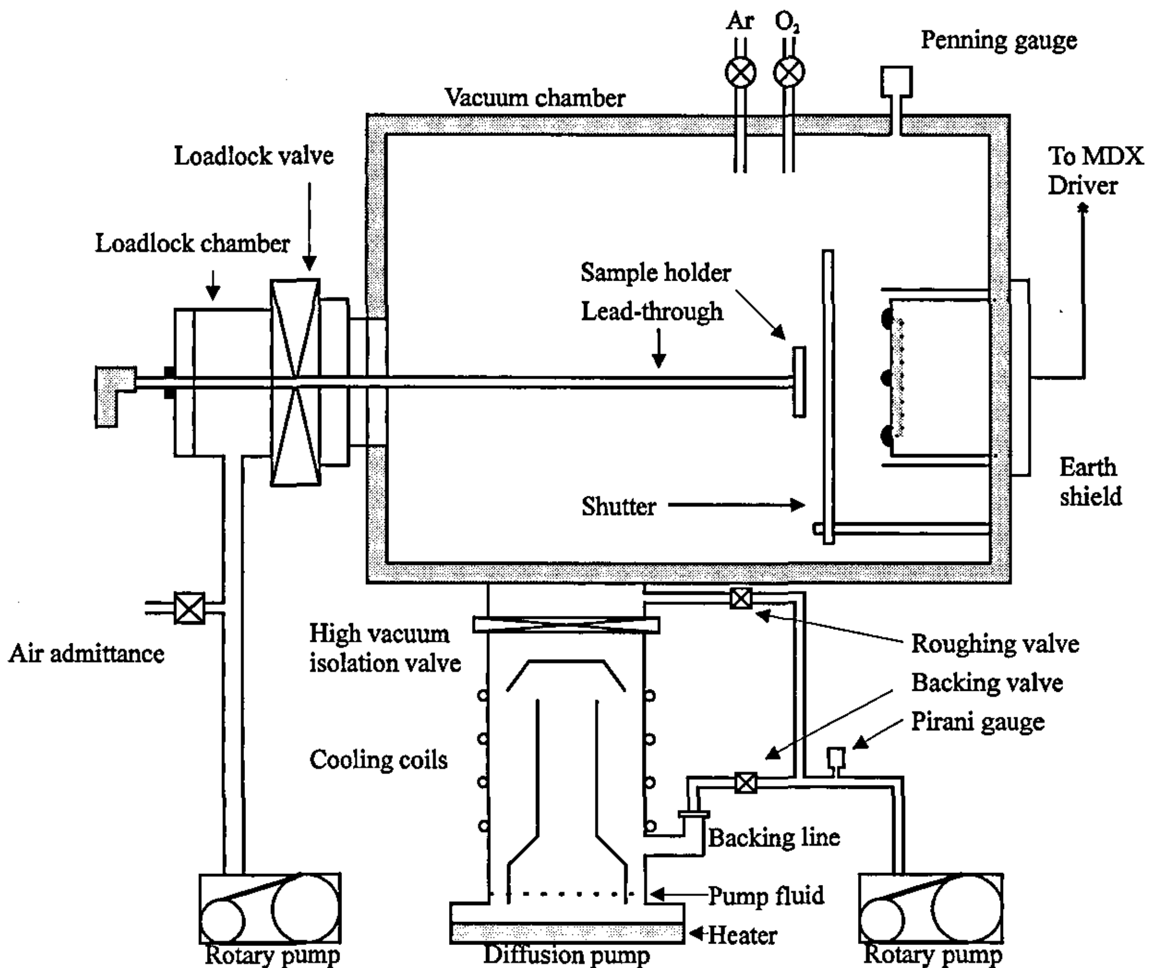

Figure 6.1 : The deposition system

6.1.2 Operating methodology

There are two basic premises around which industrial machines are designed. The first, applied to large volume, high throughput, and many repetitions of the same coating formula, is batch processing. This technique relies on many substrates being loaded into a vacuum system and coated in the same evacuation. This inevitably leads to finished products which demand low tolerance to fluctuating process conditions, to avoid batch loss. The alternative method employed is an in-line, air to air system, where the process is susceptible to long or short term drifts in stability. A loadlock, or air to air system, allows substrates to be admitted individually to the main chamber, and hence, any drift can be observed and action taken before the next substrate is loaded, avoiding any expensive replacement of a lost batch. The machine used for this work was adapted for loadlock operation since the precise stoichiometry required can only be achieved for the majority of reactively sputtered compounds by a series of iterative depositions. It is obvious that a batch system is poorly equipped to deal with the nature of iterative deposition, hence the decision to install a loadlock into the opposite wall to the deposition source.

The loadlock chamber, constructed in-house, was 10 cm in diameter with a volume of 10^{-3} m^3 and was located axially in the chamber wall. The isolation valve, located between the chamber wall and the loadlock volume was a commercially available VAT series 12 DN100 with a manually operated lever arm. Samples could be loaded into the deposition zone in the main chamber via the differentially pumped roughing line to the loadlock, by means of the loading lead-through. This was a 6 mm diameter stainless steel shaft retained in a 25 mm thick, 16 mm diameter perspex sheet by a Wilson-sealed 1' rotary feed-through. The sealing surface of the perspex plate mates with an o-ring located in the end of the loadlock volume, so that evacuation of the loadlock chamber and substrate can be made prior to the opening of the gate-valve. Pressure evaluation within the loadlock was obtained via a CVC thermocouple gauge model GTC-360 connected to a thermocouple gauge tube. The rotary/linear lead-through enables the transfer of the loading arm and substrate to the required position in the deposition zone.

6.1.3 The pumping system

The importance of a high vacuum for thin film deposition in respect of contamination during film growth is to some extent implicit and will, therefore, not be elaborated on here.

Referring once again to figure 6.1, the deposition chamber was pumped by a conventional rotary backed diffusion pump arrangement. The rotary pump was rated at a pumping speed of 11 ls^{-1} and the diffusion pump, with its 8" diameter throat, was rated at 1400 ls^{-1} and had an array of six 300 W rod-type heaters. Typically, rough pumping to $2x10^{-2}$ torr was achieved in 30 minutes, and full evacuation to working base pressure, $\sim 1x10^{-6}$ torr, took five hours.

No cold cap facility was supplied with this pump, but a supplementary Meissner coil for use with liquid nitrogen was fitted to the chamber roof, to reduce the adverse effects on film properties of backstreaming or outgassing, a particular problem when loadlock transfer chambers are used.

Evacuation of the loadlock volume was achieved with a 10 ls^{-1} rotary pump and, via a valving system, the volume could be vented and evacuated to a pressure of $2x10^{-3}$ torr within time periods of 8 seconds and 90 seconds, respectively.

6.1.4 Gas admission and flow measurements

The total distance between the reactive gas pipe exit in the chamber and the piezo-electric valve was minimised to ~3 cm to help reduce the time constant of the pipe [1], thus, reducing the response time of the feedback loop to any changes in target status.

This modification, allied with the pipe outlet being close to the target, and other factors such as the high pumping speed of the system, enabled very efficient control of the reactive deposition process, as will be explained in chapter 9 in more detail.

6.1.4.1 Noble gas specifics

A Vacuum General (VG) FM360 Ultra Flow mass flow controller, with a built-in solenoid valve, was connected to a VG model 78-7/ratio and pressure flow command and display module. With the set-point of the latter indicating the desired mass flow, a potential is applied to the valve allowing it to open and admit an initial flow rate of argon gas, 99.5% purity, to the chamber. The measured flow rate is passed from the mass flow controller back to the flow command module, where it is compared with the set-point. The closed loop circuitry admits inert gas until the two are equal, the desired flow rate henceforth maintained by the comparator.

6.1.4.2 Reactive gas specifics

The same arrangements were used in direct control of the flow of the reactive gas to the chamber as for the inert gas. However, an external set-point, derived from the controlling technique in operation (PEM or Magnetron Voltage Control (MVC)), was used to specify the rate of gas admission to the chamber. This reactive control process is dealt with in greater detail in section 6.5.

6.2 Magnetron design and performance

The I/V characteristics for the magnetron are illustrated in figure 6.2. From these operating characteristics it can be concluded that the magnetron does not have any anomalies whilst in the power regime used throughout this work.

It has been estimated [2] that up to 80% of applied power is taken by the magnetron coolant. In order to ascertain the applicability of this statement to this system in particular, a simple experiment was devised whereby flow rate and temperature of cooling water were used to estimate the proportion of applied power removed by the medium.

The coolant flow through the magnetron was measured to be 0.02 ls^{-1} and, at a magnetron power of 800 W, the temperature rise was measured to be 4 °C. The power associated with this temperature rise can be calculated from the heat capacity of water. In this work, the ratio of power applied to the magnetron to that consumed by the water supply was 50%.

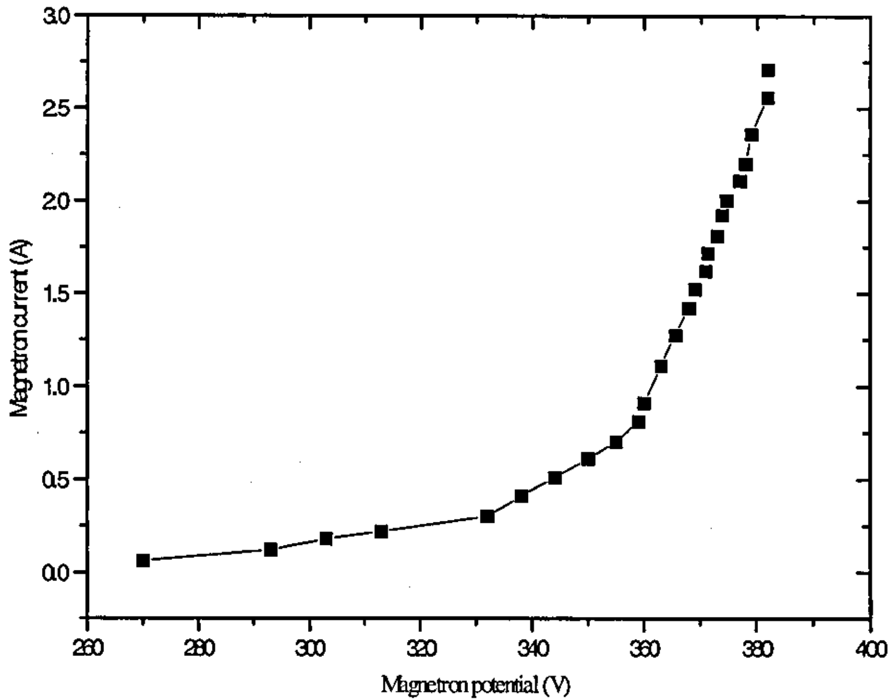

Figure 6.2 : I/V characteristics of the planar magnetron used throughout this work

6.2.1 Construction and mounting

The magnetron deposition device (plate 6.2) used throughout this work is shown schematically in figure 6.3. Because of the advantages offered by physically long magnets, section 3.3.3, the magnet array was comprised entirely of AlComax material. AlComax has a weaker magnetic flux density compared with, say, NeFBo, and was available in 95 mm deep form for the same flux density. As a direct result, the magnetron body was 120 mm deep from front to back, minimising sputtering from the outer pole piece.

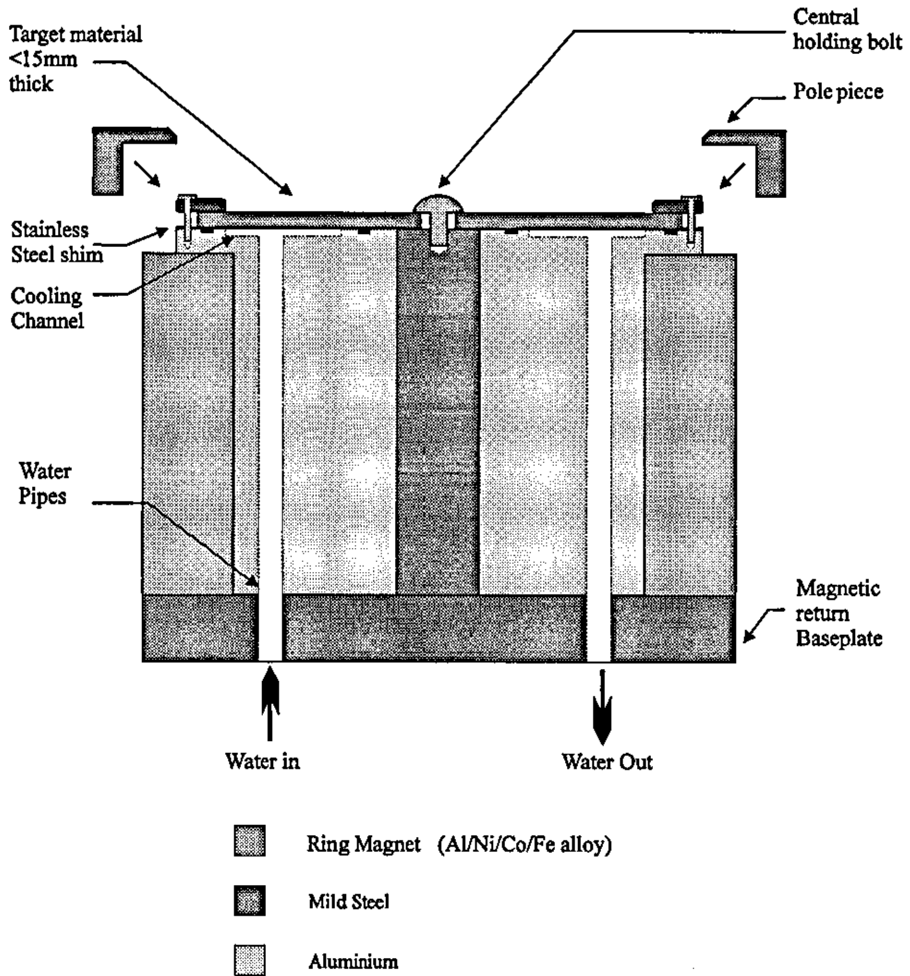

Figure 6.3 : Magnetron design

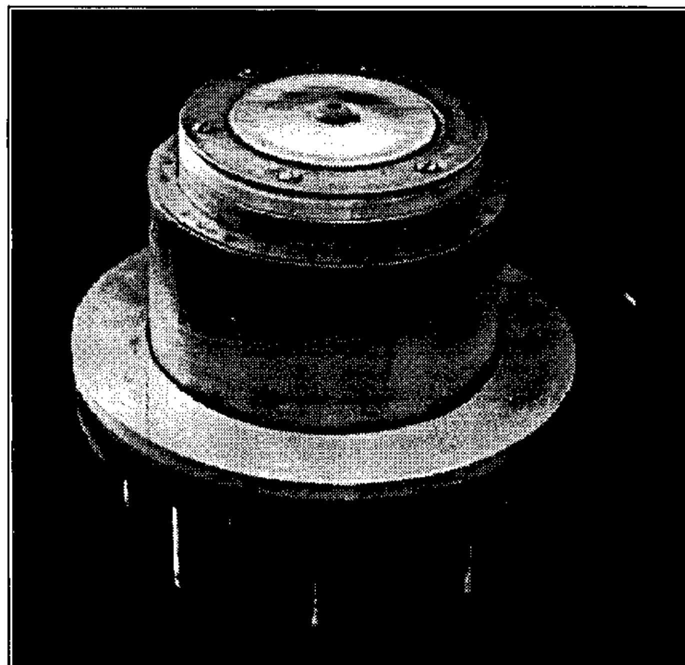

Plate 6.2 : The magnetron used throughout this work

The target material thickness was optimised at 10 mm or less. Greater thicknesses than this resulted in difficulties in plasma striking, even for non-magnetic target materials. The target itself was indirectly cooled to avoid the problems of a vacuum/water interface when the target finally wore through.

To produce a significantly unbalanced arrangement, it was decided to omit the conventional centre magnet, once it was determined that the desired magnetic field circuit could be completed with a centre core of mild steel. It must be stressed that this was only possible with this design if (i) a central retaining bolt of mild steel and (ii) a magnetic annulus outer pole piece were both in position.

Figure 6.4 shows the means of support for the magnetron, necessary because of its side sputtering orientation. Electrical isolation from the chamber wall was achieved by two insulators. The first insulator fitted between the chamber wall and the magnetron, providing a lip to match the internal diameter of the hole in the wall. The other was clamped between the outside of the chamber and the rigid steel clamping ring. This ring clamp provided equalisation of pressure for the o-rings (not illustrated on the diagram), achieved by eight 60 mm M8 bolts. Note that a disadvantage of this design is that the securing bolts are at magnetron potential during its operation and suitable covers must always be in place.

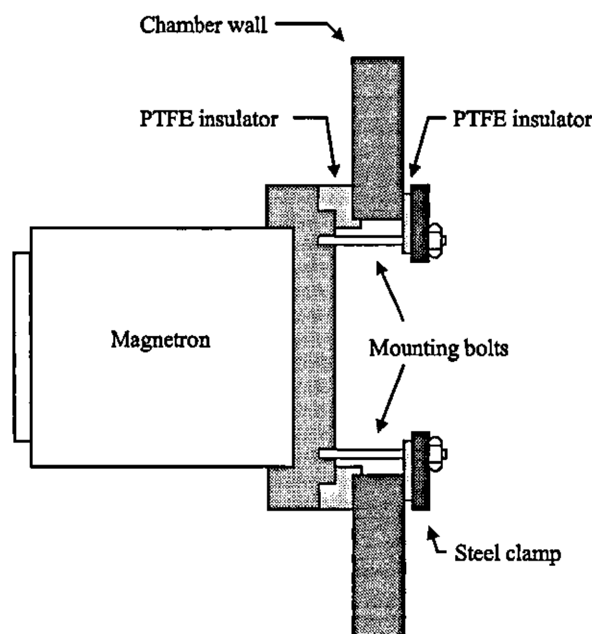

Figure 6.4 : Cross section through the magnetron mounting arrangement

6.2.2 Target utilisation

Being a planar magnetron of circular design, the target utilisation efficiency could not be expected to exceed 30%. In order to achieve high utilisation, magnetic flux lines must emerge from one or other of the poles and not become re-entrant before having followed a path parallel to the cathode surface for some considerable distance. However, because of the short distance between poles and the high field strengths of the magnet used, the majority of flux lines were re-entrant into the cathode before crossing the full radius. This is illustrated by examination of the plasma intensity, greatest intensity being at the points of maximum erosion. Plate 6.2 further illustrates this point as an erosion groove can be seen clearly on the target surface.

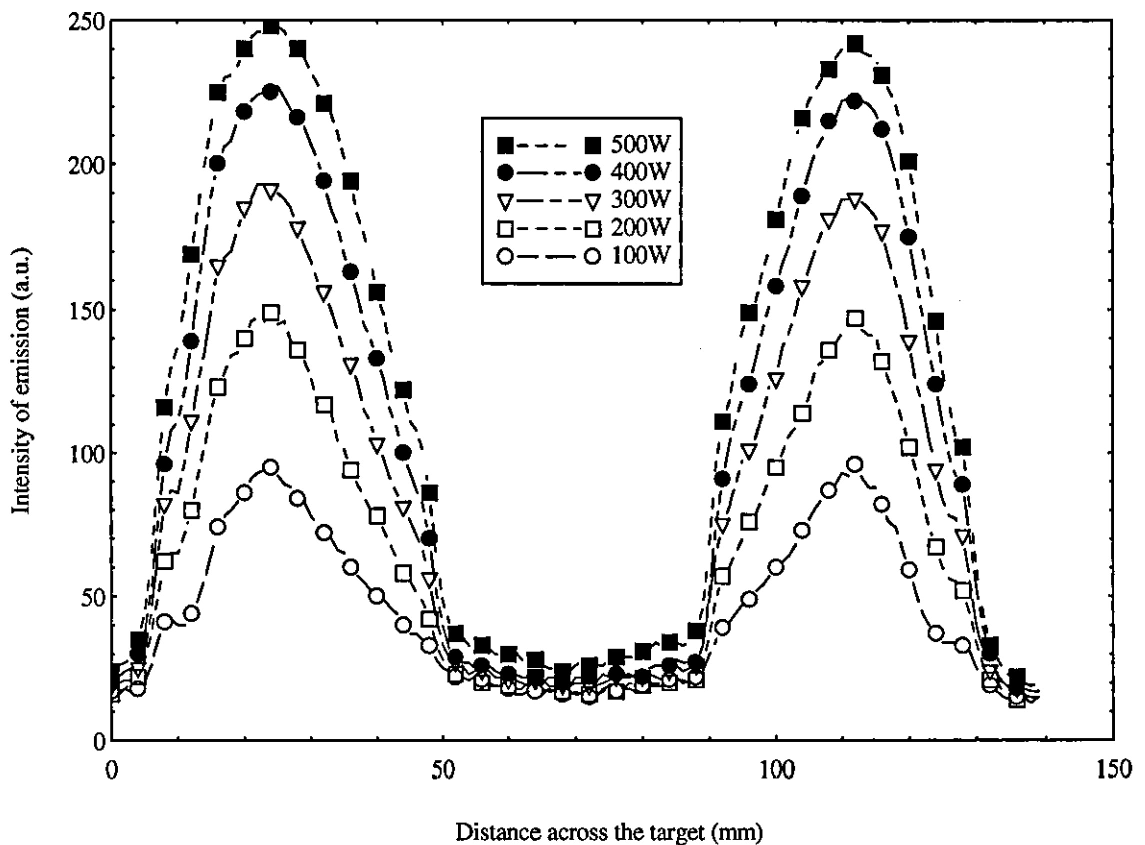

Figure 6.5 : Variation in intensity of the plasma across the diameter of the magnetron

6.3 The electron-collecting-anode

Many techniques exist in magnetron sputtering to control the ion bombardment at the substrate. These include placing an aiding or opposing auxiliary magnet behind the substrate [3], auxiliary external electrodes [4], substrate biasing [5], and controlling the degree of unbalance using electromagnets [6]. The majority of these are widely used in the industrial environment. Placing an electron-collecting anode [7] in the magnetic field, figure 6.6, has advantages over all these techniques in that the structure and properties of the film can be controlled by varying the ion bombardment, but without the disadvantages of extra cost, difficult tunability, and interference in the magnetic field. Furthermore, the anode does not form an integral part of the magnetron design and can, therefore, be added to the sputtering system with minimal structural changes.

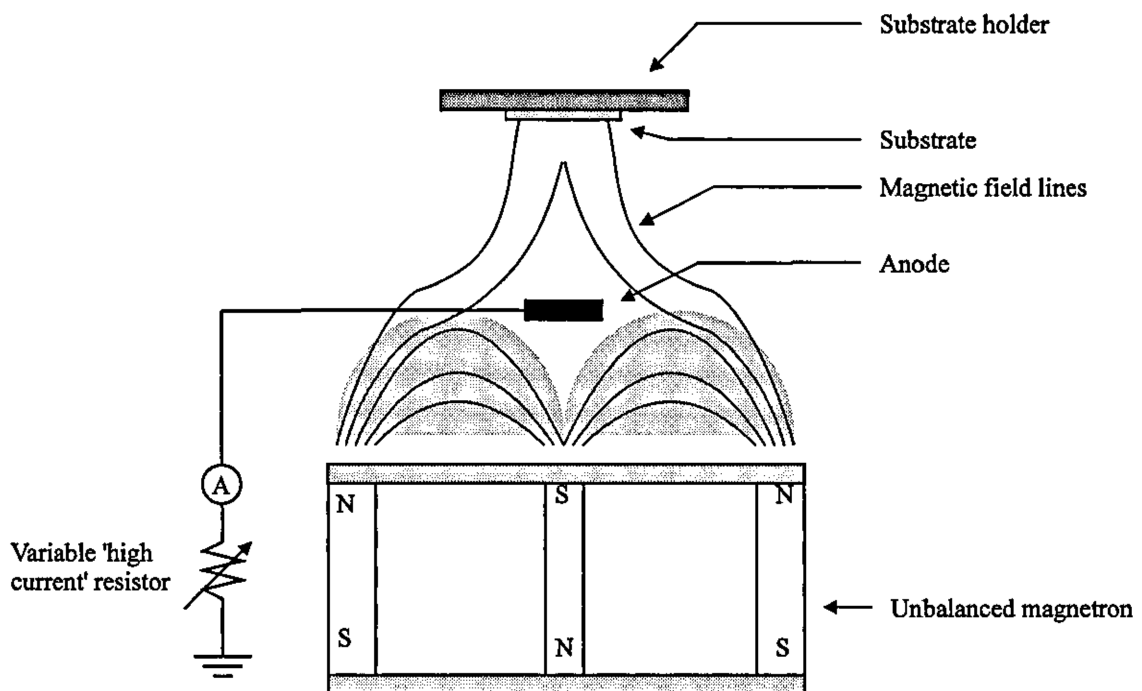

Figure 6.6 : The electron collecting anode

The role of the electron-collecting-anode in reducing the ion bombardment is two-fold;

- To prevent high energy secondary electrons, that have undergone scattering and escaped the confinement of the magnetic field lines, from reaching the substrate. These electrons follow the unbalanced magnetic field lines emerging from the cathode, taking positive ions with them owing to the potential gradient they create.

- To create a self-bias when its resistance to earth is increased above zero.

The anode was configured to operate through a variable resistance path to earth and consisted of a water cooled copper tubing welded to a small copper cylinder. It was positioned at the null point of the magnetic field [8] so that it did not interfere with the operation of the magnetron and was not sputtered. Whenever the system was opened, however, the anode was cleaned so that easily oxidisable materials such as Al did not form an insulating layer that would charge up. A 420 Ω, 1 A variable resistor was connected between the anode and earth. This resistor enabled variable control of the bombardment at the substrate as will be discussed in chapter 8. Plates 6.3a and 6.3b show the effect the anode has on the magnetron plasma when it is used in floating and grounding modes respectively.

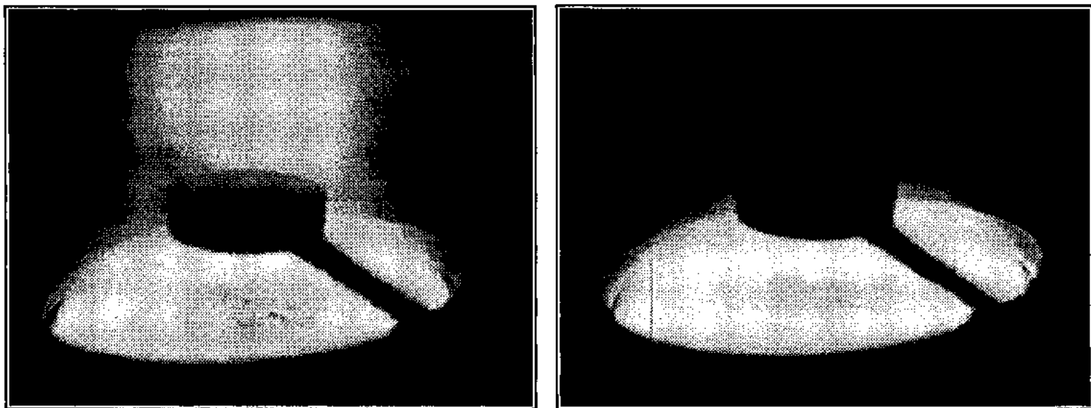

(a) Anode floating (b) Anode grounded

Plate 6.3 : The effects of the anode on the plasma beam

6.4 Magnetron power deliverance

The requirements of a practical power supply for sputtering applications are demanding. Impedance matching of the output stage to the cathode is important, as is stability with

low ripple voltage. Regulation in either power, current or voltage modes is desirable, and a high degree of arc suppression is paramount when sputtering certain materials. There are at present only two competitive makes of power supply worthy of use as magnetron drivers in pressure regimes of concern here. For this work, only one make of supply was used, largely for reasons of availability, not necessarily out of preference.

6.4.1 The MDX Magnetron driver

Throughout this work, the MDX range of power supplies, produced by Advanced Energy Industries Inc. were used to drive the magnetrons. Both direct current and medium frequency, alternating current magnetron drivers were utilised, each capable of controlling with any of three regulation modes; constant current, voltage or power. It was the last of these three, however, which proved more practical and was used throughout the work. Both drivers were also capable of ramping the power to a desired set-point, a feature that is useful when cleaning the target surface of any native oxide. UHF coaxial cables connected the magnetron to the power supplies, the inner core carrying the negative potential and the sheath providing earth protection.

An Advanced Energy MDX 2500 W DC magnetron drive was used throughout this work for direct current application.

6.4.1.1 AC Driver with and without output rectification

An Advanced Energy PE2500, 2.5 kW medium frequency power supply was used throughout this work for sputtering materials that were prone to arcing.

As explained in section 4.3.3, AC power application is a convenient and effective way of eliminating arc discharges. However, two magnetron sputter sources are needed with the TwinMAG™ [9] arrangement and pulsed deposition [10] requires a separate power supply, equal in expense to the initial supply. Hence, a circuit was designed in-house to enable connection and stable operation of an existing AC supply, with dual anti-phase

outputs, to a single magnetron. This circuit comprised of eight 30 A, V_{rev}=1000 V ST C501N fast recovery power diodes in a bridge rectification configuration as illustrated in figure 6.7.

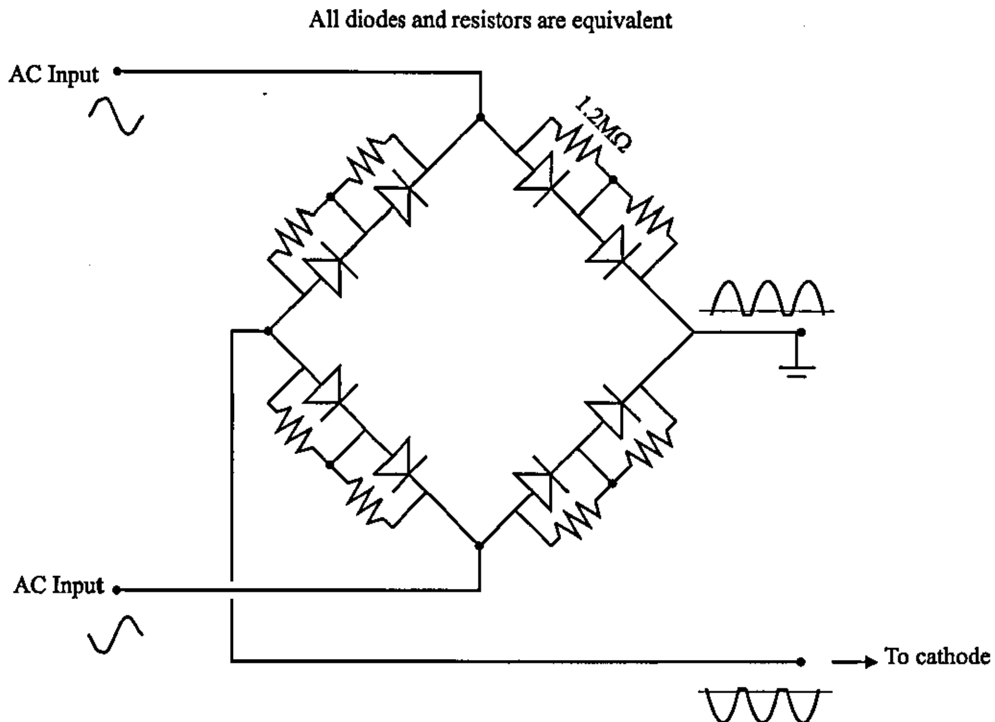

Figure 6.7 : Rectification of AC anti-phase outputs

The two diodes in series with parallel voltage drop resistors were necessary in each arm of the bridge circuit to handle reverse voltages of up to 2000 V. The positive output was grounded and the rectified negative output was connected to the magnetron. It should be noted that the outputs from the AC supply were directly connected to the cathode and ground, without the rectification circuit. However, this led to a plasma striking around the earth shield, plate 6.4. This is because the live electrode becomes both an anode and cathode. When the live electrode is an anode it takes the plasma to a positive potential, making ground a cathode relative to the plasma. The ground electrode (earth shield) is, thus, bombarded with ions, sputtered, and has a dark space around it. This did not occur with the rectified output.

The predicted voltage waveforms do not adequately describe the signal shapes observed in reality when using the rectification circuit. Figure 6.8a shows the actual voltage shapes observed. When the magnetron is powered by the rectified output, it is only

connected to a negative potential and acts as an intermittent cathode relative to the ground and plasma. The voltage at the nominal cathode is biased to -400 V, then ringing in the rectification circuit occurs, figure 6.8b, raising the voltage above 0 V and giving necessary neutralisation of the arcs.

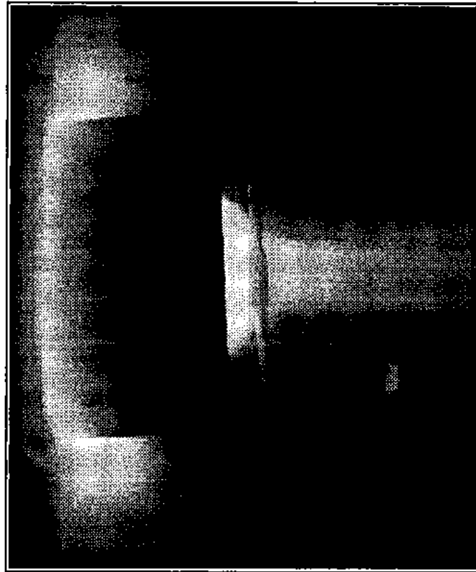

Plate 6.4 : Observed plasma formation around the magnetron earth shield when AC sputtering with one output connected to ground

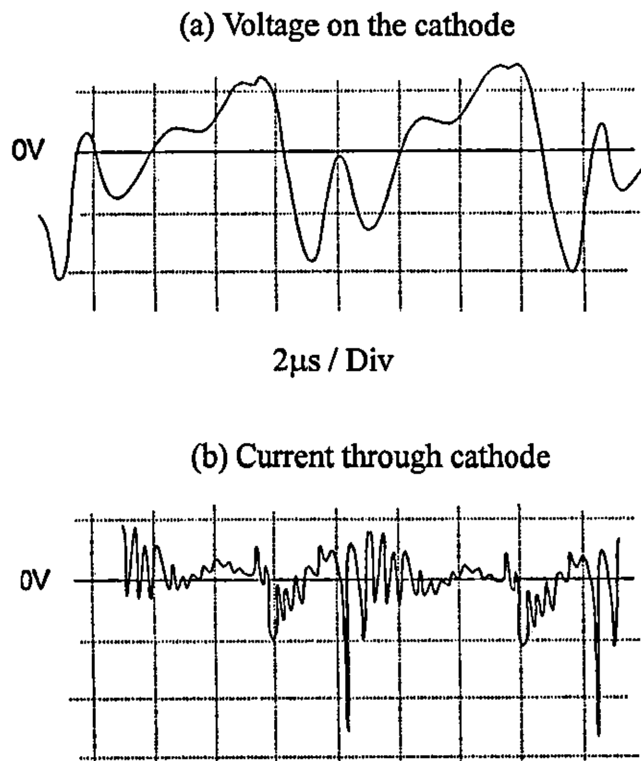

Figure 6.8 : Voltage and current waveforms obtained during rectified AC sputtering

6.5 Process control techniques

The following section introduces the control techniques used to accurately deliver the correct flow of reactive gas to the growing film. Throughout the work, one of the main aims was to investigate the viability of various processes, both conventional and novel, used in reactive sputtering. Continuous feedback control loops are described using both the plasma emission and cathode potential as measurands of target status. Although conventional techniques, such as continuous feedback control, are now widely used in both laboratory scale and industrial processes and produce quality films [11], the work here also describes an alternative control system to obtain similarly tight stoichiometry control, whilst expanding the optimum process window to give decreased sensitivity to transient process parameter aberrations, such as arcs or micro-instabilities in target status. In addition, a system was sought offering the advantages of increased cost-efficiency and ease of operator control.

As introduced in chapter 4, a control technique has recently been demonstrated [12] that is termed Successive Plasma Anodisation (SPA). This process has been shown to give advantages in reactive sputtering, but suffers from limitations introduced by mechanically rotating the substrates. This section also describes the components of a SPA process separated in time, without any mechanical movement, but pulsing the reactive gas [13] in response to a control signal proportional to the degree of target poisoning. This process is termed Successive Pulsed Plasma Anodisation (SPPA).

In addition to these reactive processes, compacted oxide target sputtering was used throughout the investigation period. The specifications of the targets used to deposit ITO and ZnO:AL are also detailed.

6.5.1 Measuring of target status

Chapter 4 demonstrated the ability to measure the poisoned state of the target by measurement of both the emission lines within the plasma and, for certain materials, the

potential of the cathode. This section details how these parameters were measured in the work described here.

6.5.1.1 Voltage used as an indication of target status, ϕ_v

Measurement of the cathode potential was derived from the user port at the rear of the MDX power supply. In the case of the DC supply, the signal was a fully buffered and ground referenced 0-5 V analogue signal, directly proportional to the full cathode potential. During medium frequency sputtering a 0-5 V (±0.05 V) analogue signal proportional to the AC average cathode potential was used.

6.5.1.2 Plasma emission used as an indication of target status, ϕ_e

Conventional PEM equipment, comprising an optical fibre, monochromator and photomultiplier, was not used throughout the investigations reported in this work. Although this equipment did exist within the laboratory, an alternative approach was investigated that maintained the accuracy of the monochromator whilst reducing cost.

The emissions in a plasma can be split into two distinct groups, those owing to the elements being sputtered and those owing to the reactive gas. There are usually many different species of the sputtered material and reactive gas in the plasma, and thus, various emission lines are present owing to electron energy level transitions. However, the emissions from the reactive gas are well separated in wavelength from the majority of the sputtered materials.

Figure 6.9 illustrates the equipment and arrangement used in the measurement of plasma emission. A modified Zenit 12xP SLR camera fitted with a 50 mm^2 photodiode with a wavelength range, 350 nm - 800 nm, was mounted onto the chamber wall and focused onto the central region of the plasma. The copper pipe allowed selective imaging of the emission and increased sensitivity to target poisoning. A filter was placed in front of the

camera to selectively image certain metal emission lines. Two different filters were used throughout this work, the specifications depending on the materials being observed.

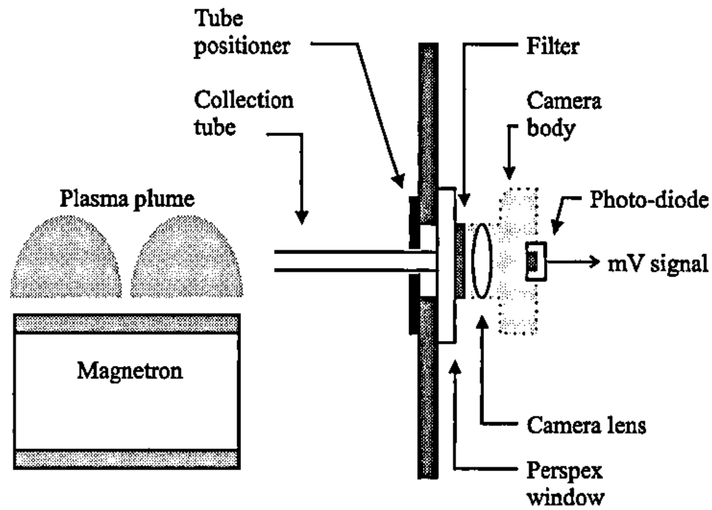

Figure 6.9 : Plasma emission measurement system

Figures 6.10a and 6.10b show the transmission characteristics of the two filters used. This design of filtering emission lines using a remote camera had the advantage over using an optical fibre in that the window did not become coated, as an optical fibre often does. This results in a reduced emission intensity, and hence, a drift in desired set-point.

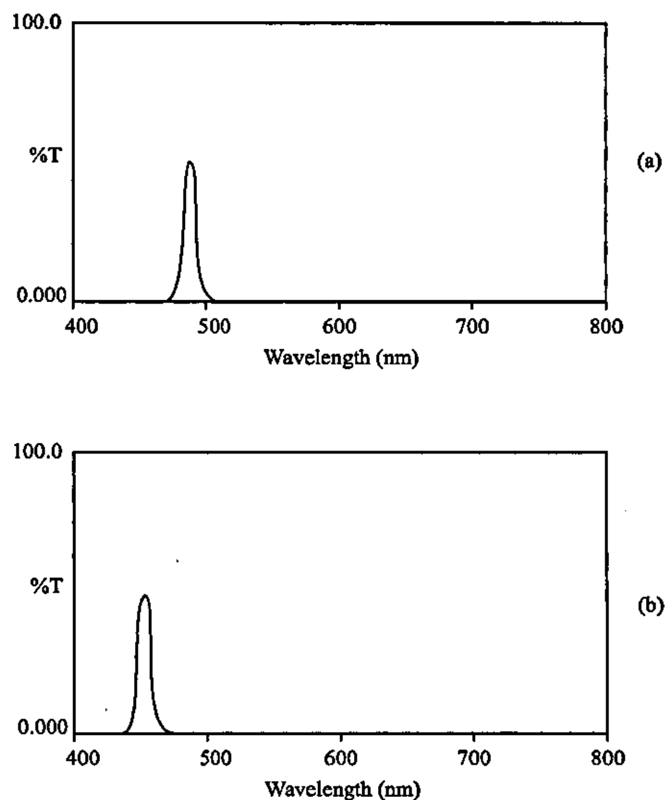

Figure 6.10 : Transmission characteristics for filters used in plasma emission monitoring

6.5.2 The feedback control unit

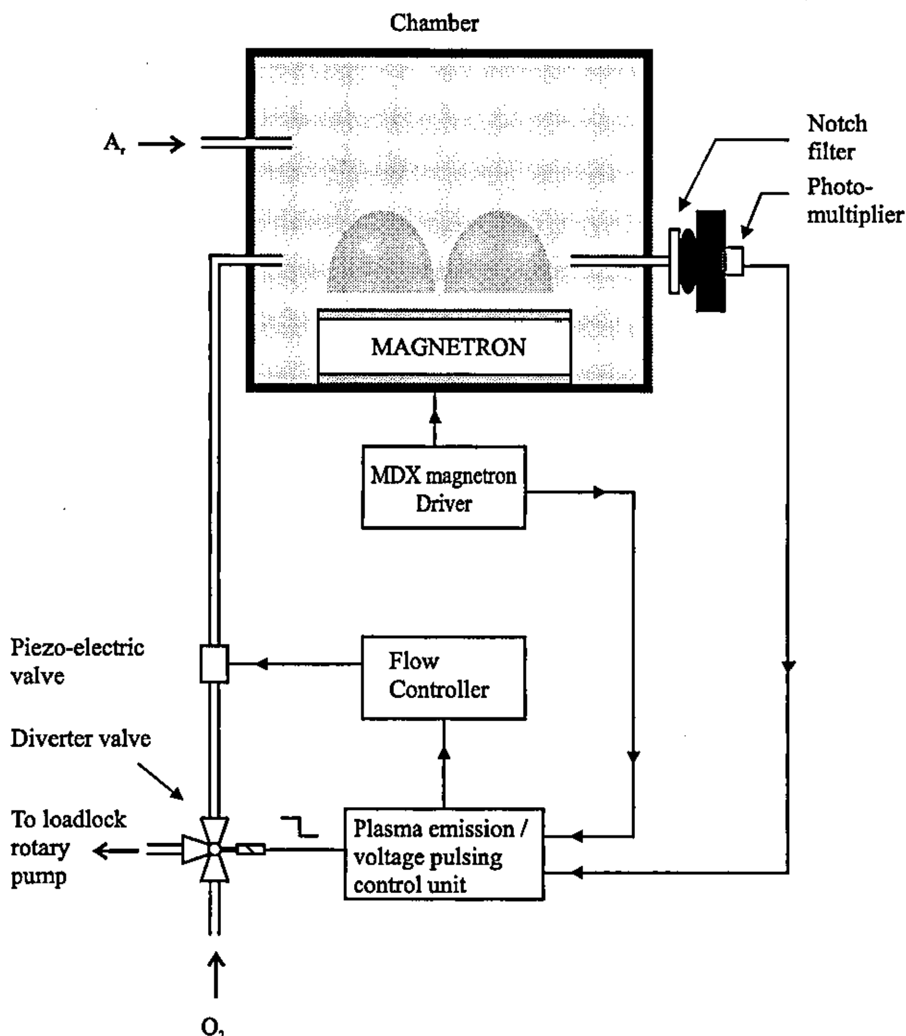

Figure 6.11 : Reactive gas control system

Figure 6.11 illustrates the main components of the feedback control system design used throughout this work. The main electronic processing unit was designed and built purposely for the investigation of the various control techniques. This unit enabled input of either the signal from the photomultiplier on the plasma emission unit, or the voltage derived from the MDX supplies, indicative of the cathode potential.

The following sections will attempt to explain the operation of this system, with each section explaining the system from a process and electronics point of view.

6.5.2.1 Continuous feedback control (CFC)

Process view

The CFC process is similar to the process described in section 4.2.4 but an explanation is repeated here for clarity.

The role of the feedback control unit (FCU) in continuous control is to normalise the input signal so that a reference signal can be supplied to the pressure controller. With the cathode operating in a fully poisoned mode, the output signal from the circuit to the pressure control unit (PCU) is offset to 0 mV through the bias setting on the FCU. Then, with the reactive gas switched off and the cathode returned to an unpoisoned state, the output signal is set to 1000 mV by altering the gain setting. This normalisation procedure was repeated for every material and at the start of every day.

The control process could then be initiated through use of the PCU. The 0 - 1 V set-point control on the unit was selected to represent the desired point on the hysteresis curve, with 0% to 100% element rate corresponding to 0 to 1 V respectively. The pressure control unit then automatically opens the piezo-electric valve to admit oxygen into the system until the signal from the feedback control unit equals the operator-selected 'set-point' on the PCU. This process is continuous, with active adjustments being made to the reactive gas flow throughout the deposition period.

Electronics view

Figure 6.12 is a schematic of the circuit diagram design for the normalisation of the measured signal obtained from the process. The input switch enables control of the process from either the photomultiplier on the plasma emission camera or the magnetron cathode potential. When the switch is placed in position 1, a pre-amp stage is engaged for the amplification of the millivolt signal obtained from the photomultiplier. In position 2 the signal representing the cathode voltage is attenuated through a potential divider to condition it for the next stages of amplification.

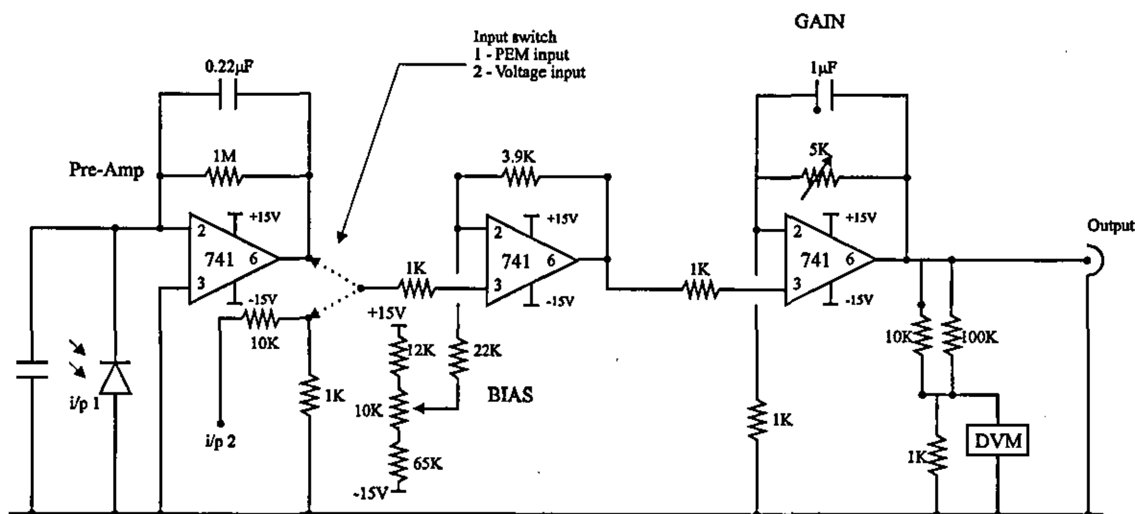

Figure 6.12 : Schematic of normalisation circuit used in gas feedback control

The measured signal is then subjected to two discrete stages; an offset or *Bias* stage followed by an amplification or *Gain* stage. Both stages are used in the initial normalisation of the feedback process, the former in setting the output to 0 V, representing a poisoned target state, the latter in setting the output to 1 V, representing an elemental or 'clean' target state.

The capacitors on both the pre-amplification stage and gain stage are there to reduce high frequency noise. It should be noted, however, that careful selection of capacitance was needed to minimise the time constants they introduced.

6.5.2.2 Successive Pulsed Plasma Anodisation (SPPA)

Chapter 4 briefly introduced the idea of pulsing the reactive gas into the chamber. This idea was first introduced by Aronson [14] and has since been used by other workers [15]. Gas pulsing has never been as successful as more conventional techniques such as PEM because of its unrepeatable and inconsistent results. No control of the process has been documented, however, and all the previous work on the technique has involved pulsing the reactive gas at a pre-defined frequency, which is prone to short term drift.

Throughout this work, a better method of pulsed control was sought. This section describes the technique of SPPA as a new, alternative method of reactive sputtering.

<u>Process view</u>

In SPPA, the planar magnetron is used both to sputter the metal and anodise it with a self-biased O_2 plasma. For SiO_2 films initially, a silicon layer is deposited from an unbalanced magnetron and then oxygen is introduced to the system to create an oxygen plasma, directed towards the substrate to provide argon and oxygen ion bombardment. This plasma oxidises the growing film and activates more desirable structures. This process of elemental deposition and oxidation is continuously repeated.

An electronic switching unit, within the original process control box, was designed to control the pulsing of the reactive gas into the chamber. Once again, the DC voltage appearing on the cathode or emission signal from the plasma was used to control the process accurately. This signal was normalised as explained above in section 6.5.2.1, and formed the input to the pulsing circuit. Selection of two voltage threshold levels determined the open and closed states of a switching valve, which directed the reactive gas to either the process or to a vacuum dump as shown in figure 6.11. Admission of a reactive gas pulse to the chamber forces the voltage signal below the selected lower threshold, U_l, and shuts off the reactive gas supply to the chamber via the switching valve, allowing the cathode to clean. The voltage signal then rises above the upper threshold, U_u, where reactive gas is diverted to the chamber and the target poisons once more. Repetition of this cycle was found to enable continuously variable but controllable target status.

<u>Electronics view</u>

Figure 6.13 is a schematic of the circuit diagram designed for pulsing the reactive gas into the chamber. The normalised signal, representing the percentage of target oxidisation, is fed into the two 311 comparators that are provided with a 0 - 1 V reference voltage by two precision 20 turn pre-set resistors. Depending on the signal

level, the comparitors output a logic 1 or 0, thus, setting or resetting the RS 74279 flip-flop. Hence, the output of the flip-flop is set high when the upper threshold is reached, opening the switching valve and poisoning the target, and low when the lower threshold is reached, closing the switching valve and sending the target back into elemental mode. An additional signal from the normalisation circuit was fed into a Tektronix 2201 digital storage oscilloscope so that the pulsing waveforms could be continuously monitored.

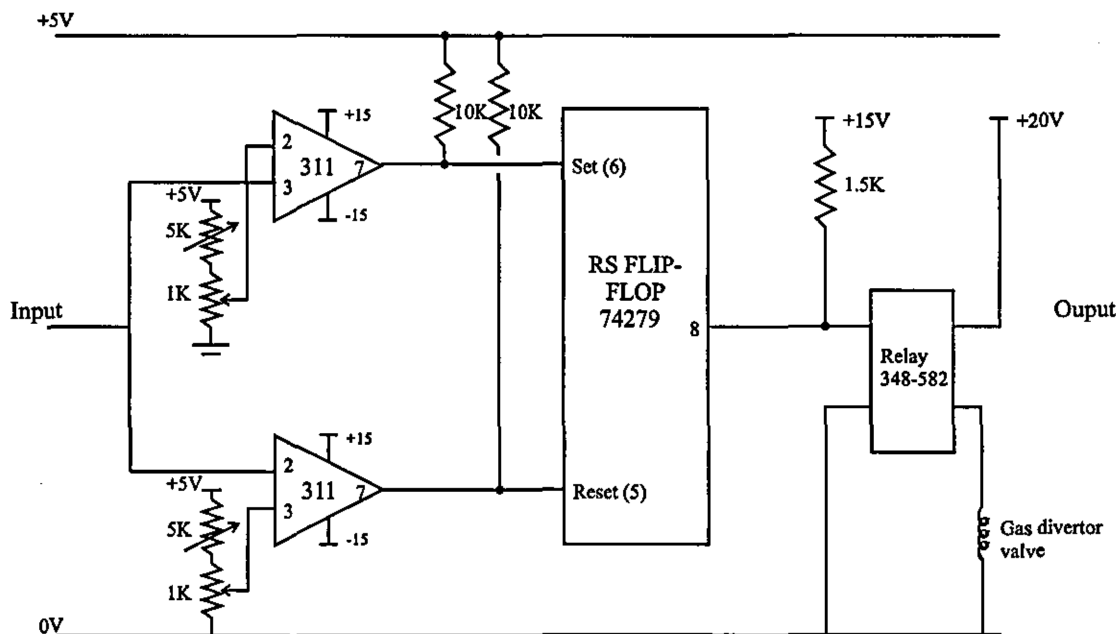

Figure 6.13 : Schematic of circuit used in gas pulsing

Careful choice of electronic components was a necessity to avoid switching problems when the upper and lower threshold levels were approached.

6.5.3 The compacted oxide targets

Compacted oxide targets were briefly introduced in chapter 4. ITO and ZnO:Al compacted oxide targets supplied by Arconium were used in this work as a comparative deposition technique for transparent conducting oxides.

ITO target

The ITO target used was a 90% In_2O_3, 10% SnO_2 composition by weight, compacted oxide sputtering target and was manufactured by pressureless sintering to a high density (95%). [16]. This technique of manufacture involves pre-processing of the ITO powder, followed by high temperature sintering (>1200 °C) in a controlled atmosphere. Pressureless sintering has advantages over processes such as hot isostatic pressing (HIP) in that higher target densities can be achieved and nodule formation on the target is significantly reduced [16].

ZnO:Al target

The same process was used to create the ZnO:Al target. The target density was 98% and contained 2% Al by weight [17].

6.6 Target specifications

The specifications of the targets are given in the following section, including ITO and ZnO:Al for completeness. The diameter of the targets used throughout this work was ~115 cm. Table 6.1 illustrates their preparation, thickness and purity.

Target material	Preparation	Total thickness (mm) Target + backplate	Purity (%)
Al	*a*	3.0	***CEG***
Cr	*b*	6.2	99.9
In:Sn	*c*	5.4	98.0
ITO	*d*	6.5	99.99
Si (Boron doped)	*b*	5.2	*
Ti	*b*	4.5	99.9
Zn:Al	*a, b, c*	6.0	Zn : 99.9 Al : ***CEG***
ZnO:Al	*d*	6.5	99.98

Table 6.1 : Specifications of the targets used

a Cut from commercially available sheet.

b Commercially available sputtering targets.

c Prepared in-house.

d Commercially available compacted oxide target (see section 6.5.3).

CEG Commercial Engineering grade.

* Resistivity of $3x10^{-5}$ Ω m.

6.7 Deposition procedure

Throughout this work, a methodical deposition procedure was continually used to avoid inconsistent results. Samples, as shown in table 6.2, were mounted to a purposely constructed sample holder. During deposition, samples were maintained at a distance of 7 cm from the target.

The glass slides were cleaned by immersion in a Decon 90 bath with ultra-sonic agitation for 5 minutes followed by a rinse in de-ionised water and finally an anti-static blow to prevent drying marks.

Substrate	Purpose
Glass slide	Refractive index and thickness determination (For $n_f > 2.0$) Transmission measurements Surface analysis (Auger)
Silicon wafer (100 orientation n-doped) Resistivity = $1.8x10^{-4}$ Ωm	Refractive index and thickness determination (For $n_f < 2.0$)
Borosilicate glass precision cover slips 80 μm thickness 150 μm thickness	Stress measurements

Table 6.2 : Specifications and purpose of substrates used

6.8 *In situ* measurements

The various causes [18] of substrate heating and substrate ion bombardment are discussed in chapter 5. This section aims to examine the methods used throughout this work to measure these effects.

6.8.1 Substrate temperature

Substrate temperature is very difficult to measure during film deposition [19]. Common ways to attempt this measurement have involved the use of thermocouples or infrared detectors. However, these methods can give unrealistic results by measuring the temperature of the substrate table or the plasma, rather than the substrate surface. In this work, an *in situ* substrate temperature measuring system, utilising a commercially calibrated [20], planar-insulated, platinum resistance element, fixed to a glass slide, provided the sensor arrangement, figure 6.14. The sensor was fixed to the lead-through arm and care was taken to isolate the depositing material, metal lead-through and resistance element to avoid any thermal cooling. The measurements had an estimated error of ~5%, mainly because of the uncertainty in the thermal contact between the sensor and the microscope slide.

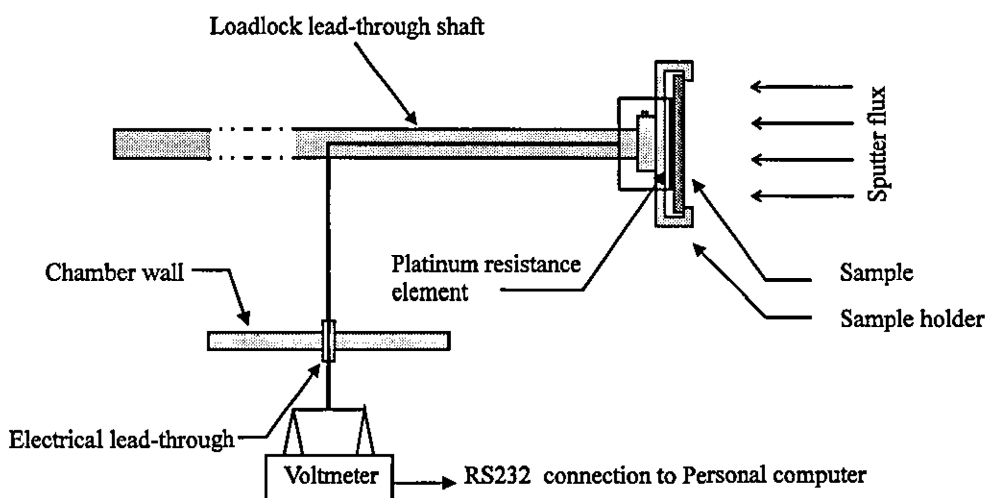

Figure 6.14 : Construction and mounting of temperature sensor

The platinum resistance element was connected via spot welded 60 Ωm insulated wire, about 0.5 cm in length, to two insulated electrical lead-throughs on a 5.5 cm port situated in the wall adjacent to the magnetron. External connection to these lead-throughs enabled PC data logging of up to 10 samples/sec. This made it possible to monitor continuously the temperature of deposition whilst changing other system parameters.

6.8.2 Ion bombardment

The two parameters of prime interest throughout this work were the ion bombardment occurring at the substrate and the bias voltage obtained by the substrate. As described in section 2.1.3, when an isolated probe is placed into a plasma, it acquires a space sheath, in which there is a potential gradient, and hence, an electric field. In the plasma diagnostic technique first introduced by Langmuir in 1924 [21], the probe is connected electrically to a variable voltage power supply which, in turn, is connected to a reference electrode immersed in the plasma, in this work, one of the walls of the vacuum chamber.

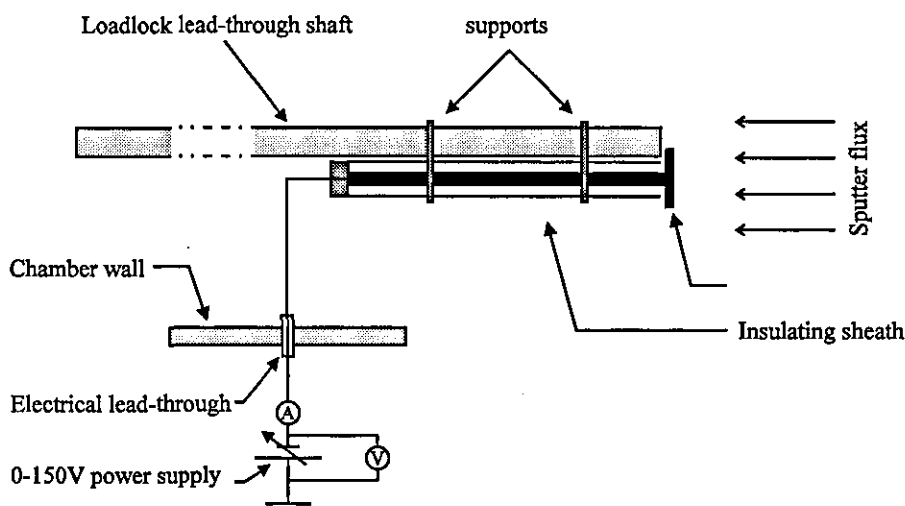

Figure 6.15 : Construction and mounting of Langmuir probe

A Langmuir probe was constructed for the ion bombardment measurements taken throughout this work, figure 6.15. The probe consisted of a tungsten plate, 1 cm^2 in area, enabling direct measurement of ion current in $mAcm^{-2}$, and 0.5 mm thick, spot-welded to

a metal arm, encased in a hollow glass sleeve. This arrangement was fixed to the lead-through arm, directly replacing the substrate, as in the temperature measuring module. Surrounding the probe head was a disc of stainless steel, 5 cm in diameter and containing a cut-out region to allow the central location of the probe. The 5 cm disc reduced the edge effects at the probe head associated with the plasma sheath [22]. A Philips PE1649 power supply, rated 7 A, 150 V, was used to supply the bias voltage to the probe and disc via two electrically insulated wires connected to the vacuum lead-throughs, enabling I/V data for all the regimes and under different plasma operating conditions to be obtained.

Care was taken when biasing the probe both negatively and positively. A bias of -120 V is regularly used, because whilst it is sufficiently negative to repel electrons in the plasma, for the design of magnetron it is not so negative that ions are accelerated to energies where they would produce significant secondary electrons and sputter the probe head.

CHAPTER 6 REFERENCES

[1] **Spencer, A.G.**, *'High rate reactive magnetron sputtering'*, (1989). Ph.D. Thesis, Loughborough University of Technology, U.K..

[2] **Bishop, C.A.**, (1986). *'The deposition of coatings onto polymer substrates by planar magnetron sputtering'*, Ph. D. Thesis, Loughborough University of Technology, U.K..

[3] **Fraser, D.B. & Cook, H.D.**, (1977). *J. Vac Sci. Technol.*, 14, 147.

[4] **Fraser, D.B.**, (1978). in *'Thin Film Processes'*, ed. by Vossen, J.L. & Kern, W., Academic Press.

[5] **Ja'fer, H.A. & Howson, R.P.**, (1993). *Vacuum*, 44, 381-383.

[6] **Howson, R.P., Ja'fer, H.A. & Spencer, A.G.**, (1993). *Vacuum*, 44, 191-195.

[7] **Schiller, S., Heisig, U. & Goedicke, K.**, (1977). *Thin Solid Films*, 40, 327.

[8] **Coburn, J.W. & Kay, E.**, (1972). *J. Appl. Phys.*, 43, 4965.

[9] **Brauer, G., Dicken, W., Szczyrbowski, J., Teschner, G. & Zmelty, A.**, (1995). *Proc. of the 3rd ISSP*, Tokyo, 63-70.

[10] **Schiller, S., Goedicke, K., Reschke, J., Kirchhoff, V., Schneider, S. & Milde, F.**, (1993). *Surface and Coatings Technology*, 61, 331-337.

[11] **Schiller, S., Beister, G. & Sieber, W.**, (1984). *Thin Solid Films*, 111, 259-268.

[12] **Hall, G.W., Howson, R.P. & Chew, A.**, (1993). *Vacuum*, 44(3/4), 227-230.

[13] **Toyoda, S., Kiyota, T., Tamagawa, K. & Yamakawa, H.,** (1993). *Materials Science and Engineering,* A163, 167-170.

[14] **Aronson, A.J., Chen, D. & Class, W.H.,** (1980). *Thin Solid Films,* 72, 535-540.

[15] **Howson, R.P., Suzuki, K., Bishop, C.A. & Ridge, M.I.,** (1984). *Vacuum,* 34, 291-294.

[16] **Lewis, B.G.,** (1994). *SVC 37th A.T.C.P.,* 'Structure and performance of ITO sputtering targets'.

[17] **Lewis, B.G.,** (1995). Personal Communication, Arconium.

[18] **Andritschky, M., Guimaraes, F. & Teixeira, V.,** (1993). *Vacuum,* 44, 809-813.

[19] **Snyder, J.E. & Kryder, M.H.,** (1989). *Rev. Sci. Instrum.,* 60(4), 749-751.

[20] **Radio Spares,** RS data sheet number 003-914 March 1987.

[21] **Langmuir, I. & Mott-Smith, H.,** (1924). *General Electric Review,* 27(7), 449-455.

[22] **Clements, R.M.,** (1978). *J. Vac. Sci. Technol.,* 15(2), 193-198.

CHAPTER 7

FILM EVALUATION AND ANALYSIS

The following chapter describes the characterisation procedures used to analyse the films deposited in the course of the research. Optical, electrical and mechanical properties were measured, and the techniques that were used are thoroughly characterised with appropriate background theory. Stress was analysed throughout the work and a detailed description of its measurement, using a purposely devised interferometric technique, is also given in this chapter.

7.1 OPTICAL CONSTANT ASSESSMENT 139
7.1.1 Ellipsometry *139*
7.1.2 Transmittance and reflectance *140*
7.2 MECHANICAL PROPERTIES : INTRINSIC STRESS 142
7.2.1 The Stoney Formulation *142*
7.2.2 Interferometric analysis *146*
7.2.2.1 Curvature determination and measurement 147
7.2.2.2 Thermal compensation stage construction 151
7.3 THICKNESS DETERMINATION 153
7.3.1 Tolansky technique - Fizeau fringes *153*
7.4 ELECTRICAL CHARACTERISTICS 155
7.4.1 Sheet Resistance *155*
7.5 AUGER ELECTRON SPECTROSCOPY (AES) ANALYSIS 157

7.1 Optical constant assessment

In the current age of increasing demands on the performance, efficiency and technological advancement of novel multilayer materials, precise control and determination of the optical constants of the individual materials is essential. The following section details the techniques used throughout this work for optical constant assessment.

7.1.1 Ellipsometry

Many techniques are available for the determination of the optical constants of a transparent thin film. However, the measurement and analysis of refractive index and deposition rate were mainly determined using ellipsometry.

Ellipsometry is a highly accurate superficial technique, able not only to determine the optical constants of a clean surface quickly and with high precision, but also to measure quantitatively the growth of surface films. The widespread use of ellipsometry dates back to 1963[1] and now accuracies of up to 0.07 Å have been reported [2]. Major advantages of ellipsometry over other methods of measuring thickness include;

- Measurement of film thickness of an order of magnitude smaller than can be measured by other means.
- Determination of the index of refraction of thin films of unknown thickness. Neither interferometry nor reflectrometry permit this determination.
- Special conditions, such as vacuum, heat, and electron bombardment are not required, but ellipsometry permits measurements under such conditions, if desired.

The analysis is dependent upon the incident, elliptically polarised light having its state of polarisation altered on reflection at the sample's surface. This state of polarisation is

determined by the relative amplitude of the parallel and perpendicular components of radiation, and the phase difference between the two components. These ratios undergo changes on reflection from the sample surface, which depend on the optical constants of the film and substrate, n_f, k_f and n_s, k_f, respectively, the angle of incidence, θ_I, and the film thickness, τ_f.

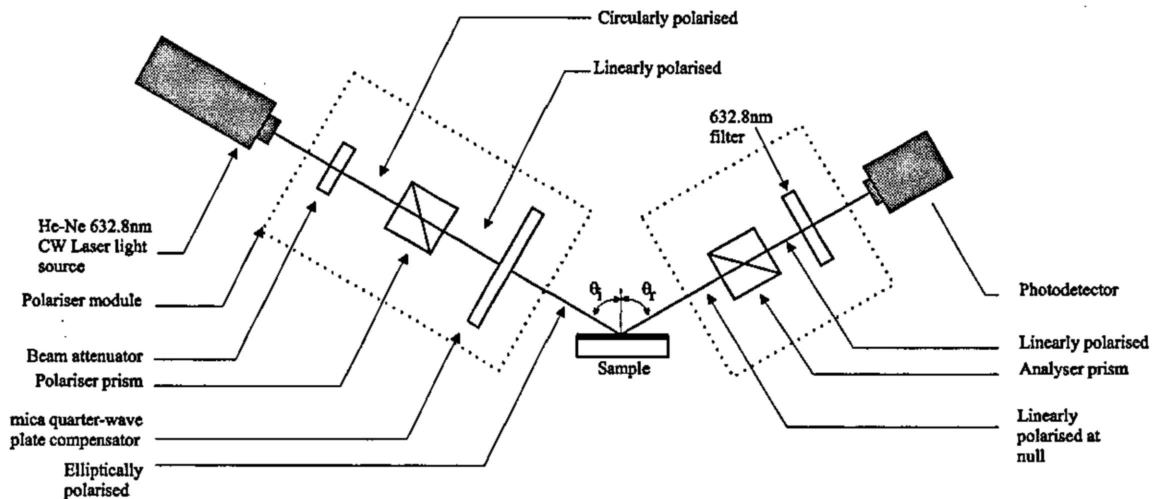

Figure 7.1 : AutoELR - II Automatic Ellipsometer

The samples to be analysed were mounted on the adjustable table, part of the AutoELR - II Automatic Ellipsometer, as shown in figure 7.1. The plane polarised monochromatic radiation (A HeNe laser (λ = 632.8 nm)) is then incident on the sample. The deposited film on the substrate modifies this polarisation state and the reflected radiation is elliptically polarised, with characteristics dependent on the optical parameters of the film. The ellipsometer automatically rotates the polariser and analyser, eventually obtaining zero intensity at the photodiode. The resulting angles of the polariser and analyser were entered into a specifically designed computer program which calculated the film's refractive index, n_f, and thickness, τ, given the optical constants of the substrate.

7.1.2 Transmittance and reflectance

The optical properties of any thin film material designed for specific practical applications are closely related to, and not independent of, electrical performance. There

is little benefit to be had in attaining an ability to deposit highly conducting thin films for use in photovoltaic application, if the associated optical transmittance cannot be similarly predicted, and repeated. For the full characterisation of film performance, it is essential that optical data is obtained over the desired wavelength range for each stoichiometry variation in order to identify the best compromise between factors competing for high figures of merit.

Optical transmittance and reflectance, as defined above, were consistently obtained throughout the work using a Hitachi U-2000 double beam scanning spectrophotometer, programmed to scan between 400 nm and 800 nm; the visible spectrum. Wavelength data was collected every 1 nm, with a scan speed of 100 nm/minute.

A choice has to be made between measuring the transmittance of the films with respect to an uncoated substrate, or with respect to air. The latter is considered to be of use since it yields data for the film + substrate combination rather than the film alone. In practical situations, such as transparent dielectric coatings on nominally transparent substrates, which are used as aircraft canopy laminates, it is of far greater importance to quantify the overall transmittance of the completed device than to know the transmittance of the thin film. However, for the fundamental research performed in this work, the optical properties of the film alone were considered to be of greater importance for inter-comparative film assessment. Hence, all transmittance data was measured with reference to an uncoated substrate of the same material as that onto which films were deposited.

Figure 7.2 shows the optical system of the U-2000 spectrophotometer configured for use in both transmittance and reflectance mode. The tungsten iodine lamp emits visible radiation, 300 nm - 1100 nm, and the deuterium discharge lamp emits UV radiation, 190 nm - 300 nm. The radiation emitted from the light source is directed to the Seya-Namioka mount monochromator, utilising a concave diffraction grating, with a grading constant of 1/600 mm, a blaze wavelength of 250 nm, and grating area of 20 mm x 25 mm, where it is transformed into a monochromatic beam. The beam emerging from the monochromator passes through the filter, F, is reflected by the toroidal mirror, M2, and is then separated into reference beam and sample beam by the half mirror, HM.

The two beams which have passed through the sample compartment are focused by lenses, and are then irradiated into the detectors, D1 and D2, where they are converted into electrical signals and are subsequently processed by the control system.

The spectrophotometer has a spectral bandpass of 2 nm with a wavelength accuracy of ± 0.4 nm.

Since most of the films in this work were deposited onto glass microscope slides, a piece of such material was used to establish a calibration baseline for the subsequent measurements. Using this calibration technique, the transmittance of a glass slide was automatically used to normalise the spectrophotometer.

7.2 Mechanical properties : Intrinsic stress

It was thought essential to examine the mechanical properties of thin films, not only as part of a comprehensive analysis into the film's quality, reliability and performance, but as a direct measure of the effects of substrate ion bombardment. Therefore, determination of the magnitude and state of the total stress in the deposited film was performed.

The following section outlines the method used for stress assessment and details the relevant practical and theoretical aspects involved.

7.2.1 The Stoney Formulation

When a thin film is deposited onto a thin substrate, *i.e.* less than 100 μm, then the film substrate combination will bow to a detectable amount, indicative of the residual stresses in the thin film. Measurement of this bowing can be used to determine the stress, as will be shown in the following sections.

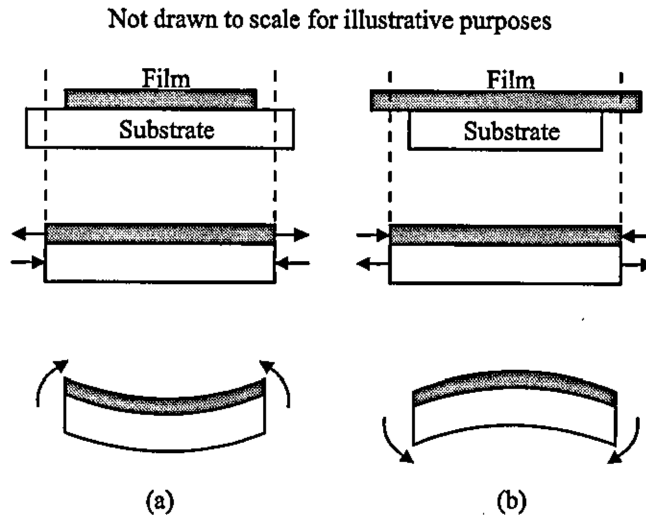

Figure 7.3 : Events leading to (a) tensile stress in the film; (b) compressive stress in the film

Figure 7.3 illustrates the effects of tensile stress and compressive stress. In tensile stress the film initially shrinks relative to the substrate for reasons explained in chapter 5, section 5.5. However, compatibility requires that the film and substrate have the same length and the constrained film stretches the substrate accordingly. This mechanical equilibrium states that the net force, F, and bending moment, M, are equal to zero across the film-substrate section. Hence

$$F = \int \sigma dA = 0 \qquad [7.2]$$

$$M = \int \sigma x dA = 0 \qquad [7.3]$$

where A is the section area and x is the moment lever arm. However, the combination is still not in mechanical equilibrium owing to uncompensated end moments. Thus, the internal stresses bend the substrate combination concavely upwards to preserve mechanical equilibrium.

The Stoney formulation, first presented in 1909 [3], relates the radius of curvature of the substrate-film combination to the internal stresses in the film, and is used in virtually all experimental determinations of the film stress.

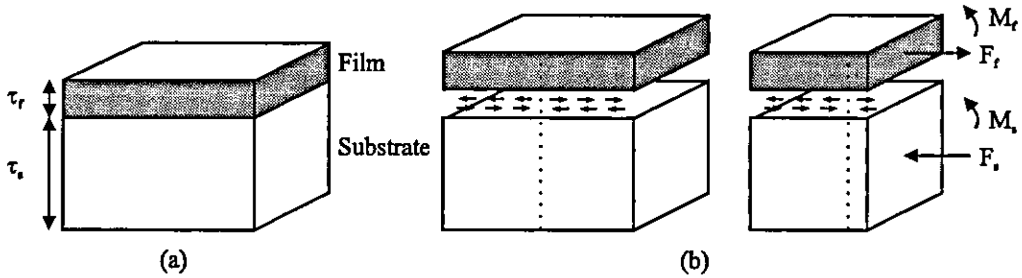

Figure 7.4 : Stress analysis of film substrate combination (a) composite structure (b) free-body diagrams showing interfacial forces and end moments [4]

Figure 7.4 [4] illustrates the mechanics of the stresses occurring at the film-substrate combination boundary where τ_s and E_s are the substrate thickness and Young's modulus respectively. Similarly τ_f and E_f represent the film thickness and Young's modulus respectively. As shown in the free-body diagrams of figure 7.4b, each set of interfacial forces can be replaced by a static force and moment combination

where

$$F_f = F_s. \tag{7.4}$$

Force, F_f, can be imagined to act uniformly over the film cross-section (τ_f W), giving rise to the film stress. The clockwise and counterclockwise moments responsible for the substrate bowing, therefore, require equilibrium as expressed in equation 7.4. Thus

$$\frac{\tau_f + \tau_s}{2} F_f = M_f + M_s. \tag{7.5}$$

Now, consider an isolated beam, bent by moment M, as shown in figure 7.5 [4]. The stress distribution consists entirely of the extension or contraction of longitudinal beam fibres by an amount proportional to their distance from the neutral axis, and varies linearly across the section from maximum tension, $+\sigma_{max}$, to maximum compression, $-\sigma_{max}$.

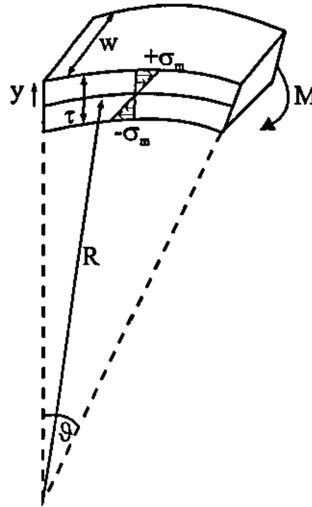

Figure 7.5 : Elastic bending of beam under applied end moment [4]

Hooke's law can now be applied in terms of the beam radius of curvature, R, and the angle ϑ subtended,

$$\sigma_{\max} = E_{beam}\left(\frac{\left(R \pm \frac{\tau}{2}\right)\vartheta - R\vartheta}{R\vartheta}\right) = \pm\frac{E_{beam}\tau}{2R}. \qquad [7.6]$$

The bending moment across the beam section corresponding to this stress distribution is

$$M_{beam} = 2\int_{0}^{\tau/2} \sigma_{\max} W\left(\frac{x}{\tau/2}\right)x dx = \frac{\sigma_{\max}\tau^{2}W}{6} = \frac{E_{beam}\tau^{3}W}{12R}. \qquad [7.7]$$

Using this result for the film-substrate combination yields

$$M_{f} = \frac{E_{f}\tau_{f}^{3}W}{12R}, \qquad [7.8]$$

$$M_{s} = \frac{E_{s}\tau_{s}^{3}W}{12R}. \qquad [7.9]$$

Substitution of these terms into equation 7.5 gives

$$\left(\frac{\tau_f + \tau_s}{2}\right)F_f = \frac{W}{12R}\left(E_f\tau_f^3 + E_s\tau_s^3\right). \qquad [7.10]$$

In addition, compensation must be made for conditions of biaxial stress. Hence, it is necessary to replace E_f by $E_f/(1-\nu_f)$ and similarly for E_s where ν is Poisson's ratio. $\tau_s >> \tau_f$, and substitution of these terms into equation 7.10 yields the force per unit width, S

$$S = \frac{F_f}{W} = \frac{1}{6R}\frac{E_s\tau_s^2}{(1-\nu_s)}. \qquad [7.11]$$

The average stress in the film is then the force per unit width divided by the film thickness, τ_f

$$\sigma_f = \frac{1}{6R}\frac{E_s\tau_s^2}{(1-\nu_s)\tau_f}. \qquad [7.12]$$

Equation 7.12 is the Stoney formula.

7.2.2 Interferometric analysis

Various methods can be employed to determine the amount of bowing in a substrate-film combination, and a comprehensive explanation of all these techniques can be found in a review by Campbell [5]. Accurate measurements of the surface curvature are most commonly made by cantilevered beam, laser, X-ray, and interferometric methods. It is the technique of interferometry that was used throughout this work in determining substrate-film radius of curvature.

This is not to say that the other techniques do not have their merits. The scanning laser reflection method [6] can be easily used to measure stress *in situ*, and thus, can

continually give results on the substrate curvature as the film grows. Furthermore, X-ray measurements [7] can be used to detect the bending of the lattice planes, and diffraction measurements can be used to measure the strain in the film directly by determination of the lattice parameters. The main advantage of this technique is that the strain profile can be obtained through the thickness of the film by analysis of the X-ray line shapes [8,9].

7.2.2.1 Curvature determination and measurement

As shown in section 7.2.1, if films are deposited on substrates thin enough, then the substrate-film combination will bow by an amount related to the intrinsic and thermal stresses in the film, as shown quantitatively by Stoney's formulation.

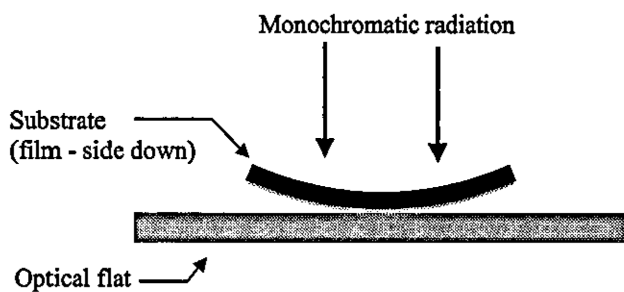

Figure 7.6 : Creation of Newton's rings

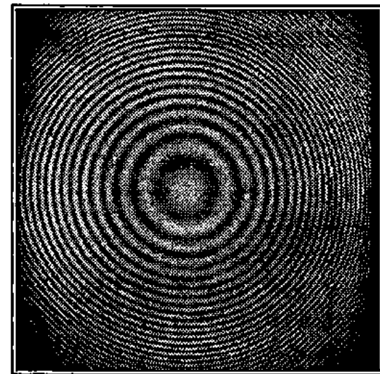

Plate 7.1 : Resulant interference fringes formed

When the bowed substrate is placed on an optically flat surface, figure 7.6, and monochromatic radiation is directed perpendicular to the interface created, a series of interference fringes are formed, plate 7.1. This resulting interference is caused by reflected light at the two faces enclosing the air boundary, and the fringes are localised in the air wedge.

If the two surfaces are in near contact, the central region, at which the path difference $\Rightarrow$ 0 appears dark•. The geometry of these rings can be calculated by reference to figure 7.7.

• It should be noted that a central bright region does not occur as one might have expected because there is a phase change on reflection as Thomas Young pointed out at the beginning of the nineteenth century.

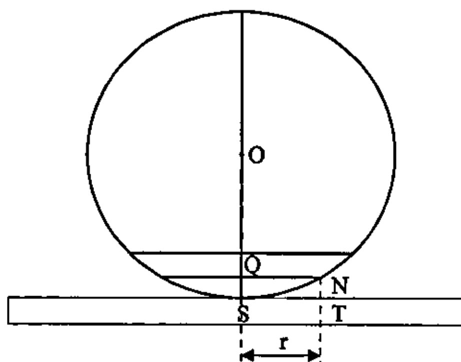

Figure 7.7 : Illustration used in calculation of Newton's ring and radius of curvature

Let distance $NT = t$. [7.13]

On moving out from the point of contact, S, T is the nth dark ring such that the path difference

$$2t = n\lambda \quad [7.14]$$

but NT=QS, and if the radius of the nth ring, ST, is called r, then

$$r^2 = t(2R - t). \quad [7.15]$$

However, QS<<R

$$\therefore r^2 = 2tR = nR\lambda \quad [7.16]$$

and hence,

$$r = \sqrt{n}\sqrt{R\lambda}. \quad [7.17]$$

It is now obvious from this equation that the radii of the rings are proportional to the roots of the natural sequence of numbers. However, it should be noted that the equation only holds for a special case when the incident angle of radiation, $\theta = 90^{\circ}$. If the monochromatic light is not normal to the sample interface then the interference rings will

become elliptical. These ellipses are not to be confused with ones obtained with anisotropic stress.

From equation 7.17, the radius of the curvature of the substrate was calculated. This calculation was implemented by inputting data, obtained from a CCD camera and computer system as described in the next section, into a computer program specifically designed for this work.

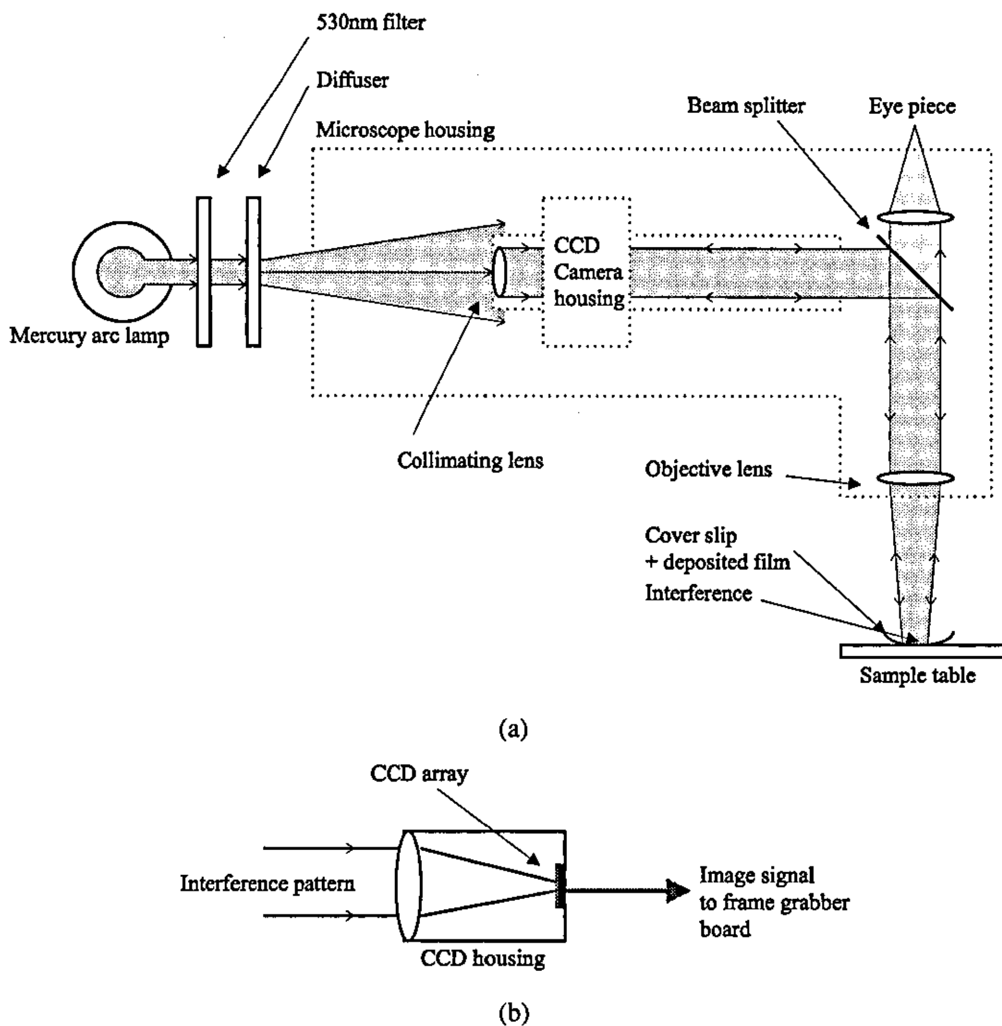

Figure 7.8 : Apparatus used in interferometric analysis (a) Microscope (b) CCD housing

The films were deposited onto quality cover slip substrates, selected for their initial flatness, and the thickness of the cover slips was measured, before every deposition, using a micrometer. After coating, the substrate was mounted onto an optically flat thermal compensation stage, the details of which are given in the next section. The stage was clamped to an aluminium base via insulating blocks and the whole assembly placed

onto a M41 Vickers photoplan microscope metallurgical stage to enable accurate focusing. The microscope was operated in reflection mode to enable interference patterns to be observed during analysis of both highly reflective opaque films and transparent optical films. Substrate-film illumination was provided by a high power mercury arc lamp, through a filter, to provide pseudo-monochromatic light from the 546 nm line of the mercury vapour discharge, and through a diffuser for homogeneous sample illumination. The reflected interference pattern obtained from the sample and optical flat combination was focused via a x25 objective into a CCD camera as shown in figure 7.8a and b.

Figure 7.9 shows a comparison between substrate thickness and induced stress. The largest measurable radius of curvature was found to be 1.5 m. Curvatures larger than this were difficult to measure as too few fringes could be detected. Examination of the graph demonstrates that when using the thinnest available substrates, of 80 μm, stress values down to ~100 Nm^{-1} could be measured with the desired accuracy of ~5%. Thinner substrates were investigated, however, these were not able to give meaningful results because they interacted electrostatically with the optical flat.

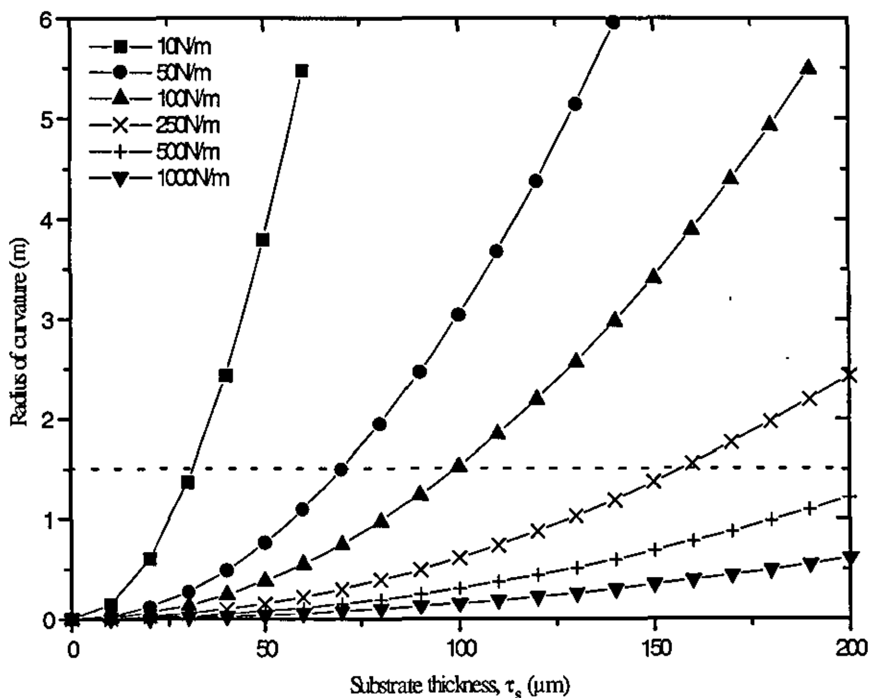

Figure 7.9 : Variation of substrate curvature with thickness for varying induced stress

7.2.2.2 Thermal compensation stage construction

As explained in chapter 5, section 5.5, the stress in a thin film deposited by any CVD or PVD technique comprises two components. That owing to intrinsic stress and that owing to thermal stress. The intrinsic stress gives an indication as to film structure, durability and general effects of ion bombardment, whereas thermal stress reflects the thermal coefficients of the deposited film. Although investigation into thermal stress is of great interest, unknown material properties, such as Young's modulus, E_f and thermal expansion coefficient, α_f, for a deposited film make it difficult to characterise this quantitatively. Moreover, these properties vary greatly from the bulk values and are functions of deposition conditions such as ion bombardment. It was, therefore, decided to concentrate on characterisation of intrinsic stress by eliminating the thermal component at the measurement stage.

When the coatings are made at elevated deposition temperatures, they only possess intrinsic stress owing to their inherent internal structure. It is only when they are cooled that the thermal mismatch between film and substrate creates the extra stress component. Hence, it was decided that if the substrate-film composite could be heated to the deposition temperature during stress analysis, thermal stresses at the boundary could be suppressed and a direct measurement of intrinsic stress performed. A thermal compensation stage was designed and constructed for this purpose and is detailed in the following section.

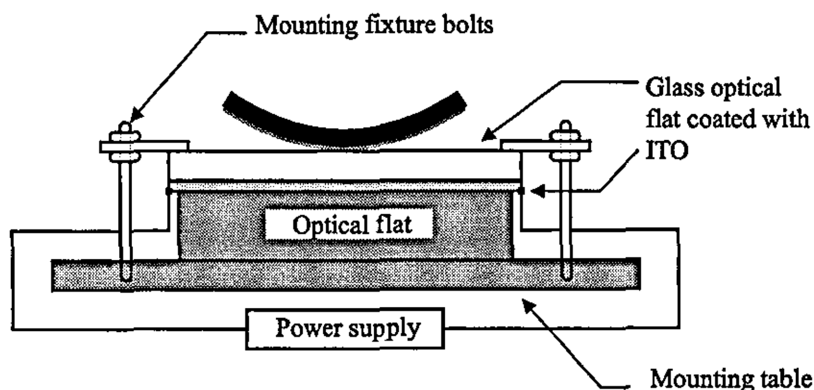

Figure 7.10 : Thermal platten used in stress measurement

The stage, illustrated in figure 7.10, was an in-house design made up of a glass optical flat, coated on the underside with a transparent conducting film of indium tin oxide (ITO), with a sheet resistance of 400 $\Omega\square^{-1}$. Copper strips of approximately 100 nm were deposited onto the ITO to provide a means of electrical contact to which a voltage could be applied.

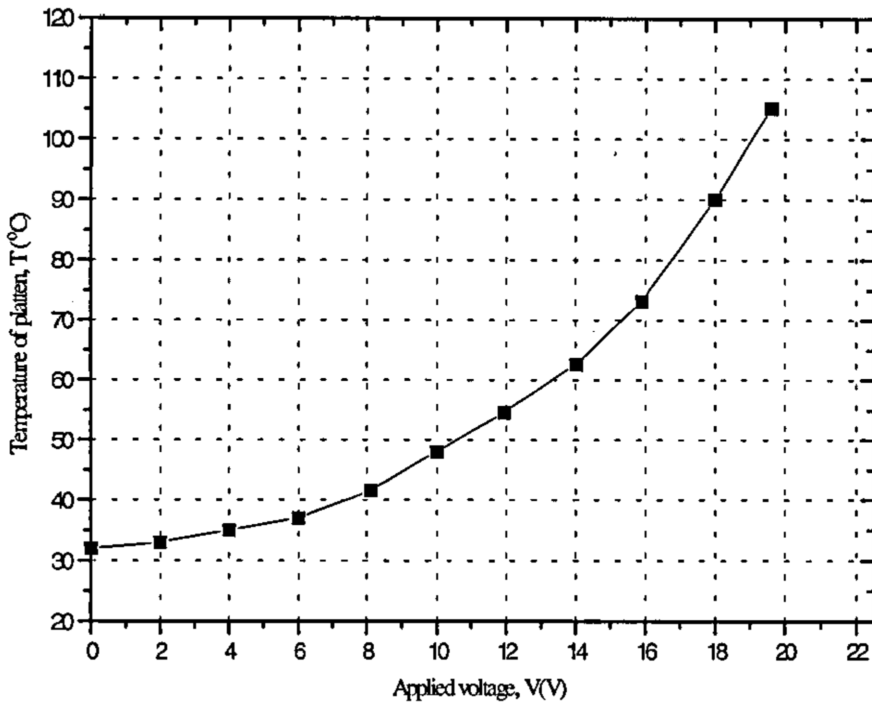

Figure 7.11 : Variation in temperature of the ITO/COPPER Thermal platten with applied voltage

Calibration of the stage was performed by using a commercially calibrated platinum resistance element [10] attached to the optical flat. Voltage was applied to the two electrical contacts by a Philips PE1649, 150 V, supply and the temperature measured when an equilibrium state was achieved. Figure 7.11 shows the calibration data. Accurate temperature control was now possible and the thermal component could be irradicated from the stress configuration. It should be noted, however, that a small error owing to thermal cycling is introduced into the stress calculation, but this is insignificant compared with the large component owing to thermal mismatch.

7.3 Thickness determination

In addition to the ellipsometric techniques for determination of film thickness, as described in section 7.1.1, optical interference techniques were also used as a continuous check on measurements made.

7.3.1 Tolansky technique - Fizeau fringes

The Tolansky technique is based on a phenomena known as Fizeau fringes. These fringes are generated by monochromatic light and represent contours of equal thickness arising in an area of varying thickness.

If two glass plates are placed in contact so that they form a slight wedge, at an angle, α, then consecutive fringes are produced. The smaller, α, then the further apart the fringes appear. The fringes can be considered as height contour lines, exactly as on a geographical contour map. It thus follows that if either of the two surfaces are irregular, then the fringes will contour the irregularity, each following a path of constant optical thickness in the air film.

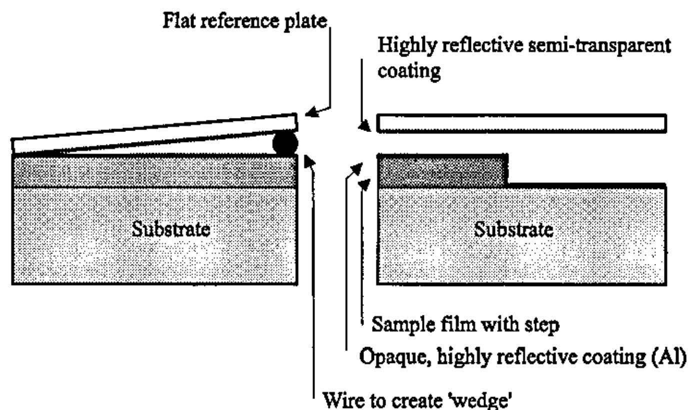

Figure 7.12 : Film thickness measurement by Tolansky interference technique

Figure 7.12 shows how this technique was used to measure the thickness of a film. A channel in the film was formed during deposition by the use of a mask specifically designed for the purpose. Following this, a thin, ~10 nm, highly reflecting opaque film

of aluminium was sputtered onto the coating. A semi-transparent optical flat was then placed over the film/channel in a wedge arrangement and the configuration located in the microscope used for stress determination. By identical means of monochromatic illumination, interference fringes were obtained and appear as shown in plate 7.2, where each fringe represents a contour of equal thickness.

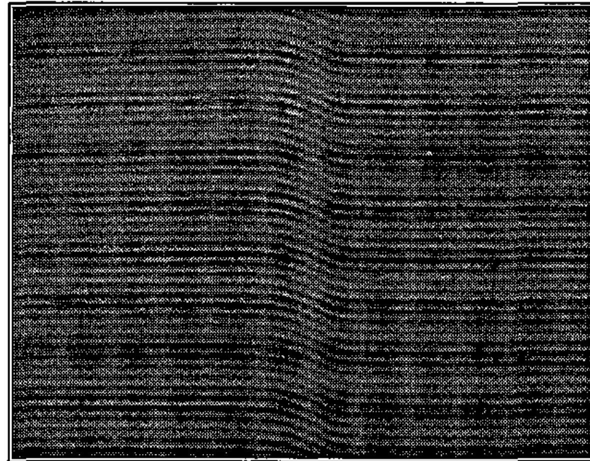

Plate 7.2 : Interference fringes formed during thickness analysis using Tolansky technique

Sometimes fringe connectivity was not obtained, usually arising from an abrupt step, figure 7.13. However, equation 7.18 could be used to determine the film thickness, τ_f.

$$\tau_f = \frac{n\lambda}{2} \pm \frac{\lambda}{2}\frac{a}{b} \qquad [7.18]$$

where n is the order of the fringe and λ the wavelength of the monochromatic light.

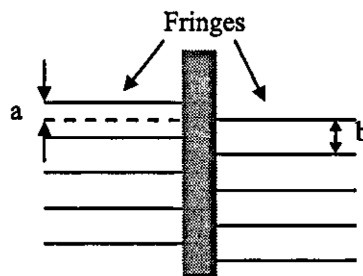

Figure 7.13 : Calculation of step thickness when no fringe connectivity was seen

7.4 Electrical characteristics

Electrical characteristics, such as resistivity of conducting oxides, tend to have a strong correlation with the film stoichiometry. It is, therefore, possible to use this technique as a simple and efficient way to pinpoint the formation of a specific stoichiometry.

7.4.1 Sheet Resistance

Figure 7.14 shows a rectangular section of deposited film. It can be seen that the resistance of this film in a direction parallel to the substrate is given by

$$R = \frac{\rho L}{W\tau_f}. \qquad [7.19]$$

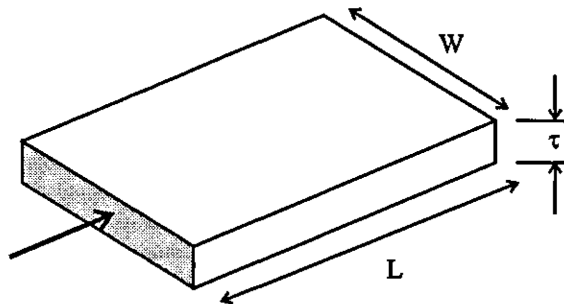

Figure 7.14 : Rectangular section of deposited film

The sheet resistance, R_s, is defined as the resistance of one square of the film. Hence, if W=L then

$$R = \frac{\rho}{\tau_f} = R_s. \qquad [7.20]$$

Hence, the resistivity of the film can be found, knowing the sheet resistance and thickness.

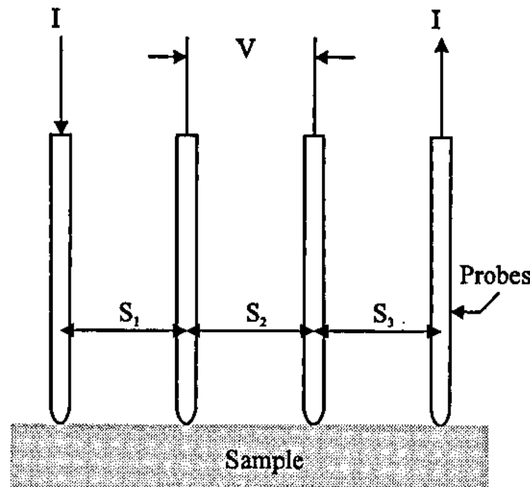

Figure 7.15 : Four point probe used to measure film sheet resistance

In order to determine whether the resistivity of the film was uniform across its surface an in-line four point probe was specifically designed as shown in figure 7.15. Valdes [11] examined this configuration in detail and showed that when the probes are placed on a material of semi-infinite volume, the resistivity is given by

$$\rho = \frac{V}{I} \frac{2\pi}{\frac{1}{s_1} + \frac{1}{s_2} - \frac{1}{(s_1 + s_2)} - \frac{1}{(s_2 + s_3)}} \qquad [7.21]$$

and can be reduced to

$$\rho = \frac{V\pi}{I \ln 2} \qquad [7.22]$$

when $s_1=s_2=s_3=s$ and the material on which the probes are placed is an infinitely thin slice resting on an insulating support.

$$\therefore R_s = 4.532 \frac{V}{I}. \qquad [7.23]$$

However, in reality, the probe spacings s_1, s_2, and s_3 were not equal and this introduced a systematic error of ~8%. Furthermore, significant edge effects are introduced into the measurement when sheet resistance readings are taken close to the boundary of the film.

The four point probe used in this work was constructed from a PVC body, in which four spring-loaded precision pins, 15 mm long, 1.7 mm in diameter, were mounted, and the intra pin spacing was 2.5 mm at the needle tips. The needle tips were rounded, rather than sharp to reduce film penetration and the creation of surface voids. A Schlumberger/Solartron Limited 'Datastore microprocessor Voltmeter' was connected to the device and enabled quick turnaround of sheet resistance through a specifically designed program. The program measured the resistance by supplying a potential difference to the two inner pins, and dividing this by the current flowing between the outer pins. The meter was auto-ranging, and was sensitive to 1 μV.

7.5 Auger electron spectroscopy (AES) analysis

AES was only briefly used in the work during the deposition of ZnO:Al and only the basics of the technique are introduced here. High sensitivity, rapid acquisition speed, composition depth profiling and the ability to detect all elements from lithium to uranium are the advantages of the technique. The technique has now emerged as one of the most widely used analytical techniques for obtaining the composition of solid surfaces.

Pierre Auger [12] discovered the Auger effect in 1925 while working with X-rays. The technique of using electron excited Auger electrons to identify surface impurities was suggested by Lander [13] in 1953, but the high sensitivity of the technique was not realised until 1968, when Harris [14] demonstrated Auger spectra in their present form.

Simplistically, the Auger process is understood by considering the ionisation of an isolated atom under electron bombardment. When an incident electron with sufficient primary energy, E_p, ionises a core level, the vacancy is immediately filled by another electron from, for example, level L1. The energy from this transition can either be released in the form of characteristic X-rays, or be transferred to another electron, in the L2 level, for example. This is ejected from the surface as an Auger electron. The Auger electron energies are characteristic of the target material and independent of the incident beam energy.

The apparatus used was a Varian 10 kV Auger electron spectrometer [15]. Normal operating conditions were ~1.1 μA, 3×10^3 eV primary beam energy in a 100 μm diameter spot. Argon was used in a static back-filled ion gun having a current density of 7.5×10^{-5} Acm^{-2}, and the base pressure of the system was 5×10^{-9} torr.

CHAPTER 7 REFERENCES

[1] **Passaglia, E., Stromberg, R. & Kruger, J.** (1964)., *NBS Misc. Publ.* 256.

[2] **Archer, R.J.**, (1964). *National Bureau of Standards Misc. Publications,* 256, 255.

[3] **Stoney, G.G.**, (1909). *Proc. Roy. Soc. London,* A82, 172.

[4] **Basset, G.A., Menter, J. W.**, (1977) *'Structure and properties of thin films'* Academic Press, 76

[5] **Campbell, D.S.**, (1970). *'Handbook of thin film technology'*, Maissel, L.I., Glang, R., McGraw-Hill, New York, 12.

[6] **Meng, W.J., Sell, J.A., Eesley, G.L. & Perry, T.A.**, (1993). *J. Appl. Phys.*, 74(4), 2411-2414.

[7] **Berry, W.S.**, (1983), Adv. *X-Ray Anal.*, 26,255

[8] **Borie, B., Sparcks, C.J., & Cathcart, J.V.**, (1962) *Acta Metall.*, 10, 691

[9] **Houska, C.R.**, (1970), *J.Appl. Phys.*, 41, 69.

[10] **Radio Spares**, RS data sheet number 003-914 March 1987.

[11] **Valdes, L.B.**, (1954). *Proc. Ire,* 42, 420.

[12] **Auger, P.**, (1925). *J. Phys. Radium,* 6, 205.

[13] **Lander, J.J.**, (1953). *Phys. Rev.*, 91, 1382.

[14] **Harris, L.A.**, (1968). *J. Appl. Phys.*, 39, 1419.

[15] **Critchlow, G.**, (1991). *'Personal Communication'*, Surface Analysis Group, Loughborough Consultants Ltd.

CHAPTER 8

RESULTS I : PRELIMINARY WORK

The following chapter introduces the preliminary results obtained during this work. To ensure that the stress technique developed obtained meaningful and consistent results, materials of known mechanical behaviour were initially tested. Whilst it is recognised that the pressure transition work for chromium is well documented [1], it is repeated here for completeness. This chapter also describes the calibration of the electron collecting anode used throughout the work for accurate control of ion bombardment. Furthermore, stress measurements obtained for titanium are presented when varying the ion bombardment at the substrate by two different processes.

8.1 CHROMIUM (CR) 160
8.2 TITANIUM (TI) 161
8.2.1 Langmuir probe measurements *161*
8.2.1.1 Argon partial pressure, Ar_{pp} 162
8.2.1.2 Anode 163
8.2.2 Stress *164*
8.2.2.1 Argon partial pressure 164
8.2.2.2 Anode 165
8.3 CHAPTER SUMMARY 166

8.1 Chromium (Cr)

The brief work undertaken on chromium was carried out at the beginning of the research period and only the stress was measured. The transition curve obtained, however, merits a description as it represents many of the stress mechanisms that occur in a thin film.

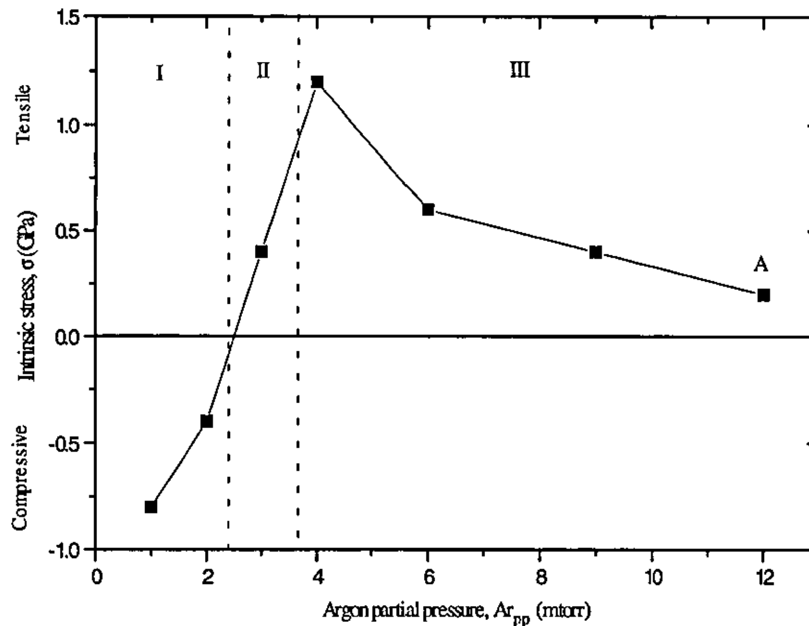

Figure 8.1 : Dependence of intrinsic stress as a function of sputtering pressure for Cr

Figure 8.1 illustrates the stress-Ar_{pp} curve for Cr and represents the behaviour characteristic of the majority of metals. Region I represents a high compressive stress-saturation regime at very low pressures, and thus, high bombardment. This region is followed by an abrupt transition from tension to compression, illustrated in region II. Region III represents a decrease in tensile stress with increasing pressure. This region is a result of reduced re-sputtering of oxygen based contaminants (which tend to produce compressive stress) and the formation of pores occurring simultaneously.

When the gas pressure is increased within the sputtering chamber, an increase is observed in the scattering of particles, illustrated in plate 6.3. This scattering affects the growing film in two equally important, but significantly different ways. Most obviously, the average energy of the arriving particles (sputtered atoms, reflected neutrals, electrons,

and ions) is reduced owing to elastic and inelastic collisions. Added to this, however, the angular distribution of the sputtered atoms is more uniform owing to an increase in the oblique component of the depositing material through enhanced scattering. These conditions promote a porous, columnar type structure of the film, increasing tensile stress. At point A on figure 8.1, approximately zero stress was observed in the Cr film. This is because the microstructure is unable to sustain lateral forces caused by decoupling of neighbouring grains or columns.

When the pressure was decreased, the scattering was reduced, thereby increasing both the normal flux component and the particle energy striking the film. Both these factors promote a more densely packed structure, suppressing the development of columnar growth, as explained in section 5.3.2. When the pressure was further reduced, evolution of a denser microstructure most probably occurs as the probability of atomic displacement of surface atoms into the film interior by forward sputtering increases. This densification was accompanied by a stress transition from tensile to compressive, as the compressive stress generated by the atomic peening mechanism compensates the reducing tensile stress

8.2 Titanium (Ti)

TiO_2 was the first oxide to be deposited in the research. It was decided to investigate the techniques of controlling ion bombardment whist depositing Ti metal. This enabled the anode to be characterised and developed, with initial problems irradicated, without any additional factors such as the reactive gas complicating matters. Titanium films were deposited using a power of 500 W, and each sample was deposited for 10 minutes.

8.2.1 Langmuir probe measurements

The following section details the variation in ion bombardment at the substrate. Two processes were used to impart this modification in ion current, variation in argon partial pressure and variation in the resistance of the anode to ground. This dual technique of

ion bombardment modification was used throughout this work and in this section the I/V characteristics of the Langmuir probe are examined.

8.2.1.1 Argon partial pressure, Ar_{pp}

The Ar_{pp} was varied from 1 mtorr through to 11 mtorr, the higher pressures (>7 mtorr) being obtained by throttling off the pumping aperture (to prevent the diffusion pump stalling owing to excessive pumping of the argon gas). Figure 8.2 illustrates the variation in ion current, I_{si}, and floating potential, V_f, with varying argon partial pressure. As the Ar_{pp} was reduced, the floating potential became more negative as the mean free path of the ions was increased. The ion saturation current was maximum at 2.5 mtorr. This can be explained in terms of the volume density of the gas, the excitation energy of the electrons, and the mean free path of the electrons. As the pressure rises, the volume density goes up, but the energy of the exciting electron goes down because of the reduction of the mean free path. Hence, the ion current will peak at a certain Ar_{pp}, 2.5 mtorr in this case.

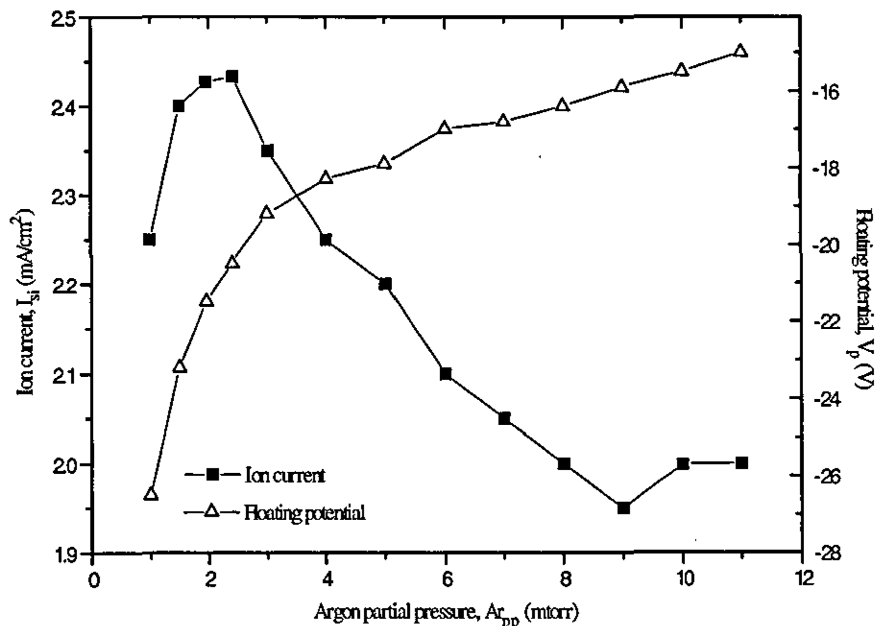

Figure 8.2 : Variation in ion current at the substrate and floating potential of the substrate as a function of argon partial pressure for Ti

8.2.1.2 Anode

The second technique of altering the ion bombardment at the substrate involved using the electron collecting anode, as described in chapter 6. All measurements were made at a partial pressure of 2.5 mtorr of argon, a value coinciding with the approximate ion current maximum obtained when varying the Ar_{pp}. Figure 8.3 shows the variation in ion current, I_{si}, at the substrate when increasing the resistance of the potentiometer. From this curve, the desired value of ion bombardment at the substrate can be obtained by simply altering the resistance of the potentiometer.

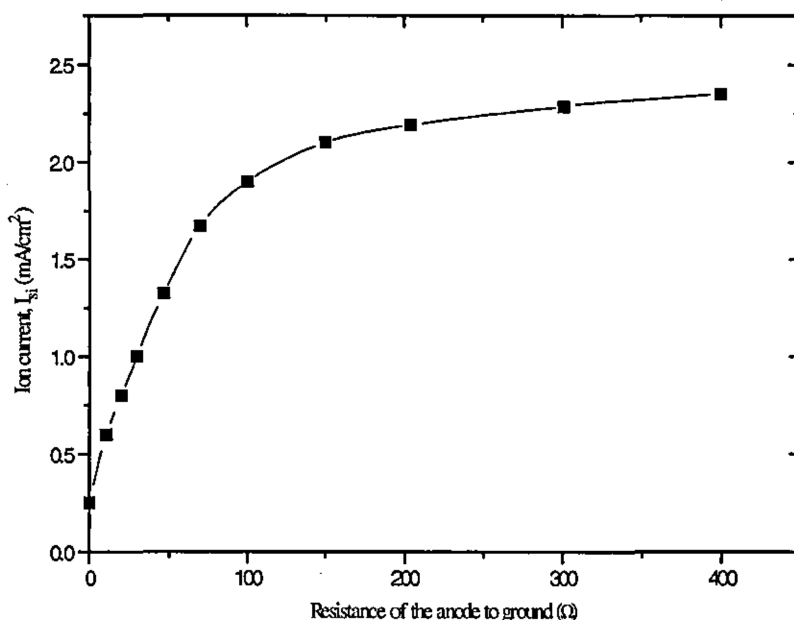

Figure 8.3 : Variation of ion current at the substrate as a function of resistance of the anode to ground for Ti

The floating potential remained constant to within ±0.2 V when varying the ion bombardment using the electron collecting anode. This is because the mean free path of ions is unaltered, and hence, the energy with which they bombard the substrate is unaltered.

8.2.2 Stress

A comparison was made between the stress imparted by changes in argon partial pressure and that owing to variation in the ion bombardment, without changing the mean free path of the ions (*i.e.* by use of the anode).

8.2.2.1 Argon partial pressure, Ar_{pp}

Figure 8.4 shows the effect of argon partial pressure on the deposition rate of the titanium films.

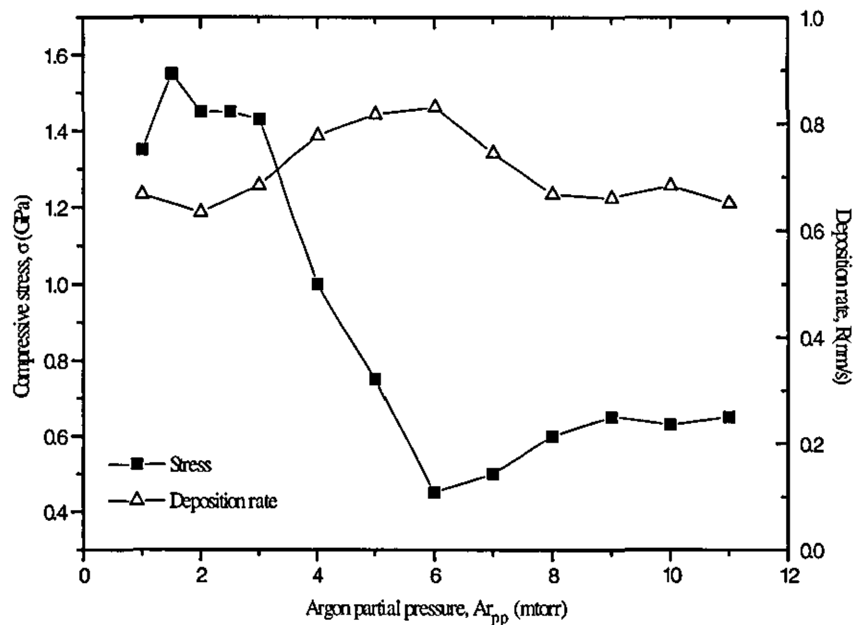

Figure 8.4 : Variation of intrinsic stress and deposition rate as a function of argon partial pressure for Ti

Figure 8.4 also shows intrinsic stress measurements made on films formed at different argon pressures. A significant feature of the stress within the titanium films is that it appears to be dependent on the amount of ion bombardment at the substrate.

The stress in the Ti film did not undergo a transition from compressive to tensile. All the films made were in a state of compression. However, the stress did follow a very similar

pattern to that observed in Cr when varying the Ar_{pp}, and the regions still exist. The variation in stress can, thus, be explained by the same phenomena as explained in section 8.1.

8.2.2.2 Anode

Figure 8.5 shows the variation in intrinsic stress within the film when varying ion bombardment. The results are as expected, and the compressive stresses within the film increased with increasing I_{si}. These results confirm those made by varying the Ar_{pp} in that the stress is dependent on I_{si}.

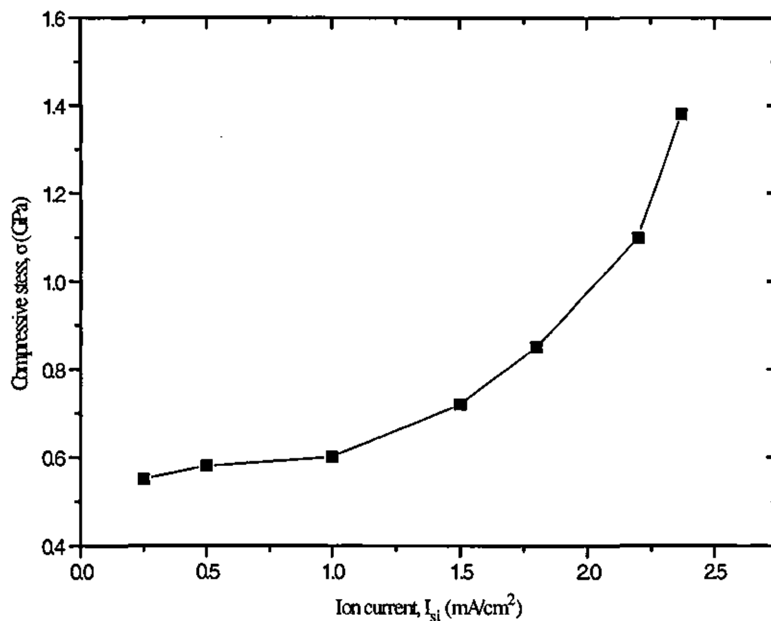

Figure 8.5 : Variation of intrinsic stress as a function of resistance of the anode to ground for Ti

The deposition rate varied from 0.69 nms^{-1} when the anode was floating (*i.e.* I_{si} = 2.38 $mAcm^{-2}$) to 1.06 nms^{-1} when the anode was grounded (*i.e.* I_{si} = 0.25 $mAcm^{-2}$) . It is interesting to note that the high deposition rate occurs at lower bombardment. This phenomena can be explained in that the lower bombardment has associated lower intrinsic stress within the film, which suggests that the film is porous. A porous film would have a higher volume than a densely packed film, and hence, a higher apparent

deposition rate. (*N.B.* in fact, the rate of arrival of target species reaching the film is probably similar in both cases.)

8.3 Chapter summary

- Sputtered films of Cr under varying Ar_{pp} showed a stress transition from tension to compression with decreasing Ar_{pp}.
- It has been shown that the ion bombardment can be accurately altered by variation of the resistance of the electron collecting anode to ground.
- Variation in argon partial pressure also achieved ion current variation, but was not as versatile as the anode and was limited to ion currents between 2.5mAcm^{-2} and 1.9mAcm^{-2} for Ti. Furthermore, varying the Ar_{pp} significantly affects the mean free path of the species bombarding the substrate.
- Stress has been shown to be strongly dependent on ion bombardment.

CHAPTER 8 REFERENCES

[1] **Hoffman, D.W.**, (1977) *Thin Solid Films*, 40, 355.

CHAPTER 9

RESULTS II : FEEDBACK CONTROL : A NEW APPROACH

The technical details of how the feedback control techniques were constructed from both an electronic and process point of view were given in chapter 6. This chapter develops the understanding of these techniques and characterises their behaviour. When controlling the sputtering process in a reactive environment, a universal technique is sought that works for the majority of materials. The technique needs to be tolerant, easy to operate, versatile and repeatable. Conventional techniques, such as plasma emission monitoring using continuous control, achieve versatility, but suffer from other problems such as complicated initialisation procedures and additional expensive equipment. The novel techniques developed throughout this work are shown in this chapter to provide greater tolerance and usability while maintaining versatility.

9.1 THE CONTROL SIGNAL : VOLTAGE OR LIGHT EMISSION 168
9.2 THE CONTROL METHOD : CONTINUOUS OR PULSED 169
9.2.1 Continuous feedback control (CFC) *169*
9.2.1.1 Process instability to arcs 171
9.2.2 Successive Pulsed Plasma Anodisation (SPPA) *171*
9.2.2.1 The pulse waveform 172
9.2.2.2 Factors affecting the SPPA process 173
9.2.2.3 Initialisation routine 176
9.3 CHAPTER SUMMARY 178

9.1 The control signal : Voltage or light emission.

Before any feedback control technique can be developed, an input to the control system has to be determined and characterised.

The following section describes the advantages and disadvantages of magnetron voltage control and plasma emission monitoring observed in the course of this research. Although, in chapter 6, the technical details were given of how the indicators of target status were measured, the following text summarises, along with table 9.1, the observations made throughout this work. A more detailed analysis specific to each material deposited will be given in chapter 10.

Material	MVC	PEM
Al_2O_3	Yes	***Not analysed***
ITO	Yes ***a***	Yes ***c***
SiO_2	Yes	Yes
TiO_2	No ***b***	Yes
ZnO:Al	Yes ***a***	No ***c***

Table 9.1 : Observation made on measure of target status for materials sputtered during this work

a : Significant hysteresis, SPPA only.

b : Dual set-point on O_2 flow/set-point curve.

c : Need to analyse two or more emission lines because differential poisoning occurs.

SiO_2 controlled well with MVC using SPPA and CFC owing to the characteristic behaviour of its cathode voltage, exhibited with addition of oxygen. ITO could be controlled using both MVC and PEM, however, SPPA control was required when using the voltage as a target measure. When sputtering ZnO:Al from a metal alloy target, PEM was problematic because of the need to monitor emissions from both materials. Al_2O_3 was only sputtered using CFC whilst monitoring the cathode voltage, however, SPPA would be possible. Table 9.2 gives the advantages and disadvantages of both control indicators.

	MVC	PEM
Advantages	Easy to set up. Fast feedback. Requires no additional equipment. Direct measure of target status.	Works for most materials.
Disadvantages	Does not work with all materials (Dual set-point) [1]. Long term drift owing to change in targets electrical properties [2].	Expensive. Less tolerant to system aberrations. Problems with alloys.

Table 9.2 : Advantages and disadvantages of PEM and MVC

9.2 The control method : Continuous or pulsed.

Once it was determined that voltage could be used for the majority of elements as a control signal indicative of target status, a comparison of pulsed control over continuous control was investigated.

9.2.1 Continuous feedback control (CFC)

During initial investigations into material properties, continuous feedback control was used to obtain accurate stoichiometric variation in the deposited film. It was found that when sputtering reactive materials, such as aluminium, the process behaved as expected and accurate results were obtained. Problems did arise, however, when reactively sputtering indium tin oxide from an indium tin target.

Figure 9.1 shows the dependence of both voltage and emission signal as a function of O_2 flow rate obtained when sputtering ITO from an $In_{0.9}$:$Sn_{0.1}$ target. The large hysteresis curve with voltage, combined with the slow reaction time of O_2 with indium compared with tin (owing to their very disparate values of heat of formation) caused problems. When the continuous feedback process was initiated, under voltage control, stable operation was only achieved after about 5 minutes. Moreover, repetition of the process

initialisation was inconsistent. Sometimes the flow controller would add too much oxygen in an attempt to reach the desired set-point, ϕ_d, resulting in a different point, ϕ_a, being reached on the flow curve, figure 9.2. This was characterised by a significantly lower flow rate, f_a. This resulted in inconsistent results whilst depositing ITO using CFC and the cathode voltage as the process control signal.

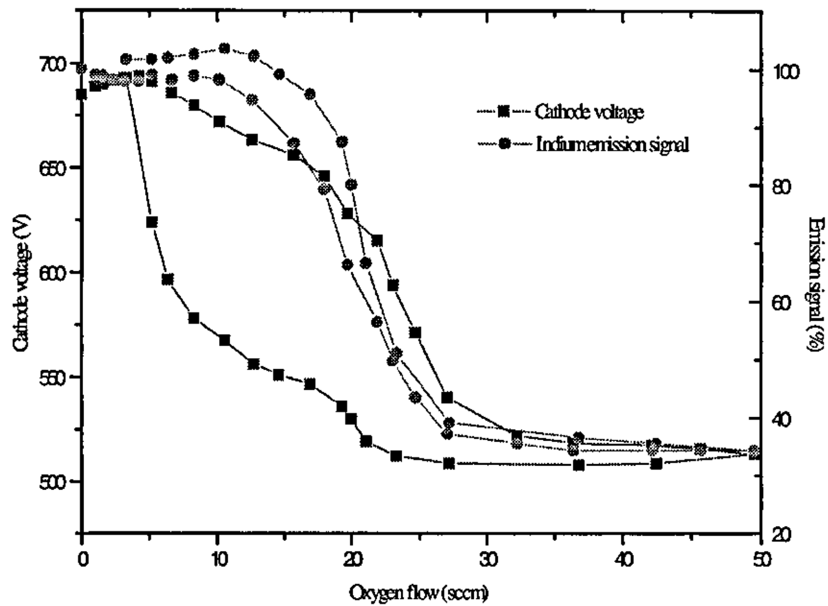

Figure 9.1 : Variation in the cathode voltage and emission signal with O_2 flow rate for indium tin target

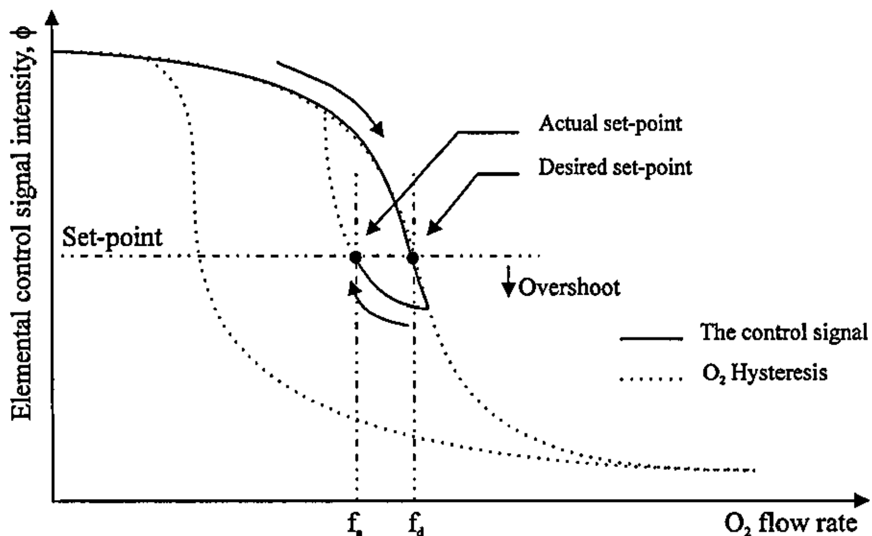

Figure 9.2 : Initiation problems with a large hysteresis when using CFC

9.2.1.1 Process instability to arcs

As mentioned in section 4.3, when sputtering a dielectric material using DC power, charge builds up on the target surface and an arc is initiated. This causes major problems when using a continuous feedback control system. If a material with a small hysteresis in the O_2 flow/Cathode voltage curve is being deposited, such as SiO_2, then the disturbance only affects the deposition for the length of the post-disturbance oscillation. However, when a material with a large hysteretic behaviour was being deposited then a more serious effect occurred. Figure 9.3 depicts the disturbance to an arc within the system when sputtering TiO_2 and monitoring the emission intensity. Initial disturbance results in the flow controller attempting to regain the set-point, ϕ_E, by the addition of oxygen to the system. This created a similar problem to that observed during process initiation; a different set-point was reached within the system, again characterised by a significantly lower oxygen flow rate.

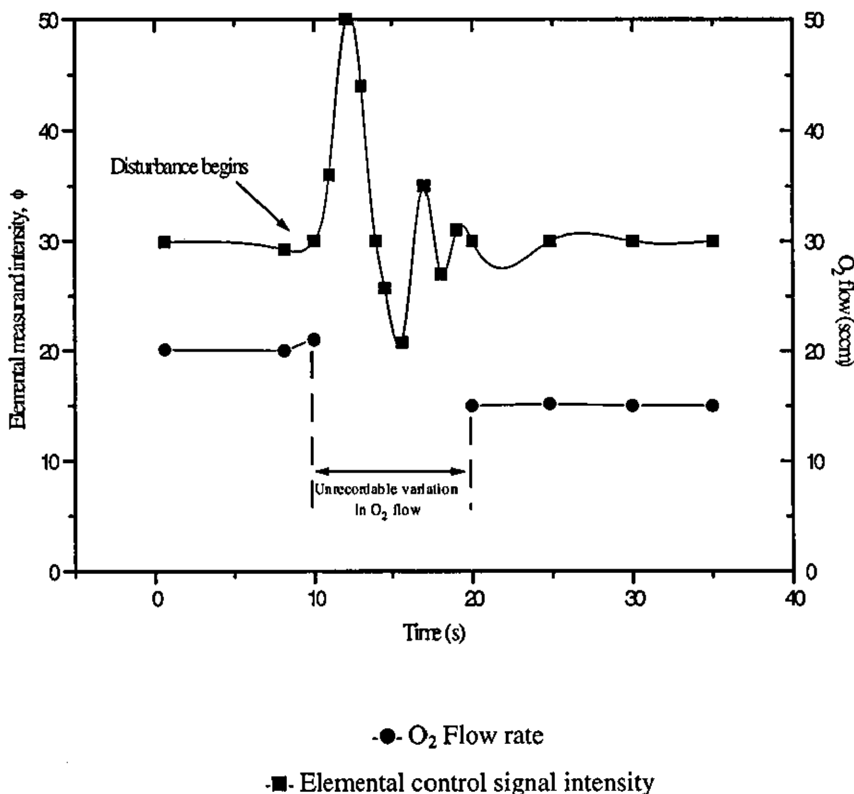

-●- O_2 Flow rate

-■- Elemental control signal intensity

Figure 9.3 : Observed response in measured signal to an arc disturbance for TiO_2 using CFC

It became obvious that MVC using CFC would not give reproducible results when sputtering certain materials. The SPPA process detailed in section 6.5.2.2 overcomes this problem. Furthermore, the instability to process aberrations observed while reactively sputtering insulating compounds, using conventional continuous control techniques, was solved by this technique of pulsing the reactive gas. This SPPA will be shown, in chapter 10, to have the advantages of increased stability and controllability, resulting in greater coating versatility and increased process tolerance.

9.2.2.1 The pulse waveform

It is first useful to explain the various features of the oscillating control signal that was obtained whilst pulsing the reactive gas within the system. Figure 9.4 illustrates a typical curve obtained for SiO_2 using target voltage as a control signal. There are four different regions of interest on the control curve.

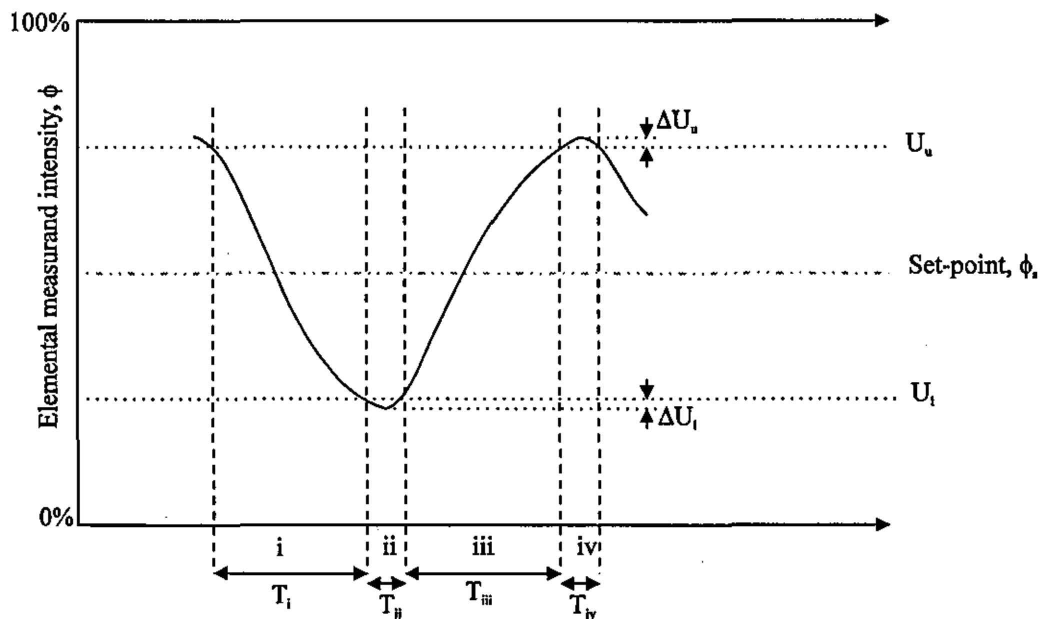

Figure 9.4 : Various regions of the SPPA control curve

$$\text{Period, } T_T = T_i + T_{ii} + T_{iii} + T_{iv}. \qquad [9.1]$$

Region i : *Drift to poisoned state* : Here the oxygen has been diverted into the system at a pre-determined flow rate and the target becomes poisoned with an associated drop in control signal intensity (*n.b.* for some materials the control signal intensity increases).

Region ii : *Lower threshold switching* : When the measured signal reaches the lower threshold, U_l, then the gas is diverted away from the system. This section represents the 'overshoot', ΔU_l, a value that needs to be minimised. Hence, minimising the duration of this region, T_{ii}, ensures accurate and consistent switching.

Region iii : *Drift to elemental state* : In this region the target returns to the elemental mode with no oxygen remaining in the system. Its gradient is dependent on the duration of region ii, T_{ii}. As T_{ii} becomes larger, then the gradient of region iii becomes less, and its duration larger, leading to metal rich films.

Region iv : *High threshold switching* : The control signal reaches the upper threshold, U_u, and oxygen is once again diverted into the system. This region also has a characteristic overshoot, ΔU_u, a value that also needs to be minimised.

To ensure accurate and reliable switching, T_{ii} and T_{iv} need to be equal. Furthermore, regions i and iii should have equivalent periods, T_i and T_{iii} respectively.

9.2.2.2 Factors affecting the SPPA process

Time constants and the gas switching valve

It is well documented that any time delay in the feedback loop leads to an oscillation [3] during CFC. The response time of the gas inlet tube and the piezo-electric valve, and the rate of poisoning and cleaning of the target contributes to this time delay in the system [2]. As in continuous feedback control, the time constants associated with the reactive gas deliverance within the system are also of great importance to the SPPA process. All the same parameters apply equally to the precise regulation of the control

process. However, the switching valve now replaces the piezo-electric valve, the latter maintaining a constant flow, the former switching the flow from the chamber.

The switching time of the switching valve is not as critical as for the piezo-electric valve in CFC. However, it was found to be critical to divert the reactive gas to a vacuum dump, the rotary pump on the loadlock in this case. Figure 9.5 shows the control curves obtained with and without a vacuum dump for the reactive gas.

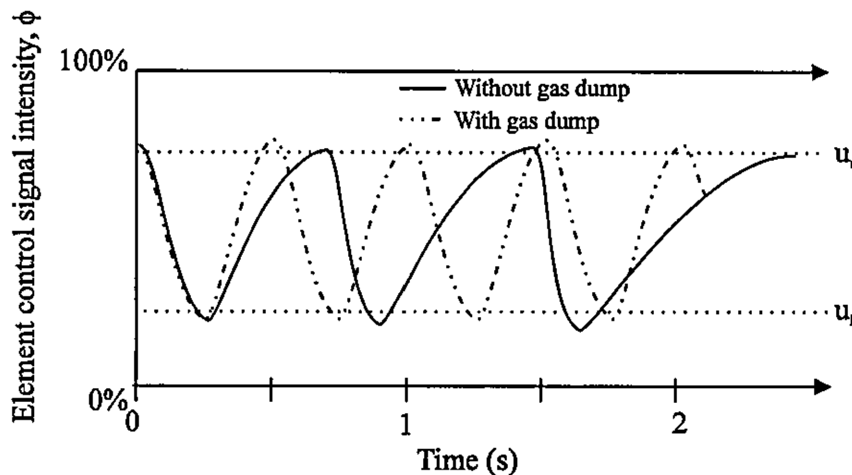

Figure 9.5 : SPPA control curves with and without a vacuum dump for the reactive gas

It can be seen that periodic pulsing was not obtained when the process did not have a pumped reactive gas dump. This was because of excess oxygen in the gas flow pipes, leading to increased effective gas flow rates, and hence, greater lower threshold overshoot, ΔU_l. The excess oxygen did not allow the target to sputter clean at the rate observed with a gas dump. Added to this, the length of tube between the switching valve and the chamber was also critical to ensure accurate process control.

O_2 flow rate

The effect of increasing the reactive gas flow rate into the chamber was investigated. With a magnetron power of 0.5 kW, sputtering SiO_2, the lower and upper threshold were kept constant at 30% and 80% respectively and the oxygen flow was varied. The resulting control traces are given in figure 9.6. Figure 9.6a illustrates a control trace with a low oxygen flow rate. At this flow rate, the control signal asymptotically approaches

the lower limit, U_l, but never exceeds it, and hence, the trigger for diversion of reactive gas away from the process is never received. This rate is termed the flow limit, F_l.

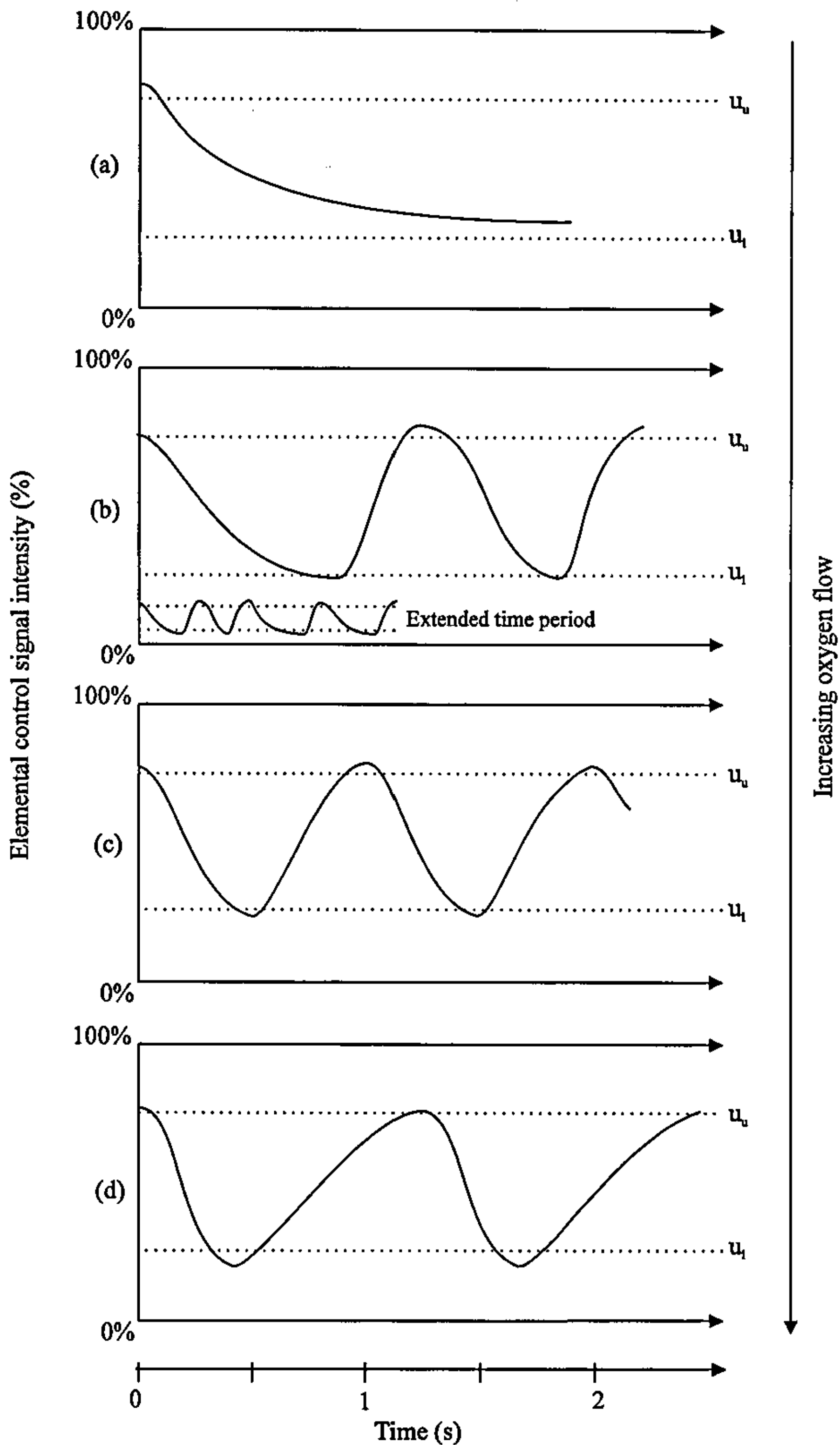

Figure 9.6 : Effect of oxygen flow on SPPA control curve (a) 2sccm (b) 6sccm (c) 10sccm (d) 14sccm

When the flow rate was increased to a level where lower threshold switching occurred, then pulsing was observed, albeit without any periodicity, figure 9.6b. This low rate is also characterised by a small gradient in region i and large gradient in region iii with little over shoot in region ii. Increasing the flow rate further resulted in periodic pulsing, and thus, reproducible films, figure 9.6c. In this state $T_i = T_{iii}$ and $T_{ii} = T_{iv}$, with $\Delta U_l = \Delta U_u$. Further increase in the flow rate, figure 9.6d gave the inverse of figure 9.6b. Here the flow rate was too great and a large overshoot was observed in region ii, with $T_{ii} >> T_{iv}$.

Time

After the process had been initiated, time had to be allowed for the system to stabilise, as in continuous control. Failure to allow for this stabilisation resulted in inhomogeneous films. A reliable measure of the process stability was found to be the pulsing period, T_T. Figure 9.7 illustrates the variation in pulsing period with time for both stable and unstable conditions (*e.g.* incorrect oxygen flow rate). It can be seen, in the stable process, that after ~30 s the period becomes constant within ± 0.1 s.

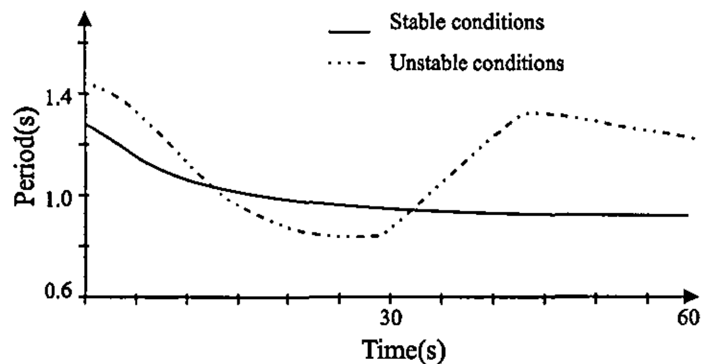

Figure 9.7 : Variation of pulsing period with time for both stable and unstable conditions

9.2.2.3 Initialisation routine

The following section describes the initialisation routine implemented throughout the use of the SPPA process during this work.

Initially, the control signal from the process was normalised, as described in section 6.5.2.1. The upper and lower threshold levels were then set to 80% and 20% respectively and the gas flow rate was increased until uniform pulsing, as detailed in section 9.2.2.1, was observed. A sample was then deposited and measured for the desired properties (*e.g.* resistivity, refractive index, etc.). The upper set-point was then either increased or decreased and a series of samples produced. If U_u exceeded 90 % during the deposition, then the lower set-point was increased to enable the desired stoichiometric films to be deposited. When the set-points became too close then uncontrollable pulsing was observed. This was found to be caused by voltage spikes occurring when the switching valve was switched, figure 9.8. This problem also occurred because of a superimposed sinewave on the DC voltage (~5% of the DC voltage). This interference proved to be a larger problem when sputtering with the medium frequency AC supply than the DC supply and was overcome by adding additional smoothing capacitors across the amplification stages of the normalisation circuit, as illustrated in figure 6.15, chapter 6.

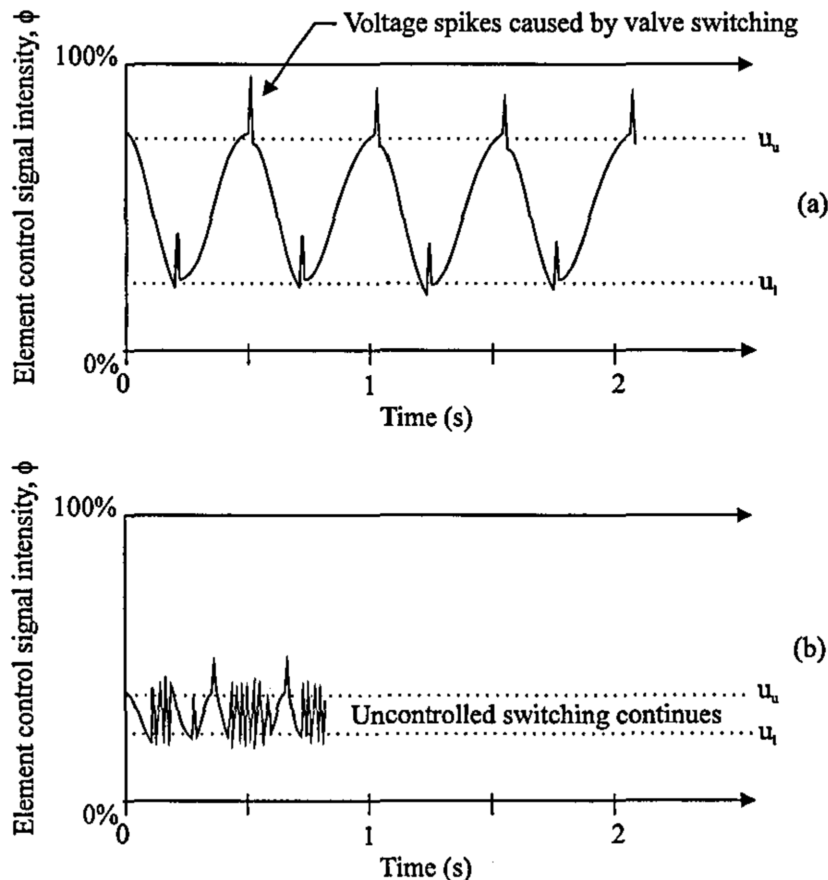

Figure 9.8 : Voltage spikes and uncontrollable pulsing observed in the SPPA process

If uncontrollable switching still occurred, because of the voltage spikes, then the lower threshold level was reduced to obtain a lower set-point and a more oxygen rich sample. Care had to be taken, however, not to pulse at too low an average set-point ($[U_u+U_l]/2$) as this reduced the deposition rate, as will be shown for SiO_2 in chapter 10.

If the voltage spikes that occurred could have been removed by more careful examination of the electronics, then as the two levels converged, the SPPA process would approach that of a CFC system. By separating these levels, the SPPA process decreases the sensitivity of the system to disturbances.

9.3 Chapter summary

- Magnetron voltage has been shown to be an accurate indication of the poisoned state of the magnetron cathode for Al_2O_3, ITO, SiO_2 and ZnO:Al.

- Continuous feedback control was unstable when controlling on the cathode voltage for ITO and ZnO:Al.

- An alternative process of reactive sputtering, termed SPPA, was introduced and characterised. The technique was shown to give greater versatility, control and tolerance over the reactive sputtering process.

CHAPTER 9 REFERENCES

[1] **Danson,N., Hall, G.W., Howson, R.P.**, (1995) *Thin Solid Film*, In press

[2] **Spencer, A.G.**, (1989). *'High rate reactive magnetron sputtering'*, Ph. D. Thesis, Loughborough University of Technology, U.K..

[3] **Hmiel, A.F.**, (1985). *J. Vac. Sci. Technol.*, A3(3), 592-595.

CHAPTER 10

RESULTS III : MATERIALS

The following chapter presents and discusses the results obtained whilst depositing various materials by reactive magnetron sputtering. Comparisons are made between different sputtering techniques used for the deposition of the coatings, but a significant proportion of the material results obtained have original scientific merit in themselves. Each section represents the deposition of a different class of coatings and to highlight the significant results obtained, each is set out in an individual manner. It should be noted that, because all the films were deposited as separate experiments, certain conditions such as power could not be kept constant throughout, and thus, inter-comparative studies on the ion bombardment were difficult. For this reason, a comparison of the atom to ion ratio and energy per depositing atom is given at the end of this chapter for all the materials deposited.

10.1 OPTICAL FILMS 180
10.1.1 Titanium dioxide, TiO_2 ..... *180*
10.1.2 Silicon dioxide, SiO_2 ..... *183*
10.2 TRANSPARENT CONDUCTING OXIDES (TCO) 190
10.2.1 Indium tin oxide, ITO *190*
10.2.1.1 Compacted oxide ITO target 191
10.2.1.2 Indium tin target 198
10.2.1.3 Comparison of the two sputtering techniques 200
10.2.2 Zinc aluminium oxide, ZnO:Al *200*
10.2.2.1 ZnO:Al Compacted oxide target 201
10.2.2.2 Zn:Al tiled target 202
10.3 ALUMINIUM OXIDE, AL_2O_3 209
10.4 THE ION/ATOM RATIO 211
10.5 CHAPTER SUMMARY 212

10.1 Optical films

Dielectric thin films are an important class of materials since they form the basis of most thin-film optical coatings such as filters, beam-splitters and anti-reflection coatings. It is important that the films are durable, of low absorption, and have stable refractive indices. All these properties can be achieved at room temperature using unbalanced magnetron sputtering. The following section details the results obtained for the high index material of TiO_2 and low index material of SiO_2.

10.1.1 Titanium dioxide, TiO_2

Titanium dioxide is a material widely used in thin film technology and a significant amount of research has been performed on various ways of depositing it [1]. TiO_2 in the rutile crystalline phase is the most desirable oxide. It is a hard, chemically resistant material, transparent in the visible spectrum and has a high refractive index ($2.1 < n_f < 2.7$). Applications of TiO_2 include anti-reflection coatings [2] and automotive mirrors. Many factors affect the phases that TiO_x can form, and work by Suzuki and Howson [3] has shown that the refractive index of TiO_x is sensitive to both oxygen partial pressure and deposition rate.

TiO_2 was studied in the preliminary investigations of the reactive control process. Sputtering of TiO_2 using conventional techniques proved to be both problematic and time consuming. The following section outlines the problems involved when sputtering such a material and details a reactive control solution that was subsequently developed to accurately deposit SiO_2, ITO and ZnO:Al.

Figure 10.1 shows the behaviour of the cathode voltage to manual admission of O_2. It can be seen that the U_c/F_r curve has a dual voltage set-point, and hence, MVC cannot be used to control accurately the film's stoichiometry. This is because the reversal of the voltage characteristics (at 4 sccm) would be disastrous, with the response preventing recovery back to the correct set-point. The pressure/flow control unit would merely add oxygen to the system in an attempt to increase the voltage.

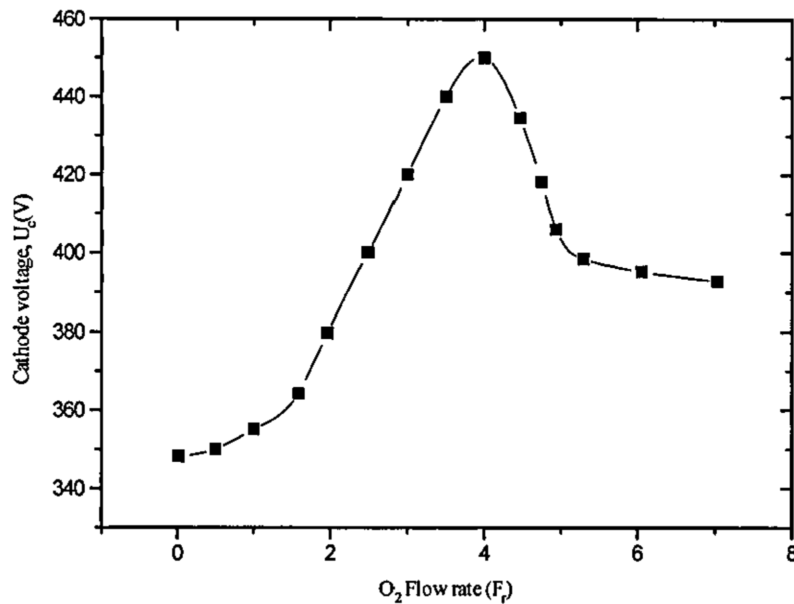

Figure 10.1 : Dual set-point obtained in cathode voltage when varying oxygen flow rate for TiO_2

A similar voltage change with reactive gas partial pressure has been reported for a TiO_x system by Schiller *et al* [4]. The increase of the voltage, at lower F_r, is caused by the oxidation of the target surface and formation of TiO_x (probably $x < 2$) for which the secondary electron emission coefficients are smaller than those of Ti. With increasing F_r ($F_r > 4$ sccm), oxygen is ionised and because it has a lower ionisation potential than argon, the ion flux at the target surface increases. This increases the current and decreases the voltage (constant power). The decrease in voltage can also be partly attributed to an increase in total pressure.

It was, hence, necessary to use the plasma emission as an indication of the target status. The camera was set up, as explained in section 6.5.1.2, for observation of the 453 nm titanium emission line. Figure 10.2 clearly reveals the sensitivity of the titanium to O_2 and a large hysteresis loop is noted. Therefore, as previously described in chapter 4, control of the flow of oxygen into the system was needed.

Using CFC, the target was sputter cleaned until no further variation in emission intensity was observed, and then, as described in section 6.5.2, the control signal was normalised using both this elemental and poisoned mode. The CFC was then initiated and various

samples were obtained at different set-points, ϕ_E, at a power of 500 W, figure 10.3. An argon partial pressure of 2.5 mtorr was used and the deposition time was 4 minutes. This process was successful in the first couple of instances and repeatable results were obtained. However, after 4 to 5 runs at the set-point of 26%, corresponding to stoichiometric TiO_2 ($n_f = 2.45$), the refractive index could not be maintained. The only solution to this was to clean the target and re-normalise the system.

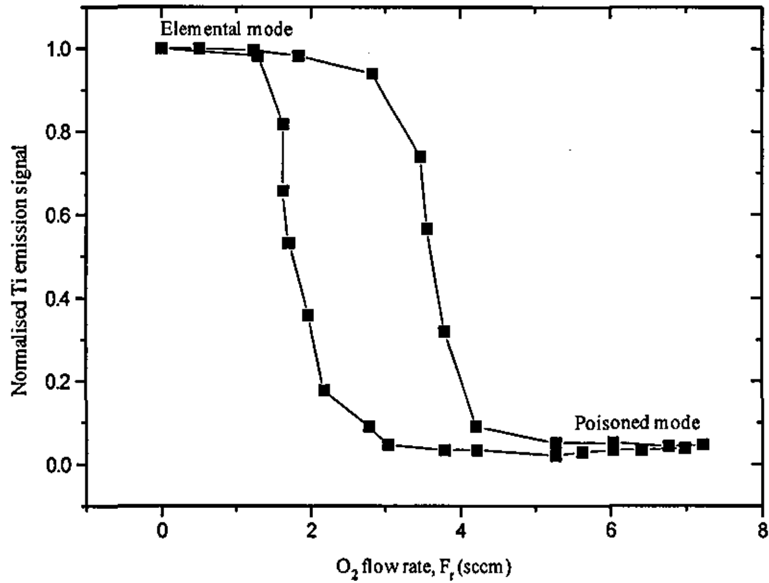

Figure 10.2 : Variation of titanium emission line intensity with addition of oxygen

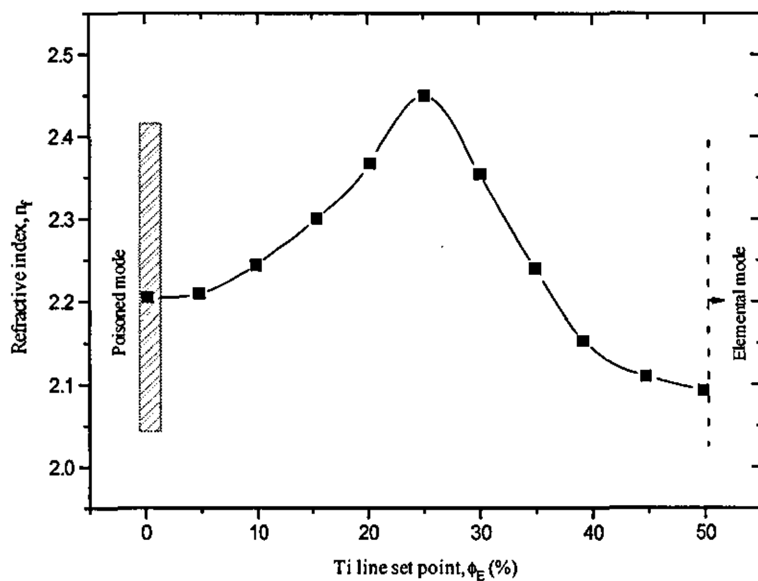

Figure 10.3 : Variation of refractive index of TiO_2 as a function of Ti line set-point

This was one of the problems that led the project into the development of the SPPA process. Early work by Howson *et al* [5] had shown that consistent results were obtained by pulsing the gas. In their work, the reactive gas was rate controlled, but was delivered to either a vacuum dump or the chamber by a switching valve, controlled by a square wave generator, operated at ~1 Hz. This early gas pulsing did have its problems, however, as no control signal was used to regulate the process. Hence, a more sophisticated system was developed during this work as described in chapters 6 and 9. This pulsing process solved the problem of maintaining a single set-point as the target surface was continuously 'cleaned' when the gas was diverted away from the chamber. Control of the gas pulsing was at first problematic, with the emission signal as the indicator of cathode status. Switching of the valve caused interference in the millivolt emission signal from the CCD detector array. The SPPA unit was, therefore, developed when depositing SiO_2, using the cathode potential as the control signal.

Consistent results whilst depositing TiO_2 were obtained after initial development depositing SiO_2. Using the SPPA system for the deposition of TiO_2, a refractive index, $n_f = 2.47 \pm 0.02$, was obtained at a rate of 0.6 nms^{-1}. The magnetron was powered by the DC supply at 500 W, and in an Ar_{pp} of 2.5 mtorr. This rate was significantly greater (10%) than that obtained when depositing TiO_2 by CFC means.

10.1.2 Silicon dioxide, SiO_2

Silicon dioxide is one of the most common materials used in multilayer optical stacks as the low index material. The behaviour of these stacks, for example anti-reflection (AR) coatings, is highly dependent on the refractive index of this material. Work recently undertaken [6] on AR coatings showed that a change in the SiO_2 refractive index, unrecordable by the ellipsometer, significantly altered the AR curve. However, it is necessary not only to be able to control precisely the deposition of SiO_2 and such properties as the deposition rate and refractive index, but also to increase its environmental durability. The techniques developed throughout this work are ideally suited to this, and the following section details the effects of the process parameters on film stress, refractive index, and durability.

SiO_2 was deposited throughout the development of the gas pulsing process and most of the samples investigated for stress and structure were deposited using SPPA. However, some samples were made to compare the performance of films deposited with the two control techniques, CFC and SPPA.

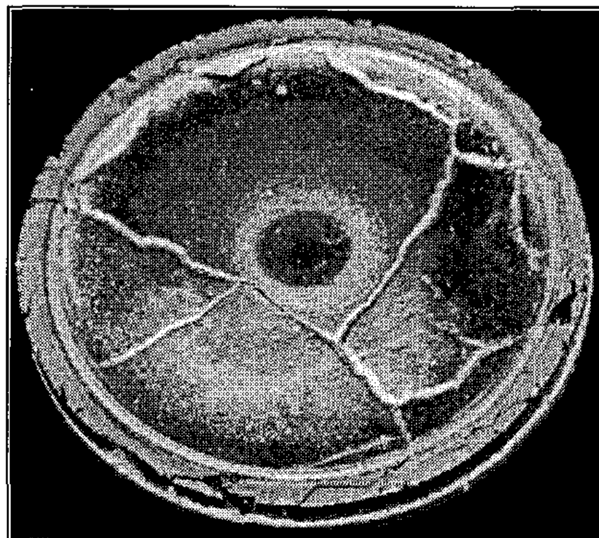

Plate 10.1 : Silicon target showing significant cracking

The DC power supply was initially tested, though arcing was found to be a major problem and no reliable control could be achieved. This occurred because of the reactivity of the silicon with oxygen and the dielectric properties of the SiO_2 formed on the target surface, as explained in section 4.3. Furthermore, silicon targets are prone to cracking, as shown in plate 10.1. This is mainly because of the stresses exerted by the differential thermal expansion coefficients of the backplate and target. Stresses are also exerted by the one atmosphere pressure drop across the target and peripheral target clamping. Silicon is brittle and these forces cause cracks to propagate along the crystal orientations and fractures present in the target (even though the target specifications are given as polycrystalline, single crystal orientations can exist along its radius). The cracks in the target increased the frequency of arcs observed owing to localised power densities at the crack interfaces [7]. Hence, power application was obtained from the rectified AC arrangement and limited to 200 W throughout. Films were sputtered in 3 mtorr of argon, and with the anode floating unless otherwise stated. The deposition time of each sample was 3 minutes.

For this work, PEM was not considered the optimum measure of the target status for two reasons. Firstly, the majority of the silicon spectral emission lines are found in the ultra-violet, necessitating the use of quartz optics, and secondly, because the recovery time from arcs can be a large percentage of deposition time, as illustrated in the previous chapter. Figure 10.4 shows the variation in cathode voltage with oxygen flow rate, F_r. It can be seen that there are no anomalies across this flow range and only a small hysteresis exists.

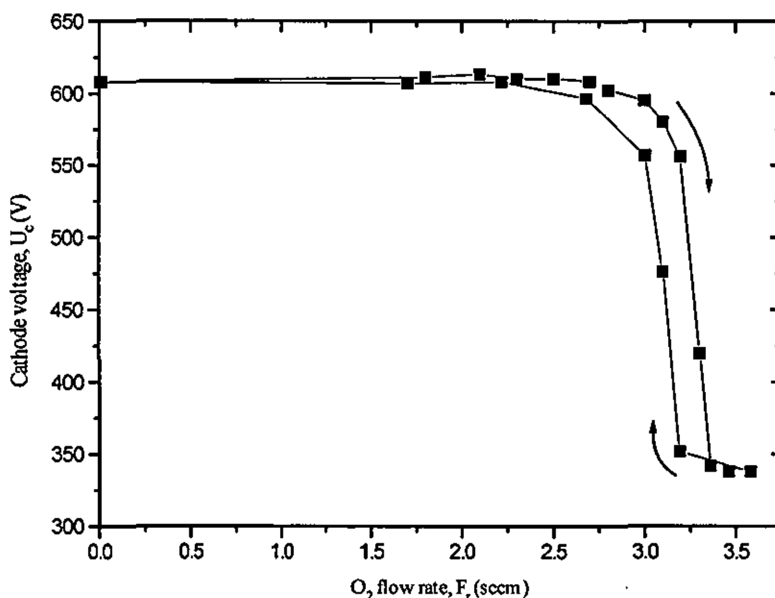

Figure 10.4 : Variation in cathode voltage as a function of O_2 flow rate for Si target

The ion bombardment, as mentioned in section 8.2.1, was varied by two different methods. Figure 10.5 shows the variation in ion current at the substrate at various argon partial pressures. At the Ar_{pp} used for the majority of this work (3 mtorr), the ion current, I_{si}, was measured to be 3.35 $mAcm^{-2}$ and the floating potential, V_p, measured at -15 V.

Figure 10.6 shows the variation of refractive index of films prepared with CFC. A well observed increase in n_f with increasing set-point, ϕ_v, is demonstrated, as was expected. Also shown in figure 10.6 is the relationship between deposition rate and ϕ_v, which relates to the behaviour of the refractive index. At a refractive index of $n_f = 1.46$, the deposition rate was 0.7 nms^{-1}.

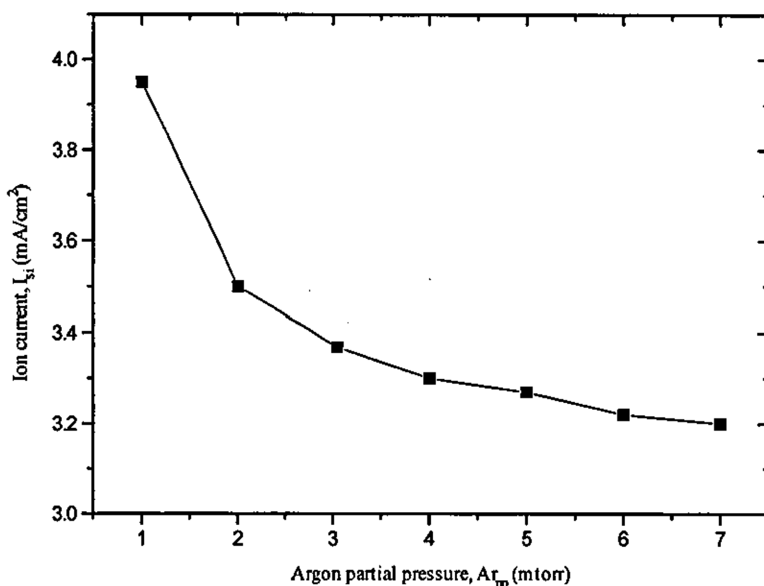

Figure 10.5 : Variation of ion current at the substrate as a function of Ar_{pp}

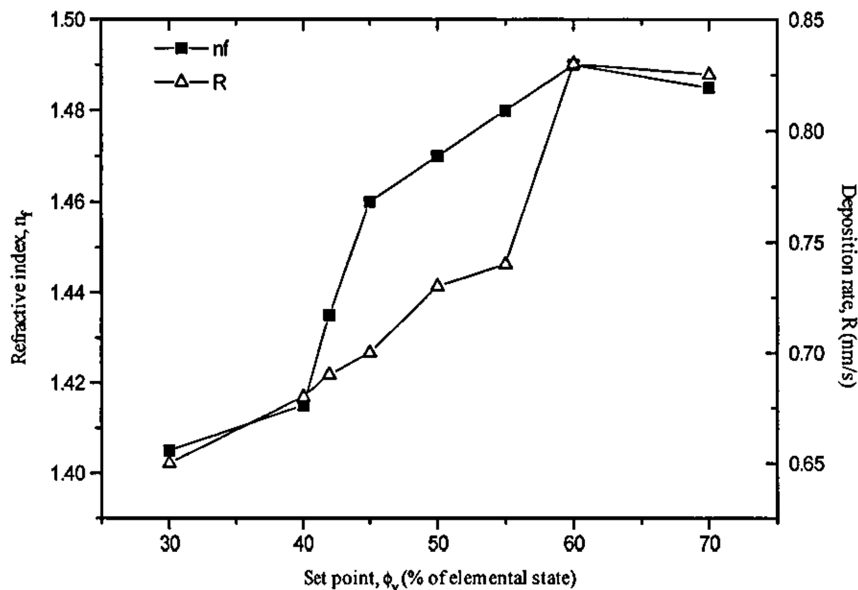

Figure 10.6 : Variation of refractive index and deposition rate in SiO_2 as a function of set-point

When pulsing the reactive gas, a greater degree of linearity between refractive index and upper threshold, U_u, was observed than was seen with variation in set-point using CFC.

Figure 10.7 illustrates this at a lower threshold, U_l, of 30% and O_2 flow rate, F_r, of 8 sccm. Again, the deposition rate followed a similar trend to that observed with CFC. At a refractive index of $n_f = 1.46$, the deposition rate was 0.71 nms^{-1}.

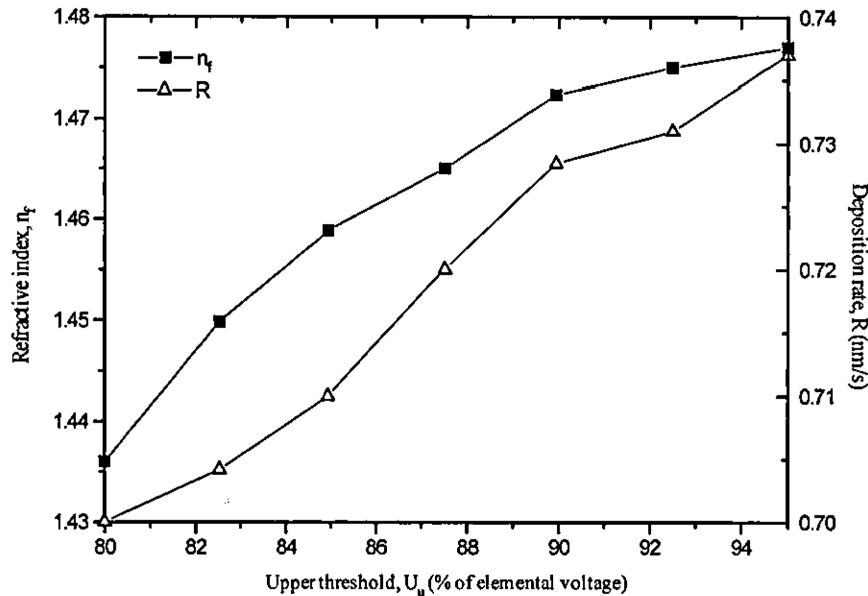

Figure 10.7 : Variation of refractive index and deposition rate in SiO_2 as a function of upper threshold

The effect of the variable ion bombardment on the refractive index was also assessed. Samples were made with the anode grounded, with an associated ion current, I_{si}, of 1.1 $mAcm^{-2}$. Measurements made on the samples sputtered with low ion bombardment gave $n_f = 1.43$ (*c.f.* $n_f = 1.46$ for the films with $I_{si} = 3.35$ $mAcm^{-2}$). This reduction can be attributed to a more porous film being grown under lower ion current, a phenomena emphasised by the increased deposition rate. Whilst a lower refractive index is desirable for many optical applications, further analysis of the films made with low ion bombardment showed instability in their refractive indices. The film produced under low I_{si} increased in refractive index from 1.43 - 1.49 one day after deposition. This is attributed to the inclusion of water into the pores of the film as explained in section 5.4.1.

Modification of the reactive gas flow rate, whilst keeping U_u and U_l constant, did not result in a corresponding change in refractive index, as may have been intuitively

expected. The reasons for the behaviour of the SPPA process associated with changes in reactive gas flow are explained in section 9.2.2.2.

All the samples made within the refractive index range 1.400 - 1.490 were found to be transparent in the visible spectrum. No noticeable difference was observed between the transmission curves of the samples, even up to a film thickness of 500 nm. A typical transmission curve showed transmission above 98% across the visible wavelength range.

Two samples were made at equivalent thickness and refractive index of 500 nm and 1.460 respectively using both CFC and SPPA control. Qualitative comparative scratch tests on both samples indicated that those prepared using the latter technique were significantly more durable to the test than the former. Possible reasons for this will be given in the next section.

All the samples made in this investigation into SiO_2 were found to be in a state of intrinsic compressive stress.

Figure 10.8 shows the variation in compressive stress with refractive index for both CFC and SPPA control. A significant feature of this figure is the stress peak at the optimum established refractive index for SiO_2. This may have been because of an increase in film density associated with stoichiometric SiO_2, and hence, an increase in compressive stress. It can also be seen from this figure that the films produced using pulsed control have greater compressive stress than the films deposited by the continuous control technique. A dense structure obtained by the deposition of a layer type structure could be a possible reason for this observed increase in intrinsic stress. This film densification could also explain the difference in hardness observed between the two control techniques.

The variation in compressive stress with varying Ar_{pp} for stoichiometric films (constant n_f to an accuracy of 0.5%) was found to be highly dependent on the ion bombardment, as observed throughout this work for all materials. This correlation is emphasised by observing the variation of stress with anode controlled ion current, as shown in figure 10.9. A well observed increase in stress with controlled ion current, I_{si}, is demonstrated.

The increase in stress can be expected in films deposited under high ion flux because of an increasingly dense, fibrous structure [8].

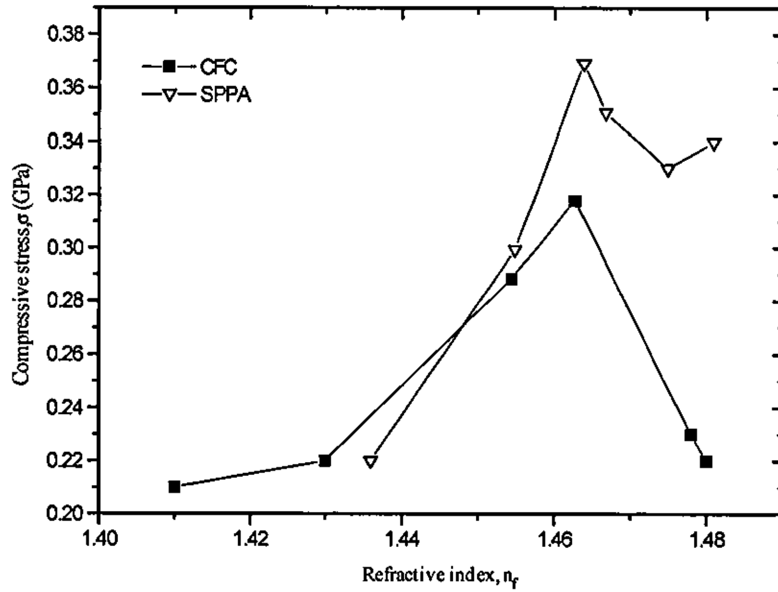

Figure 10.8 : Variation of intrinsic stress in SiO_2 films prepared by CFC and SPPA as a function of refractive index

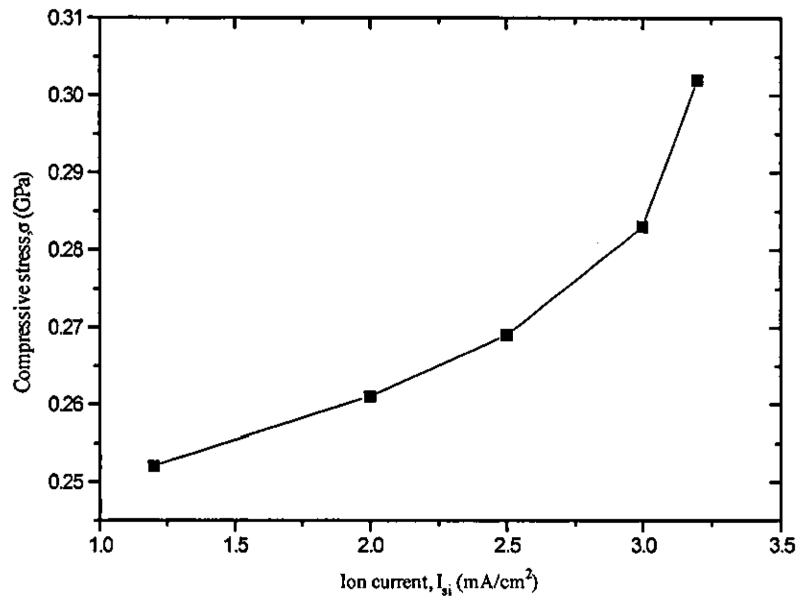

Figure 10.9 : Variation of intrinsic stress as a function of anode controlled ion current for SiO_2 films deposited using SPPA control

From the collated refractive index, film thickness and optical transmission data, it was shown that reactive deposition by pulsing oxygen into the system could be realised. This gave a close degree of control of n_f and τ_f. Iteration along the refractive index/upper threshold figure enabled precise selection of the film index to be made within 0.5%. Furthermore, the SPPA process showed greatly enhanced process stability compared with CFC.

10.2 Transparent conducting oxides (TCO)

TCO materials need to be both good electrical conductors (*i.e.* $< 5\times10^{-5}$ Ωm) and transparent in the appropriate region of the electromagnetic spectrum, usually the visible region. The existence of both these properties in the same material is not trivial and is only possible with semiconductor materials like indium oxide, cadmium oxide and zinc oxide.

The following section describes the properties of the coatings obtained for the two TCO materials deposited during this work; indium tin oxide (ITO) and zinc aluminium oxide (ZnO:Al). This section of work compares films sputtered from both alloy targets and compacted oxide targets. Comparisons are made of the industrial applicability of the two targets and the coating performance.

10.2.1 Indium tin oxide, ITO

Undoped indium oxide is an n-type degenerate semiconductor or even semi-metal at high electron concentrations. It has a low resistivity, the magnitude varying with deposition conditions, but usually between $\sim10^{-4}$ and 10^{-6} Ωm. It has a band gap of between 3.7 and 4.4 eV, and has high transmission in the visible spectrum. Tin is added to the compound to create n-type donors and increase durability. Applications of ITO include spectrally selective heat reflecting films [9], contact and anti-reflection layers in hetero-junction photovoltaics [10], protective coatings [11], active and passive aircraft transparency

coatings, transmitting electrodes for opto-electronics [12], laser-resistant coatings [13] and antistatic coatings for satellites [14].

The following sections detail the results obtained when sputtering ITO from a compacted target and from an indium-tin alloy target using SPPA to control the admission of oxygen to the system.

10.2.1.1 Compacted oxide ITO target

The initial experimental procedure consisted of iterating towards a resistance minimum found with ITO, by manually increasing the oxygen partial pressure using the flow controller. The argon partial pressure was maintained at 3 mtorr, and DC power at 200 W, and substrates were coated for a deposition time of 5 minutes.

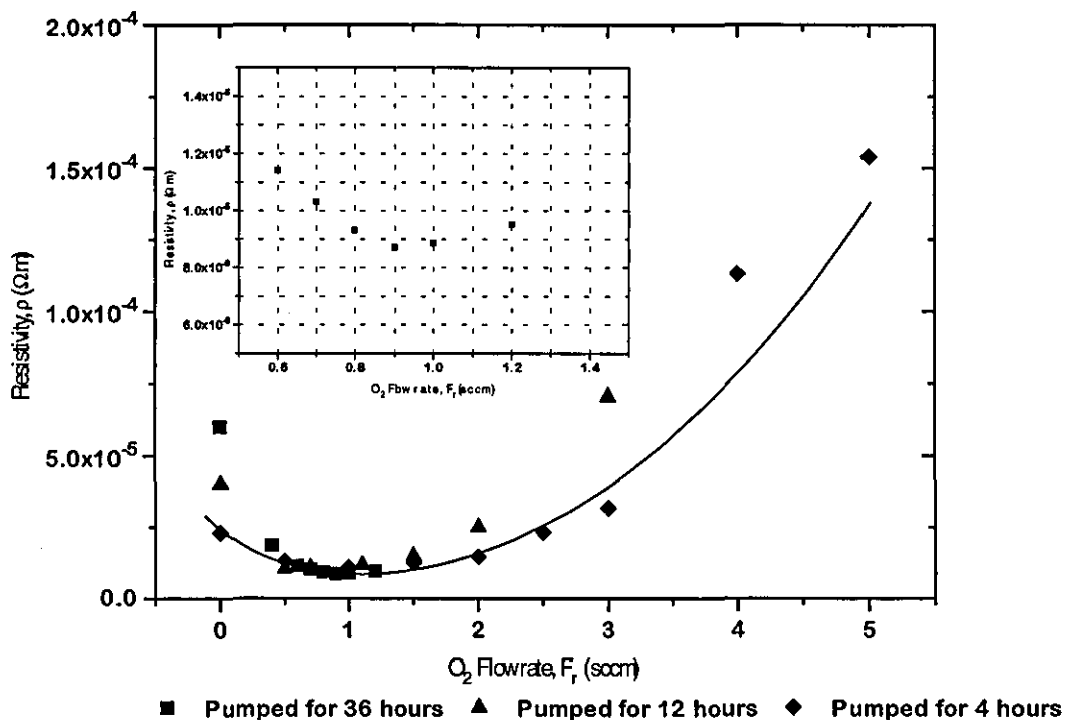

Figure 10.10 : Resistance minimum obtained for ITO target as a function of O_2 flow rate

Figure 10.10 illustrates a resistivity/oxygen flow rate curve for the samples sputtered near the resistance minimum. Table 10.1 shows the percentage transmission at 550 nm for samples sputtered at different flow rates.

Oxygen flow rate, F_r (sccm)	Transmission at 550 nm (%)
0	48.8
0.4	60.6
0.6	71.6
0.7	76.6
0.8	81.1
0.9	81.7
1.0	82.3
1.2	82.4
1.4	82.4

Table 10.1 : Transmission of ITO samples at various O_2 flow rates

It was determined that the base pressure of the vacuum chamber significantly influenced the resistivity at high and low sputter rates, but did not adversely affect the resistance minimum or the optical properties of the films. A minimum resistance of 8.8 $x10^{-6}$ Ωm was observed at 0.9 sccm with a corresponding transmission of 81.7% at 550 nm. However, this minimum was particularly broad, located between a F_r of 0.8 sccm and 1.2 sccm. Moreover, this minimum was stable and no hysteresis was observed in the resistivity while varying the O_2 flow rate.

The refractive index is unaffected by the O_2 flow rate between 0.5 sccm and 6 sccm and maintains a value of 2.04. This illustrates that the film's resistivity is most sensitive to changes in sputtering conditions and a better measure of the film's stoichiometry.

Figure 10.11 illustrates the variation in deposition rate and ion current with varying oxygen flow rate. It can be seen that whilst the ion current is independent of any changes in F_r, the deposition rate shows a linear decrease with increasing F_r. This is caused by target poisoning, as is seen whilst reactively sputtering metal targets. The increase in O_{pp} does not significantly increase the scattering of the ions within the plasma and reduce the ion current. However, the ion current measurement neglects the O_2^- and O^- ion bombardment at the substrate.

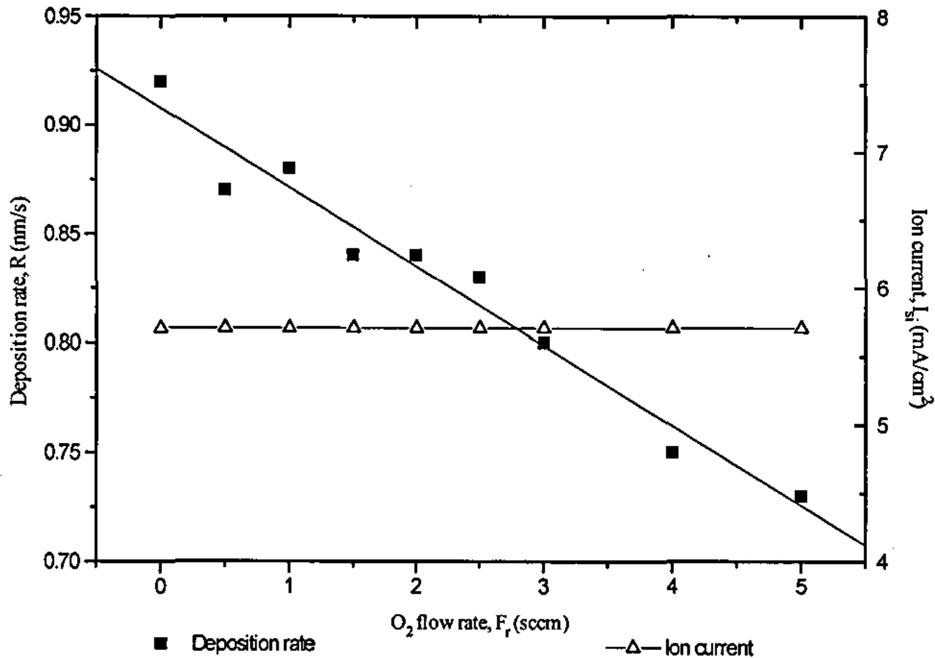

Figure 10.11 : Variation of deposition rate and ion current as a function of O_2 flow rate for ITO films deposited using the compacted oxide target

The intrinsic stress in the films was also measured, figure 10.12, and found to be in a state of high compression. The stress showed a marked increase from ~1 GPa with no oxygen to ~1.5 Gpa at 1.5 sccm where it approached a constant value of 1.51 Gpa and was unaffected by any further increases in O_2 flow. This increase is probably because of increased film densification by high energy O^- ions accelerated across the cathode dark space to 200 eV. These O^- ions can cause ion implantation and increased adatom mobility, thus, increasing the compressive stress in the film as explained throughout chapter 5.

The effect of ion bombardment was also investigated by altering the Ar_{pp} and by grounding the anode to earth through a variable resistor.

Figure 10.13 illustrates the variation in resistivity with Ar_{pp}. It can be seen that there is a resistance minimum of 5.7×10^{-6} Ωm at 4.5 mtorr of Ar. Maintaining an argon pressure of 4.5 mtorr, an F_r/ρ curve was plotted. However, the position of the resistance minimum was unchanged at 0.9 sccm.

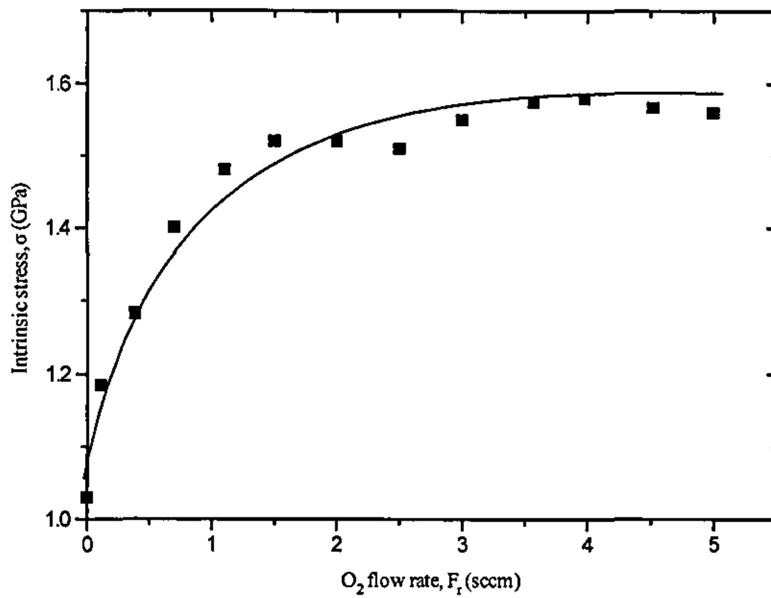

Figure 10.12 : Variation of intrinsic stress in ITO films deposited using the compacted oxide target as a function of O_2 flow rate

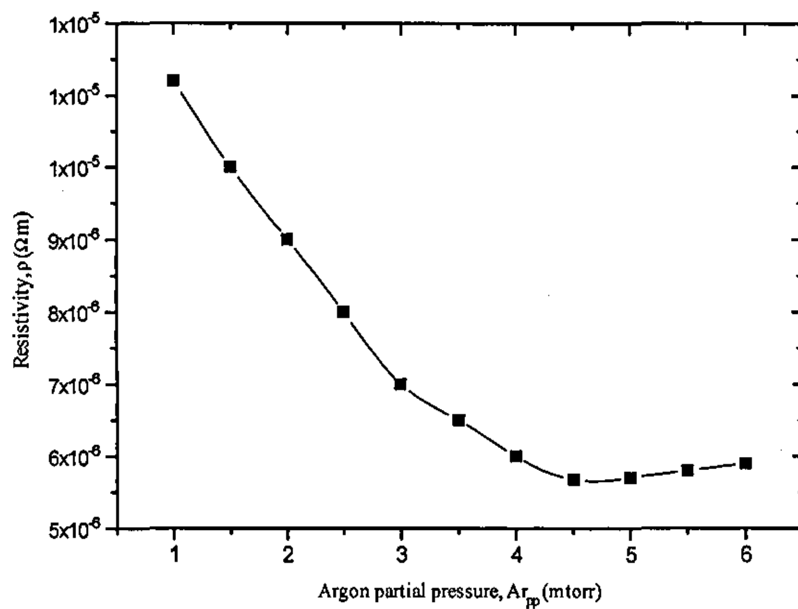

Figure 10.13 : Variation in resistivity of ITO films deposited using the compacted oxide target as a function of Ar_{pp}

Figure 10.14 shows the variation in ion current and deposition rate for varying Ar_{pp}. The opposite effect to varying the O_{pp} was observed. The deposition rate is only slightly affected by variations in Ar_{pp}, and I_{si} shows a linear decrease with an increase in Ar_{pp}. The decrease in I_{si} can be attributed to an increase in scattering and decrease in ion mean free path. Hence, at first glance, the resistivity would seem to be dependent on the ion current when varying the Ar_{pp}. However, when the ion current was altered by variation of the anode characteristics and the Ar_{pp} was maintained at 3 mtorr and the F_r at 0.9 sccm, only a small drop in resistivity was observed, figure 10.15. This could be owing to the ion energy being unaltered by varying the electrical characteristics of the anode.

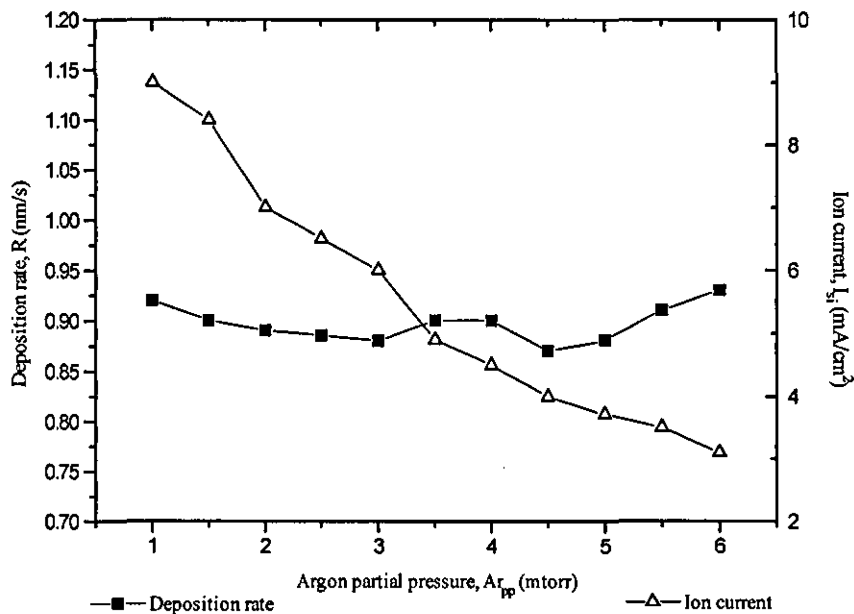

Figure 10.14 : Variation of deposition rate and ion current as a function of Ar_{pp} for ITO films deposited using the compacted oxide target

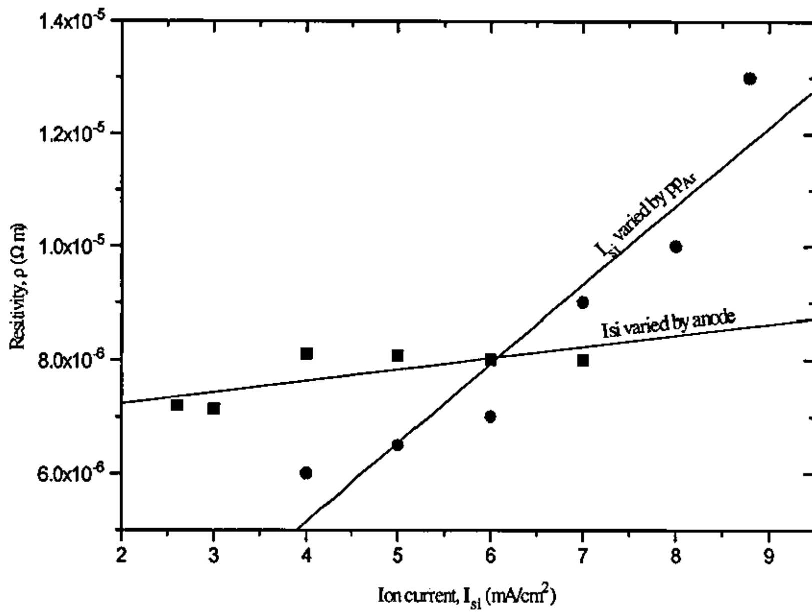

Figure 10.15 : The effect of ion current on the resistivity of ITO films deposited using the compacted oxide target

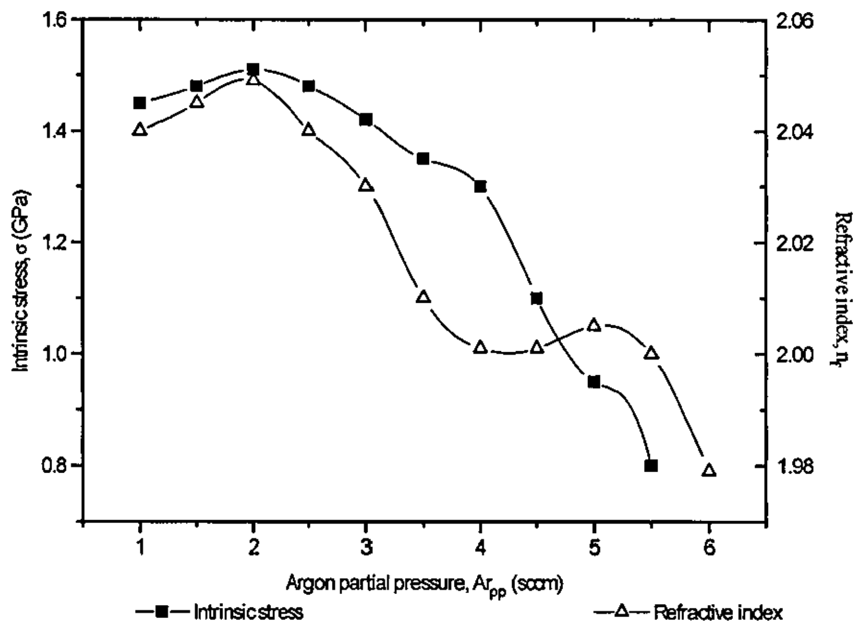

Figure 10.16 : Variation of intrinsic stress and refractive index of ITO films deposited using the compacted oxide target as a function of Ar_{pp}

Figure 10.16 shows the variation in refractive index and intrinsic stress with Ar_{pp}. It can be seen, as would have been intuitively expected, that both parameters follow a similar

trend to the ion current. An increase in ion bombardment caused by lower Ar_{pp} results in a more densely packed structure and an increase in compressive stress and refractive index.

It has been shown that easy stoichiometry control can be obtained by sputtering with an ITO compacted target in an oxygen environment. The process is both stable and repeatable and at the resistance minimum, $\rho_{min} = 5.7 \times 10^{-6}$ Ωm, deposition rates of 0.9 nms^{-1} were obtained with a sputtering power of 200 W.

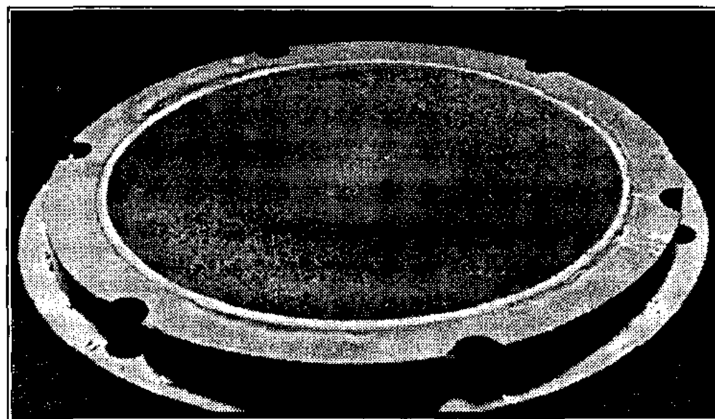

Plate 10.2 : Formation of small nodules on ITO target surface caused by preferential sputtering

Plate 10.2 illustrates one of the problems encountered when sputtering ITO from a compacted target. The small nodules are formed owing to preferential sputtering of the indium compared to the tin. These nodules cause two problems. They form sharp points on the magnetron surface which lead to local increases in current density, and so increasing the likelihood of arcs. Furthermore, the preferential sputter alters the operating characteristics of the magnetron (*e.g.* voltage and emission), and hence, drift occurs in the deposition parameters.

The power to the magnetron cathode was increased to determine the maximum power density the target could withstand. At 800 W there was a significant change in operating characteristics and one could see a large crack down the centre of the target. The crack was caused by the large thermal expansion mismatch between the target and backplate. Therefore, to maintain high power densities, and hence, high sputtering rates, the target must be mounted on a backplate with a similar expansion coefficient.

10.2.1.2 Indium tin target

Only a brief examination of sputtering from an indium-tin target was investigated to determine the viability of using the SPPA process and as a comparison to the films sputtered by the compacted oxide.

The indium tin target was prepared by melting indium and tin pieces into a cylindrical target backplate. Investigations made by Howson *et al* [15,16] of the optimum doping of the indium with tin have demonstrated that the addition of excess tin results in a loss of performance both electrically and optically. A balance has, hence, to be made between electrical, optical and mechanical properties and to some extent the decision is application dependent. Throughout this work a weight ratio of nine times indium to one times tin was used.

The reactive sputtering of ITO from a metal target is more demanding on process stability than most other materials, in that the region of stoichiometric oxides which are both optically transparent and electrically conducting is very narrow. This is attributed to the presence of the dopant by Mukherjee [17]. Moreover, this process window falls directly in the instability described in section 4.1.

Much work has been undertaken to control within this instability using PEM [18,19] and coatings have been deposited successfully with acceptable electrical and optical properties. This work sought an alternative to PEM and this section outlines the application of the SPPA process, as previously described, to the deposition of ITO. Chapter 9 discussed the various problems encountered when controlling the reactive deposition of ITO from an indium tin target using CFC and the cathode potential as an indicator of the target status. The process was unstable and many different set-points could be reached depending on the initialisation conditions and aberrations encountered during deposition.

SPPA provided a solution to the problem encountered with CFC and accurate control of the process was achieved. The SPPA system was set-up and normalised as described in section 6.5.2.2.

The control in the transition of the magnetron, and thus, stoichiometry of the film, was achieved by altering the upper threshold, U_u, of the pulsing process. All the films were deposited for 2.5 minutes at an argon partial pressure of 3 mtorr. A power of 200 W was applied, so that a direct comparison could be made between the two different targets.

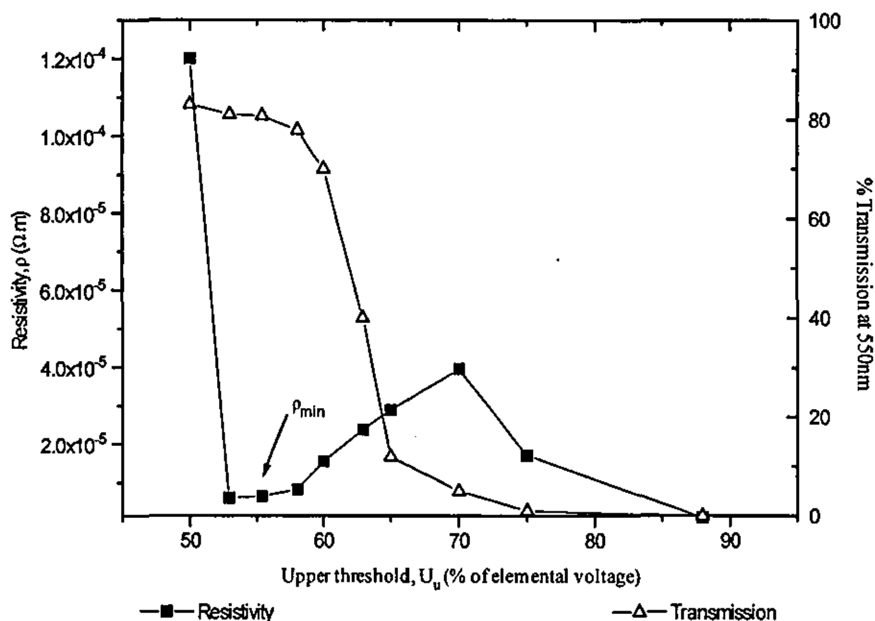

Figure 10.17 : Resistance minimum obtained when depositing ITO using the SPPA process

The control of the stoichiometry of the film, represented by a variation in resistivity is shown in figure 10.17 as a function of upper threshold level, U_u. The variation in transmission at 550 nm is also given. The resistance minimum is obtained when U_u = 52-58% at U_l = 22.5 % and F_r = 30 sccm. This window of resistance minimum is significantly larger than that obtained by conventional PEM, and continuous control techniques used by other workers [18]. The deposition rate associated with this control point was 1.12 nms^{-1}. The intrinsic stress was determined to be 1.1 GPa and the associated ion bombardment 9 $mAcm^{-2}$.

10.2.1.3 Comparison of the two sputtering techniques

Table 10.2 compares the two sputtering techniques used in the deposition of ITO.

	ITO compacted oxide target	Reactive sputtering from indium tin target using SPPA process
Usability and initiation procedure	The simplest of the two techniques to initialise and control with only a small amount of non-critically controlled oxygen needed to give adequate electrically conducting and visible coatings.	More difficult to set-up and control (*c.f.* compacted oxide target). However, the use of SPPA techniques made the resistance window larger.
Versatility	Can obtain low ρ but cannot change the film composition in terms of percentage doping. To get different In/Sn ratio need to replace target.	Changes in target composition can be easily realised. Film stoichiometry is more versatile owing to greater control over reactive gas inclusion.
Process stability	As the deposition continues preferential sputtering means more nodule formation and a drift in film performance.	A stable process is achieved and any nodules that do form can be removed by re-casting the target.
Cost	Expensive. The initial cost of the target is high and the target is difficult to re-process. Need to tile the target and rotate the tiles to prevent localised erosion.	Cheaper initial cost because no complicated manufacturing process is required. Re-processing possible.

Table 10.2 : Comparison of the two control techniques used in the deposition of ITO

10.2.2 Zinc aluminium oxide, ZnO:Al

Zinc oxide is similar to indium oxide in the respect that it is also a wide band gap (~3.3 eV) n-type semiconductor, where band gap states are introduced either by the addition of

foreign dopants, or by oxygen vacancies evolving interstitial zinc atoms [20]. Any impurities introduced in the host material are ionised, and the associated electrons occupy the bottom of the conduction band.

It has attracted interest for use in many low cost applications such as window coatings [21], LCDs and solar cells [22], because of its amenability to defect or impurity doping. ZnO doped with Al [23] has not attracted as much interest as ITO but does offer similar characteristics at a lower cost. The following sections show that resistivity values, almost as good as ITO, can be obtained at room temperature by sputtering ZnO:Al from a Zn/Al alloy target, with careful control of the O_{pp} to achieve the necessary stoichiometry.

10.2.2.1 ZnO:Al Compacted oxide target

The same sputtering strategy was used to sputter from the ZnO:Al target as was from the compacted ITO target. A small flow of oxygen was introduced into the chamber to achieve stoichiometric ZnO:Al.

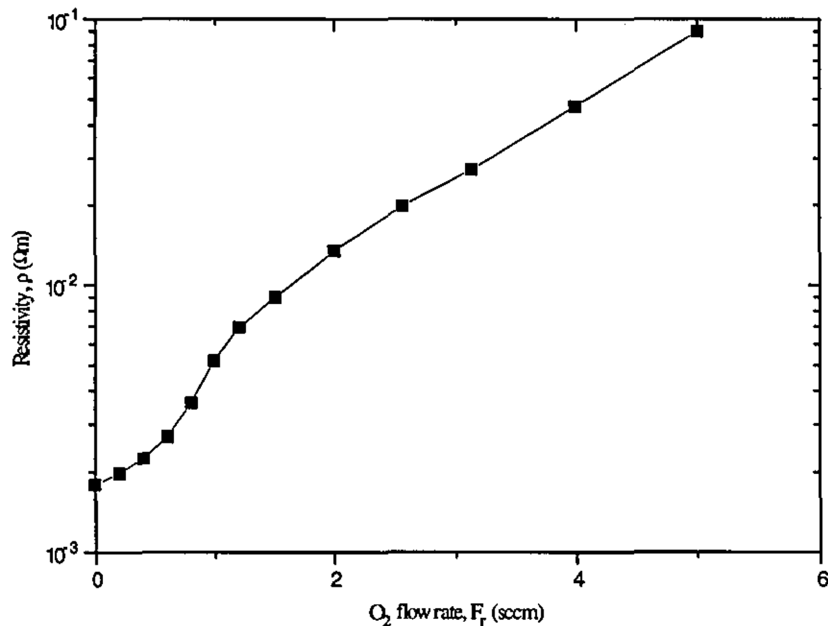

Figure 10.18 : Variation in resistivity as a function of O_2 flow rate for ZnO:Al deposited from the compacted ZnO:Al target

Figure 10.18 shows the variation in resistivity with O_2 flow rate. It can be seen that the minimum resistivity, $\rho = 1.8 \times 10^{-3}$ Ωm, was obtained when sputtering in pure Ar. Ogawa *et al* [24] have reported a sheet resistance of 200 $\Omega\square^{-1}$ using an identical target supplied by Arconium, the suppliers of the ZnO:Al target used during this work. It was determined, however, that the base pressure they obtained was $<1 \times 10^{-7}$ torr. It was concluded that the base pressure of the system used in this work was not low enough and that the impurities introduced into the film degraded its electrical performance.

10.2.2.2 Zn:Al tiled target

Two techniques are regularly used to introduce small concentrations of a dopant into a thin film. The first is to simultaneously sputter two cathodes [25], with one cathode operating at a relatively low power to provide the dopant. The alternative, used throughout this section of work, capitalises on the well documented property [26-29] of sputtering, in that where a target is a composite of several different materials, the film composition reflects that of the target.

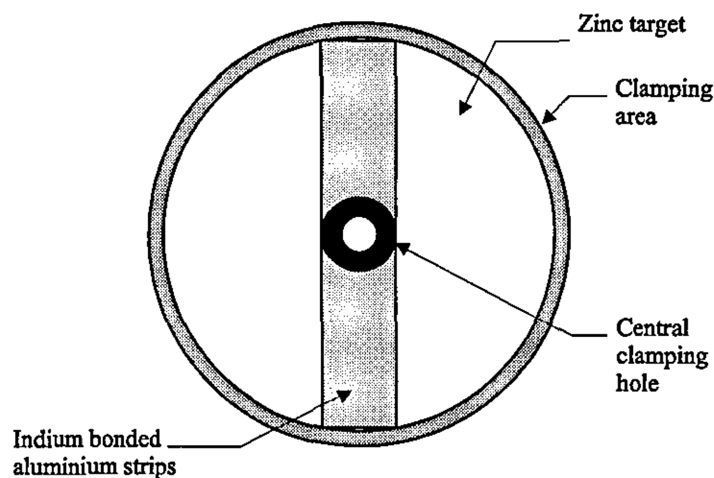

Figure 10.19 : Bonding of aluminium strips to the zinc target

Strips of aluminium were cut to widths of increasing units of 5 mm, and bonded across the diameter of the zinc target with indium, figure 10.19. The bonding process involved melting indium to the back of the aluminium strips and the target surface to be covered.

The two surfaces were then brought into contact, the target heated on a hot-plate, and allowed to cool, creating a durable and electrically 'sound' bond.

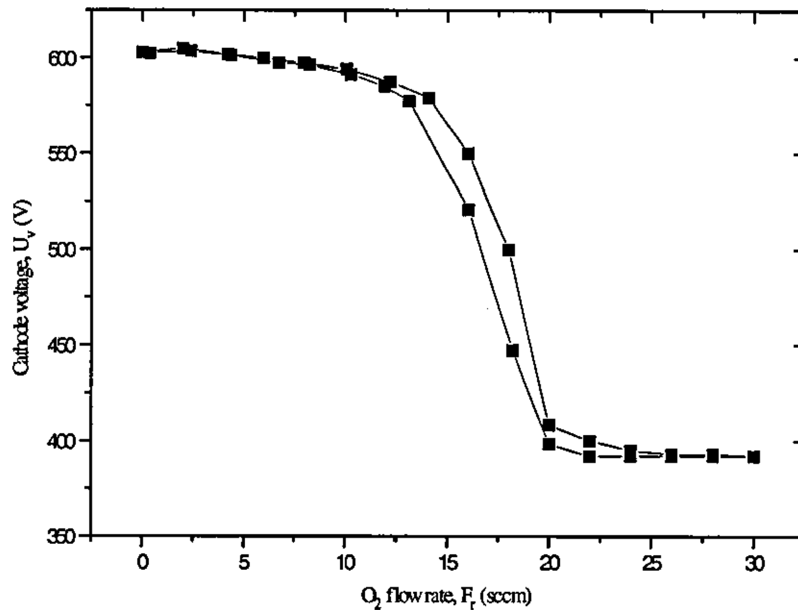

Figure 10.20 : Variation of cathode voltage as a function of O_2 flow rate for Zn/Al_{10mm} tiled target

Throughout the deposition of ZnO:Al from the tiled target, a DC power of 500 W and an Ar_{pp} of 3 mtorr was maintained. The deposition time was 2 minutes unless otherwise stated. Figure 10.20 shows the variation of the cathode voltage with oxygen flow rate, F_r, for a target with 10 mm strips. It can be seen that the measure, ϕ_v, of the target status showed a slight hysteresis during the addition of oxygen. The plasma emission followed a similar trend. It was decided, however, that the voltage would be used as the control signal, as plasma emission had been used unsuccessfully by other workers during the deposition of ZnO:Sn [18].

Table 10.3 shows the variation in cathode voltage in elemental mode for various strip thicknesses of Al. Aluminium has a higher secondary electron coefficient to zinc, and hence, a lower operating voltage. The relatively small amount of aluminium on the target shifts the discharge characteristics significantly towards those of pure Al, owing to the strong reactivity of O_2 with Al.

Al strip thickness	0	5	10	15	20	25
% of Target area	0	7.5	14	18	26	34
Cathode voltage , Uc	667	620	603	580	574	547

Table 10.3 : Variation in cathode voltage as a function of percentage Al target coverage

Initially, continuous feedback control was attempted with a zinc target, with no aluminium pieces present. Accurate control at any point on the U_c/F_r curve was obtained, and figure 10.21 shows the variation of resistivity and transmission, at 550 nm, of the films as a function of set-point, ϕ_V. It can be seen that undoped ZnO does not provide the desired conductivity. The lowest resistivity obtained for a sample that had acceptable optical properties (*i.e.* an average transmission > 70% across the visible spectrum) was 5.3 x 10^{-3} Ω m, a factor of 2000 larger than was obtained for ITO.

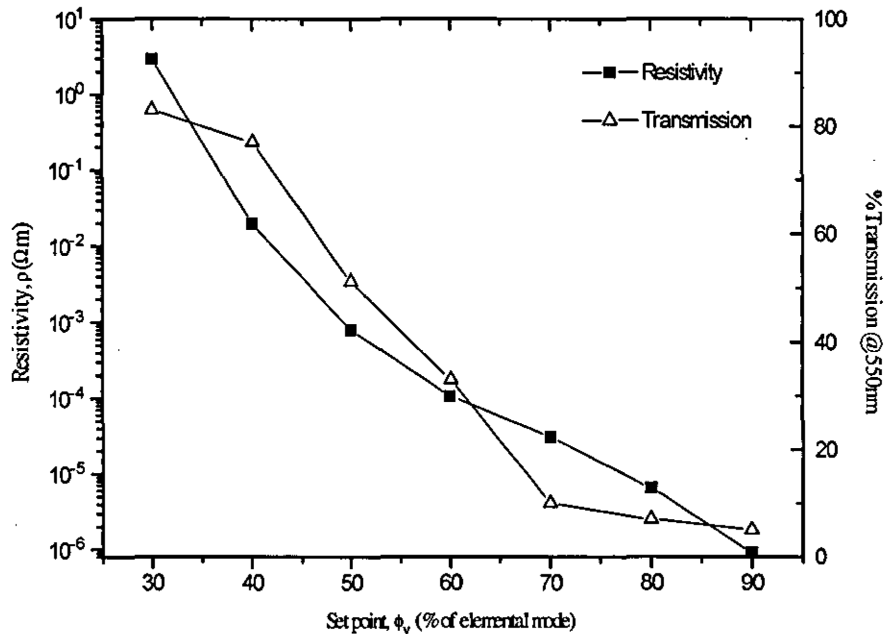

Figure 10.21 : Variation in resistivity and transmission as a function of set-point using CFC to deposit ZnO from a zinc target

As initially thought, it was, thus, necessary to dope the ZnO films to enhance their electrical properties. 5 mm Al strips were bonded to the surface of the target, as

described above, and the process was initiated. Stable control was still achieved using CFC. However, arcing, caused by poisoning of the Al strips, occurred during some of the deposition runs. Moreover, the resistivity was not significantly altered by the addition of the aluminium strips. Larger strips were bonded to the target but still had no significant effect on the resistivity of the film.

Auger analysis was performed on the samples and revealed that no detectable aluminium was being incorporated in the film, even when 40% of the target was covered. The full results obtained from Auger analysis are given at the end of this section. The problem seemed to originate from the control technique. As mentioned previously, Al_2O_3 has a larger negative enthalpy of formation than ZnO (ΔHf_{Al2O3} = -1670 Kg mol^{-1}, ΔHf_{ZnO} = -348 Kg mol^{-1} [30]) and is, hence, more readily oxidised. It was, thus, possible that when controlling at the correct set-point to enable stoichiometric ZnO to be deposited, the aluminium strips were completely oxidised. Al_2O_3 has a deposition rate 4-9 times smaller than Al [31]. Thus, it was concluded that insignificant amounts of Al were being incorporated into the coating.

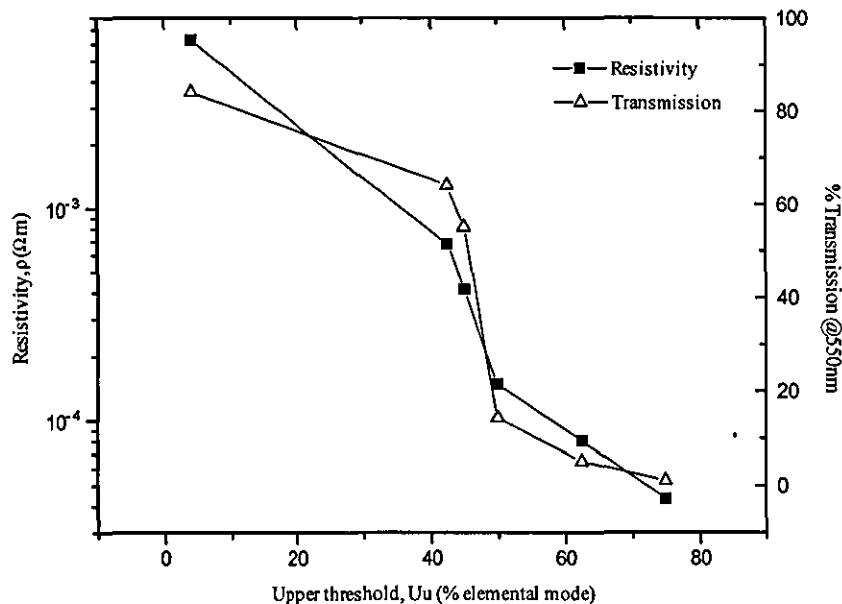

Figure 10.22 : Variation in resistivity and transmission as a function of upper threshold using the SPPA process to deposit ZnO:Al from a Zn/Al_{5mm} tiled target

It was decided to pulse the reactive gas into the chamber in an attempt to increase the amounts of Al incorporated into the coating. It was thought that if the oxygen could be directed away from the chamber, then pure aluminium could be sputtered and incorporated into the film. The gas flow rate was set at 22 sccm and low threshold, U_l, to 16% and all other conditions were kept constant. Figure 10.22 shows the variation in resistivity and transmission at 550 nm obtained with upper threshold, U_u, for 5 mm strips of Al. Lower resistivities ($\rho \sim 1.6 \times 10^{-3}$ Ω m) were now being obtained for films of similar optical properties to those obtained with ZnO.

Figure 10.23 shows the variation of resistivity with transmission at 550 nm for films with 5 mm, 10 mm, 15 mm, 20 mm, and 25 mm strips of aluminium respectively.

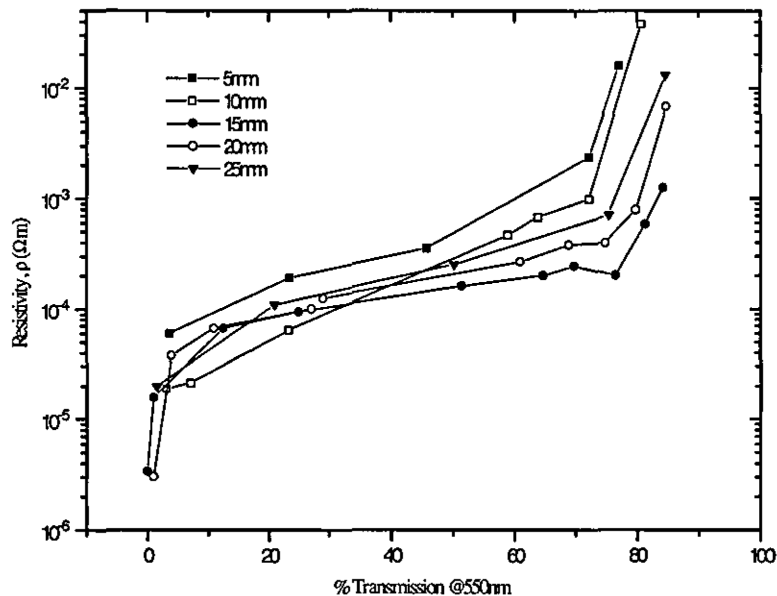

Figure 10.23 : Variation in resistivity as a function of percentage transmission at 550nm for ZnO:Al films deposited using the SPPA process from a $Zn/Al_{5\text{-}25mm}$ tiled target

Figure 10.24 shows the variation in resistivity at 75% transmission (550 nm) with strip thickness. It can be seen that the minimum resistivity should occur when strips of aluminium 17 mm thick are used. Strips of this thickness, 21% of the total target area, were bonded to the zinc target and samples were again deposited using the SPPA technique in the same configuration as described above.

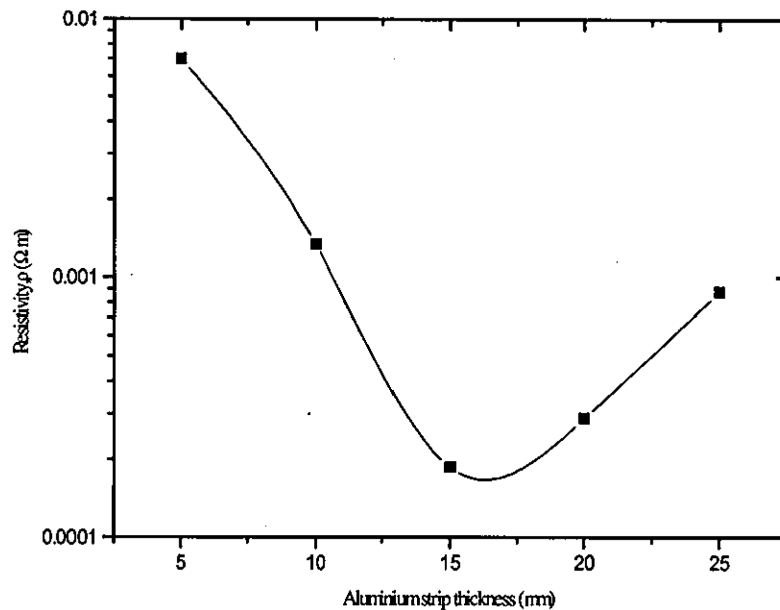

Figure 10.24 : Predicted ρ_{min} as a function of aluminium strip thickness for ZnO:Al films deposited from a Zn/Al tiled target using the SPPA process

Figure 10.25 shows the transmission curves for a series of samples deposited at varying set points, U_u. Figure 10.26 shows the variation of resistivity with transmission at 550 nm. It can be seen that there now appears to be a significant drop in resistivity under specific sputtering conditions. This drop in resistivity ($\rho_{min} = 4.11 \times 10^{-5}$ Ωm) occurred at an upper threshold of 40% and is associated with the formation of stoichiometric ZnO:Al. The deposition rate at this set-point was 1.7 nms^{-1} and the film's refractive index was 2.09. The stress in the film was measured to be 1.05 GPa.

Post-deposition annealing in argon at 400 °C, for one hour, was attempted on selected samples to increase transmission and reduce resistivity. However, the resistivity rose by a factor of at least 500 in all the samples analysed. This feature corresponds to the work by Minami *et al* [32], who quote a change in resistivity from 4×10^{-6} Ωm to 5×10^{-3} Ωm for ZnO:Al, following post-deposition annealing in air for one hour at 400 °C. In hindsight, the annealing time may have been too long. Ellmer *et al* [33] showed that annealing ZnO:Al films in air at 400 °C for 5 minutes reduced the resistivity by a factor of 2, any longer resulted in deterioration in the film's electrical properties.

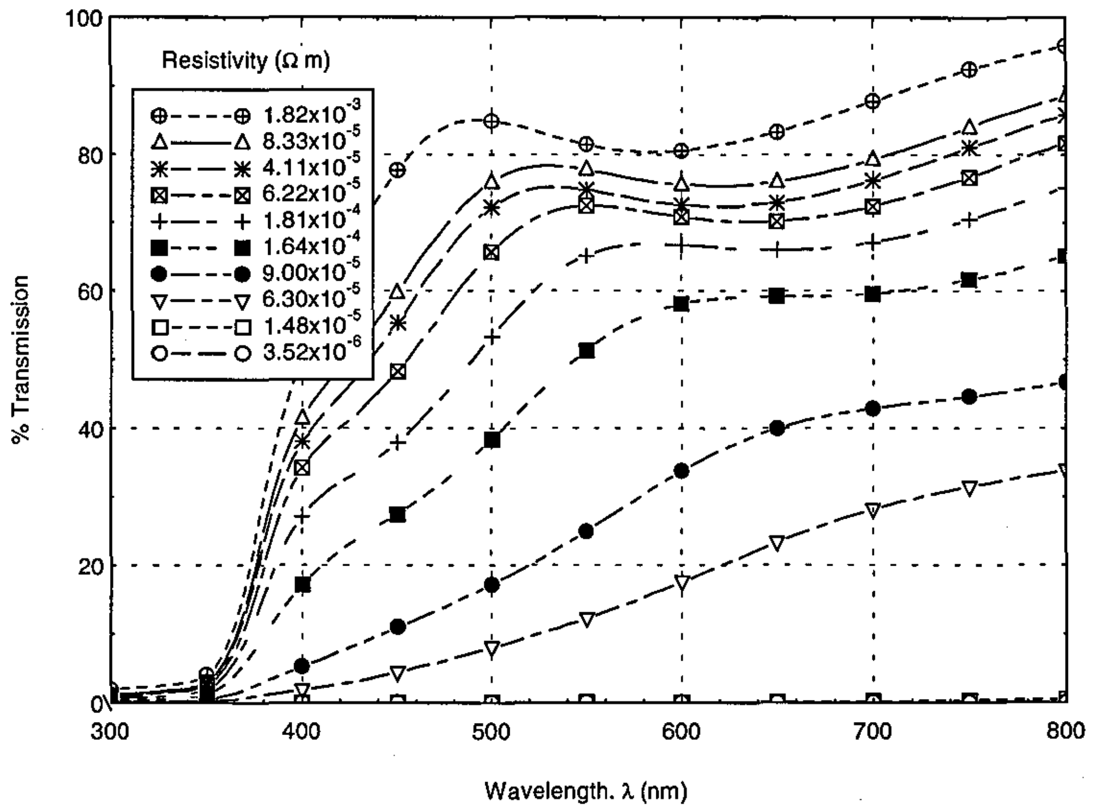

Figure 10.25 : Optical transmission curves for ZnO:Al films deposited at various upper threshold levels from a Zn/Al_{17mm} tiled target

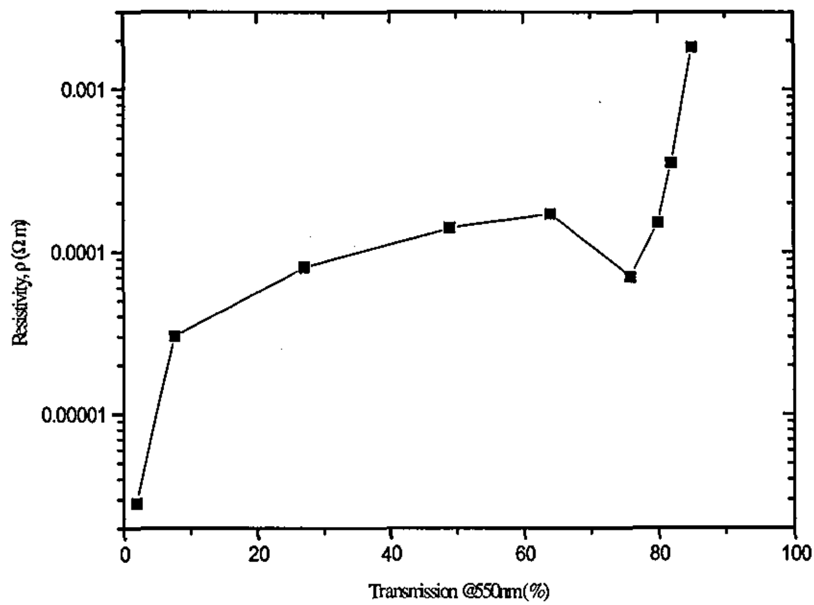

Figure 10.26 : Variation in resistivity and transmission as a function of percentage transmission using the SPPA process to deposit ZnO:Al from a Zn/Al_{17mm} tiled target

Auger analysis was performed on selected samples to determine the Zn:Al ratio and percentage weight of Al in the film. It was determined that the surface of the films was contaminated, with C, S and Cl omnipresent. Table 10.4 shows the atomic percentages of aluminium, zinc and oxygen in films grown with various amounts of aluminium bonded to the target surface. The detection limit for aluminium was 0.2%. It should also be noted that when performing the depth profiling, Al detection is increased owing to the preferential sputtering of the zinc (sputter yield of Zn ~ 4, *c.f.* Al ~1.3). Hence, the results have been modified for preferential sputtering. Also detailed in table 10.4 are the percentages for a film made using CFC.

% target coverage of Al	Atomic % Al	Zn	O	Al % by weight
	As a % of the total Al, Zn and O in the film.			
7.5	1.0	48.0	51.0	0.68
14	1.8	48.6	49.6	1.22
18	2.4	47.3	50.3	1.66
21 (17 mm strips)	2.6	47.6	49.8	1.80
26	2.0	44.0	54.0	1.44
34	1.7	42.3	56.0	1.25
40 Using CFC	0.3	50.1	49.6	0.20

Table 10.4 : Auger analysis results showing the percentage Al in the ZnO:Al films

The results show that the film that exhibited the best electrical properties has the highest aluminium content by weight, 1.80%. It has been well documented [33] that in order to get the best electrical and optical properties, 2% weight Al has to be incorporated into the film.

10.3 Aluminium oxide, Al_2O_3

Aluminium oxide is a versatile film used in both the electrical industry as a passivating layer in semiconductor devices, and in optics as a transparent, protective, and hard wearing film.

Very little work was undertaken on analysing Al_2O_3 films deposited during the course of this research, but it warrants a mention because the rectified AC technique was developed whilst depositing Al_2O_3. Aluminium severely arcs under DC power when reactively sputtering [34] and any control of the gas into the sputtering environment is completely impossible. The reasons for this are given in section 4.3.1. The problem is worse for aluminium because of its large negative enthalpy of formation with oxygen, coupled with the insulating properties of the Al_2O_3 formed on the target surface. Previously, Al_2O_3 has been sputtered by RF diode sputtering [1] of aluminium in an argon-oxygen atmosphere. However, only low deposition rates, typically 0.2 - 0.6 nms^{-1}, can be achieved and expensive power supplies means the technique is rarely used in industry.

Rectified AC power deliverance, as detailed in section 6.4.1.1 completely stopped the target from arcing when sputtering Al_2O_3 and enabled accurate gas control. Therefore, CFC control using the cathode voltage as control signal could be used throughout this section of work. Stoichiometric Al_2O_3 was deposited with characteristics as detailed in table 10.5. The major purpose of Al_2O_3 is as a protective barrier layer, and hence, the hardness of the coating was quantitatively assessed whilst varying the ion bombardment. The films were deposited at 250 W and an Ar_{pp} of 3 mtorr, using the anode in both a grounded and floating state as a means of controlling the ion current. Deposition time was 15 minutes.

	Grounded anode	**Floating anode**
Refractive index, n_f	1.62	1.71
Intrinsic stress, σ	0*	0*
Ion current, I_{si}	1.0 $mAcm^{-2}$	3.4 $mAcm^{-2}$
Deposition rate, R	0.61 nms^{-1}	0.57 nms^{-1}
Durability	From qualitative assessment, the sample made whilst the anode was floating was significantly harder	

* The stress was too small to measure.

Table 10.5 : Properties of the Al_2O_3 films deposited using CFC and rectified power application

10.4 The ion/atom ratio

Table 10.6 summaries the ion/atom ratio and the energy per depositing atom achieved for each material at the substrate (calculated from equation 5.3). The deposition parameters given are those obtained under optimum coating conditions.

Material	**Deposition conditions Ar_{pp} in mtorr**	**Refractive index/ resistivity, ρ (Ω m)**	**Deposition rate, R (nms^{-1})**	**Ion current, Isi ($mAcm^{-2}$)**	**ion to atom ratio, n_i/n_a**	**Energy per depositing atom (eV)**
SiO_2	SPPA 200 W Ar_{pp} = 3.0 AC Power	nf=1.46	0.71	3.35	10.8	150
ITO	Compacted oxide target 200 W Ar_{pp} = 4.5 Fr = 0.9 sccm DC Power	$\rho = 5.7x10^{-6}$	0.87	4.1	5.2	78
ITO	SPPA In/Sn target 200 W A_{pp} = 3.0 DC Power	$\rho = 6.1x10^{-6}$	1.12	9.0	10.8	141
ZnO:Al	SPPA Zn/Al target 500 W Ar_{pp} = 3.0 DC Power	$r = 6.0 \times 10^{-5}$	1.70	8.1	5.0	65
Al_2O_3	CFC 250 W Ar_{pp} = 3.0 AC Power	n_f = 1.71	0.57	3.4	2.97	46

Table 10.6 : Deposition flux properties for SiO_2, ITO, ZnO:Al and Al_2O_3 films

The energy per atom was greater than that necessary for the bond formation in all the compounds deposited (typically 20 - 30 eV is needed to form the bonds). Hence, there was enough energy left to densify the structure of the film and ensure favourable mechanical properties.

10.5 Chapter summary

- The problems encountered with the instabilities in the reactive deposition process have been overcome by a combination of SPPA control to minimise target poisoning and decrease sensitivity to process aberrations, and rectified AC to reduce instabilities within the process.

- The SPPA process was shown to be successful in the deposition of a number of materials; including TiO_2, SiO_2, ITO and ZnO:Al. Each material had significantly different optical, electrical and mechanical properties illustrating the versatility of the process.

- The rectified AC power supply completely suppressed the formation of any arcs during the sputtering of SiO_2 and Al_2O_3.

- All the films deposited were found to be in a state of compressive stress. The magnitude of this stress was found to be dependent on ion current.

- A peak was observed in the σ/n_f curve for SiO_2 films deposited by CFC and SPPA control processes. The peak coincided with the production of stoichiometric SiO_2.

- An ITO compacted target was shown to provide a simple alternative to the reactive sputter deposition of indium tin oxide. However, when versatility in the deposition parameters (such as film stoichiometry) and high deposition rates are required, the SPPA reactive control process proved to be more advantageous.

- ZnO:Al was successfully deposited with a resistance minimum, $\rho_{min} = 5.7 \times 10^{-5}\ \Omega m$, from a Zn/Al tiled target using SPPA to control the flow of oxygen into the system. Aluminium doping of the film could not be achieved by using CFC control techniques as the Al strips poisoned at a significantly different O_{pp} that Zn, forming Al_2O_3.

CHAPTER 10 REFERENCES

[1] **Pawlewicz, W.T., Martin, P.M., Hays, D.D. & Mann, I.B.,** (1982). *Optical Thin Films,* 325, 105-116.

[2] **Westra, S.W.T.,** (1995). *Proc. of the 3rd ISSP,* Tokyo, 301-305.

[3] **Suzuki, K., and Howson, R.P.,** (1983). *Proc. Int. Ion Eng.,* vol.2 p.889.

[4] **Schiller, S., Beister, G., Schneider, S. & Sieber, W.,** (1980). *Thin Solid Films,* 72, 475.

[5] **Howson, R.P., Suzuki, K., Bishop, C.A. & Ridge, M.I.,** (1984). *Vacuum,* 34, 291-294.

[6] **Applied Vision Ltd.,** (1993-1995).

[7] **Spencer, A.G.,** *'High rate reactive magnetron sputtering',* (1989). Ph.D. Thesis, Loughborough University of Technology, U.K.

[8] **Cerny, R., Kuzel, R. & Valvoda, V.** (1994). *Surface And Coatings Technology,* 64, 111-117.

[9] **Frank, G., Kauer, E. & Kostlin, H.,** (1981). *Thin Solid Films,* 77, 107-117.

[10] **Dubow, J.B. & Burk, D.E.,** (1976). *Appl. Phys. Lett.,* 29, 494.

[11] **Puyane, R.,** (1981). *Thin Solid Films,* 77.

[12] **Fillard, J.P. & Manifacier, J.C.,** (1970). *Jp. J. Appl. Phys.,* 9, 1012.

[13] **Pawlewicz, W.T., Mann, I.B. & Lowdermilk, W.H.,** (1979). *Appl. Phys. Lett.,* 34, 196.

[14] **Ito, K. & Nakazawa, T.,** (1979). *Surf. Sci.,* 86, 492.

[15] **Howson, R.P., Danson, N., Safi, I. & Hall, G.W.,** (1996). To be published in *J. Vac. Sci. Technol.*.

[16] **Howson, R.P. & Ja'fer, H.A.,** (1992). *J. Vac. Sci. Technol.,* A10, 1784.

[17] **Mukherjee, A.,** (1989). *Vacuum,* 39(6), 537-540.

[18] **Hall, G.W.,** (1993). *'Control of the properties of semiconducting thin films deposited using magnetron sputtering',* Ph.D. Thesis, Loughborough University of Technology, U.K..

[19] **Larsson, T.,** (1989). *Vacuum,* 39, 949-954.

[20] **Vasanelli, L., Valentini, A. & Losacco, A.,** (1987). *Sol. Energy Mat.,* 16, 91.

[21] **Zin, Z.C. & Granqvist, C.G.,** (1987). *SPIE,* Vol. 823, 28-35.

[22] **Maniv, S., Miner, C.J. & Westwood, W.D.,** (1983). *J. Vac. Sci. Technol.,* A1(3), 1370-1375.

[23] **Harding, G.L., Window, B. & Horrigan, E.C.,** (1991). *Solar Energy Materials,* 22, 69-91.

[24] **Ogawa, N., Iwamoto, T., Mouri, T., Minami, T., Satoh, H. & Takata, S.,** (1994). *Society Of Vacuum Coaters,* 37th Annual Technical Conference Proceedings, 41-46.

[25] **Anderson, G.S., Jorgenson, G.V. & Wehner, G.K.,** (1966). Applied Science Division, *Litton Annual Report on Sputtering,* ONR Contract, 1589(15).

[26] **Flur, B.L. & Riseman, J.,** (1964). *J. Appl. Phys.,* 35, 344.

[27] **Khan, I.H. & Francombe, M.H.,** (1965). *J. Appl. Phys.,* 36, 1699.

[28] **Patterson, W.L. & Shirn, G.A.,** (1967). *J. Vac. Sci. Technol.,* 4, 343.

[29] **Sernelius, B.E., Berggren, K.F., Jin, Z.C., Hamberg, I. & Granqvist, C.G.,** (1988). *Phys. Rev. B,* 37(17), 1024.

[30] **Weast, R.C.,** 62nd Ed., (1981). *'Handbook of Chemistry and Physics'*, CRC Press.

[31] **Zafer, S., Ferekides, C.S., Morel, D.L.,** (1995). *J. Vac. Sci. Technol.,* 13, 2177.

[32] **Minami, T., Oohashi, K., Takata, S., Mouri, T. & Ogawi, N.,** (1990). *Thin Solid Films,* 193/194, 721-729.

[33] **Ellmer, K., Kudella, F., Mientus, R., Schieck, R. & Fiechter, S.** (1994). *Thin Solid Films,* 247, 15-23.

[34] **Frach, P., Heisig, U., Gottfried, Ch. & Walde, H.,** (1993). *Surface and Coatings Technology,* 59, 177-182.

CHAPTER 11

CONCLUSIONS AND FUTURE WORK

The objective of this work was two-fold. Firstly to devise and evaluate novel techniques for the control of the reactive sputtering process and secondly, to analyse the effect these techniques had on resultant film properties.

It has been shown that the measurement of magnetron potential is an accurate alternative to PEM as an indication of the poisoned state of the cathode for Al_2O_3, ITO, SiO_2 and ZnO:Al. Monitoring the potential has obvious advantages over PEM as no expensive optics equipment is necessary and no short term drift exists. It does not, however, work for all materials and observations of TiO_2 showed that a dual set-point occurred as a function of reactive gas flow.

A novel technique to control the process of reactive magnetron sputtering was successfully constructed and developed. The technique, termed successive pulsed plasma anodisation (SPPA), consisted of pulsing the reactive gas flow into the deposition environment. It enabled greater stoichiometric control during the deposition of optical, electrical and mechanical films than that obtained with conventional continuous feedback processing techniques. Greater versatility and increased process tolerance were also achieved using the SPPA process.

Another, perhaps not so obvious, advantage of the SPPA system over the CFC system was that the response time of the SPPA system was not as critical as for the CFC system. Whilst the piezo-electric valve in the CFC system needed a response time of ~1 ms to respond to any changes in target conditions, the SPPA system only needed to divert the reactive gas flow approximately every 1 second (half the typical pulsing period). This represents an opportunity for further work in that the SPPA process could easily by controlled by a computer. By controlling the pulsing threshold levels, computer control could allow more elaborate films to be deposited such as graded index filters.

Whilst it is recognised that in the last few years much work has been undertaken in the search for arc-free deposition of insulating compounds during reactive sputtering, rectifying the dual outputs of an AC power supply proved to be a significant advancement. It allowed an existing AC supply to be modified and used with one magnetron, but still providing charge neutralisation, which is an obvious economic advantage over the TwinMAG^{TM} arrangement. Al_2O_3 was successfully deposited from an aluminium target with a deposition rate of 0.57 nms^{-1} at a power of 250 W.

It was shown that placing an anode in front of the magnetron gave the desired modification of the substrate ion current. This technique, allied with variable argon partial pressure used to modify the ion current at the substrate, was shown to have beneficial effects on the film properties. Examination of the intrinsic stress in the films emphasised a direct correlation between ion current and stress, indicating that the ion bombardment from the unbalanced magnetron changing the film properties. An average energy per depositing atom of ~50 - 140 eV was measured. This was enough to activate the oxygen molecules, leaving sufficient energy to modify the film structure. It is suggested that any further investigation on the effects of the ion current on film properties should concentrate on film microstructure.

From the collated refractive index, film thickness and optical transmission data, it was shown that reactive deposition by pulsing oxygen into the system could be realised for SiO_2. Iteration along the refractive index/upper threshold figure enabled precise selection of the film index to be made within 0.5%. Furthermore, the SPPA process showed greatly enhanced process stability compared with CFC during the deposition of SiO_2.

The investigations into two contrasting techniques used in the deposition of transparent conducting oxides proved very interesting. CFC was unsuccessful whilst using the cathode potential as an indicator of target status during the reactively depositing ITO and ZnO:Al. However, process control complications, introduced by the hysteresis effect inherent in reactive sputtering, were overcome successfully using SPPA.

Deposition of ITO from a compacted oxide target using a DC power source gave films with transmission in excess of 75% across the visible spectrum and resistivities of ~ 6 x 10^{-6} Ωm. It proved to be the simplest of the two techniques to initialise and control, with considerable tolerance affordable in deposition conditions. However, if it is acceptable to have less tolerance in these conditions and a more versatile deposition system, then films with higher deposition rates can be obtained using reactive sputtering. The SPPA process produced films with comparable electrical and optical properties at a deposition rate 28 % higher than those produced with the compacted oxide.

Probably one of the most noteworthy advantages of SPPA was realised whilst depositing ZnO:Al. CFC was unable to control the reactive deposition of ZnO:Al from a Zn/Al alloy tiled target and could not achieve Al doping in the ZnO film. This was shown to be caused by the aluminium strips poisoning at a different O_{pp} than the Zn target, and hence, significantly lowering the deposition rate of aluminium. The SPPA process overcame this problem by its successive metal deposition and anodisation procedure. It made the experiment of finding the optimum doping possible in a simple way that can be applied to many different materials. The minimum film resistivity obtained was 6.0 x 10^{-5} Ωm and Auger analysis indicated that 2% Al by weight was incorporated in the film. It would be interesting to investigate higher cathode powers in an attempt to provide *in situ* bombardment, and hence, reduce the resistivity without the need for any post-deposition annealing.